

Magazine of Civil Engineering

106(6), 2021

ISSN
2712-8172





ПОЛИТЕХ
Санкт-Петербургский
политехнический университет
Петра Великого

Инженерно-строительный институт
Центр дополнительных профессиональных программ
195251, г. Санкт-Петербург, Политехническая ул., 29,
тел/факс: 552-94-60, www.stroikursi.spbstu.ru,
stroikursi@mail.ru

**Приглашает специалистов организаций, вступающих в СРО,
на курсы повышения квалификации (72 часа)**

Код	Наименование программы	Виды работ*
Курсы по строительству		
БС-01-04	«Безопасность и качество выполнения общестроительных работ»	п.1,2, 3, 5, 6, 7, 9, 10, 11, 12, 13, 14
БС-01	«Безопасность и качество выполнения геодезических, подготовительных и земляных работ, устройства оснований и фундаментов»	1,2,3,5
БС-02	«Безопасность и качество возведения бетонных и железобетонных конструкций»	6,7
БС-03	«Безопасность и качество возведения металлических, каменных и деревянных конструкций»	9,10,11
БС-04	«Безопасность и качество выполнения фасадных работ, устройства кровель, защиты строительных конструкций, трубопроводов и оборудования»	12,13,14
БС-05	«Безопасность и качество устройства инженерных сетей и систем»	15,16,17,18,19
БС-06	«Безопасность и качество устройства электрических сетей и линий связи»	20,21
БС-08	«Безопасность и качество выполнения монтажных и пусконаладочных работ»	23,24
БС-12	«Безопасность и качество устройства мостов, эстакад и путепроводов»	29
БС-13	«Безопасность и качество выполнения гидротехнических, водолазных работ»	30
БС-14	«Безопасность и качество устройства промышленных печей и дымовых труб»	31
БС-15	«Осуществление строительного контроля»	32
БС-16	«Организация строительства, реконструкции и капитального ремонта. Выполнение функций технического заказчика и генерального подрядчика»	33
Курсы по проектированию		
БП-01	«Разработка схемы планировочной организации земельного участка, архитектурных решений, мероприятий по обеспечению доступа маломобильных групп населения»	1,2,11
БП-02	«Разработка конструктивных и объемно-планировочных решений зданий и сооружений»	3
БП-03	«Проектирование внутренних сетей инженерно-технического обеспечения»	4
БП-04	«Проектирование наружных сетей инженерно-технического обеспечения»	5
БП-05	«Разработка технологических решений при проектировании зданий и сооружений»	6
БП-06	«Разработка специальных разделов проектной документации»	7
БП-07	«Разработка проектов организации строительства»	8
БП-08	«Проектные решения по охране окружающей среды»	9
БП-09	«Проектные решения по обеспечению пожарной безопасности»	10
БП-10	«Обследование строительных конструкций и грунтов основания зданий и сооружений»	12
БП-11	«Организация проектных работ. Выполнение функций генерального проектировщика»	13
Э-01	«Проведение энергетических обследований с целью повышения энергетической эффективности и энергосбережения»	
Курсы по инженерным изысканиям		
И-01	«Инженерно-геодезические изыскания в строительстве»	1
И-02	«Инженерно-геологические изыскания в строительстве»	2,5
И-03	«Инженерно-гидрометеорологические изыскания в строительстве»	3
И-04	«Инженерно-экологические изыскания в строительстве»	4
И-05	«Организация работ по инженерным изысканиям»	7

*(согласно приказам Минрегионразвития РФ N 624 от 30 декабря 2009 г.)

**По окончании курса слушателю выдается удостоверение о краткосрочном повышении
квалификации установленного образца (72 ак. часа)**

Для регистрации на курс необходимо выслать заявку на участие, и копию диплома об образовании по телефону/факсу: 8(812) 552-94-60, 535-79-92, , e-mail: stroikursi@mail.ru.

Magazine of Civil Engineering

SCHOLAR JOURNAL

ISSN 2712-8172

Свидетельство о государственной регистрации:
Эл № ФС77-77906 от 19.02.2020,
выдано Роскомнадзором

Специализированный научный журнал.

Выходит с 09.2008.

Включен в Перечень ВАК РФ

Индексируется в БД Scopus

Периодичность: 8 раз в год

Учредитель и издатель:

Санкт-Петербургский политехнический университет
Петра Великого

Адрес редакции:

195251, СПб, ул. Политехническая, д. 29

Главный редактор:

Екатерина Александровна Линник

Научный редактор:

Виталий Владимирович Сергеев

Заместитель главного научного редактора:

Галина Леонидовна Козинец

Редакционная коллегия:

PhD, проф. Т. Аввад;
д.т.н., проф. М.И. Бальзанников
д.т.н., проф. А.И. Белостоцкий;
к.т.н., проф. А.И. Боровков;
д.т.н., проф. А. Бородинец;
PhD, проф. М. Велькович;
PhD, проф. Р.Д. Гарг;
PhD, М.Р. Гарифуллин;
Dr.-Ing, проф. Т. Грис;
д.т.н., проф. Т.А. Дацюк;
д.т.н., проф. В.В. Елистратов;
Dr.-Ing., проф. Т. Кэрки;
д.т.н., проф. Д.В. Козлов;
д.т.н., доцент С.В. Корниенко;
д.т.н., проф. Ю.Г. Лазарев;
д.т.н., проф. М.М. Мухаммадиев;
Dr.-Ing. Habil., проф. Х. Пастернак;
Dr.-Ing., проф. Ф. Рёгинер;
д.т.н., проф. Т.З. Султанов;
д.т.н., проф. М.Г. Тягунов;
акад. РАН, д.т.н., проф. М.П. Федоров;
Dr.-Ing., проф. Д. Хецк;
д.г.-м.н. А.Г. Шашкин;
д.т.н. В.Б. Штильман

Дата выхода: 29.10.2021

© ФГАОУ ВО СПбПУ, 2021

© Иллюстрация на обложке: Илья Смагин

Magazine of Civil Engineering

SCHOLAR JOURNAL

ISSN 2712-8172

Peer-reviewed scientific journal

Start date: 2008/09

8 issues per year

Publisher:

Peter the Great St. Petersburg Polytechnic University

Indexing:

Scopus, Web of Science (ESCI, RSCI), Compendex,
EBSCO, Google Academia, Index Copernicus, ProQuest,
Ulrich's Serials Analysis System, CNKI

Corresponding address:

29 Polytechnicheskaya st., Saint-Petersburg, 195251,
Russia

Editor-in-chief:

Ekaterina A. Linnik

Science editor:

Vitaly V. Sergeev

Deputy chief science editor:

Galina L. Kozinetc

Editorial board:

T. Awwad, PhD, professor
M.I. Balzannikov, D.Sc., professor
A.I. Belostotsky, D.Sc., professor
A.I. Borovkov, PhD, professor
A. Borodinecs, Dr.Sc.Ing., professor
M. Veljkovic, PhD, professor
R.D. Garg, PhD, professor
M. Garifullin, PhD, postdoctorant
T. Gries, Dr.-Ing., professor
T.A. Datsyuk, D.Sc., professor
V.V. Elistratov, D.Sc., professor
T. Kärki, Dr.-Ing., professor
D.V. Kozlov, D.Sc., professor
S.V. Korniyenko, D.Sc., professor
Yu.G. Lazarev, D.Sc., professor
M.M. Muhammadiev, D.Sc., professor
H. Pasternak, Dr.-Ing.habil., professor
F. Rögener, Dr.-Ing., professor
T.Z. Sultanov, D.Sc., professor
M.G. Tyagunov, D.Sc., professor
M.P. Fedorov, D.Sc., professor
D. Heck, Dr.-Ing., professor
A.G. Shashkin, D.Sc.
V.B. Shtilman, D.Sc.

Date of issue: 29.10.2021

© Peter the Great St. Petersburg Polytechnic University.
All rights reserved.

© Coverpicture – Ilya Smagin

Contacts:

E-mail: mce@spbstu.ru

Web: <http://www.engstroy.spbstu.ru>

Contents

Auta, S.M., Jamiu, O., Alhaji, A. Effect of vertical circular openings on flexural strength of reinforced concrete beam	10601
Dashevskij, M.A., Mitroshin, V.A., Mondrus, V.L., Sizov, D.K. Impact of metro induced ground-borne vibration on urban development	10602
Fedosov, S.V., Malichenko, V.G., Toropova, M.V. Formation of a software calculation model for restoring building structures after a fire	10603
Suwaid, H., Aziz, K., Hama, S. Behavior of composite steel plate- sustainable concrete slabs under impact loading	10604
Sabitov, Y.Y., Dyusseminov, D.S., Zhumagulova, A.A., Bazarbayev, D.O., Lukpanov, R.E. Composite non-autoclaved aerated concrete based on an emulsion	10605
Kurochkina, K.A., Suleimanova, L.A., Kolomatsky, A.S. Porosity of autoclave aerated concrete and foam concrete: origin of porosity and pore size	10606
Shekhovtsova, S.Yu., Korolev, E.V. Nanomodified rejuvenators and protective materials for asphalt concrete	10607
Lesovik, V.S., Ahmed, A.A., Fediuk, R.S., Kozlenko, B., Mugahed Amran, Y.H., Alaskhanov, A.Kh., Asaad, M.A., Murali, G., Uvarov, V.A. Performance investigation of demolition wastes-based concrete composites	10608
Tupikova, E.M., Rynkovskaya, M.I. Analytical approach to stress-strain analysis of right and oblique helicoid structures	10609
Waruwu, A., Deni Susanti, R., Napitupulu, N., Oges Sihombing, J. The combination of bamboo grid and concrete pile as soil reinforcement under the embankment	10610
Korolev, A.S., Vatin, N. Layer model in elasticity modulus of cement composites with the light aggregate predicting	10611
Al-Rousan, R. Impact of elevated temperature on the behavior of strengthened RC beams with CFRP	10612
Kiselev, V.G., Kalyutik, A.A. Corrosive behavior of low-alloy structural steels	10613
Ramezani, M. Performance of composite connections strengthened with CFRP laminate	10614
Cherkashin, A.V., Radaev, A.E., Olekhovich, Y.A., Sulatskiy, K.S. The dependence of the gathering characteristics of nanocarbon cement on the parameters of its production process	10615



DOI: 10.34910/MCE.106.1

Effect of vertical circular openings on flexural strength of reinforced concrete beam

S.M. Auta* , O. Jamiu, B. Alhaji

Federal University of Technology Minna, Minna, Nigeria

*E-mail: samuel.auta@futminna.edu.ng

Keywords: vertical, circular, openings, flexural, strength, ANSYS, building.

Abstract. Modern building construction techniques sometimes involve the passing of pipes or ducts for water supply, electrification, and telecommunication through reinforced concrete beams to protect them against mechanical damages and add aesthetic value to buildings. This study looks into the effect of vertical circular openings on the flexural strength of the reinforced concrete beam. Two (2) sets of beam samples were investigated during this study: computer simulated reinforced concrete (RC) beam using ANSYS 19.1 and laboratory cast. The results of the flexural strength test conducted show the following: Reinforced concrete beam with vertical circular openings of diameter greater than 33.3 % of beam width (B) reduced its flexural strength by at least 20 %; maximum compressive stress of concrete occurs at the openings region of the beam; the difference in ultimate load capacity of finite element (FE) beam models and experimental beam specimen is 3.5 %. It can be deduced that ANSYS software is an appropriate finite element (FE) tool to predict the behaviour of RC beams. Hence, it is hereby recommended that the diameter of the vertical circular opening in RC beam should not exceed 33.3 % of the beam width and its location from beam support should not exceed $L/6$.

1. Introduction

Modern building construction technique sometimes requires many pipes and ducts in order to accommodate essential services such as water supply, air conditioning, electricity, telephone, and computer network [1]. Normally, these ducts and pipes are surface mounted, clipped to the wall thereby exposing them to harsh weather condition and are prone to mechanical damages. In recent time, these pipes are being concealed in the wall as conduits and are made to pass through web of beams as means to secure them against damages, harsh weather condition and equally add more aesthetics to buildings.

The creation of such openings in existing reinforced concrete beams produces discontinuity in the normal flow of stresses which would reduce the beam shear capacity and stiffness [2]. The reduced stiffness of the beam may also give rise to excessive deflection under service load and result in a considerable redistribution of internal forces and moments in a continuous beam [3]. More significant reduction in the shear capacity was recorded when the openings interrupted the natural load path, that is, the line connecting the load and support points [4].

Flexural strengths of reinforced concrete beams with horizontal web openings have been researched; however, limited information is available when web openings are vertical. Hafiz *et al.* [4] verified the FE beam model with horizontal circular openings against experimental test data of RC solid beam without openings and discovered that the rectangular RC beams with circular openings diameter more than 44 % of beam depth (D) reduced the ultimate load capacity by at least 34.29 % [4]. Saksena¹ and Patel [5] stated that the performance of the beams with horizontal circular openings at centre of span has lesser effect on the ultimate load capacity of the RC rectangular section beams and more so, introducing the

Auta, S.M., Jamiu, O., Alhaji, B. Effect of vertical circular openings on flexural strength of reinforced concrete beam. Magazine of Civil Engineering. 2021. 106(6). Article No. 10601. DOI: 10.34910/MCE.106.1

© Auta, S.M., Jamiu, O., Alhaji, B., 2021. Published by Peter the Great St.Petersburg Polytechnic University.



This work is licensed under a CC BY-NC 4.0

circular openings of diameter of 45 % of depth near the support reduces the ultimate load capacity of rectangular section RC beams by at least 32 % compared to solid beam [5].

On the other hand, Maaddawy and Ariss [6] concluded that the inclusion of web horizontal openings drastically reduced the beam shear capacity and stiffness [6]. Abdalla *et al.* [7] carried out studies on reinforced concrete beams with horizontal openings un-strengthened and strengthened with FRP sheets. The effect of this strengthening technique on deflection, strain, cracking, and ultimate load was investigated. It was discovered that the presence of an un-strengthened openings in the shear zone of a reinforced concrete beam significantly decreases its ultimate load carrying capacity. An un-strengthened opening with height of 0.6 of the beam depth may reduce its load capacity by 75 % [7]. Guidelines have been provided for creating openings in new and existing slabs in British standard [8] and America building code [9].

A number of studies have been conducted on effect of openings in slabs, beams considering the web and columns but limited information is available as regards vertical openings in reinforced concrete beam which has become a common practice on construction field around this part of the world without caution. In order to provides guide lines to professionals in construction field on how and where to introduce vertical circular openings on reinforced concrete beam when need arises thus research into the effect of vertical circular openings is recommended [4]. If the beam is pre-designed to have vertical circular openings of known sizes and location, this will be sufficient to ensure the safety and serviceability of the structure.

The need of openings in structural element for passage of pipes or ducts in modern buildings is inevitable; however, the consequence of this is a reduction in shear and ultimate load capacity of the structural element (beam) which is of great concern to smart construction industry [2]. This study aims to evaluate the bending behaviour of reinforced concrete beams with vertical circular openings across its web by determining the physical and mechanical properties of aggregates; determining the flexural strength of laboratory cast reinforced concrete beams with vertical circular openings using flexural testing machine and; determine the flexural strength of computer simulated reinforced concrete beam with vertical circular openings using ANSYS 19.1 software.

2. Materials and Method

2.1. Description of specimen

For the purpose of this research, total numbers of ten (10) beam specimens were produced during the laboratory cast experiment. Dimension of beam specimen considered was 150 mm x 250 mm x 1200 mm as shown in Fig. 1. Two number of twelve (12) millimeter diameter bars each were used for both tension and compression reinforcement respectively. Eight (8) millimeter diameter bar was used for stirrup. The concrete cover to reinforcement was limited to 20 mm in accordance to the importance of concrete cover [10]. Table 1 gives the identification details of the beam specimens investigated in this study. Each beam was identified using seven alphanumeric characters, the first two letters BM indicates beam model, while the first two numbers indicates the diameter of the circular openings in millimeter and the last three numbers indicates the distance of the openings from the supports. For instance, BM 25-150 means beam model with 25 diameter openings located 150 mm from the supports.

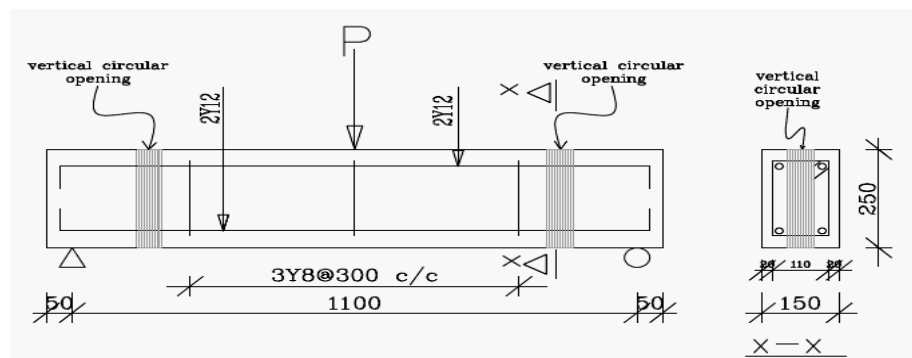


Figure 1. Reinforced concrete beam with openings (Dimensions in mm).

2.2. Laboratory investigation

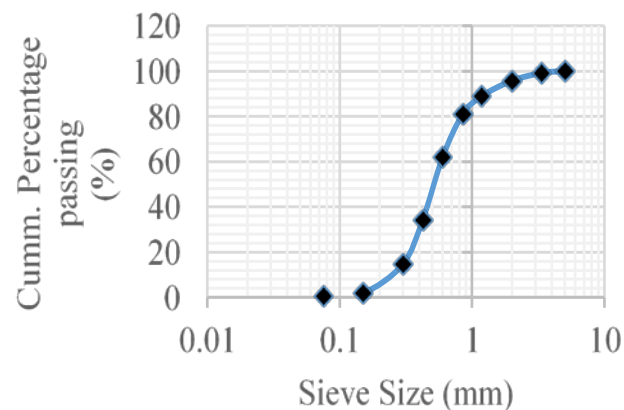
The preliminary tests such as Aggregate Crushing Value (ACV), Aggregate Impact Value (AIV) and particle size distribution tests for aggregates were carried out prior to concrete making. In order that the materials should not differ from materials used in general practice, the coarse aggregate (granite), fine aggregate (sharp sand), cement, and reinforcing bars were purchased in the open market.

Table 1. Beam specimens studied in this research.

Beam Identification	BM 25-150	BM 50-150	BM 25-350	BM 50-350	BM 0-0
Diameter of openings (mm)	25	50	25	50	–
Distance of openings from supports	150	150	350	350	–

On the coarse aggregate used in this study, both ACV and AIV were carried out in accordance with the British standard requirements [11, 12]. ACV was conducted to check the resistance of the coarse aggregate against gradually applied compressive load while AIV check the suitability of the coarse aggregate under applied impact loading condition. Results obtained for ACV and AIV were 25.9 and 18.3 % respectively which falls within limits of 23–30 % for ACV and 17–21 % for AIV. Thus, coarse aggregate used in this research is good granite.

Particle size distribution test was conducted on the fine aggregate in accordance to British standard requirements [13] and the result obtained is shown in Fig. 2. Percentage passing by mass for fines on sieve number 200 (75 μm) was 0.8 % which satisfied the requirements of 4 % maximum limit for uncrushed, partially crushed and crushed gravel sand. Dangote (42.5 N Grade) Ordinary Portland Cement was selected for this study due to its availability within the vicinity of the laboratory where the experiment was carried out [14].

**Figure 2. Particle size distribution curve for the fine aggregate.**

Tensile test was conducted to determine the characteristics strength for the reinforcing bars used in this research. Results obtained showed that the reinforcing bars used for this study have characteristics strength of 389 N/mm² which is lower than 460 N/mm² minimum requirements specified in British standard [15].

Compressive strength test was conducted on concrete for the beam specimens in accordance to British standard [16]. Results obtained showed that the concrete satisfied the minimum requirement for C20/25 grade concrete.

Flexural strength test was conducted on beam specimens as shown on plate I in accordance to British standard [17]. The breaking load (F) value was recorded from the testing machine and the flexural strength was calculated using the formula: $F_{cr} = \frac{PX1}{bd^2}$, where P is the breaking load (in N); l is the distance between the supports (in mm); b is the width of the beam (in mm); d is the depth of the beam (in mm).



Plate I: Experimental set-up for the centre-point load bending test.

2.3. Computer modeled beam specimen

ANSYS is a finite element analysis (FEA) code widely used in the computer-aided engineering field [18]. ANSYS software allows engineers to construct computer models of structures, machine components or systems; apply operating loads and other design criteria; and study physical responses, such as stress levels, temperature distributions, pressure, etc. It permits an evaluation of a design without having to build and destroy multiple prototypes in testing. ANSYS 19.1 is the FEM software employed for simulation of beam models in this research.

2.3.1. Modeling of beam specimen

Analysis of the beam model in ANSYS begins with the geometry definition which is defined based on the type of simulation to be carried out [19]. Static structural option on ANSYS 19.1 workbench was adopted in this analysis. Solid 65 was used to model concrete and Link 180 was used to model the steel reinforcement.

2.3.2. Meshing

Meshing is the breaking down of the model into smaller elements that can be separately analysed. The accuracy of the analysis result is proportional to the meshing size. Smaller mesh size gives accurate result but with longer computational time [20]. In this research, accurate results were obtained using mesh size of 25 mm.

2.3.3. Loading and boundary condition

To ensure that the modeled specimen behave the same way as the experimental beam, boundary conditions were set similar to the laboratory cast. Setting the boundary conditions and constrains is an essential step in Finite Element Analysis. The key step to starting analysis is the setting of boundary conditions [19].

3. Results and Discussion

3.1. Flexural strength

The results obtained from the flexural strength test carried out in this study are presented in Table 2 while the pictorial representation of relationship between beam specimens investigated is shown in Fig. 2. Rectangular solid beam without vertical circular openings (BM 0-0) recorded the highest flexural strength of 13.50 N/mm² and this serves as reference beam to compare other specimen with openings. BM 25-150 recorded flexural strength of 13.50 N/mm² which is similar to that of solid beam without openings while BM 50-150 recorded 10.50 N/mm² as flexural strength. Both specimens whose openings were located at 150 mm from supports have their flexural strength reduced by 0 and 8.74 % respectively when compared with solid beam without openings. BM 25-350 and BM 50-350 recorded significant loss in flexural strength by having 17.4 and 19.63 percentage reduction respectively when compared to solid beam without openings. The results show that presence of vertical circular openings leads to reduction in flexural strength of rectangular reinforced concrete beam specimen.

In addition, increase in sizes of the vertical circular openings leads to corresponding decrease in load bearing capacity of the beam specimens. Vertical circular openings that are located far from supports recorded lower flexural strengths when compared to openings located close to the supports as shown in

Fig. 3. BM 50-350 with 50 mm diameter openings located at 350 mm from supports record the lowest flexural strength of 10.85 N/mm², which represents 20 % loss in bending strength of the beams.

It can be deduced that reinforced concrete beams with circular openings of diameter less than or equal to 33.3 % of the beam width (without special reinforcement in openings zone) located within distance of L/6 from the supports behave in similar way compared to solid beams without openings, where L is the overall length of the beam. In another word, RC beams with circular openings of diameter greater than 33.3 % of the beam width located at distance L/3 from supports shows reduction of 19.63 % in the flexural strength. Most critical position of vertical circular openings in RC beams made of normal concrete is near the mid-span. Also, the best position for location of openings in beams is near the supports.

Table 2. Flexural strength of experimental beam specimens at 28 days.

S/No.	Beam Specimen	Average Ultimate Load (kN)	Flexural Strength (N/mm ²)	Percentage reduction (%)
A	BM 0-0	115	13.50	–
B	BM 25-150	115	13.50	–
C	BM 50-150	105	12.32	8.74
D	BM 25-350	95	11.15	17.40
E	BM 50-350	92.5	10.85	19.63

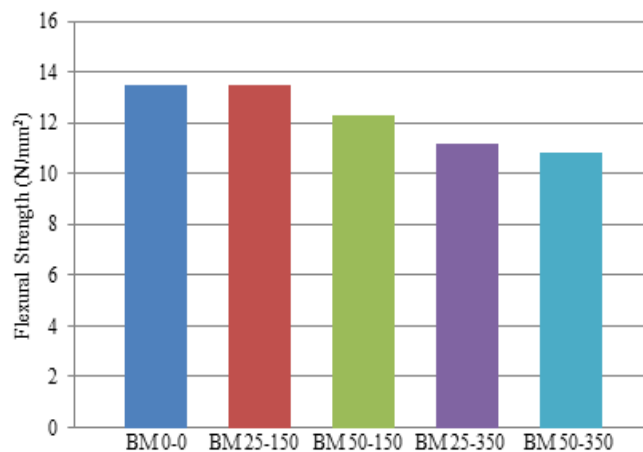


Figure 3. Flexural strength of Beam specimen at age of 28 days.

3.2. Stresses at Ultimate Load for ANSYS Beam Specimens

Both BM 25-150 and BM 50-150 recorded maximum compressive stress of concrete at mid-span of the beam around the area where load was applied as shown in Fig. 3. It is an indication that introducing vertical circular openings with diameter of about 33.3 % of beam width at L/6 from supports has little or no effect on the flexural behaviour of the RC beam, where L is the overall length of the beam. Therefore, location of circular openings close to the beam supports induces little or no stress in reinforced concrete beam and does not make it behave differently from solid beam without vertical circular openings.

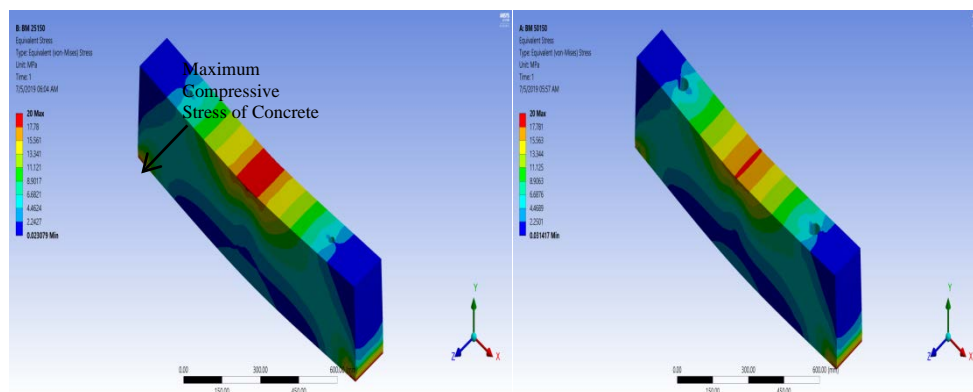


Figure 4. Equivalent (von-mises) stress for BM 25-150 and BM 50-150.

Beam specimens with circular openings located at $L/3$ from supports, that is, BM 25-350 and BM 50-350, maximum compressive stress were recorded at the edge of openings as shown in Fig. 3. Failure in these beam samples started from the edges of the openings, thus location of openings close to mid-span of the beam is detrimental to the flexural strength of reinforced concrete beam.

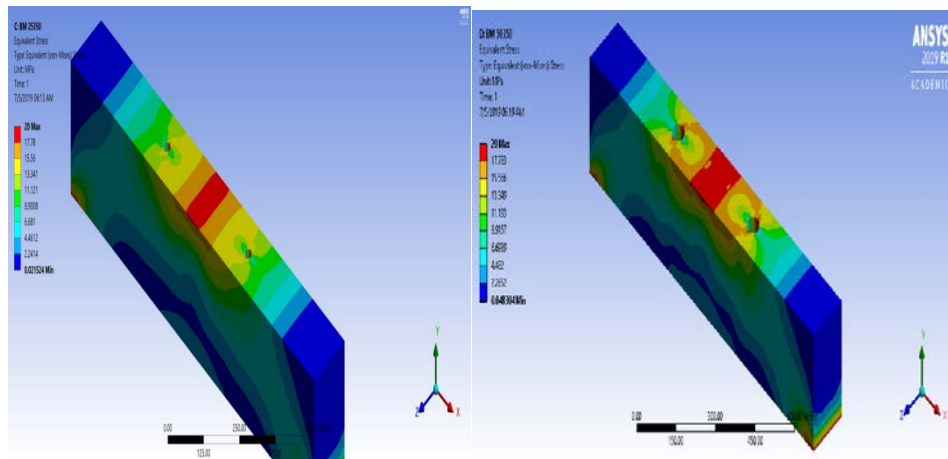


Figure 5. Equivalent (von- mises) stress for BM 25-350 and BM 50-350.

3.3. Comparison of Results with Reviewed Literatures

When compared with previous study [4] though with horizontal web openings, it was observed that 44 % of beam depth maximum opening diameter recommendation for web openings may not be valid for vertical circular openings in RC beam.

Contrast to what was observed in previous research on horizontal web openings [5], present study showed that the most critical area to locate vertical circular openings in RC beams is towards the mid span ($L/3$ from the support) which falls within the bending zone of the beam or in other words, it is safer to locate vertical openings close to beam supports.

4. Conclusion and Recommendations

4.1. Conclusion

Effect of vertical circular openings on behaviour of reinforced concrete beam has been explored and the following conclusions were drawn from the study: Diameter of vertical circular openings in RC beam should not exceed 33.3 % of beam width and their location on the beam should not exceed $L/6$ from beam supports where L is the overall length of the beam; most critical position to locate vertical circular openings in RC beam is within the flexure zone ($L/3$) towards the midspan and the best size for vertical circular openings is the narrower one whose diameter is less than 33.3 % of the beam width; and the computer aided simulation for beams with vertical circular openings using ANSYS 19.1 software as implemented in the present study shows good agreement with experimental data.

4.2. Recommendations

Based on the conclusion made from this research, following recommendations are hereby suggested:

1. Vertical circular openings in RC beams for multi-storey buildings should be discouraged as this could leads to compromise on the safety of the structural elements (beams) involved.
2. Further study should be conducted on strengthening the region of vertical circular openings in reinforced concrete beam.

References

1. Nishitha, N., Kavitha, P. Effect of openings in deep beams with varying span to depth ratios using strut and tie model method. IOSR Journal of Mechanical and Civil Engineering (IOSR-JMCE). 2016. Vol. 20. No. 201. Pp. 78–81.
2. Vivek, R., Madhavi, T.C. Behaviour of Reinforced Concrete Beam with Web Openings. ARPN Journal of Engineering and Applied Sciences. 2016. Vol. 11. No. 9. Pp. 5993–5995.
3. Jithinbose, K.J., Thomas, J., Parappattu, N.B. Effect of Openings in Beams – A Review. International Journal of Innovative Research in Advanced Engineering (IJIRAE). 2016. Vol. 3. No. 09. Pp. 15–19.

4. Hafiz, R.B., Ahmed, S., Barua, S., Chowdhury, S.R. Effects of Openings on the Behaviour of Reinforced Concrete Beam. IOSR Journal of Mechanical and Civil Engineering (IOSR-JMCE). 2014. Vol. 11. No. 2. Pp. 52–61.
5. British Standards Institution BS 812-110: 1990. Testing Aggregates-part 110: Methods for Determination of Aggregate Crushing Value. British Standards Institution, London.
6. British Standards Institution BS 812-112:1990. Testing Aggregates-part 112: Methods for Determination of Aggregate Impact Value. British Standards Institution, London.
7. British Standards Institution BS 812-103.1:1985. Methods for determination of particle size distribution – Sieve tests. British Standards Institute, London.
8. British Standards Institution. BS 882:1992. Specification of aggregates from natural sources for concrete. British Standards Institute, London.
9. British Standards Institutions BS 4449:1997. Carbon steel bars for the reinforcement of concrete. British Standards Institute, London.
10. British Standards Institution BS 1881-118:1983 Testing Concrete-part 118: Methods for Determination of Flexural Strength. British Standards Institution, London, 1983.
11. Wilson, P.P., Nair, E.M.S. Investigation on Reinforced Concrete Columns with Holes. International Research Journal of Engineering and Technology (IRJET). 2017. Vol. 04. No. 05. Pp. 1393–1395.
12. Talikoti, B., Kurbet, S.N., Kuppast, V.V., Arvind, M. Harmonic analysis of a two cylinder crankshaft using ANSYS. Inventive Computation Technologies (ICICT). DOI: 10.1109/INVENTIVE, 2016.7823219
13. QiongyingLv, Y.M. Modal analysis of a magnetic climbing wall car frame based on the ANSYS. IEEE Workshop on Electronics, Computer and Applications. 2014. Pp. 938–940.
14. El-Maaddawy, T., El-Ariss, B. Behavior of Concrete Beams with Short Shear Span and Web Opening Strengthened in Shear with CFRP Composites. Journal of Composites for Construction, 2012.
15. Hafiz, R.B., Ahmed, S., Barua, S., Chowdhury, S.R. Effects of Opening on the Behavior of Reinforced Concrete Beam. IOSR Journal of Mechanical and Civil Engineering (IOSR-JMCE). e-ISSN: 2278-1684, p-ISSN: 2320-334X. 2014. Vol. 11. No. 2. Ver. VII (Mar – Apr.). Pp. 52–61.
16. Mansur, M.A. Design of reinforced concrete beams with Web openings. Proceedings of the 6th Asia-Pacific Structural Engineering and Construction Conference. 2006. Vol. A. Pp. 104–120.
17. Mansur, M.A., Tan, K.H. Concrete beams with openings: analysis and design. CRC Press LLC, Boca Raton, Florida, USA, 1999. 220 p.
18. Mansur, M.A. Effect of openings on the behavior and strength of RC beams in shear. Cement Concrete Composite. 1998. 20(6). Pp. 477–486.
19. Mansur, M.A., Tan, K.H. Design procedure for reinforced concrete beams with large web openings. ACI Structure J. 1992. 93(4). Pp. 404–410.
20. Mansur, M.A., Tan, K.H., Lee, Y.F., Lee, S.L. Piecewise Linear Behavior of RC Beams with Openings. J. Struct. Eng. 1991. Pp. 1607–1621.
21. Mansur, M.A., Ting, S.K., Lee, S. Torsion Tests of R/C Beams with Large Openings. J. Struct. Eng. 1983. Pp. 1780–1791.
22. Mota, M., Kamara, M. Floor Openings in Two-Way Slabs. Concrete international, 2019. Pp. 33–36.
23. Naik, N., Kumar, R., Rajaiah, K. Optimum Hole Shapes in Beams under Pure Bending. J. Eng. Mech. 1986. Vol. 112. Pp. 407–411.
24. Ogunbiyi, M., Olawale, S., Alabi, O., Thanni, M. Assessment of the Qualities of Dangote and Elephant (Portland) Cement Brands commonly used in the Nigerian Construction Industry. International Journal of Innovative Research in Science, Engineering and Technology (IJIRSET). March 2017. Vol. 6. No. 3.
25. Prentzas, E.G. Behaviour and reinforcement of concrete beams with large rectangular apertures. Ph.D. Thesis, University of Sheffield, U.K., 1968. 230 p.
26. Saksena, N.H., Patel, P.G. Effects of the Circular Openings on the Behaviour of Concrete Beams without Additional Reinforcement in Opening Region Using FEM Method. International Journal of Advanced Engineering Technology e-ISSN 0976-3945/IJAET/Vol. IV/ Issue II/April-June, 2013/40-42.

Contacts:

Samuel Mahuta Auta, samuel.auta@futminna.edu.ng

Oladipo Jamiu, oladipojamiuconsult@gmail.com

Bala Alhaji, bala.alhaji@futminna.edu.ng



DOI: 10.34910/MCE.106.2

Impact of metro induced ground-borne vibration on urban development

M.A. Dashevskij^a, V.A. Mitroshin^{b*} , V.L. Mondrus^b, D.K. Sizov^a

^a OOO "Vibrorejsmozashchita", Moscow, Russia

^b National Research Moscow State Civil Engineering University, Moscow, Russia

*E-mail: mitroshin.vasily@gmail.com

Keywords: vibration from the subway, vibration measurements, vibration acceleration

Abstract. Metro trains are a source of increased noise and vibration, whose negative impact on residential development and production processes can lead to a deterioration in the quality of life or products. Fluctuations from metro trains spread with a certain frequency, depending on the operating train quantity. The level of recorded fluctuations depends mainly on the geological structure of the site, the depth of the line, and the distance to the observer. Instrumental study of the vibration levels on the ground surface is of practical interest in terms of assessing the impact of vibration on the projected buildings or structures, as well as scientific interest in terms of analyzing the spectrum of RMS values of vibration accelerations for each octave band on the ground surface. A four-channel vibrometer was used to measure the levels of vibrations in the overpass between the Belomorskaya and Khovrino stations on the Zamoskvoretskaya line of the Moscow metro, and then the frequency spectra were analyzed. The conclusion is made that the impact at the rail junction significantly contributes to the overall vibration load when the train enters the station, which is confirmed by a sharp increase in vibration levels at the corresponding observation points. The calculation of the natural vibration forms of the tunnel fragment is performed. Analysis of the measurements showed that a moving train excites vibrations in all octave bands, but the maximum levels of vibration acceleration were registered in octaves 16, 31.5 and 63 Hz. This is consistent with the results of the numerical simulation since the calculated natural vibration frequencies of the tunnel fragment are close to those measured on the ground surface.

1. Introduction

There has been an increase in new construction in large cities in recent years and, as a result, the intensive development of the transport network. The metro is the only modern mode of transport, the route of which can be laid regardless of the existing buildings on the surface. As a result, it is necessary to take into account the impact of noise and vibration acting on buildings and structures located within the sanitary zone of the subway (40–45 m from the outer walls of the tunnel), both from the movement of trains in its normal operation [1], so and from the sinking shields during the construction of the line [2] at the design stage. The object of research in this work is the rolling stock of the metro in a tunnel of shallow laying, located in the middle of urban development. The subject of the study, respectively, is the vibrations registered on the ground surface.

Vibration transmitted to building structures can worsen the quality of life of people [3, 4], as well as affect sensitive technological processes in modern production. [5, 6], for example, special electron microscopes, which are equipped with some research centers, are sensitive to the vibration amplitudes of the foundation less than 1 μm [5, 6]. It is also necessary to consider that the Central part of large cities mostly consists of cultural heritage sites. In some cases, the subway lines in close (less than two meters) from the foundations of the architectural monuments, which can adversely affect its technical condition

Dashevskij, M.A., Mitroshin, V.A., Mondrus, V.L., Sizov, D.K. Impact of metro induced ground-borne vibration on urban development. Magazine of Civil Engineering. 2021. 106(6). Article No. 10602. DOI: 10.34910/MCE.106.2

© Dashevskij M.A., Mitroshin V.A., Mondrus V.L., Sizov D.K., 2021. Published by Peter the Great St.Petersburg Polytechnic University.



This work is licensed under a [CC BY-NC 4.0](https://creativecommons.org/licenses/by-nc/4.0/)

without special measures [2, 7–10]. In connection with the above, there is an important and actual scientific and technical problem of measurement, analysis of experimental data and subsequent minimization of the impact of increased structural noise and vibration on people and buildings [7–15]. The purpose of this work is to study the vibration background on the ground surface near residential buildings above the new metro line of shallow Foundation. To achieve this goal the following tasks were completed:

1. Long-term vibration measurements were made using a special device at various points above the crossing and the station.
2. The files recorded by the device are processed and converted into visual graphs – vibration acceleration spectra.
3. The data obtained were analyzed and compared with current national and foreign sanitary standards.
4. Numerical modeling of a tunnel fragment was carried out to determine its own vibration modes.

2. Methods

The dynamic load from the moving subway trains is characterized by its discreteness, i.e. at the studied point, the registration of vibration accelerations is possible only for about 10 seconds, which corresponds to the time of the train passing through the measurement range. Further fluctuations almost instantly fade up to the moment of the beginning of passing of the next train [16]. This process – 10 seconds of increased vibration and noise and a subsequent break for 1.5–2 minutes – continues every day for 22 hours. Therefore, the only way to measure vibration levels, which allows the most complete analysis of the vibration background – spectral method [12, 13], without any averaging for 30 minutes of movement. The reliable average maximum of vibration accelerations is determined from the analysis of the full spectrum of the maximum number of trains.

Measuring oscillations of the surface of the soil was performed by a four-channel vibration meter SVAN 958. The device is designed for multi-channel measurement of vibration and noise. Three channels were used, the sensitive elements of which were in three perpendicular directions for registration:

- Vertical oscillations along the Z axis;
- Horizontal oscillations along the subway line (along the X-axis);
- Horizontal oscillations across the subway line (along the Y-axis).

During the experiment, 5 points along the route between the stations Belomorskaya and Khovrino of the Zamoskvoretskaya line of the Moscow metro were examined (Fig. 1). All measurements have a duration of at least 12 minutes for the collection of reliable data and their subsequent analysis. The average interval of train traffic during the study ranged from one to one and a half minutes.

Point number 1 is located above the station Belomorskaya, point number 2, 3, 4 – directly above the overtake, and point number 5 – above the station Khovrino.

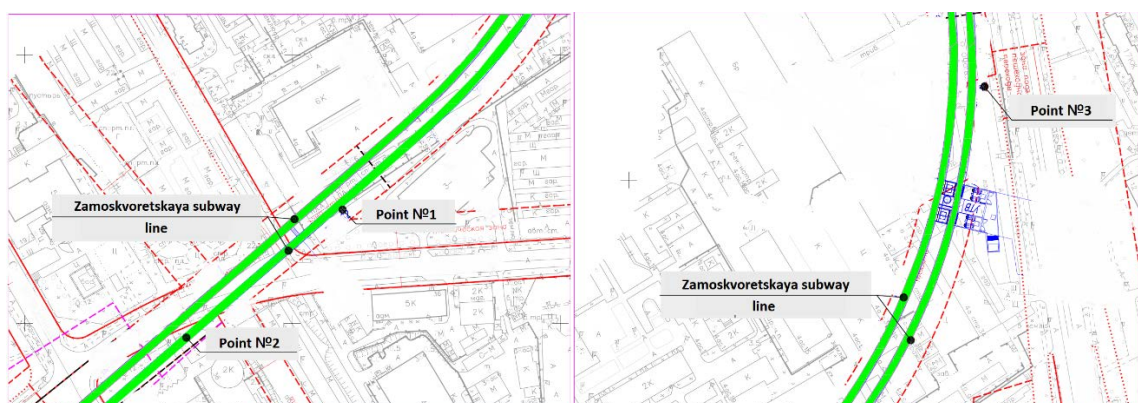


Figure 1. Schemes of location of measurement points No. 1, 2, 3 on topographic survey.

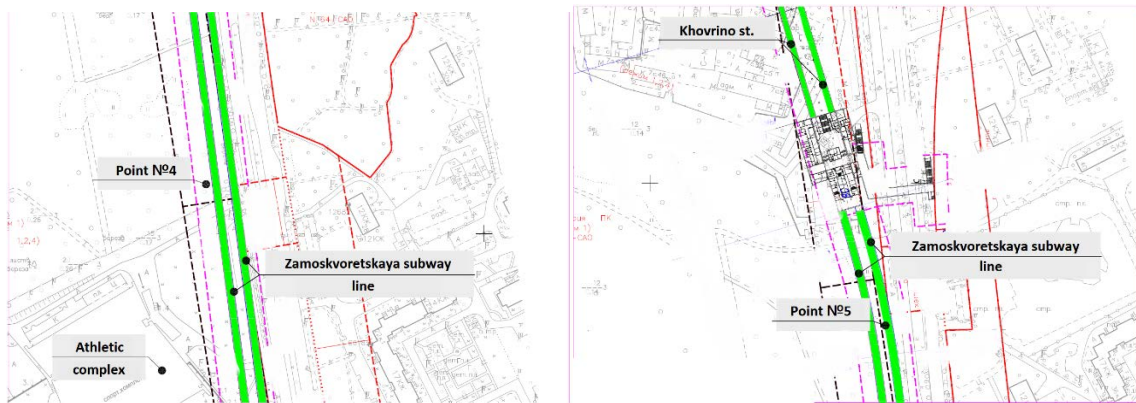


Figure 2. Schemes of location of points No. 4, 5 on topographic survey.

3. Results and Discussion

The device was used to register the vibration accelerations recorded the data separately on three channels into a special file, which was then converted into a graphical form using Svantek PC++ software (Fig. 3–8). The graphs show the vertical and horizontal components of vibration accelerations for different octave bands (4 Hz, 8 Hz, 16 Hz, 31.5 Hz, 63 Hz).

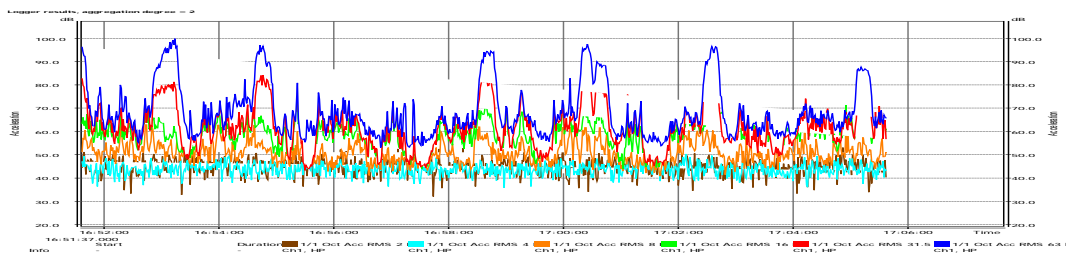


Figure 3. Point No. 1. Vertical component of vibration accelerations (z-axis).

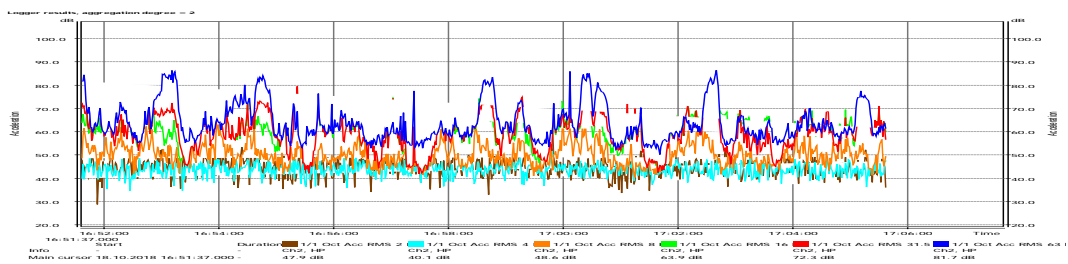


Figure 4. Point No. 1. Horizontal component of vibration accelerations (x-axis).

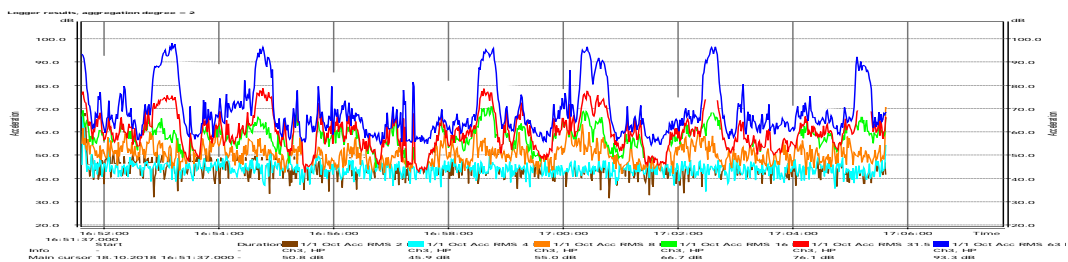


Figure 5. Point No. 1. Horizontal component of vibration accelerations (y-axis).

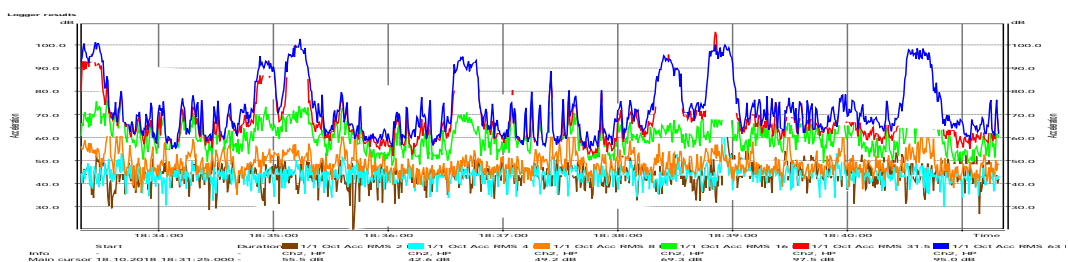


Figure 6. Point No. 5. Vertical component of vibration accelerations (z-axis).

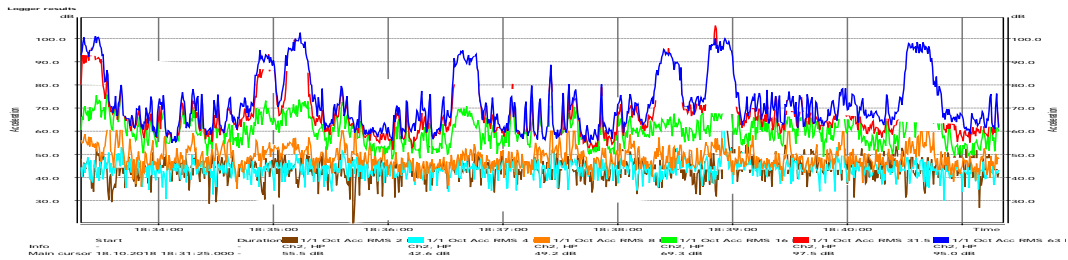


Figure 7. Point No. 5. Horizontal component of vibration accelerations (x-axis).

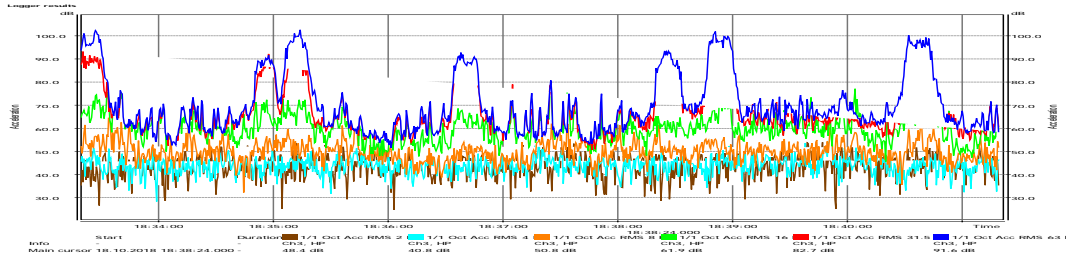


Figure 8. Point No. 5. Horizontal component of vibration accelerations (y-axis).

The study of graphs allows to select and tabulate the average maximum values of the recorded levels of acceleration in these octave bands (Table 1).

Table 1. Maximum levels of vibration acceleration.

		Vibration acceleration levels (dB) in (1/1) octave bands					
		2 Hz	4 Hz	8 Hz	16 Hz	31.5 Hz	63 Hz
Measurement point No.	Direction	Value	Value	Value	Value	Value	Value
1	Z	51.5	44.8	59.3	71.2	83.9	100.8
	X	47.6	48.0	62.9	75.3	78.2	86.5
	Y	54.6	44.9	57.1	69.2	77.6	97.5
2	Z	50.4	47.8	52.6	67.1	78.2	75.3
	X	47.9	47.0	58.9	68.3	73.2	86.0
	Y	53.7	50.1	52.5	58.1	75.6	82.4
3	Z	50.7	44.7	57.2	65.4	85.0	81.3
	X	47.7	49.0	59.6	66.9	83.7	84.8
	Y	47.3	47.8	61.1	67.6	89.4	85.1
4	Z	53.1	47.9	53.5	57.9	88.0	87.6
	X	45.9	48.4	58.9	65.5	88.5	99.8
	Y	48.6	50.4	55.5	63.9	90.4	96.4
5	Z	48.2	48.2	57.6	69.2	83.4	93.7
	X	50.0	45.8	56.8	68.8	95.3	98.0
	Y	50.9	51.4	54.7	71.9	92.2	99.1
Maximum	X	50.0	49.0	62.9	75.3	95.3	99.8
	Y	54.6	51.4	61.1	71.9	92.2	99.1

The values shown in the Table are the average values of the highest vibration levels for all measurements, determined by analyzing the spectrum of RMS values of vibration accelerations for each octave band on the ground surface using the following formula:

$$L_{dB} = 20 \lg \frac{a}{a_0}, \text{ dB} \tag{1}$$

From these spectra it is possible to distinguish the dominant frequencies of external influence, as well as to understand the nature of attenuation depending on the distance to the source. The method of frequency analysis is suitable for determining the influence of metro trains on a structure, since it can be used to select the average maximum of the mean square values of vibration accelerations from the entire ensemble of measurements during the passage of one train [9]. The train interval is not considered. This approach is adopted in most States as the main [13, 17], as it allows to assess the greatest negative effect of vibration on people and buildings, taking into account the discrete nature of the impact and guided by the principle of "no significant concern" (Sanitary code of Russian Federation, p. 3.2).

After analyzing the spectra obtained as a result of measurements within the framework of the task, it can be concluded that vibration acceleration recorded on the surface of the soil (these values in octaves of 31.5 and 63 Hz are highlighted in the tables) can cause exceeding the normalized vibration parameters in the designed buildings, the construction of which is planned in close proximity to the existing or projected sections of the subway route. The spectra analysis also showed that the vibration acceleration levels at points 1 and 5 are higher than at other surveyed points, which can serve as a confirmation of the contribution to the overall vibration load from a moving train of a wheel impact at the inevitable "parted" junction of the rails at the station at the entrance and exit of the train [16].

For completeness, the study should consider ways to assess the levels of vibration acceleration, presented in international, as well as some foreign regulatory documents, namely, the interstate standard ISO 2631 and the recommendations of the US Department of transportation.

The ISO 2631 document, developed by the international organization for standardization, establishes a methodology for calculating parameters that, applicable to national legislation, determine the permissibility of vibration values, as well as the degree of impact of vibration on human health using health criteria, comfort level, sensitivity to vibration and susceptibility to motion sickness.

The main measured value in the document is vibration acceleration, the formula for calculating the RMS value of which has the form:

$$a_w = \left[\frac{1}{T} \int_0^T a_w^2(t) dt \right]^{1/2}, \text{ m/c}^2. \quad (2)$$

It is assumed that the human body is affected by the average (smoothed) vibration. It should be noted that the calculation uses a weighted value of vibration acceleration obtained from the entire set of measured data [18]. It should be noted that ISO 2631 does not contain limit values for the defined vibration parameters, but only provides methods for calculating them for further comparison with existing national hygiene regulations, which may set appropriate limits for different conditions and different types of vibration.

The recommendations of the US Department of transportation (USDT recommendations) define the frequency (spectral) method as the main approach to assessing the impact of vibration on a person, calculating logarithmic levels of vibration speeds as follows:

$$v_{dB} = 20 \lg \frac{v_{rms}}{5 \times 10^{-8}}, \quad (3)$$

where v_{rms} is the mean square values of the vibration velocity, and the denominator is the reference value of the vibration velocity.

In addition, the recommendations use the concept of PPV (peak particle velocity) – the maximum vibrational speed, that is, the maximum instantaneous positive or negative value of the vibration velocity. This value is often used to analyze the effects of explosive impacts.

For residential buildings with so-called "frequent events" (more than 70 "events" of vibration from a single source per day), USDT recommendations set the maximum value of the vibration level at 72 dB.

The Russian Federation sanitary code set logarithmic levels of vibration velocity L_v and vibration acceleration L_a as normalized parameters, which can be calculated using the following expressions:

$$L_v = 20 \lg \frac{v}{5 \times 10^{-8}}, \quad (4)$$

$$L_a = 20 \lg \frac{a}{1 \times 10^{-6}}, \quad (5)$$

where the numerators of formulas (4) and (5) contain, respectively, the root mean square value of vibration velocity, m/s and RMS acceleration, m/s^2 ; in the denominators of the recorded reference value of vibration velocity, m/s acceleration m/s^2 .

The total vibration is considered as an octave or 1/3 octave bands with average geometric frequencies from 0.8 Hz to 80 Hz. The main difference between the method used in the codes of the Russian Federation and the United States from the ISO standard is the fact that no weighing is applied to the measured signal [18].

It should be also noted that there is a common approach to assessing the impact of vibration on a person or building structures in applicable legislation of the Russian Federation and the United States.

In the scientific literature, various methods of modeling the static and dynamic behavior of the tunnel under the action of the load from the movement of metro trains are considered, which allows us to consider the problem from different sides. For example, in [19] to assess the effect of the speed of movement of the point load from the wheel pairs of cars on the levels of induced vibrations, the tunnel is represented as a beam of constant cross-section on an elastic-viscous base. The train speed was consistently assumed to be 10, 20, and 30 m/s. The resulting calculations the highest levels of vibration velocity and vibration acceleration of tunnel meet train speed of 30 m/s. For the maximum speed of trains on the railway haul, usually not more than 80 km/h (22.2 m/s), calculated vibration level of the surface of the tunnel is 62 dB. Actual measurements of vibration on the ground surface, although performed under different conditions, differ in a large way by an average of 30 %, and with increasing distance from the observer, as is known, vibrations in the ground fade. Thus, the representation of the tunnel as a beam on an elastic-viscous base, loaded with concentrated forces from the wheel pairs of cars, allows only preliminary estimation of the vibration levels of the tunnel lining with some error.

In M.A. Dashevsky's doctoral thesis, a wide range of problems related to the radiation of waves in the ground (elastic-viscous half-space) during the movement of a pulsating load of the metro type in a cylindrical shell (tunnel) is considered. In [20] is published a solution of the problem in a flat statement about the radiation of vibrations by a circular tunnel from moving metro trains. The tunnel is represented as a cavity soldered into an elastic semi-infinite plane, and the load is modeled by periodic averaged forces that change according to the harmonic law. The results of calculations are qualitatively consistent with full-scale experiments. In [21], numerical modeling is used to consider the propagation of vibrations in the ground mass from impacts when damaged wheels and rails interact with defects of various types, including the joint of rails with a break. Rolling stock, rail support and ballast are modeled as a complex interacting multi-mass system located on an elastic base. To verify the model, measurements were made of ground surface vibration from a passing train at 12 m from the track. It is shown that any connection of rails with artificial irregularities during the passage of the train leads to an abrupt increase in the levels of vibration acceleration.

As part of this study, the MSC Patran/Nastran software package performed a numerical calculation of a tunnel fragment in a ground environment to determine its own vibration patterns. The tunnel is modeled by beam end elements with a variable thickness and a constant width of 1 m. the Thickness in the upper part of the tunnel is 0.3 m, and a local thickening is created in the lower part to represent the tray. The soil is modeled using elastic elements located along the contour of the tunnel (the modulus of elasticity is set to 25 MPa).

When performing the calculation to determine the natural frequencies of vibrations, the tunnel structures were modeled using generalized beam finite elements that allow for shear to be considered, that is, they correspond to Timoshenko rods. The tunnel diameter is 6 m. Each of the finite elements of the tunnel is adjacent to the finite element of finite stiffness, which simulates the elastic properties of the subgrade. The tunnel thickness is assumed to be 300 mm. The stiffness of each of the finite elements that simulate the soil surrounding the tunnel is determined based on the average stiffness of the subgrade of 25 MPa. The width of the finite elements of a beam with concrete stiffness parameters is 1 m. The finite elements simulating the elastic properties of the soil are rigidly fixed at their farthest ends from the center of the tunnel, and the other end is connected to the elements simulating the tunnel. That is, in fact, the problem of determining the natural frequencies of vibrations of an elastic ring in an elastic medium is being solved. There are no external loads, additional stiffness and mass from the track concrete is modeled by local thickening of the beam elements within the tunnel element located under the half sleepers.

Fig. 10–11 show the first few variations of the tunnel fragment.

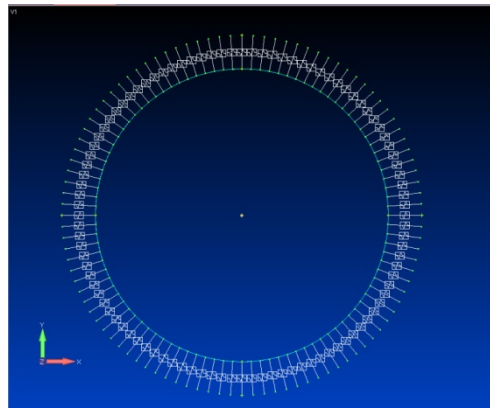


Figure 9. Tunnel design scheme.

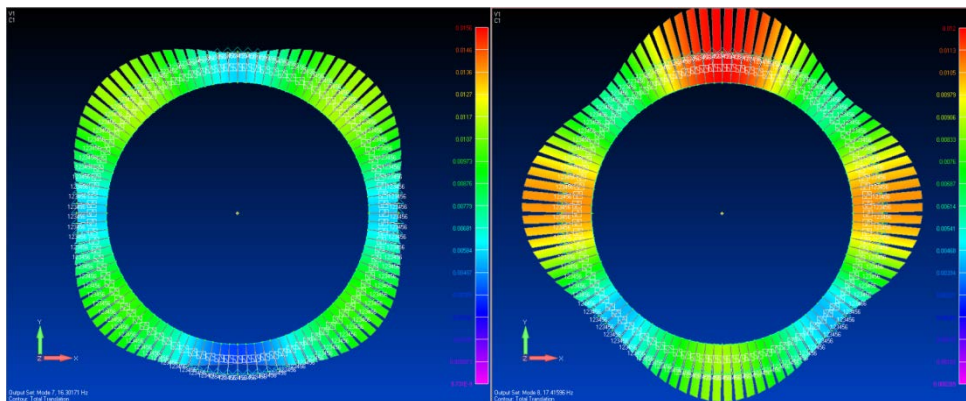


Figure 10. The first (left, frequency 16.3 Hz) and the second (right, frequency 17.4 Hz) forms the vibrations of the tunnel fragment.

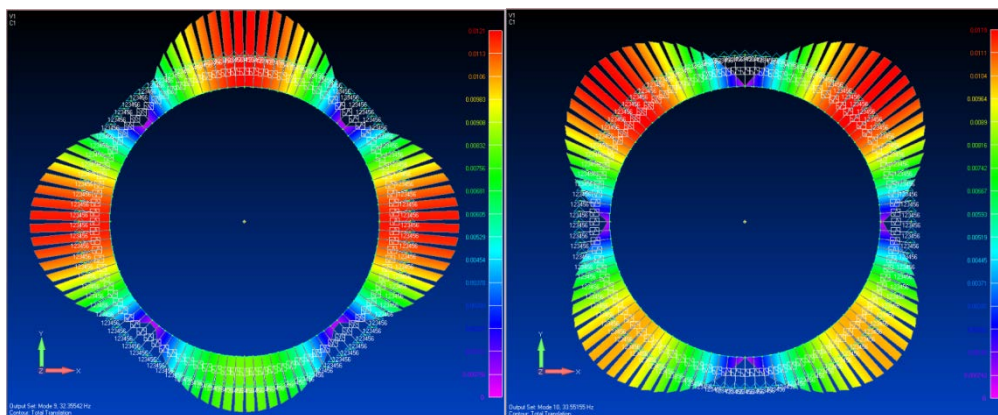


Figure 11. The third (on the left, the frequency of 32.3 Hz) and fourth (right, frequency of 33.5 Hz) mode shapes of the fragment of the tunnel.

The vibration levels of the soil surface obtained during the measurements have characteristic bursts at frequencies in octaves of 16 Hz, 31.5 Hz and 63 Hz, which can be explained, among other things, by the characteristic eigenfrequencies of the tunnel fragments located in the soil massif.

4. Conclusions

The analysis of the results of the measurement of oscillations over the subway track and numerical simulation of the tunnel fragment led to the following conclusions:

- shock at the junction of the rails excites all forms of vibrations, but the predominant are vibrations with frequencies close to 31.5 Hz and 63 Hz;
- bursts at frequencies of 16 Hz, 31.5 Hz and 63 Hz occur also due to the characteristic natural frequencies of the underground tunnel surrounded by the ground;

- the vibration levels measured in octaves 31.5 and 63 Hz, significantly exceeds the allowable by Sanitary code of the Russian Federation. To account for floor resonances, 3.5 dB should be added to vibration levels.
- when determining the need for the device of vibration protection systems, it is necessary to use a spectral method based on the assessment of the expected vibration levels in individual octave bands, since it allows to determine the "response" of individual structural elements to the vibration effect at a certain frequency.

References

1. Dashevskiy, M.A., Motorin, V.V. The effective antivibration underground railway superstructure. *Metro i tonneli*. 2015. 2. Pp. 28–33. (rus)
2. Kurbatsky E.N., Elgaev V.S. Impact on the buildings during tunnel boring. *World of Transport and Transportation*. 2012. 2. Pp. 162–167. (rus)
3. Sica, G. Groundborne vibrations caused by railway construction and operation in buildings: design, implementation and analysis of measurement for assessment of human exposure University of Salford, United Kingdom, 2014.
4. Dashevskiy, M.A., Mondrus, V.L. Prognosis of vibration levels of buildings from underground train traffic. *Promyshlennoye i grazhdanskoye stroitelstvo*. 2013. 11. Pp. 52–54. (rus)
5. Smirnov, V.A. Metody razmeshcheniya vysokotochnogo oborudovaniya v sushchestvuyushchikh zdaniyakh [Methods for placing precision equipment in existing buildings]. *Zhilishchnoye stroitelstvo*. 2012. 6. Pp. 76–77.
6. Mondrus, V.L., Smirnov, V.A. Numerical analysis of nonlinear vibration isolation system for electron microscope. *Academia. Arkhitektura i stroitelstvo*. 2012. 3. Pp. 125–128.
7. Dashevskiy, M.A., Mondrus, V.L., Sizov, D.K., Shutovskiy, S.N. The Features of vibration protection in existing buildings of VXIII-XIX century ex-mansion within the set of buildings of the state museum of fine arts named after A.S. Pushkin. *Nauchno-tekhnicheskiy vestnik Povolzhya*. 2013. 6. Pp. 251–253.
8. Isakov, A.L., Smolin, Yu.P. A comparative estimation of vibration level of track concrete in the metro with various types of under-rail bases. *Vestnik Sibirskogo gosudarstvennogo universiteta putiy soobshcheniya*. 2017. 4. Pp. 40–44.
9. Isakov, A.L., Smolin, Yu.P. The use of vibration isolation structures Podbelskogo grounds on the metro lines to reduce the effects of vibration in buildings. *Izvestiya vysshikh uchebnykh zavedeniy. Stroitelstvo*. 2017. 4. Pp. 5–14.
10. Vogiatzis, K. Protection of the Cultural Heritage from Underground Metro Vibration and Ground-Borne Noise in Athens Centre: The Case of the Kerameikos Archaeological Museum and Gazi Cultural Centre. *International Journal of Acoustics and Vibrations*. 2012. 17. Pp. 59–72. DOI: 10.20855/ijav.2012.17.2301
11. Stepanov, K.D., Loktev, A.A., Yarmolenko, V.A. Modelling the effects of vibration from subway trains to the building design and selection of system parameters of vibro-acoustic protection. *Vnedreniye sovremennykh konstruktivnykh i peredovykh tekhnologiy v putevoye khozyaystvo*. 2018. 12. Pp. 19–25.
12. Dashevskiy, M.A., Mondrus, V.L., Motorin, V.V. Effective vibroprotection of the underground upper track structure. *Academia. Arkhitektura i stroitelstvo*. 2017. 4. Pp. 111–117.
13. Dashevskiy, M.A., Mondrus, V.L., Motorin, V.V. The concept of vibroprotection of buildings and structures in the field of construction standards of the Russian Federation. *Academia. Arkhitektura i stroitelstvo*. 2018. 4. Pp. 109–115. DOI: 10.22337/2077-9038-2018-4-109-115
14. Hildebrand, R. Countermeasures against railway ground and track vibrations. Royal Institute of Technology, Stockholm, 2001.
15. Kouroussis, G., Verlinden, O. Efficiency of resilient wheels on the alleviation of railway ground vibrations. *Journal of Rail and Rapid Transit*. 2012. 226(4). Pp. 381–396.
16. Dzyuba, A.V., Mironets, T.L. Influence of motion of train of underground passage on height housing building. *Vestnik Natsionalnogo aviatsionnogo universiteta*. 2010. 4. Pp. 143–146.
17. Pei-wen, C. Vibration of nearby structures induced by high-speed rail transit University of Southern California, 2008.
18. Kouroussis, G., Conti, C., Verlinden, O. Building vibrations induced by human activities: a benchmark of existing standards. *Mechanics & Industry*. 2014. 5(15). Pp. 345–353. DOI: 10.1051/meca/2014041
19. Kurbatskiy, Ye.N., Nguyen, Ch.T. Otsenka vibratsii tonnelya pri dvizhenii sosredotochennykh sil. [Estimation of tunnel vibrations under the action of moving concentrated forces]. *Inzhenerno-stroitelnyy vestnik Prikaspiya*. 2014. 2. Pp. 38–42. <https://elibrary.ru/item.asp?id=22111966>
20. Kolotovichev, Yu.A. Dynamic stress definition technique during the passage of metro trains in soil media. *Regionalnaya arkhitektura i stroitelstvo [Regional architecture and engineering]*. 2010. 1. Pp. 34–44.
21. Kouroussis, G., Connolly, D., Alexandrou, G., Vogiatzis, K., Verlinden, O. Modelling the singular rail and wheel surface defect for predicting railway ground vibration. *Proceedings of the 22nd International Congress on Sound and Vibration*. Florence. Italy. 2015. 8 p.

Contacts:

Mikhail Dashevskij, michdash@mail.ru

Vasiliy Mitroshin, mitroshin.vasiliy@gmail.com

Vladimir Mondrus, mondrus@mail.ru

Dmitriy Sizov, newfff@mail.ru



DOI: 10.34910/MCE.106.3

Formation of a software calculation model for restoring building structures after a fire

S.V. Fedosov^a , V.G. Malichenko^{b*} , M.V. Toropova^b 

^a National Research Moscow State Civil Engineering University, Moscow, Russia

^b Ivanovo State Polytechnic University, Ivanovo, Russia

*E-mail: mvg84@bk.ru

Keywords: fire resistance limit, fire, construction designs, bearing capacity, fire extinguishing, mathematical modeling.

Abstract. The collapse of building structures after a fire is not uncommon. Taking into account the parameters that affect the elements of the building exposed to extreme temperatures of fire and extinguishing allows assessment of the durability of the entire structure. The analysis of regulatory documents on the survey of buildings and structures after a fire allowed us to establish they lack consideration of such parameters, including the Code of Practice 329.1325800.2017 “Buildings and constructions. Examination rules after a fire”. The decision on the appropriateness of the further operation of buildings after the occurrence of both single and multiple fires is possible based on mathematical modelling of this process, and its software and algorithmic support. The technical objective of the study is to create a universal model for the software calculation of the restoration of structures after fire and fire extinguishing. The object of the study is the fire-related damage and destruction of building structures due to thermal effects. The research method consists in developing a cellular model of a thermally insulated plate based on the localization of the heat source in a certain position above the plate and characterized by the temperature distribution in the cells. The evolution of this distribution is a transition probability matrix that describes the change in thermal conductivity along with the plate in two directions and by the functions of the sources. One of the sources describes the supply of heat to a particular cell (a localized moving source), and the other describes the removal of heat due to heat emission to the environment. As a result of the study, a universal model for the formation of a software calculation for the restoration of structures after fire and fire extinguishing has been developed. The purpose of this model is to establish the residual fire resistance of a building structure after a fire with a minimum calculation time and receive recommendations on the possibility of further operation of the building.

1. Introduction

The heat-resistant properties of structural materials are always a significant component in deciding on their use in the design of various buildings and structures. The influence of temperature effects on the structure during the fire and the results of studies of the heat-resistant properties of materials of building structures have always worried designers. Indeed, without information on heat resistance and an index of fire resistance, it is impossible to make a decision on the use of this material for the design and subsequent construction of buildings and structures for various functional purposes. In addition, sudden cooling during fire extinguishing of materials or double heating of building structures during irregular or periodic fire extinguishing, both by fire departments and sprinkler and deluge fire extinguishing systems, will lead to a change in the structural characteristics and will affect its bearing capacity.

Fedosov, S.V., Malichenko, V.G., Toropova, M.V. Formation of a software calculation model for restoring building structures after a fire. Magazine of Civil Engineering. 2021. 106(6). Article No. 10603. DOI: 10.34910/MCE.106.3

© Fedosov, S.V., Malichenko, V.G., Toropova, M.V., 2021. Published by Peter the Great St.Petersburg Polytechnic University.



This work is licensed under a [CC BY-NC 4.0](https://creativecommons.org/licenses/by-nc/4.0/)

The object of the study is damage and destruction of building structures caused by thermal effects due to fire.

There is a large amount of methodological literature on the diagnosis of damage and destruction of buildings and structures [1–5]. Various approaches and methods for assessing the technical condition of structures after a fire when modeling fire resistance are presented in the publications: A. Krivtsov, M. Gravit, S. Zimin, O. Nedryshkin, V. Pershakov (2016), J. Schmid, M. Klippel, A. Just, A. Frangi, M. Tiso. (2018), M.B. Dwaikat, V.K.R. Kodur (2009), Y.J. Kwon, D.J. Kim, S.G. Kang, B.C. Kim, B.C. Han, J.Y. Leesp, H. Kazunori. (2013), M. Cvetkovska., M. Knezevic., Q. Xu, C. Chifliganec, M. Lazarevska., A.T. Gavriloska (2018), W.Y. Gao, J.G. Dai, J.G. Teng, G.M. Chen (2013) [6–11] and others too.

The technical task of our study was to create a universal model for the software calculation of the restoration of structures after fire and fire extinguishing.

Existing requirements for water supply to the structure by fire departments in order to extinguish a fire do not regulate the direction of the stream (extinguishing point or points on the structure). Water can be supplied to any point in the structure, but at the same time its characteristics will vary unevenly from where the water is supplied.

You can divide the water supply into the structure in the following ways up, in the middle, down the structure or into the corners of the structure, both in the upper and lower. With a different choice of the cooling location of the structure heated during a fire, its fire resistance limit will change, which can significantly affect the further operational characteristics of the structure.

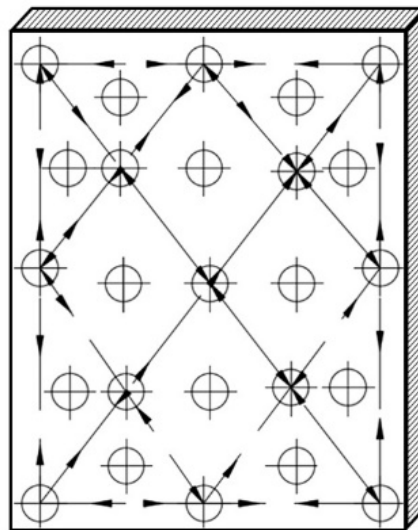


Figure 1. Possible cooling points when extinguishing a fire.

According to the nature of the same type of damage and destruction of building structures, the volume of a building (structure) exposed to fire is divided according to Code of Rules 329.1325800.2017 “Buildings and Structures. Inspection rules after a fire”, in three (in the absence of collapse) or four (in the presence of collapse of structures) the main areas of fire exposure on building structures (the tables B.1-B.5 of the appendix B) [1]:

- zone of emergency degree of fire exposure (fire exposure);
- zone of a high degree of fire exposure (fire exposure);
- a zone of moderate fire exposure (fire or heat);
- zone of low degree of fire exposure (thermal effect or smoke).

In the zone of emergency degree of fire exposure, all defective structures must be dismantled and replaced with new structures.

In areas of severe and moderate fire exposure, a visual and instrumental examination of building structures is necessary.

In the zone of low degree of fire impact, an instrumental examination of building structures after a fire is not required according to the set of rules, but at the same time, thermal radiation affected the structure and requires an assessment of its condition.

Defects and damage to building structures (cracks, deflections, deformations, discoloration of the material of the structure, the presence of metal fusion, exposure and buckling of reinforcing bars, etc. are significant signs of determining the further operation of the structure.

After the fire, to make a decision on the further operation of the structure, it is necessary to carry out verification calculations of the building structure, and the automation and simplification of such calculations by modern informatization methods by compiling the software are dictated by time.

The actual design of the building (structure) is determined by the results of the inspection after the fire and should reflect:

- the actual conditions of abutment or conjugation of adjacent structures;
- the actual geometric dimensions of the cross sections, the values of spans, eccentricities;
- the type and nature of the actual (or required) loads;
- the presence of damage and structural defects.

The actual duration of intense burning of materials and structures in the fire is set without taking into account the duration of its initial stage of ignition and the final stage of attenuation. The initial stage of ignition can be 5-40 minutes and is characterized by the ignition of materials with a slight increase in the temperature of the environment in the room (150 °C–200 °C). The stage of intense combustion is characterized by a rapid increase in temperature (up to 1200 °C–1500 °C, sometimes up to 2000 °C), stabilization of maximum fire temperatures and subsequent sharp decrease in temperature to 600 °C–400 °C.

According to indirect signs remaining after the fire, it is possible to establish the values of temperatures that were in effect during the fire, namely:

- by changing the appearance and shape of individual objects and materials remaining after the fire;
- to change the structure and condition of heavy concrete;
- by changing the color of concrete;
- by the fusion temperature of various metals;
- color discoloration (color of oxides on the surface) of steel;
- on the color change of polymer coatings and paints;
- the presence of soot and soot, the condition of paper and wood;
- on a change in the state of metal structures;
- by changing the state of masonry;
- by changing the state of gypsum plaster;
- by changing the state of cement-sand plaster.

However, at the same time, the formation of cracks and changes in the properties inside the structures, which cannot be visualized without the use of special equipment and sampling for laboratory studies, are possible.

The relevance of the study lies in the adoption of very quick decisions on the further operation of the building and structure after the fire, since people who live in buildings may live on a permanent basis and may not be able to live in another place until the end of a long study of structures for their bearing capacity after fire and fire extinguishing.

When structures are heated during a fire and during the process of extinguishing, various processes occur, these processes have restrictions on the speed and uniformity of heating, in most fires the size of the heat source is less than the heated surfaces of the structures.

In a fire, heat sources cannot be fixed local, they are constantly increasing, and thermal energy is moving along the surfaces of structures. It is also impossible to exclude delays of sources in different zones due to the presence of a greater fire load in these areas, while the areas that were previously heated and the combustion process in these areas stopped, have time to cool significantly.

The conditions for such heating depend on the materials of the structures, heat transfer from the heat source to the product, from heat transfer from the product to the environment, and from the thermophysical properties of the material from which the product is made.

Under the conditions of the diversity of these parameters and their combinations, the empirical search for the optimal paths and velocities of the source along the heated product is a laborious and lengthy task. The choice of rational warm-up conditions can be greatly simplified and facilitated using mathematical models of this process and its software and algorithmic support, especially since the current level of

development of building thermo-physics already contains mathematical descriptions of the individual components of this process, allowing their sufficiently reliable forecasting for timely identification of the need restoration of structures damaged by fire and the possibility of their further safe operation.

The purpose model is to establish the residual fire resistance of a building after a fire (with rapid cooling) to minimize the time to obtain accurate results on the further operation of buildings. The tasks are:

- selection of a management solution for extinguishing, to maintain the bearing capacity of the building structure;
- reduction of damage during fire extinguishing;
- establishing the possibility of further operation of buildings exposed to fire;
- development of a universal model for the formation of a software calculation for the restoration of structures after fire and fire extinguishing.

2. Methods

As a theoretical basis for constructing mathematical models of heat transfer processes, the Markov chain theory method was chosen [12, 13], which has proven itself in solving a number of practical engineering problems [14].

We give an example of modeling a process with constructing a cellular model of a thermally insulated plate, a diagram of which is shown in Fig. 2. Let the heat source be localized in a certain position above the plate. The thermal state of the plate is characterized by the temperature distribution over the cells, and the evolution of this distribution is characterized by a transition probability matrix describing the thermal conductivity of the plate in two directions and by the functions of the sources, one of which describes the heat supply to a particular cell (localized moving source), and the other heat removal due to heat transfer to the environment.

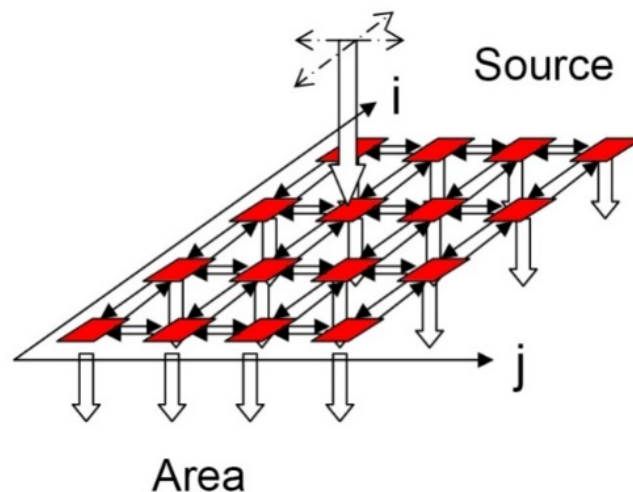


Figure 2. The cell model of the plate and the heat flow diagram in it.

In particular, the transition matrix (thermal conductivity matrix) for a grid of 4×4 cells in the most common case of modeling with square cells has the form

$$P = \begin{bmatrix} 1-2d & d & 0 & d & 0 & 0 & 0 & 0 & 0 \\ d & 1-3d & d & 0 & d & 0 & 0 & 0 & 0 \\ 0 & d & 1-2d & 0 & 0 & d & 0 & 0 & 0 \\ d & 0 & 0 & 1-3d & d & 0 & d & 0 & 0 \\ 0 & d & 0 & d & 1-4d & d & 0 & d & 0 \\ 0 & 0 & d & 0 & d & 1-3d & 0 & 0 & d \\ 0 & 0 & 0 & d & 0 & 0 & 1-2d & d & 0 \\ 0 & 0 & 0 & 0 & d & 0 & d & 1-3d & d \\ 0 & 0 & 0 & 0 & 0 & d & 0 & d & 1-d \end{bmatrix}, \quad (1)$$

where

$$d = \alpha \frac{\Delta t}{\Delta x^2}, \quad (2)$$

α is coefficient of heat diffusivity of material; Δx is side length of a square cell.

Since no more than four transitions are possible from this cell, the smallest probability of staying is $1 - 4d$, which implies the stability condition of the computational procedure $d \leq 1/4$, since, in accordance with the physical meaning, the probabilities cannot be negative.

Thus, temperature redistribution over a fully thermally insulated plate can be described by recurrence matrix equality

$$T^{k+1} = PT^k, \quad (3)$$

where initial distribution of temperature of T^0 has to be set.

As the sum of elements of matrix P (1) is equal in every line to unit (normalization in the lines), asymptotic distribution of temperature at $k \rightarrow \infty$ will be uniform that corresponds to physical essence of process.

With a moving source, the cell number to which heat is supplied changes, that is, $i = i(k)$ and $j = j(k)$. In the heating procedure for the same type of recording operations, it is advisable to introduce the temperature matrix of the sources $T_s(k)$ is a matrix where all elements are zeros, except for element ij , where $i = i(k)$ and $j = j(k)$, and which is equal to T_s . Then the transfer of heat to the cell ij at the k th transition can also be described by the matrix equality

$$T^j = T + a_2 (T_s(k) - T), \quad (4)$$

in which the program and the speed (delay in the cell) of the source movement are given by the equalities $i = i(k)$ and $j = j(k)$.

Thus, equality (4), which describes the heat transfer to the plate cell, together with equality (3), which describes the propagation of heat through the plate through heat conduction, completely describes the heating of a heat-insulated plate both stationary ($i, j = \text{const}$) and mobile ($i = i(k)$ and $j = j(k)$) by a local heat source.

Heating a fully insulated plate leads to an asymptotically uniform temperature distribution, and this temperature is equal to the temperature of the source. However, the uniformity of distribution in the transitional stages of heating for a stationary and moving source is significantly different. In Fig. 3 the source motion program is defined by the radius vector $rs(k)$ with projections $is(k)$ and $js(k)$, the law of change of which is the motion program

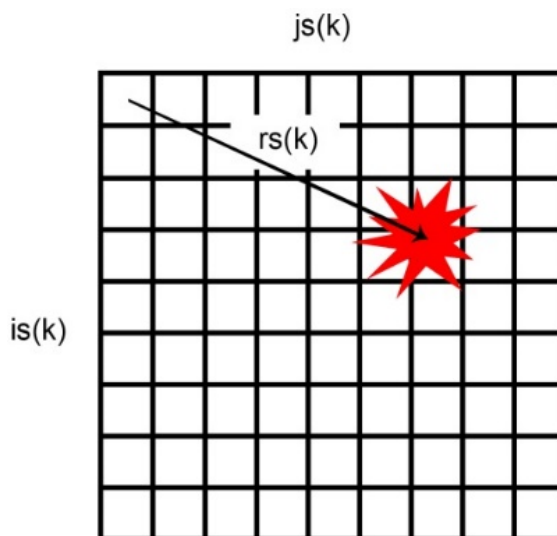


Figure 3. To the program of the movement of source.

In Fig. 4 shows the influence of the program of movement along the contour: first along its two points, then along four, and then along the same contour with an increasingly dense coating of its points.

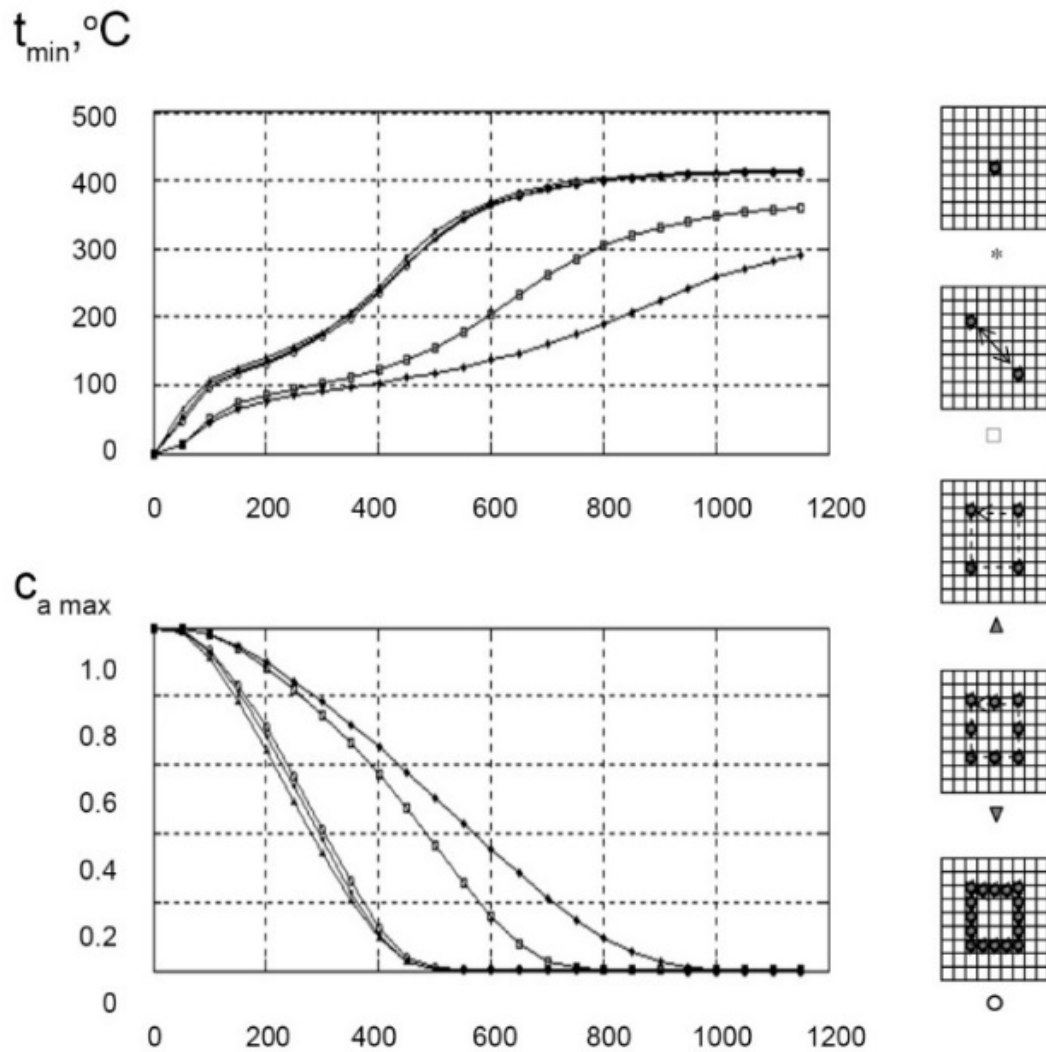


Figure 4. Change in minimum plate temperature and maximum concentration with various source movement programs.

3. Results and Discussion

If the above simulation of the process of constructing a cellular model of a thermally insulated plate is shifted to a real fire, then will see that in the initial stage any fire is characterized by a focal zone (temperature effect at one point in the room). In the initial stage, a local temperature effect occurs on the structure, with increasing temperature, the fire area increases and, accordingly, the source moves along the surface of the structure according to various movement programs, while the areas where the combustible load is contained in a smaller amount cool down. Because of which there is an uneven heating of the structure and its more rapid destruction. In this case, heat transfer to the external environment takes place not without taking into account the possibility of the origin of fires in different climatic zones and at different environmental temperatures, which affect the uneven change in the characteristics of structures. This circumstance necessitates the development of a universal fire extinguishing model, which will lead to the least destruction of the structure in different environmental conditions. In view of the foregoing, we described in Fig. 5 universal model for the formation of a software calculation of the restoration of structures after fire and fire extinguishing.

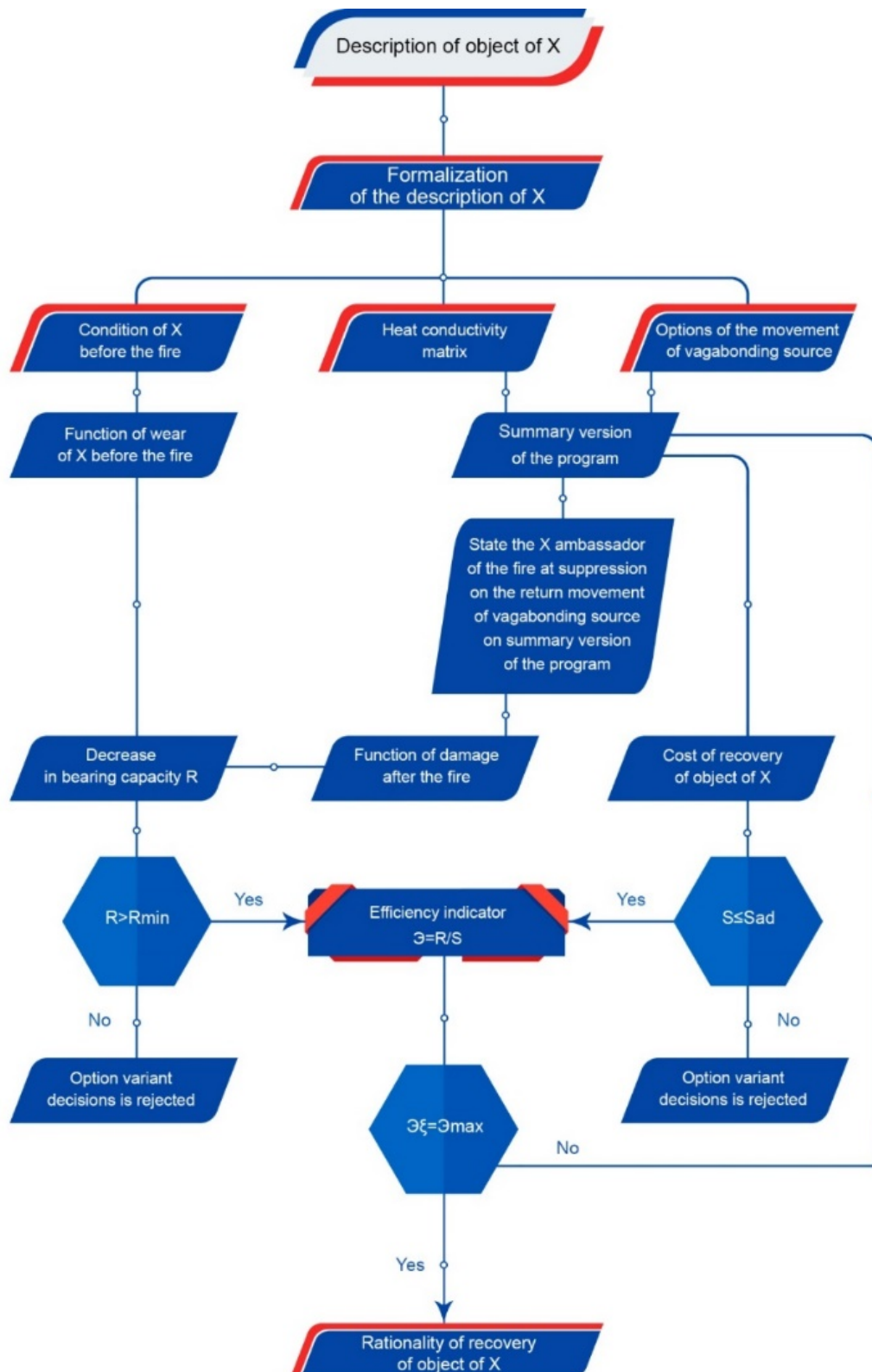


Figure 5. Universal model for the formation of software calculation of restoration of structures after fire and fire extinguishing.

The description of the model is as follows: the description of the object X are includes subsystems ($x_1...x_{15}$) of structures subjected to thermal action. The state of the subsystem is characterized by an indicator of possible structural failure, which (the remainder R is bearing capacity) can be caused as a result of a fire.

The content of the structures is characterized, firstly, by the list of objects on which the fire occurred. Secondly, the type of destruction, which is reflected by the thermal conductivity matrix. The totality of the proposed movement of the stray source forms a variant of accepting the proposed model of motion of the

stray source, with the worst result of the remainder (R) adopted for this design. The elements of the object X are the amount of expenditure of various resources for the most complete restoration of bearing capacity.

The difference between the proposed model and other models of program calculation, for example, W.Y. Gao, J.G. Dai, J.G. Teng, G.M. Chen, consists in assessing the recovery after sudden cooling of the structure during fire extinguishing by fire departments using a heat conduction matrix [11].

Here is one of the possible algorithms for the program to work according to the model have described.

B1 – wall with probability r_1 remained intact as a result of fire. B2 – the wall after the fire does not meet the required fire resistance limit, but it can be fixed. We apply the probability r_2 to this event. B3 – the wall with probability r_3 after the fire is hopelessly damaged and cannot be restored. C1 – after the fire, the house with probability p_1 remained suitable for further operation. C2 – As a result of the fire, the house with probability p_2 became unsuitable for further operation. Obviously, the first three and the last two events form complete groups: $r_1 + r_2 + r_3 = 1$, $p_1 + p_2 = 1$.

For the sake of simplicity, the main event options are listed here. In real conditions, there may, of course, be more complex situations, however, they can easily be reduced to the cases listed above.

As a result of the onset of these events, the "house-wall" system is in one of the following six states (Fig. 6).

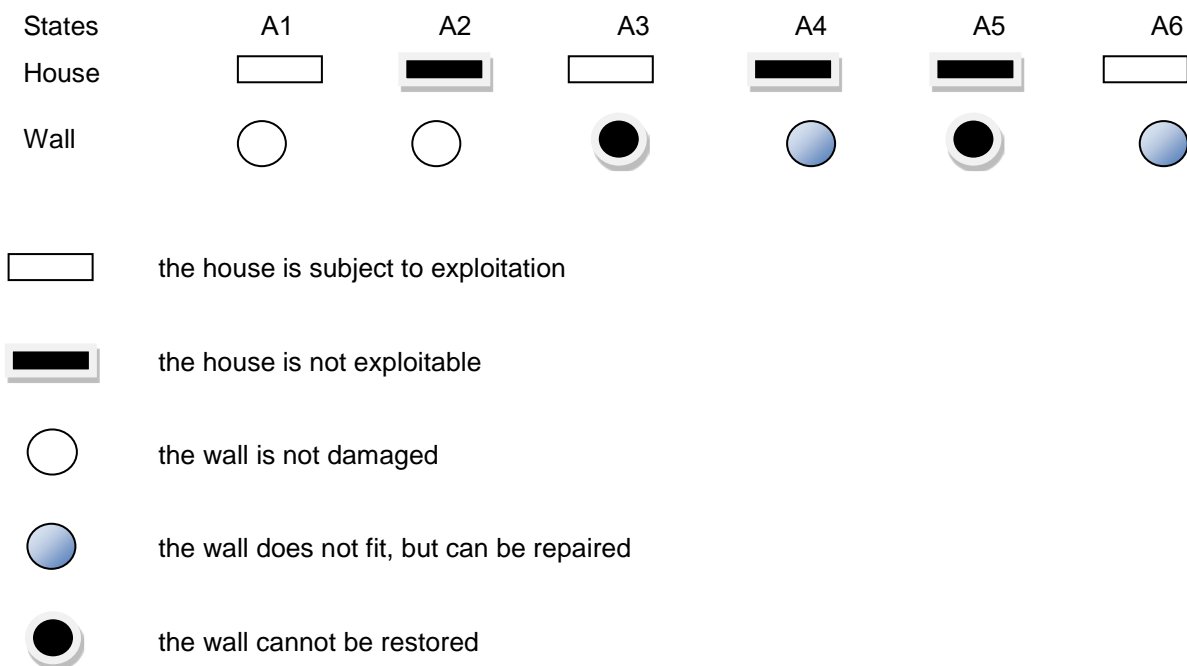


Figure 6. System event status.

According to the classification adopted above, the states A1 and A2 will be absorbing, as in either case, in the indicated state, the goal is achieved. True, the possibility of getting into the A2 state, i.e. receiving an undamaged wall with an unused house. The house may be emergency, its maximum wear has occurred as a whole, and a separately taken wall has not yet reached its maximum wear and tear and a fire has occurred in the house.

One more remark should be made. In this model, the states with an intact and damaged wall, but which can be restored, are considered the same, although this is not entirely true.

Obviously, state A6 should appear as the initial state in this example.

The transition probabilities are determined very simply here.

Since the states A1 and A2 are absorbing, then $P_{11} = 1$ and $P_{22} = 1$, and the probabilities of transition from the first and second to all subsequent states are equal to zero. If you get into the A3-A5 states, it will be necessary to repeat the operation (with the replacement of the wall, repair of the house, or with the replacement and repair at the same time), i.e., they will return to the initial state A6. Therefore, the corresponding transition probabilities P_{36} , P_{46} , P_{56} will be equal to 1.

Since the events B1-B3 and C1-C2 are compatible, the probabilities of transition from the initial state to all subsequent states are determined as the product of the probabilities of the corresponding events. The easiest way to find these works is using the event tree shown in Fig. 7.

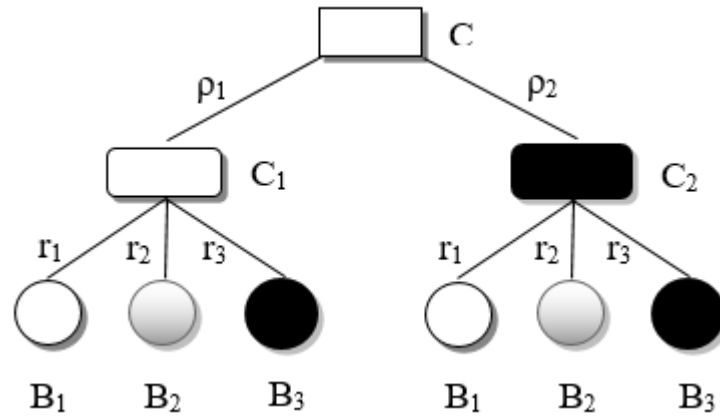


Figure 7. Transient probabilities event tree.

For example, from the initial state A6 to the absorbing A1, we will pass with the simultaneous occurrence of events B1 and C1. Consequently, the total probability of a common event will be equal to the product of private events:

$$P_{61} = r_1 \rho_1$$

Arguing similarly, we obtained

$$P_{62} = r_1 \rho_2; P_{63} = r_3 \rho_1; P_{64} = r_2 \rho_2; P_{65} = r_3 \rho_2; P_{66} = r_2 \rho_1.$$

If we assume that in each trial (operation) the transition probabilities do not change, then the process can be described by a simple homogeneous Markov chain. The graph that visually displays possible transitions in the system is shown in (Fig. 8).

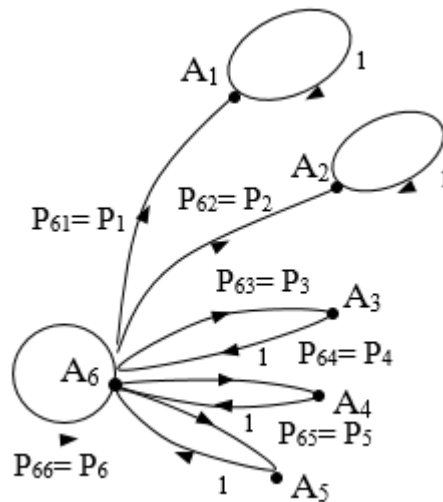


Figure 8. Possible transitions in the system.

The transition probabilities are designated hereinafter for the multiplicity P1, P2, P3, P4, P5, P6. Now the transition matrix can be represented, as before, in canonical and fundamental forms. But first of all, it would be necessary to answer the question: what can be obtained in practice?

First, let us pay attention to the fact that getting into any state is accompanied by certain expenditures of material resources and time.

For example, getting into the A3-A5 state entails costs associated with repairing a house or building a new house, etc.

If the wall is damaged, when its fire resistance limit is reduced, you also have to pay for its partial restoration. In short, along with the transition matrix, a cost (or damage) matrix must be compiled. It will have the same form as the transition matrix, but its elements are costs, $P_{61} = r_1 \rho_1$ corresponding to transitions in a certain state (Fig. 8). In the conditions associated with the restoration of the wall, one must take into account the loss of time, etc. and in cases of failure or impossible restoration of the wall – the cost of buying the whole house.

Timely restoration of the wall after a fire will reduce the likelihood of scrap collapse and the time that the house will not be used, which will extend the life of the house.

We will assume that during the period of time we are observing, the house can be in three states:

A1 – normal operation;

A2 – collapse repair;

A3 – repairs after each fire.

We will serve the house according to the following scheme. Let's assume that at time t_0 the operation of an absolutely serviceable wall begins. If the wall plaster does not collapse during the planned period of time T , at $t = T$ it is replaced with a new one (re-plastered) (preventive replacement).

If the operation continues without plastering, a fire still occurs, it destroys the wall itself, while the house is evicted and emergency repairs are carried out. For any type of repair, the destroyed element is replaced with a new one of equal quality. Of course, full equality will not be achieved. There are always some differences that lead to variances in uptime.

As a result, the time of trouble-free operation will be a random value, obeying some law of probability distribution $F(t)$.

The intervals of time during which one or another type of repair occurs – emergency t_a and preventive t_{pr} , i.e. random process. Let us depict one of its implementations graphically (Fig. 9).

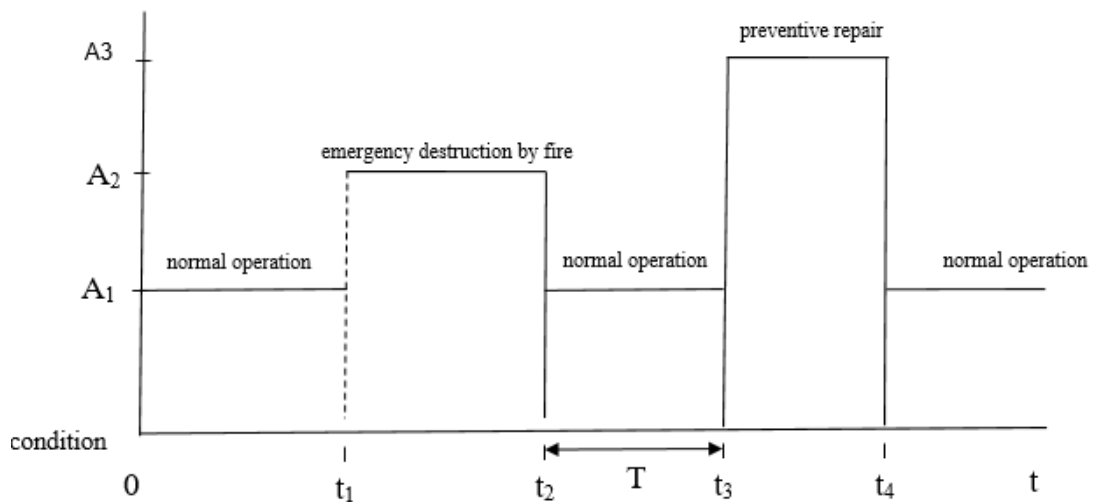


Figure 9. State graph over time intervals.

Here, the segment $0 - t_1$ corresponds to the state of normal operation. At the moment t_1 , the wall collapses, and the system jumps into state A2 – emergency repair. In the interval $t_1 - t_2$, the element (wall) is restored, and from the moment t_2 it is normally operated again. Further, the section $(t_2 - t_3) = T$ ends favorably. The wall is in operation, a fire occurs, the plaster is destroyed, and at time t_3 , preventive maintenance begins, which lasts until time t_4 . Then again in normal operation, etc. Consider now the likely picture of the process. Since the residence times in the states A1-A3 are random and not necessarily subject to the exponential law. An exception is the transition from state A1 to state A3, which always occurs after a certain time equal to T . Such processes were previously called semi-Markov processes, the transition matrix in this case will have the form:

$$P_{[3]} = \begin{bmatrix} 0 & 1-F(t) & F(t) \\ 1 & 0 & 0 \\ 1 & 0 & 0 \end{bmatrix}. \quad (5)$$

There are zeros on the diagonal of the matrix. This means that transitions within the same states are impossible. The units in the first column follow from our adopted preventive maintenance scheme. It is believed that after this or that type of repair, normal operation of the premises will begin. To assess the correctness of our actions, a matrix of expenses is compiled. Here the main task is to minimize the cost of operation, then the matrix elements will be the losses associated with the stay of the wall in a particular state. For example, during the transition from state A1 to A2 – emergency repair – the losses are equal C_{ac}

If we update the plaster prophylactically, then the costs will be less indicated $C_{pr}(C_{pr} < C_{ac})$. We write them in the form of a matrix:

$$U_{ij} = \begin{cases} C_{ac}, & \text{if } a \ A_1 \rightarrow A_2 \\ C_{pr}, & \text{if } a \ A_1 \rightarrow A_3 \\ 0, & \text{in all other cases} \end{cases} \quad (6)$$

If the goal is to assess the effectiveness of preventive repairs after a fire. Then you need to take into account the income from the normal operation of the house. It can be written like this

$$U_{ij} = \begin{cases} C_{ac}, & \text{if } a \ A_1 \rightarrow A_2 \\ C_{n.e}, & \text{if } a \ A_1 \rightarrow A_3 \\ C_{n.e,t}, & \text{if } a \ A_1 \end{cases} \quad (7)$$

4. Conclusions

1. Monitoring existing approaches to analyzing the problem of restoring building materials, products and structures after a fire confirms the importance of this problem. This, in turn, allows us to state that the existing engineering methodologies for forecasting, mathematical and software allow the researcher and designer to determine rational directions for searching for new promising and original ways to restore construction objects.

2. A management decision has been found that, when applied, will cause the least damage when extinguishing a fire in accordance with the selected conditions, and determine the remaining strength of the structure, as well as the possibility or impossibility of its further restoration, taking into account previous fires, climatic zone and operating time designs.

3. Given the complexity of establishing the further operation of buildings after a fire and the direct impact on the bearing capacity, reducing the fire resistance when cooling structures as a result of extinguishing a fire. A universal model has been developed for the formation of a software calculation for the restoration of structures after fire and fire extinguishing, to establish the residual fire resistance of a building structure after a fire in order to minimize time, which will lead to accurate results on the further operation of the building (s).

4. An option is proposed for taking into account the sharp cooling of the structure during the formation of the program calculation of decision making on the long-term operation of buildings and structures exposed to fire.

References

1. Set of rules 329.1325800.2017. Buildings and structures. Rules of inspection after the fire. [Online]. URL: <http://ivo.garant.ru/#/basearch/%D0%A1%D0%9F%20329.1325800.2017> (reference date: 05.02.2020). (rus)
2. Set of rules 54.13330.2016. Multi compartment residential buildings. [Online]. URL: <http://docs.cntd.ru/document/456054198/> (reference date: 05.02.2020).(rus)
3. Sayt MCHS Rossii [Website of the EMERCOM of Russia] [Online]. URL: <http://www.mchs.gov.ru/> (reference date: 05.02.2020). (rus)
4. Federalnyy zakon ot 22.08.2008 No 123-FZ. Tekhnicheskii reglament o trebovaniyakh pozharной bezopasnosti. [Federal law No. 123-FZ of 22.08.2008. Technical regulations on fire safety requirements]. [Online]. URL: <http://docs.cntd.ru/document/902111644/> (reference date: 05.02.2020). (rus)
5. Travush, V.I. Tsifrovyye tekhnologii v stroitelstve. [Digital technologies in construction]. Academia. Arkhitektura I stroitelstvo. 2018. No. 3. Pp. 107–117. (rus)
6. Krivtsov, A., Gravit, M., Zimin, S., Nedryshkin, O., Pershakov, V. Calculation of Limits of Fire Resistance for Structures with Fire Retardant Coating. MATEC Web of Conferences. 2016. No. 53. 1032 p. DOI: 10.1051/mateconf/20165301032
7. Schmid, J., Klippel, M., Just, A., Frangi, A., Tiso, M. Simulation of the Fire Resistance of Cross-laminated Timber (CLT). Fire Technology. 2018. No. 54 (2). DOI: 10.1007/s10694-018-0728-9
8. Dwaikat, M.B., Kodur, V.K.R. Hydrothermal model for predicting fire-induced spalling in concrete structural systems. Fire Safety Journal. 2009. No. 42. Pp. 482–488. DOI: 10.1016/j.firesaf.2008.09.001
9. Kwon, Y.J., Kim, D.J., Kang, S.G., Kim, B.C., Han, B.C., Leesp, J.Y., Kazunori, H. Fire resistance performance analysis of reinforced concrete members using Galerkin finite element method. Procedia Engineering. 2013. No. 12. Pp. 156–165.
10. Cvetkovska, M., Knezevic, M., Xu, Q., Chifliganec, C., Lazarevska, M., Gavriloska, A.T. Fire scenario influence on fire resistance of reinforced concrete frame structure. Procedia Engineering. 2018. No. 211. Pp. 28–35. DOI: 10.1016/j.proeng.2017.12.134

11. Gao, W.Y., Dai, J.G., Teng, J.G., Chen, G.M. Finite element modeling of reinforced concrete beams exposed to fire. *Engineering Structures*. 2013. 32 p. DOI: 10.1016/j.engstruct.2013.03.017
12. Annerel, E., Taerwe, L. Evolution of the strains of traditional and self-compacting concrete during and after fire. *Materials and Structures/Materiaux et Constructions*. 2011. No. 44. Pp. 1369–1380. DOI: 10.1617/s11527-010-9703-8
13. Turchin, V.N., Turchin, E.V. Markov chains: Basic concepts, examples, tasks: Textbook for University students. Dnepropetrovsk: Lizunovpress, 2016. 192 p.
14. Aloyan, R.M., Fedosov, S.V., Mizonov, V.E. Teoreticheskiye osnovy matematicheskogo modelirovaniya mekhanicheskikh i teplovykh protsessov v proizvodstve stroitelnykh materialov. [Theoretical bases of mathematical modeling of mechanical and thermal processes in the production of building materials]. monografiya. Ivanovo. IGASU. 2011. 256 p. (rus)
15. Batoyeva, E.V. Opredeleniye naiboleye effektivnykh innovatsiy v sfere zhillishchnogo stroitelstva. [Determination of the most effective innovations in the field of housing construction]. *Baikalsk Research Journal*. 2017. No. 4 (8). Pp. 25–35. (rus)
16. Zaytsev, A.M., Chernykh, D.S. O sistemnoy pogreshnosti approksimatsii temperaturnogo rezhima standartnogo pozhara matematicheskimi formulami. [On the system error of approximation of the temperature regime of a standard fire by mathematical formulas]. *Fire and explosion safety*. 2011. No. 7 (20). Pp. 14–18. (rus)
17. Zaytsev, A.M., Zaryayev, A.V., Lukin, A.N., Rudakov, O.B. Vykhod toksichnykh letuchikh veshchestv iz otdelochnykh stroitelnykh materialov na ranney stadii pozhara. [Release of toxic volatile substances from finishing building materials at an early stage of a fire]. *Scientific Bulletin of the Voronezh state University of architecture and construction. Physical and chemical problems and high technologies of building materials science*. 2011. No. 3–4. Pp. 127–133. (rus)
18. Zaytsev, A.M., Bolgov, V.A., Chernykh, D.S. Opredeleniye koeffitsiyenta teplotdachi v stroitelnyye konstruksii pri standartnom pozhare. [Determination of the heat transfer coefficient in building structures in a standard fire]. *Heliogeophysical research*. 2014. No. 9 (9). Pp. 49–53. (rus)
19. Zaytsev, A.M., Bolgov, V.A. Osobennosti ucheta nachalnoy stadii pozhara pri raschete progreva stroitelnykh konstruksiy pozhare. [Features of accounting for the initial stage of fire when calculating the heating of building structures]. *Bulletin of the Voronezh Institute of GPS EMERCOM of Russia*. 2015. No. 2 (15). Pp. 7–14. (rus)
20. Zaytsev, A.M., Bolgov, V.A. K raschetu vremeni podogreva stalnykh konstruksiy pri pozharakh do kriticheskikh temperature. [To calculate the time of heating steel structures in case of fires to critical temperatures]. *Kompleksnyye problem tekhnosfernoy bezopasnosti: tezisy dokladov*. Voronezh: VGTU, 2016. Pp. 195–201. (rus)
21. Zaitsev, A.M. The analytical solution of the problem of warming up of the sandwich constructions at fires *Scientific Israel. Technological Advantages*. 2016. No. 2 (18). Pp. 124–135.
22. Mkrtychev, O.V., Sidorov, D.S. Raschet zhelezobetonnoy zdaniya na temperaturnoye vozdeystviye. [Calculation of a reinforced concrete building on the temperature effect]. *Bulletin of the Moscow state University of civil engineering*. 2012. No. 5. Pp. 50–55. (rus). DOI: 10.22227/1997-0935.2012.5.50-55
23. Roytman, V.M., Pristupyuk, D.N. Otsenka znacheniy koeffitsiyenta usloviy raboty materiala konstruksiy i kriticheskoy temperatury progreva materiala dlya sluchaya kombinirovannykh osobykh vozdeystviy (SNE) s uchastiyem pozhara. [Evaluation of the values of the Coefficient of working conditions of the material of structures and Critical temperature of heating of the material for the case of combined special effects (SNE) involving fire]. *Bulletin of the Moscow state University of civil engineering*. 2011. No. 1 (2). Pp. 341–345. (rus)
24. Fedosov, S.V., Ibragimov, A.M., Solovyev, R.A., Murzin, N.V., Tarakanov, D.V., Lapshin, S.S. Matematicheskaya model razvitiya pozhara v sisteme pomescheniy. [Mathematical model of fire development in the premises system]. *Bulletin of the Moscow state University of civil engineering*. 2013. No. 4. Pp. 121–128. (rus). DOI: 10.22227/1997-0935.2013.4
25. Roytman, V.M. Inzhenernyye resheniya po otsenke ognestoykosti proyektiruyemykh i rekonstruiruyemykh zdaniy. [Engineering solutions for evaluating the fire resistance of designed and reconstructed buildings]. *Fire science*, 2001. 384 p. (rus)
26. Gravit, M.V., Serdyuk, D.O., Bardin, A.V., Prusakov, V.A., Buka-Vayvade, K. Metody opredeleniya ognestoykosti konstruksiy derevyannogo karkasa. [Engineering solutions for evaluating the fire resistance of designed and reconstructed buildings]. *Engineering and construction magazine*. 2019. No. 1(85). Pp. 92–106. (rus). DOI: 10.18720/MCE.85.8
27. Fedosov, S.V., Ibragimov, A.M., Gnedina, L.Yu., Smirnov, A.Yu. Silikatnyy kirpich v usloviyakh vysokotemperaturnykh vozdeystviy. [Silicate bricks under high temperature conditions]. *Building material*. 2009. No. 9. Pp. 48–49. (rus)
28. Brushlinskiy, N.N., Korolchenko, A.Ya. Modelirovaniye pozharov i vzryvov. [Modeling fires and explosions]. Monograph, Fire science, Moscow, 2000. 482 p. (rus)
29. Giletich, A.N., Shebeko, A.Yu., Shebeko, Yu.N., Gordiyenko, D.M. Trebuyemye predely ognestoykosti stroitelnykh konstruksiy vysotnykh zdaniy. [Required fire resistance limits for building structures of high-rise buildings]. *Fire safety*. 2012. No. 4. Pp. 31–39. (rus)
30. Shebeko, Yu.N., Shebeko, A.Yu., Gordiyenko, D.M. Raschetnaya otsenka ekvivalentnoy prodolzhitel'nosti pozhara dlya stroitelnykh konstruksiy na osnove modelirovaniya pozhara v pomeschenii. [Estimation of the equivalent fire duration for building structures based on modeling of fire in the premises]. *Fire safety*. 2015. No. 1. Pp. 31–39. (rus)
31. Alekseytsev, A.V., Geyli, L., Drukis, P. Optimizatsiya balochnykh konstruksiy karkasnykh zdaniy s uchedom trebovaniy k ikh bezopasnosti. [Optimization of beam structures of frame buildings taking into account their safety requirements]. *Engineering and construction magazine*. 2019. No. 7(91). Pp. 3–15. (rus). DOI: 10.18720/MCE.91.1
32. Chen, B., Liu, J. Residual strength of hybrid-fiber-reinforced high-strength concrete after exposure to high temperatures. *Cement and Concrete Research*. 2004. No. 34. Pp. 1065–1069. DOI: 10.1016/j.cemconres.2003.11.010
33. Fellingner, J., Stark, J., Walraven, J. Shear and anchorage behavior of fire exposed hollow core slabs. *Heron*. 2005. No. 50 (4). 50 p.
34. Lennon, T. Structural fire engineering design: fire development. Digest 485. BRE. 2002.
35. Li, L.Y., Purkiss, J. Stress-strain constitutive equations of concrete material at elevated temperatures. *Fire Safety Journal*. 2005. No. 40. Pp. 669–86. DOI: 10.1016/j.firesaf.2005.06.003
36. Jiang, J., Chen, L., Jiang, S., Li, G.Q., Usmani, A. Fire safety assessment of super tall buildings: A case study on Shanghai Tower. *Case Studies in Fire Safety*. 2015. No. 4. Pp. 28–38. DOI: 10.1016/j.cfsf.2015.06.001
37. Law, A. The role of modelling in structural fire engineering design. *Fire Safety Journal*. 2016. No. 80. Pp. 89–94. DOI: 10.1016/j.firesaf.2015.11.013
38. Hurley, M.J., Gottuk, D., Hall, J.R., Harada, K., Kuligowski, E., Puchovsky, M., Torero, J., Watts, J.M., Wieczorek, C. SFPE handbook of fire protection engineering, Fifth edition. 2016. DOI: 10.1007/978-1-4939-2565-0

39. Kodur, V.K.R., Harmathy, T.Z. Properties of building materials. SFPE Handbook of Fire Protection Engineering, Fifth Edition. 2016. DOI: 10.1007/978-1-4939-2565-0
40. Klippel, M., Leyder, C., Frangi, A., Fontana, M., Lam, F., Ceccotti, A. Fire tests on loaded Cross-laminated timber wall and floor elements. Fire Safety Science. 2014. No. 11. Pp. 626–639. DOI: 10.3801/IAFSS.FSS.11-626
41. Nedryshkin, O., Gravit, M., Grabovyy, K. Modeling fires in structures with an atrium in the FDS field model. MATEC Web of Conferences. 2018. No. 193. 3023 p. DOI: 10.1051/mateconf/201819303023
42. Gernay, T., Franssen, J.M. A plastic-damage model for concrete in fire: Applications in structural fire engineering. Fire Safety Journal. 2015. No. 71. Pp. 268–278. DOI: 10.1016/j.firesaf.2014.11.028
43. Kodur, V. Properties of concrete at elevated temperatures. ISRN Civil Engineering. 2014. Pp. 1–15. DOI: 10.1155/2014/468510
44. Romanovsky, V.I. Discrete Markov chains. Moscow. Leningrad: Gostekhizdat, 1949. 436 p.

Contacts:

Sergei Fedosov, FedosovSV@mgsu.ru

Vyacheslav Malichenko, mvg84@bk.ru

Mariya Toropova, matovs@mail.ru



DOI: 10.34910/MCE.106.4

Behavior of composite steel plate-sustainable concrete slabs under impact loading

H. Suwaid, K. Aziz , S. Hama* 

Department of Civil Engineering, College of Engineering, University of Anbar, Ramadi, Iraq

*E-mail: drsheelan@uoanbar.edu.iq

Keywords: composite steel plate-concrete slab, degree of interaction, deflection, impact loading, sustainable concrete, waste plastic fiber

Abstract. Concrete has been used as a protective structure to resist impact and blast loads for many years. Recently, researchers have been developing various strengthening methods to increase the impact resistance of concrete. The study includes, first, investigating the basic properties of normal concrete with plastic fibers such as compressive strength and flexural strength, and, secondly, a research of the low-velocity impact resistance of high-performance concrete with steel fiber specimens using a falling mass dropped from the same heights. The impact test used 500×500×60 mm slabs made of plain concrete with different volume fractions of plastic fiber. Test results indicated that incorporating plastic fibers in concrete significantly improves its impact resistance. There is a marginal increase in energy absorption for a change in fiber content from 0.5 to 0.75 %. The authors also considered other parameters besides waste plastic fiber percentages, e.g. degree of interaction (DOI), the method of fixing the stud to a steel plate (welding and epoxy), and the type of structure (composite and non-composite). A theoretical analysis revealed a difference between theoretical and experimental results due to repetitive strikes in the experimental test resulting in accumulated residual deflections.

1. Introduction

Composite structures are the structures made of two or more materials linked together by shear connectors. Steel-concrete composite structures are most common in construction field. Petkevicius and Valivonis investigated the effect of steel fiber on composite steel-concrete slabs under static short-time load. They found that the slip in the composite slabs incorporating steel fiber began at ~50–60 % higher load than in the slabs free of steel fiber [1]. Roesler et al. investigated the response of synthetic fiber-reinforced concrete slabs under monotonic loading. The results showed that 0.32 and 0.48 % of fiber increased the flexural cracking load of concrete slabs under center load by 25 and 32 %, respectively, compared to the one without fibers [2]. David et al. studied the effect of hooked end steel fiber on the redistribution of crack pattern and load-carrying capacity of two-way simply supported slabs. They found that concrete slabs contain steel fibers reinforced showed more cracks development with smaller crack widths compared to conventional slabs without fibers which means a more ductile behavior [3]. Due to the increased global interest in environment issues and waste recycling, many researchers focus on the reuse of waste material in concrete and the study of the influence these wastes exert on the properties of such concrete. Plastic fiber from PET bottles is an example of a waste used widely in concrete. Another study showed that adding plastic aggregate improved impact resistance of concrete [4]. Aziz et al. showed that plastic fibers increased the slip between concrete and steel section in push-out test [5]. Marthong and Sarma (2016) investigated the effects of the geometry of PET fibers on shrinkage cracking of cement-based composites [6]. Fibers of different geometry were under study: straight, deformed, flattened end and crimped end. They found that deformed fibers improved the anchorage effect and performed better in restraining the deformation in concrete. Hama (2017) incorporated plastic fibers in

Suwaid, H., Aziz, K., Hama, S. Behavior of composite steel plate- sustainable concrete slabs under impact loading. Magazine of Civil Engineering. 2021. 106(6). Article No. 10604. DOI: 10.34910/MCE.106.4

© Suwaid, H., Aziz, K., Hama, S., 2021. Published by Peter the Great St.Petersburg Polytechnic University



This work is licensed under a CC BY-NC 4.0

order to improve the porcelinate lightweight concrete strengths. She found that 0.75 % of plastic fiber compared to reference mix gave the highest compressive strength, while 1 % plastic fiber gave the flexural strength [7]. In addition, there are many researches on the effect of plastic fiber on concrete properties. However, the effect of this fiber on structural behavior of structural sections such as beams, slabs, columns etc. is limited. Moreover, there are several studies about the effect of plastic fiber on mechanical properties of concrete.

Zineddina and Krauthammer (2007) investigated the behavior of two-way slabs under impact loads. Tests results indicated that a slab and its failure modes are affected by the amount and details of steel reinforcement, impact load and drop height [8]. Tahmasebinia and Remennikov (2008) found that finite element analysis is capable of making reasonable estimations available in order to determine the possible failure modes of reinforced concrete slabs subjected to impact loads. The quantity of mesh density and direction of the sub-division on the surface of a concrete slab, where it may follow the trajectory of cracking, can play an important role in finite element analysis simulation [9]. Trevor and Vecchio (2014) investigated the behavior of steel fibers reinforced concrete slabs (SFRCs) under high mass, low-velocity impact loading conditions. Local damage development was found to be of less significance in the SFRCs. The slabs with $\rho = 0.00420$ and $\rho = 0.00592$ exhibited similar performance characteristics in terms of strength, stiffness, and local damage development [10]. Margareth and Matheus (2015) studied the effect of plastic fibers on energy absorption capacity. The result indicates an increase of up to 76 % in the energy absorption capacity of PFRC with 2.0 % fiber. In addition, it has been shown that the inclusion of recycled concrete is advantageous from energy point of view as it keeps the interior temperature remains lower, when the outside temperature rises, as compared to the conventional concrete. Hama investigated the effects of PET plastic aggregate on the impact resistance of concrete. The tests result indicated that adding of plastic aggregate improved impact resistance of slabs; energy capacity absorption also increased due to adding waste plastic [11]. Xiao et al. [12] tested six slabs under low-velocity impact. The results from high loading rate and impact tests were compared. The tests results indicate similar damage process, failure mode, strain rate, and energy absorption capacity, which suggests the possibility of using high load rate test to help understand slab's performance under low-velocity impact [12]. Manfred et al. studied how deformable projectiles impact reinforced concrete slabs at velocities of up to 400 m/sec. It was found that the penetration depths were smaller than those corresponding to undeformable projectiles impact, and the difference increased with the increase in velocity [13]. Al-Hadithi used styrene butadiene rubber SBR with different weight ratios of polymer to cement (3 %, 5 %, and 10 %) to improve of impact resistance of concrete. The improvements were significant in low-velocity impact resistance. The maximum increases were (33.33 %, 75 %, and 83.33 %) at ultimate failure for falling mass heights of 2400 mm, 1200 mm and 830 mm respectively. The polymer modified concrete beams have a stiffer response in terms of structural behavior, more ductility and lower cracking deflection than those of the reference concrete [14].

From literature review, one can see there is no study about the effect of plastic fiber on impact resistance of composite steel plate-concrete slabs. Therefore, this study aims to provide the necessary data in this field.

The objective of the present study is to demonstrate the effect of plastic fiber content on the behavior of composite steel plate-concrete slabs. This study deals with normal concrete with plastic fibers to assess its utility as construction materials for civilian structures.

2. Methods

2.1. Material, Mix Proportions and Specimens Tests

We used ordinary Portland cement (Type I) complying with Iraqi specification No. 5 / 1984 [15]. As the fine aggregate, we used natural sand that complied with the requirements of the Iraqi specification No. 45 / 1984. It has 2.6 specific gravity, 0.42 % sulfate content, 0.75 % absorption and 2.8 fine modulus. The crushed stone we used as the coarse aggregate had the maximum size of 12.5 mm meeting the requirements of Iraqi specification No. 45 / 1984 [16]. It has 2.6 specific gravity, 0.09 % sulfate content, and 0.52 % absorption. The waste plastic considered in this study is soft drink bottles waste plastics. We employed a shredder machine to slice the waste plastic bottles in uniform shapes with an average length of 35 mm, width of 4 mm and aspect ratio of 28. The materials were mixed in a rotating pan in accordance with ASTM C192-02 [17]. Compressive strength test was made according to ASTM C39-03 [18] for cylinder specimens (300×150 mm). We tested three specimens for each type of mixes and took the average value. Flexural strength of concrete was measured on 100×100×400 mm prism specimens in conformity with ASTM C293-03 [19]. We tested three prisms for each type of mixes and tool the average value.

2.2. Impact Test

As reported by the ACI Committee 544, a drop-weight test assessed the resistance of concrete under dynamic loadings [20]. The low velocity impact test was conducted using a 4 kg steel ball dropping freely from the height of 2.4 m. Twenty-two 500×500×60 mm composite slabs consisting of BRC reinforced concrete slabs resting on top of a hot rolled steel plate with the same dimensions and 3 mm thickness were tested under impact force. Shear stud connectors were used to ensure the composite action between concrete slab and steel plate. The composite slab was designed based on the full interaction theory. The composite slab details are clarified in Fig. 1. Two dial gauge recorders on average were placed under the steel plate to measure the central deflection (see Fig. 2). The properties of stud connection are listed in Table 1.

Table 1. Geometry and mechanical properties of stud shear connector.

Diameter (mm)	Height (mm)	Yielding stress (MPa)	Ultimate strength (MPa)	% Elongation
6	35	612	780	20.1

Slabs were placed in their position in the testing frame. The falling mass of 3 kg was then dropped repeatedly and the number of blows required to cause first crack was recorded. The number of blows required for failure (no rebound) was also recorded. The number and details of slabs, which were used in this test, are presented in Table 2.

Three parametric studies taken:

- Degree of interaction (D.O.I.) (0, 50, 100 %)
- Percentages of plastic fibers (0, 0.5, 0.75, 1 %)
- Type of connection between steel plate and stud shear connector (welding, epoxy).

Table 2. Composite slabs details.

No.	Symbol	% WPF	% Degree of interaction	Type of connection
	S1	0	50	Epoxy glued studs
	S2	0	No studs	Epoxy glued plate without studs
	S3	0	0	Welding
	S4	0	50	Welding
	S5	0	100	Welding
	S6	0	0	Control without plate with 74 mm RC slab only
	S7	0.5	50	Epoxy glued studs
	S8	0.5	No studs	Epoxy glued plate without studs
	S9	0.5	0	Welding
	S10	0.5	50	Welding
	S11	0.5	100	Welding
	S12	0.75	50	Epoxy glued studs
	S13	0.75	100	Epoxy glued studs
	S14	0.75	No studs	Epoxy glued plate without studs
	S15	0.75	0	Welding
	S16	0.75	50	Welding
	S17	0.75	100	Welding
	S18	1	50	Epoxy glued studs
	S19	1	No studs	Epoxy glued plate without studs
	S20	1	0	Welding
	S21	1	50	Welding
	S22	1	100	Welding
	S23	2	50	Welding

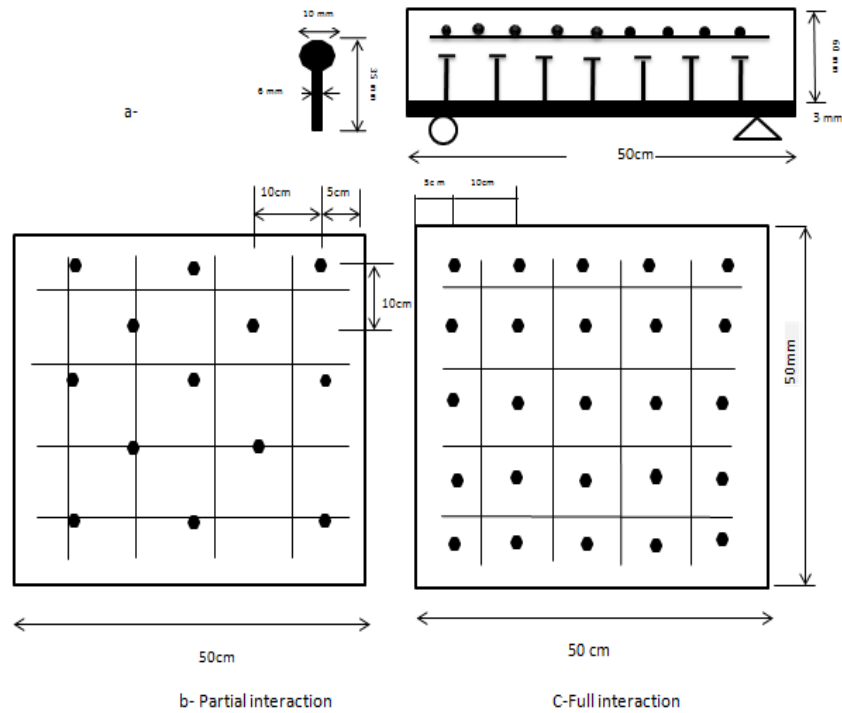


Figure 1. Details of composite slabs a) Front view; b) Top view of 50 % I.O.D slab; c) Top view of 100 % I.O.D slab.



Figure 2. Frame test for impact loading.

3. Results and Discussions

3.1. Compressive and Flexural Strengths

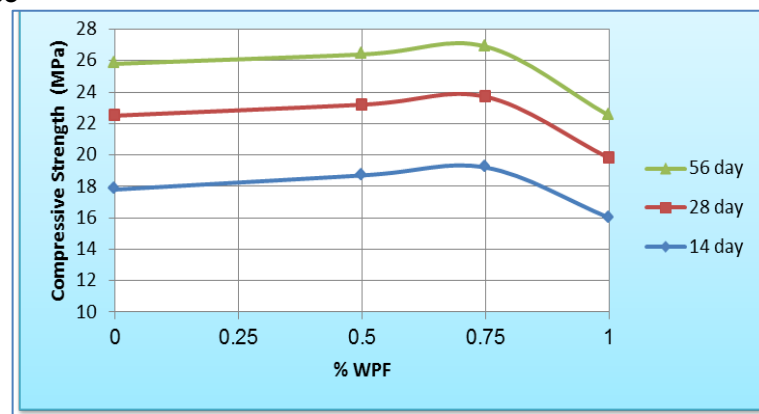
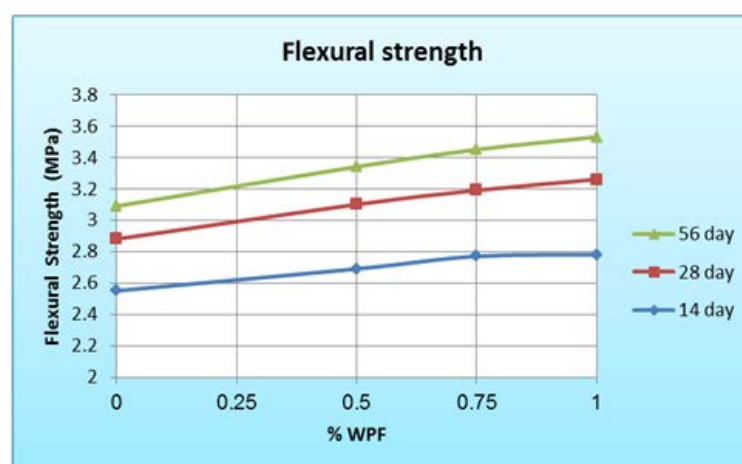
Compared with the control specimen, higher contain of WPF (waste plastic fibers) increased the compressive strength of the slabs up to the point of 0.75 % WPF as shown in Fig. 3. There is a drop in values below that for the control specimen, when the WPF percentage was equal to 1 % as shown in Table 2. Flexural strength increased along with the % WPF (see Fig. 4) due to an enhancement in tensile strength of concrete. The presence of WPF made tight microscopic cracks propagate and reinforce the concrete matrix. Addition of WPF assists in converting the brittle properties of concrete to ductile ones [4, 7].

Table 2. Test results for compressive strength.

Age (Days)	%WPF	Compressive strength – (MPa)	% change	Flexural strength (MPa)	% change
14	0.00	17.8	–	2.55	–
	0.50	18.7	+5	2.69	+5.5
	0.75	19.2	+7.9	2.77	+8.6
	1.00	16	–10.1	2.78	+9
28	0.00	22.5	–	2.88	–
	0.50	23.2	+3.1	3.1	+7.6
	0.75	23.7	+5.3	3.19	+10.8
	1.00	19.8	–12	3.26	+13.2
56	0.00	25.8	–	3.09	–
	0.50	26.4	+2.3	3.34	+8.1
	0.75	26.9	+4.3	3.44	+11.3
	1.00	22.5	–12.8	3.52	+13.9

(+) increase

(–) decrease

**Figure 3. Dependence of compressive strength on % WPF for different ages.****Figure 4. Dependence of Flexural strength on % WPF for different ages.**

3.2. Impact test results

The number of blows that cause first crack and then failure (smashing of reinforced concrete slab), and deflection due to first blow are recorded for all composite slabs. Fig. 5 shows slabs before and after failure. The following results were recorded according to the parametric study adopted in this research:

Slabs before test

Sabs after test



Figure 5. Failure of composite slabs under Impact force.

3.2.1 Effects of waste plastic fibers (WPF)

With WPF percentages growing, the number of blows causing the first crack increases regardless of the degree of interaction between concrete slab and steel plate. However, both the number of blows at failure and maximum deflection at failure experience a drop and a rise respectively for WPF of 0.75 % and higher (see Fig. 6–8).

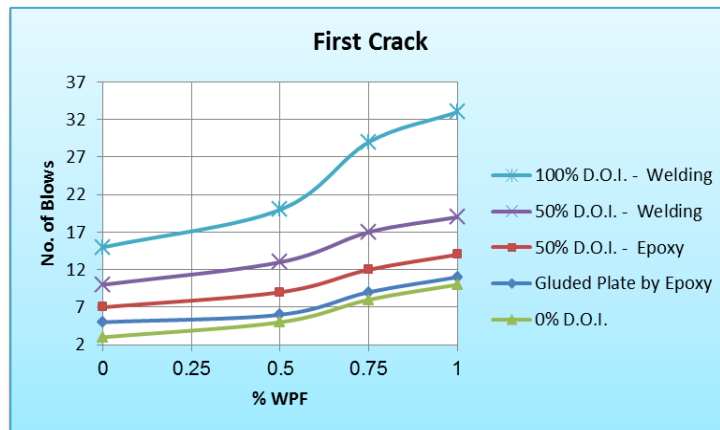


Figure 6. No. of blows at first crack dependence of the number of blows on % WPF.

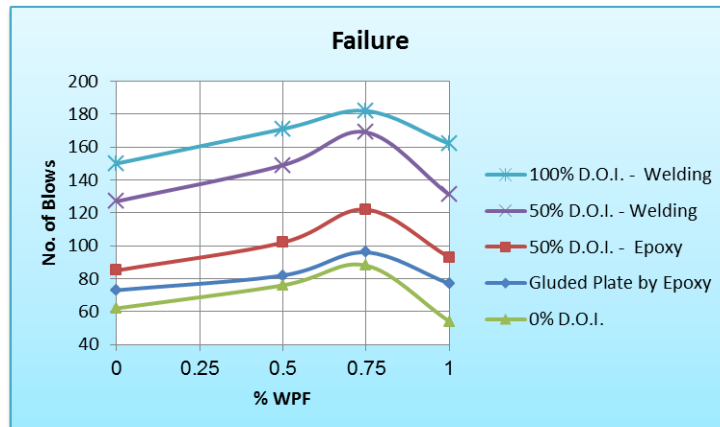


Figure 7. No. of blows at failure dependence of the number of blows on % WPF.

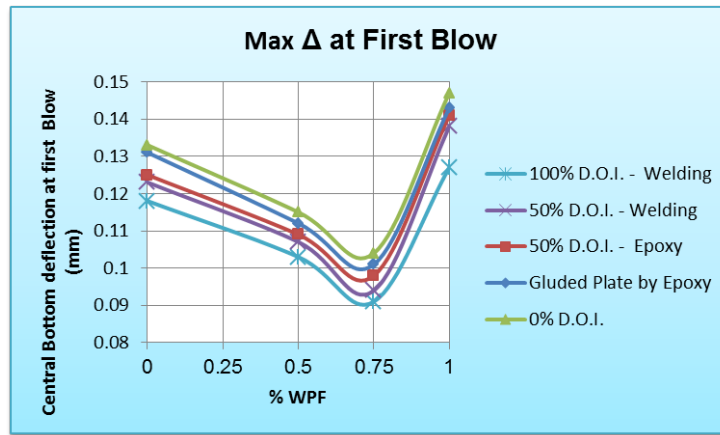


Figure 8. Deflection at failure dependence of max. deflection on % WPF.

A relatively low content of plastic fibers effectively enhances the capacity of composite slabs and makes the structural response more ductile; volume fractions of plastic fibers higher than 1.0 % slightly improve the number of blows at failure, but remarkably enhance the composite slabs ductility.

3.2.2 Effects of degree of interaction

Test results shown in Fig. 9–11, indicate that the number of blows required to reach the first crack and failure (except max. deflection at failure) are increasing along the degree of interaction in comparison with 0 % D.O.I. This explained by the fact that the composite slab strength capacity increases against the applied loading due to the increase in rigidity and stiffness. In addition, the presence of steel plate makes the composite slab more ductile.

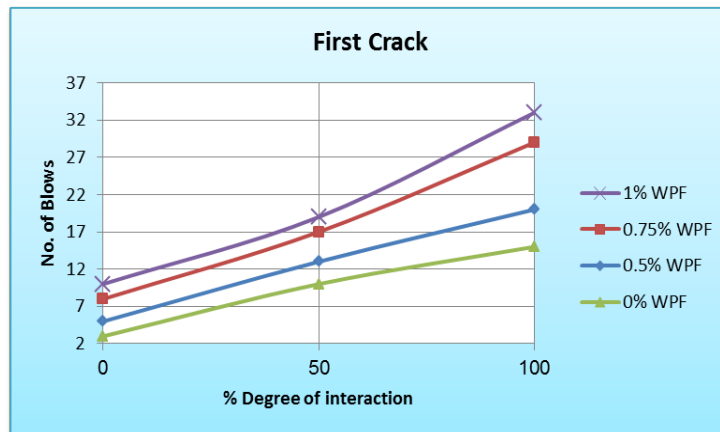


Figure 9. No. of blows at first crack dependence of the number of blows on D.O.I

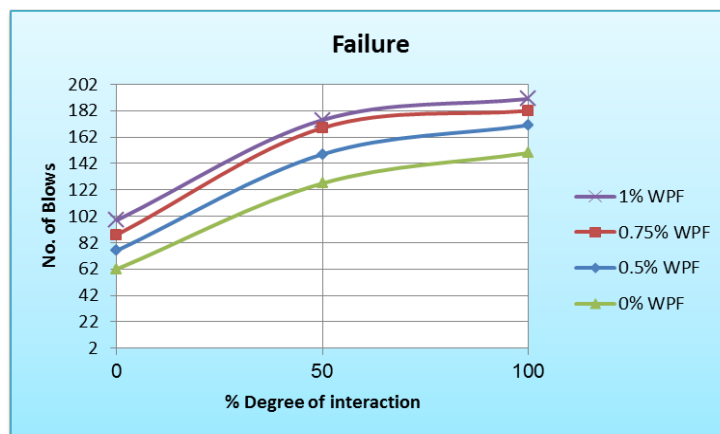


Figure 10. No. of blows at failure dependence of the number of blows on D.O.I.

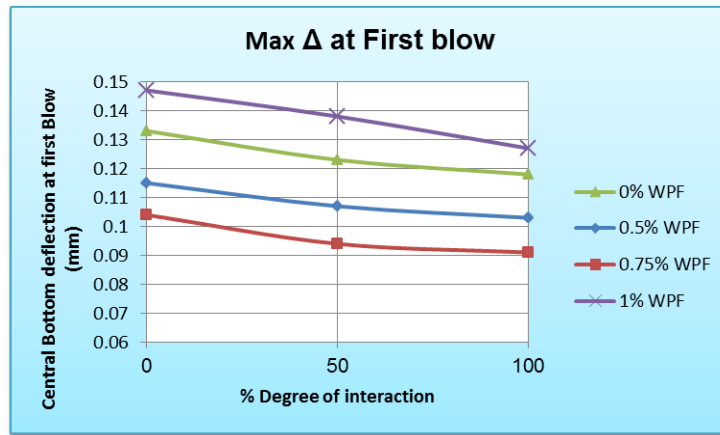


Figure 11. Deflection at failure dependence of max. deflection on D.O.I.

3.2.3 Methods of fixing stud connectors on steel plate (welding and epoxy)

Two methods were adopted to connect the stud connectors and steel plate: welding and epoxy resin.

The number of blows at the first crack and at failure stage is less for epoxy glue compared with welding for the same ratio of WPF and identical D.O.I. (see Fig. 12, 13). Moreover, the maximum deflection increases in case of using epoxy compared to welding for the same WPF % and D.O.I. (see Fig. 14). The strength resistance and capacity of welding are greater than those of epoxy.

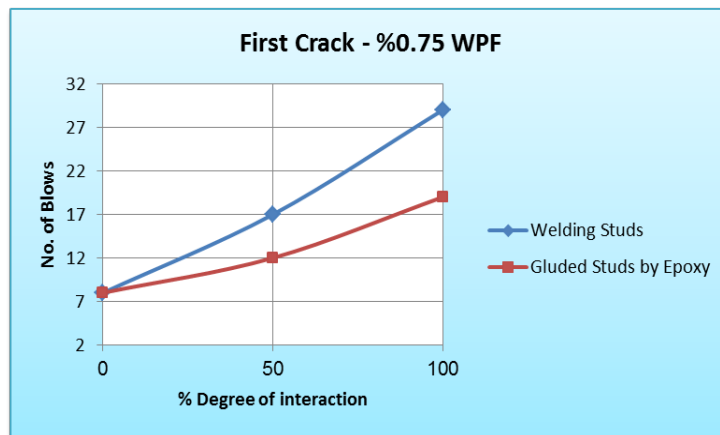


Figure 12. No. of blows vs. D.O.I. for epoxy glue and welding at first crack.

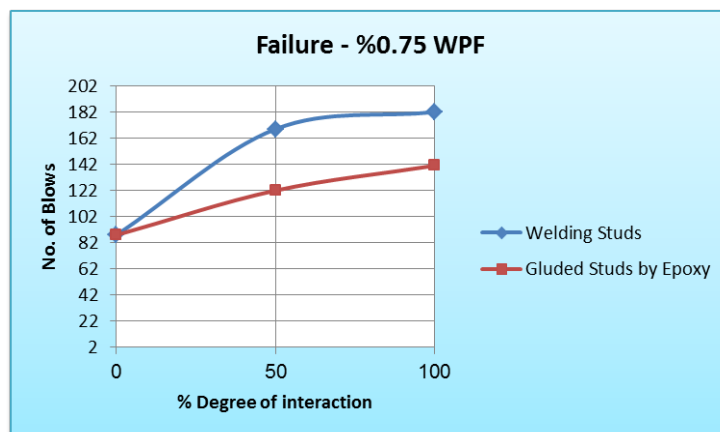


Figure 13. No. of blows vs. D.O.I. for epoxy glue and welding at failure.

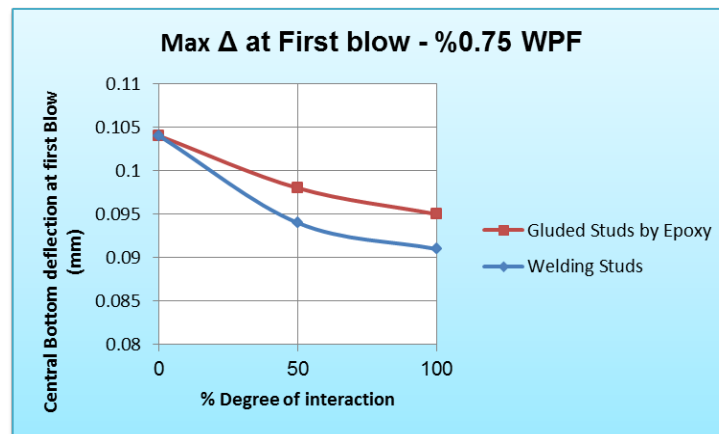


Figure 14. Maximum deflection vs. D.O.I. for epoxy glue and welding at failure.

3.3. Energy Absorption Capacity

Energy absorption capacity by can be calculated from the number of total blows that caused the failure as following:

$$\text{Impact energy capacity} = \text{Number of blows} \times \text{Mass of iron ball (4 kg)} \times 9.8 \text{ m/s}^2 \times \text{Drop distance (2.4 m)} \quad (1)$$

The results are listed in Table 3 as following.

Table 3. Impact energy capacity.

Symbol	% WPF	% Degree of interaction	Type of connection	Number of blows up to failure	Impact energy capacity, J
S1	0	50	Epoxy glued studs	85	7996.80
S2	0	No studs	Epoxy glued plate without studs	73	6867.84
S3	0	0	Welding	62	5832.96
S4	0	50	Welding	127	11948.16
S5	0	100	Welding	150	14112.00
S6	0	0	Control without plate with 74 mm RC slab only	16	1505.28
S7	0.5	50	Epoxy glued studs	90	8467.20
S8	0.5	No studs	Epoxy glued plate without studs	82	7714.56
S9	0.5	0	Welding	76	7150.08
S10	0.5	50	Welding	149	14017.92
S11	0.5	100	Welding	171	16087.68
S12	0.75	50	Epoxy glued studs	122	11477.76
S13	0.75	100	Epoxy glued studs	141	13265.28
S14	0.75	No studs	Epoxy glued plate without studs	98	9219.84
S15	0.75	0	Welding	88	8279.04
S16	0.75	50	Welding	169	15899.52
S17	0.75	100	Welding	182	17122.56
S18	1	50	Epoxy glued studs	93	8749.44
S19	1	No studs	Epoxy glued plate without studs	77	7244.16
S20	1	0	Welding	54	5080.32
S21	1	50	Welding	131	12324.48
S22	1	100	Welding	162	15240.96
S23	2	50	Welding	81	7620.48

3.3.1 Effects of waste plastic fibers (WPF)

As WPF percentage rises, the number of blows required to reach the first crack increases regardless of degree of interaction between concrete slab and steel plate, which led to an increase in strain energy capacity of slabs. For example, for a group of slabs with 50 % D.O.I and welding connection between studs and steel plate, the reference slab without plastic fibers had a strain energy capacity of 11948.16 J, while the strain energy for 0.5 %, 0.75 %, 1 % and 2 % WPF were 14017.92, 15899.52, 12324.48 and 7620.48 J, respectively. One can observe that all WPF percentage up to 1 % increased the energy capacity of composite slabs compared to the reference one. However, the slab with 2 % WPF content had a decreased energy capacity absorption compared to the reference one.

3.3.2 Effects of degree of interaction

Test results shown in Table 3 indicate that the energy capacity is increasing along with degree of interaction compared with 0 % D.O.I. For example, the slab of 0 % D.O.I. and 0 % WPF had strain energy capacity of 5832.96 J, while the slabs of 50 % and 100 % D.O.I. displayed strain energy of 11948.16 and 14112.00 J, respectively.

3.3.3 Methods of fixing stud connectors on steel plate (welding and epoxy)

Test results shown in Table 3 indicate in comparison with welding methods, the energy capacity decreases when epoxy glue is used for the same ratio of WPF and same D.O.I. This may be due to a greater strength resistance and capacity of welding, as mentioned before.

3.4. Finite Element Method and simulated models

The model in finite element analysis (FEA) was done by means of ANSYS software. A smeared cracking approach has been used to model the reinforced concrete. The elastic modulus of the material is then assumed to be zero in the direction parallel to the principal tensile stress direction which means that the concrete is not capable of resisting tensile strength exceeding the limit and the modulus of elasticity in tension equals zero. The concrete starts crushing in the elements located directly under the loads when the stresses in compression zone exceed the compressive strength of concrete. In this research, the crushing capability was turned off and cracking of the concrete controlled the failure of the finite element models.

Discrete representation of BRC reinforcements matching the actual reinforcement of concrete slabs was adopted. Three types of elements were selected and adopted to simulate composite slab models. We adopted the following types of elements in present study to simulate the composite slab are: SOLID65 for concrete slab, LINK180 for BRC, SHELL181 for steel plate, and COMBIN7 (Revolute Joint) for stud connector. Each selected element type represents and simulates the actual behavior of each material.

We used the following equation [21]:

$$\left[\frac{f(t)}{k} \right]^{2/3} = V_o \cdot t - \frac{1}{m_s} \int_0^t d\tau \int_0^\tau f(\bar{\tau}) d\bar{\tau} - Y(t)_{striker} \quad (2)$$

It can be solved to determine force-time history for impact, by using numerical integration method described by Al-Azawi [22] for slabs. Newton-Raphson equilibrium iteration has been used to solve the nonlinear problem of impact in ANSYS software and displacement convergence criterions have been used in order to monitor the equilibrium.

3.5. Impact analysis results

Analysis results are shown in Fig. 14–17. Because of non-availability of the sophisticated measuring devices of dynamic deflections, maximum transient deflection was used for comparison between theoretical and experimental deflection. Maximum theoretical mid-span deflection of the reference slab is 0.21 mm, while the experimental test gave a maximum mid-span deflection of 0.125 mm. Maximum theoretical mid-span deflection of 0.5 % WPF slab is 0.177 mm, while the experimental test gave a maximum mid-span deflection of 0.105 mm. Maximum theoretical mid-span deflection of 0.75 % WPF slab is 0.127 mm while the experimental test gave a maximum mid-span deflection of 0.09 mm. Finally, maximum theoretical mid-span deflection of 1 % WPF slab is 0.23 mm, while the experimental test gave a maximum mid-span deflection of 0.14 mm. The difference between theoretical and experimental results is related to repetition of strikes in experimental test, which results in accumulated residual deflections. Consequently, the velocity and acceleration of a sinusoidal shape represent a free vibration mode.

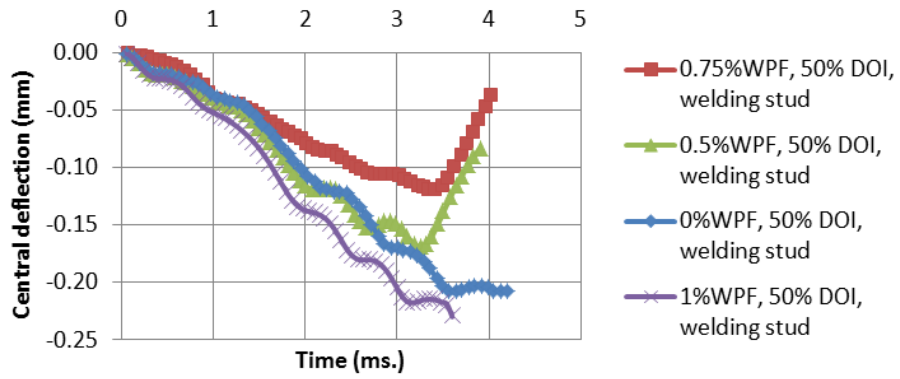


Figure 15. Mid-span deflection vs. time.

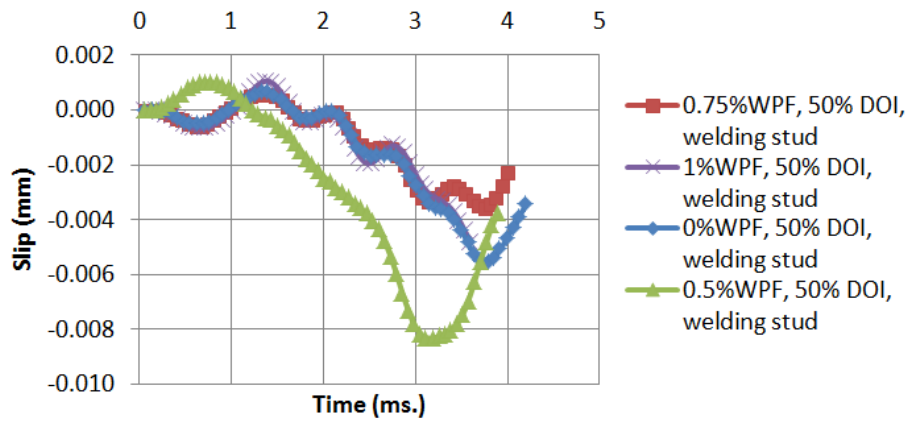


Figure 16. Slip vs. time.

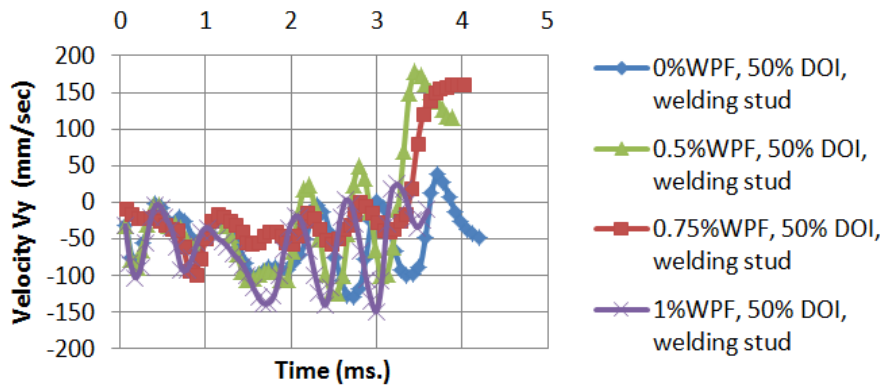


Figure 17. Velocity vs. time.

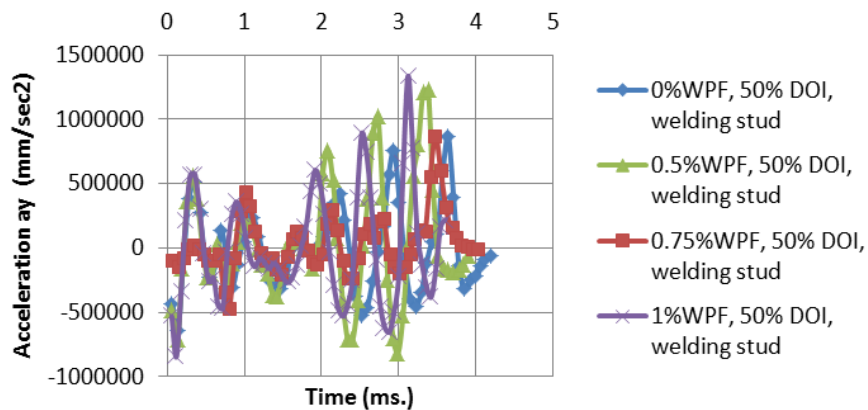


Figure 18. Acceleration vs. time.

4. Conclusions

Based on the results of the simulation and experimental tests, we can summarize the most important points as follows:

Compared with the control specimen, higher content of WPF (waste plastic fibers) increased the compressive strength of the slabs up to the point of 0.75 % WPF as shown in Fig. 3. There is a drop in values below that for the control specimen, when the WPF percentage was equal to 1 %

1. Compared with the control specimen, the compressive strength increased in the slabs containing up to 0.75 % WPF. There is a drop in values below that for the control specimen, when the WPF percentage was equal to 1 %. While flexural strength increased when %WPF increased.

2. With WPF percentages growing, the number of blows causing the first crack increases regardless of the degree of interaction between concrete slab and steel plate. However, both the number of blows at failure and maximum deflection at failure experience a drop and a rise respectively for WPF of 0.75 % and higher.

3. The number of blows required to reach first crack and failure is increasing along degree of interaction (for the same WPF percentage) in comparison with 0 % D.O.I.

4. The number of blows at the first crack and at failure stage is less for epoxy glue compared with welding for the same ratio of WPF and identical D.O.I.

5. A low content of plastic fibers up to 0.75 % effectively enhances the capacity of composite slabs and makes the structural response more ductile; volume fraction of plastic fibers equal to 1.0 % slightly improves the number of blows at failure, but remarkably enhances the composite slabs ductility.

6. As WPF percentage increases, the number of blows required to reach the first crack increases regardless of degree of interaction between concrete slab and steel plate, which led to an increase in strain energy capacity of slabs.

7. Energy capacity is increasing along with degree of interaction in comparison with 0 % D.O.I.

8. Energy capacity decreases in case of using epoxy glue in comparison with welding methods for the same ratio of WPF and same D.O.I.

9. A difference between theoretical and experimental results was noticed: the repetition of strikes in the experimental test resulted in accumulated residual deflections.

10. Velocity and acceleration of a sinusoidal shape represent a typical free vibration mode.

References

- Petkevičius, M., Valivonis, J. Analysis of bending capacity of composite steel-concrete slabs with steel fiber reinforced concrete, in The 10th International Conference "Modern Building Materials, Structures and Techniques": Selected papers, Vol. 2. Ed. by P. Vainiūnas, E.K. Zavadskas, May 19–21, 2010, Lithuania. Vilnius: Technika, 2010. Pp. 744–751.
- Roesler, J.R., Altoubat, S.A., Lange, D.A., Rieder, K., Ulreich, G.R. Effect of Synthetic Fibers on Structural Behavior of Concrete Slabs-on-Ground. *ACI Materials Journal*. 103 (1) 2006. Pp. 3–10.
- David, F., Rasmus, R., Karin, L. Experiments on Fibre Reinforced Concrete Two-Way Slabs. *Fibre Concrete*, Prague, Czech Republic. 2013. Pp. 1–10.
- Hama, S.M. Behavior of concrete incorporating waste plastic as fine aggregate subjected to compression, impact load and bond resistance. *Eur J Environ Civ Eng.* (2020). <https://doi.org/10.1080/19648189.2020.1798287>
- Aziz, K.I., Hama, S.M., Kuhair, H.M.L. Efficiency of Waste Plastic Fiber on Behavior of Composite Steel Plate-Concrete Push Out Test. 2018 11th International Conference on Developments in eSystems Engineering (DeSE), 2018, pp. 335-339, doi: 10.1109/DeSE.2018.00066.
- Marthong, C., Sarma, D.K. Influence of PET fiber geometry on the mechanical properties of concrete: an experimental investigation. 20(7) 2016. Pp. 771–784. <https://doi.org/10.1080/19648189.2015.1072112>
- Hama, S.M. Improving mechanical properties of lightweight Porcelanite aggregate concrete using different waste material" *International Journal of Sustainable Built Environment*. 6, 2017. Pp. 81–90. <http://dx.doi.org/10.1016/j.ijsbe.2017.03.002>
- Zineddina, M., Krauthammer, T. Dynamic response and behavior of reinforced concrete slabs under impact loading", *International Journal of Impact Engineering*. 34 (9) 2007. Pp. 1517–1534. <https://doi.org/10.1016/j.ijimpeng.2006.10.012>
- Tahmasebinia, F., Remennikov, A. Simulation of the Reinforced Concrete Slabs under Impact Loading. *Australasian Structural Engineering Conference (ASEC)*, 26–27 June 2008. Pp. 088 (1–10).
- Trevor, D.H., Vecchio, F.J. Behavior of Steel Fiber-Reinforced Concrete Slabs under Impact Load", *ACI Structural Journal*. 111 (5) 2014. Pp. 1213–1224. DOI: 10.14359/51686923
- Mahmoud Hama, S. Evaluations of strengths, impact and energy capacity of two-way concrete slabs incorporating waste plastic. *J King Saud Univ Eng Sci* (2021) 33:337–345. <https://doi.org/10.1016/j.jksues.2020.09.007>
- Xiao, Y., Li, B., Fujikake, K. Experimental Study of Reinforced Concrete Slabs under Different Loading Rates. *ACI Structural Journal*. 113 (1) 2016. Pp. 157–168. <http://dx.doi.org/10.14359/51688067>

13. Manfred, H., Hermann, P., Alost, S.P. Behavior of Highly Deformable Projectiles in Reinforced Concrete Slabs. Inter-Association Symposium on Concrete Structures under Impact and Impulsive Loading, Berlin, June, 1982. Cited by (Al-Azawi, T.K., "Impact Resistance of Reinforced Concrete Slabs", Ph. D. Thesis, Sheffield University, Nov. 1984.
14. Al-Hadithi, A.I. Flexural, Impact and Thermal Properties of Polymer Modified Concrete. Ph. D., Thesis, Building and Construction Department, University of Technology. 2005.
15. Iraqi specification No. 5 / 1984. Portland Cement. Central Agency for standardization and Quality Control, Planning Council, Baghdad, Iraq.
16. Iraqi specification No. 45 / 1984. Aggregate from Natural Sources for ncrete. Central Agency for Standardization and Quality Control, Planning Council, Baghdad, Iraq.
17. ASTM C192 / C192M-02, Standard Practice for Making and Curing Concrete Test Specimens in the Laboratory, ASTM International, West Conshohocken, PA, 2002, www.astm.org. DOI: 10.1520/C0192_C0192M-02
18. ASTM C39/C39M. Standard Test Method for Compressive Strength of Cylindrical Concrete Specimens. 04.03. 2003. West Conshohocken, PA.
19. ASTM C78. Standard Test Method for Flexural Strength of Concrete Using Simple Beam with Third- Point Loading. Annual Book of ASTM Standard. 2003.
20. ACI 544, Measurement of Properties of Fiber Reinforced Concrete, ACI, West Conshohocken, PA, 1999.
21. Adnan, F.A., Ali, G.A. AL-Khafaji. Nonlinear Finite Element Analysis of Reinforced Concrete Slabs under Impact Loads. Journal of Kerbala University, Vol. 13, No. 1, Scientific. 2015.
22. Al-Azzawi, T.K. "Impact Resistance of Reinforced Concrete Slab", Ph.D. Thesis, University of Sheffield, England, 1984.

Contacts:

Hashim Suwaid, raedalhiti@gmail.com

Khalil Aziz, k_ibraheem@yahoo.com

Sheelan Hama, drsheelan@uoanbar.edu.iq



DOI: 10.34910/MCE.106.5

Composite non-autoclaved aerated concrete based on an emulsion

Y.Y. Sabitov, D.S. Dyusseminov , A.A. Zhumagulova , D.O. Bazarbayev* ,
R.E. Lukpanov 

L.N. Gumilyov Eurasian National University, Nur-Sultan, Kazakhstan

*E-mail: phdd84@mail.ru

Keywords: concretes, compressive strength, cements, mixtures, water absorption, concrete testing, sodium hydroxide

Abstract. The proposed composite non-autoclaved aerated concrete based on a polymer emulsion is a solution to several problematic issues in the production of non-autoclaved aerated concrete. Using the method of joint emulsification of aluminium powder and polymer component, we obtained a polymer emulsion that contributes to high-quality saponification of the gas-forming agent. The emulsion ensures uniform gas release over the entire volume of the aerated concrete block, thereby providing a uniform pore structure. To assess the uniformity of the pore structure, we determined the density by sampling three sections of aerated concrete (upper, middle and bottom). We studied the quality of the pore structure by calculating water absorption by weight, compressive strength and freeze/thaw resistance. The results of the water absorption study showed the effectiveness of the polymer emulsion due to the hydrophobicity of the polymer component. The research also revealed the structure of composite aerated concrete cell walls. The obtained results of tests on the strength of composite aerated concrete in comparison with traditional aerated concrete also confirmed the effectiveness of using the polymer emulsion. The analysis of the conducted research contributed to the disclosure of the process that affects the increase in the strength of the material. Research on the freeze/thaw resistance of composite aerated concrete has revealed the mechanism of action of the polymer emulsion in the process of alternate freezing and thawing. In general, the paper demonstrates how polymer emulsion and aluminium powder influence the uniform distribution of pores in the composite structure, and therefore, contribute to the uniform density, low water absorption, high strength and freeze/thaw resistance of composite aerated concrete.

1. Introduction

Nowadays the construction industry is saturated with various construction materials based on binders from cement to organic [1]. Polymer binders are widely used also in the production of building materials. They have a low density and high acoustic and thermal properties, as well as low water absorption, which also positively characterizes these materials [2]. Despite a number of positive characteristics, the polymer binder has such disadvantages as flammability and non-durability [3].

The advantages of cement binder are high strength and density [4]. However, there are materials with a lower density. These include lightweight concretes on a light aggregate, as well as cellular concretes that have a low density and pore structure [5].

Due to the high demand for this cellular material, the interest in its research and improvement has increased. A major disadvantage of cellular concrete is its instability in the preparation process. Cellular

Sabitov, Y.Y., Dyusseminov, D.S., Zhumagulova, A.A., Bazarbayev, D.O., Lukpanov, R.E. Composite non-autoclaved aerated concrete based on an emulsion. Magazine of Civil Engineering. 2021. 106(6). Article No. 10605. DOI: 10.34910/MCE.106.5

© Sabitov, Y.Y., Dyusseminov, D.S., Zhumagulova, A.A., Bazarbayev, D.O., Lukpanov, R.E., 2021. Published by Peter the Great St.Petersburg Polytechnic University.



This work is licensed under a CC BY-NC 4.0

concrete is divided into foam concrete and aerated concrete [6, 7]. A distinctive feature of foam concrete is a method for obtaining a cellular structure in the material by introducing a foam concentrate, which contributes to the formation of a closed pore structure of the composite [8]. Foam concrete has many advantages, but in addition to advantages, there are certain disadvantages that negatively affect the quality of the material. A literary review showed that the disadvantages of foam concrete materials were solved by introducing reinforcement materials such as basalt, fibers, steel reinforcement, etc. in the works [9–13]. Taking into account the modern approach and new technologies, foam concrete has eventually occupied its niche in the construction industry as a monolithic thermal insulating material, since the production of construction materials has always been accompanied by a large quantity of poor quality products, foam mortar has given a large shrinkage in shape and the material has become unusable [14], [15]. Aerated concrete, on the contrary, has become more widely used in the construction industry as a wall insulation structural material. The difference between aerated concrete and foam concrete is the use of a gas-forming agent, which in the course of a chemical reaction causes the process of gas formation and thereby inflates the solution, creating communicating pores [16]. Aluminum powder and hydrogen peroxide (technical peroxide) are used as a gas-forming agent [17]. Disadvantages of aerated concrete are high water absorption and low freeze/thaw resistance associated with its communicating pore structure [18, 19]. In the technology of production of aerated concrete, measures have also been taken to improve their physical and mechanical properties by using reinforcing components with modifiers [20]. The production of composite material is of great interest to the construction industry, and therefore improvement and elimination of existing shortcomings is relevant.

After analyzing the existing shortcomings and modern achievements in the field of aerated concrete production, as well as studying the chemical processes of structure formation of the material, the possibility of using polymer components was suggested [16, 21]. Practice has shown that research on this issue has been conducted and certain results have been obtained [22, 23].

But even in these cases, the manufacturer faced certain difficulties, from chemical to technological processes [24–26]. In this regard, our study of the influence of water-soluble polymers on the quality of the composition and technological process of aerated concrete has undeniable importance.

The purpose of the research process is to obtain high-strength non-autoclaved composite aerated concrete with improved physical and mechanical properties.

To achieve this goal, the following tasks were completed:

- to study the theoretical aspects of existing technologies, their features and disadvantages;
- to develop a technological process for the production of composite aerated concrete;
- to investigate the influence of polymer on the structure of composite aerated concrete cell walls;
- to conduct a comparative analysis of the effectiveness of composite aerated concrete with its analogues.

2. Methods

Preparation of traditional aerated concrete products was carried out under production conditions according to the standard method. Composite aerated concrete was produced with the addition of a polymer component – polyvinyl acetate (PVA). The composition of this material according to traditional and composite technologies is shown in Table 1.

Table 1. Composition of aerated concrete.

Type of aerated concrete	Cement, kg	Sand, kg	Gas generator, gr	PVA polymer, kg	Sodium hydroxide, gr	Water, l
Traditional aerated concrete	270	350	350	–	500	162
Composite aerated concrete	270	350	370	1.5	–	121

For the preparation of aerated concrete were used:

Cement CEM I 42.5 N with chemical composition of CaO – 60.40 %, SiO₂ – 22.15 %, Al₂O₃ – 5.67 %, MgO – 4.9 %, Fe₂O₃ – 3.8 %.

Sand with fineness modulus 2.23, bulk density 1.5 g/cm³, true density 2.59 g/cm³, hollowness 42.8 %, contamination 1 %.

Polyvinyl acetate with a density of 1.15 g/cm³, viscosity 0.09 Pa*s, hydrogen pH 5.5, polymerization degree 1800.

In the production of traditional aerated concrete, dry components are combined in a mixer: sand and cement. Then water is poured into the mixer. The water temperature should not exceed 55 °C. Then the compound is thoroughly mixed for 5-7 minutes. After this, aluminum powder is prepared, in our case, PAP-2. Aluminum powder and sodium hydroxide are combined in hot water with a temperature not lower than 70 °C. Then a prepared aqueous solution of sodium hydroxide and aluminum powder is added to the cement-sand mixture. Finally, the composition is mixed for 5-7 minutes and distributed in the prepared forms.

After forming, the aerated concrete is expanded before setting, and excess material is removed from the surface of the mold to its level. And after 20-24 hours, the aerated concrete is removed from the formwork and sawn on the template.

For the production of composite aerated concrete, the dry components of sand and cement are also stirred in a mixer, after which water is poured into the compound at a temperature of at least 55 °C and thoroughly mixed for 5-7 minutes. Then the gasifier is prepared. To obtain a saponified gas-forming agent, we use a PVA polymer instead of sodium hydroxide. Based on the above, in the course of solving the problem of effective combination of a polymer component (PVA), a gas-forming agent (aluminum powder) with a mineral binder, a number of issues of interaction of a water-soluble polymer and aluminum powder were taken into account. The most optimal solution was to obtain an emulsion of PVA, water and aluminum powder, which is easily soluble in a cement-sand solution.

The quality of the prepared emulsion may be affected by the method of dispersion (emulsification) and the temperature regime. In this regard, the temperature regime was determined from 70 °C. This temperature allows the PVA polymer to effectively remove the paraffin foil from the surface of aluminum powder.

A rotary pulsating device (RPD) was used as a dispersant. The main factors that determine the emulsification process in a RPD type dispersant are pressure (0.5–1.0 MPa) and centrifugal force (rotor speed is 1200 rpm). These factors cause the occurrence of high-frequency vibrations in the RPD, accompanied by cavitation and hydrodynamic processes, thereby allowing to obtain a high-quality emulsion and saponified gas-forming agent. The resulting emulsion is introduced into the cement-sand compound. After that, the mixture is stirred for 5-7 minutes and poured into pre-prepared molds.

After forming, the aerated concrete is expanded before setting, and excess material is removed from the surface of the mold to its level. Further after 20-24 hours, the aerated concrete is removed from the formwork and sawn on the template.

Testing of samples is carried out according to the standard method for cellular concrete [7, 27–32].

At the end of 28 days, samples were taken. Samples of the cube for research were cut out of prepared composite non-reinforced and traditional aerated concrete blocks. The dimensions of the traditional and composite block were 600 mm in length, 400 mm in width and height. Samples for testing were cut from the upper middle and lower parts of the product, three samples from each part. The margins from the faces of the cubes were made at least 40 mm when cutting. The temperature in premises was 19 °C with a relative humidity of 35 % before the tests. The samples were kept in the laboratory for 24 hours. Samples are 28 days old. 54 samples (cubes) were made: 27 from composite aerated concrete and 27 from traditionally prepared aerated concrete. For sawing out samples, a template was used to obtain items with a smooth geometric surface with an error of up to 1 mm.

The density of the samples was determined for the beginning of the tests. The volume was determined using a caliper, since the samples (cubes) had regular geometric shapes of 100×100×100.

The density was determined according to the Eq. 1 [28]:

$$\rho_w = \frac{m}{V} * 100, \quad (1)$$

where ρ_w is density of material,

m is mass of sample, g,

V is volume of sample, cm³.

In order to see the quality of the pore structure and pore walls, the water absorption of aerated concrete by weight was determined. Determination of water absorption of aerated concrete was carried out

as follows, samples were weighed on verified calibrated scales with an error of 0.1 %, and then placed in a container with water. Since the density of the material was low, the samples floated, so a load was placed on their surface. The water level in the container was 60 mm higher than the sample level, and the water temperature was 21 °C. The samples were weighed every 24 hours to a constant mass. Fig. 1 shows the stages of the test.

Before each weighing, the samples were wiped with a damp cloth.

Calculation of water absorption by mass was determined according to the Eq. 2 [33]:

$$W_M = \frac{m_B - m_C}{m_C} * 100, \quad (2)$$

where W_M is water absorption by mass;

m_B is weight of the dried sample, g;

m_C is mass of the water-saturated sample, g.



Figure 1. Test of water absorption by mass.

The strength of aerated concrete was determined from control samples. Tests were performed on samples of 100×100×100 size prepared in advance by sawing out of a single block of 600×400×400. The age of the samples is 28 days. Concrete compressive strength test is shown in Fig. 2.



Figure 2. Concrete compressive strength test.

The samples were tested on an automatic press CONTROLS (Pilot) 500 kH. The strength of one series was determined as the arithmetic mean of the tested samples. 18 cubes were tested, 9 from each series.

The test for freeze/thaw resistance was determined on samples-cubes 100×100×100, which reached 28 days. 12 samples of two series-composite and traditional aerated concrete 6 samples of each series, placed in a container with water and gradually, every 8 hours in two stages, increased the depth of immersion. After 16 hours, samples were completely submerged and loaded so that the samples could not float, and they were kept in this state for another 24 hours.

Then the samples were loaded onto the mesh racks of the automatic climate chamber 10D 1429 / a CONTROLS, the temperature of the chamber during loading was $-18\text{ }^{\circ}\text{C}$.

The freezing time was set for 4 hours at $-18\text{ }^{\circ}\text{C}$, thawing is also for 4 hours at the temperature $+18\text{ }^{\circ}\text{C}$ and humidity 95 %.

The freeze/thaw resistance test is shown in Fig. 3.



Figure 3. Freeze/thaw resistance test.

The main criterion for the end of the test for freeze/thaw resistance was a visual change in the surface of the sample (cracks, chips), as well as a mass loss of more than 5 %. The samples were tested after 15 cycles of freezing and thawing, followed by an interval of 25, 35, 50, 75, 100 cycles.

The relative decrease in strength R_{rel} in % was determined according to the Eq. 3 [34]:

$$R_{rel} = \left(1 - \frac{R_{mtn}}{R_{mtk}} \right) * 100, \quad (3)$$

where R_{mtn} is average strength of the main samples after the specified test cycles in MPa;

R_{mtk} is average strength of control samples in MPa.

Mass loss Δ_m in % was calculated according to the Eq. 4 [34]:

$$\Delta_m = \frac{m_n(1 - W_n) - \bar{m}_n(1 - \bar{W}_n)}{m_n(1 - W_n)} * 100, \quad (4)$$

where m_n is average mass of the main samples after water saturation, g;

W_n is average value of humidity of control samples after water saturation, measured in parts of one;

\bar{m}_n is average mass of the main samples after passing the intermediate number of cycles, g;

\bar{W}_n is the average humidity value of the main samples after passing the intermediate number of cycles, measured in parts of one.

3. Results and Discussions

The results of determining the density of traditional aerated concrete in comparison with composite allowed us to objectively assess the quality of the pore structure of materials. According to the study [35, 36] of the pore structure of non-autoclaved aerated concrete, its non-uniformity and, as a result, the density difference in different sections of the material were noted. The quality of the pore structure directly depends on the difference in the density of the material in different sections of the same block.

Table 2. Density of traditional and composite aerated concrete.

Sample	Actual density		
	Upper samples	Middle samples	Bottom samples
Traditional aerated concrete	617	617.8	619.1
	616.3	617.5	617.8
	616.5	616.9	619.2
Average density	616.6	617.4	618.7
Average density of all samples			617.6
Composite aerated concrete	618.4	618.9	619.1
	618.7	618.5	618.7
	618.2	618.8	619
Average density	618.4	618.7	618.9
Average density of all samples			618.6

Based on the data from Table 2, in traditional aerated concrete, we see a difference in the density of the upper samples compared to the middle and lower ones, which indicates an uneven distribution of the pore structure. This is due to the fact that the density of aluminum powder together with paraffin foil is significantly lower than the density of the solution. As a result, during the preparation of the material, part of the aluminum powder, not fully saponified, rushed to the surface of the material in the process of mixing. However, most of the aluminum powder after forming, after passing certain stages of interaction with the surface of the cement binder, warm water and alkaline (sodium hydroxide), loses the protective paraffin foil and increases the amount of hydrogen released on the surface of the block.

Composite aerated concrete, in contrast to traditional, has a more stable density in all areas of the tested material, which is explained by its production technology. We get a positive effect from the productive saponifying of aluminum powder. This process takes place by producing an emulsion of polymer, water and a gas-forming agent in a rotary pulsating device, which under pressure and due to centrifugal force forms high-frequency vibrations accompanied by cavitation with hydrodynamic processes. The resulting water-based emulsion of PVA polymer and aluminum powder easily dissolves in water for further use. This property guarantees a uniform distribution of all components in the structure of the material, thereby providing a high-quality pore base of composite aerated concrete.

Thus, a slight difference in the density of the composition is the result of an uneven distribution of saponified grains of aluminum powder, which leads to a decrease in the quality of the material.

The next stage of determining the quality indicators of traditional and composite aerated concrete was the study of water absorption. Literary review showed that water absorption, strength, frost resistance corresponds to traditional aerated concrete [37, 38].

The results of determining water absorption by weight of traditional and composite aerated concrete are presented in Table 3.

Table 3. Water absorption by weight of traditional and composite aerated concrete.

№	Sample	Weight of the dried sample, g			Mass of the water-saturated sample, g		
		Upper samples	Middle samples	Bottom samples	Upper samples	Middle samples	Bottom samples
Traditional aerated concrete		617	617.8	619.1	801.5	800	801.8
		616.3	617.5	617.8	801	799.5	800
		616.5	616.9	619.2	800.8	801	801
	Water absorption, %				29.9 %	29.49 %	29.51 %
					29.9 %	29.47 %	29.49 %
					29.89 %	29.84 %	29.36 %
	Average water absorption, %				29.9 %	29.6 %	29.5 %
Average water absorption of all samples, %							
Composite aerated concrete		618.4	618.9	619.1	717.5	719	716.5
		618.7	618.5	618.3	718	716.9	718
		618.2	618.8	619	717.3	717	718.2
	Water absorption, %				16.02 %	16.17 %	15.73 %
					16.04 %	15.9 %	16.12 %
					16.03 %	15.86 %	16.02 %
	Average water absorption, %				16 %	16 %	16 %
Average water absorption of all samples, %							

The dependence of water absorption on the pore structure of aerated concrete is similar to the results of studies of traditional aerated concrete in the range from 28 to 30 % [39].

Based on the results of the study, we can note a significant contrast between traditional and composite aerated concrete. Taking into account the fact that composite aerated concrete has a hydrophobic component (PVA) in its structure, this difference is obvious. A 46 % reduction in water absorption of composite aerated concrete indicates that most of the water did not penetrate the structure of the aerated concrete and thus provided this result. However, considering the fact that the pore structure of aerated concrete is communicating, we can conclude that the pore can only be communicated in a certain space according to the possibilities of the gas-forming ability of the aluminum powder particle. Based on this conclusion, in the traditional production technology, the particles of the gas-forming agent, contacting the surface of the cement particles, contribute to the release of hydrogen, which, rushing vertically up, forms a pore space. Also, with a vast accumulation of aluminum powder particles, much more hydrogen is released, which reduces the thickness of the walls of the partitions in front of the standing pore, contributing to uneven density. Micro and macropores of partitions increase water absorption, while in composite aerated concrete micro and macropores are isolated by a polymer component, providing hydrophobicity.

Composite aerated concrete has a special structure: the cell walls are completely filled and practically do not have micropores due to the fact that the water-soluble polymer is a surfactant and improves the plastic properties of cement, as well as fills structural defects in the process of hydration of the cement binder, is shown in Fig. 4.

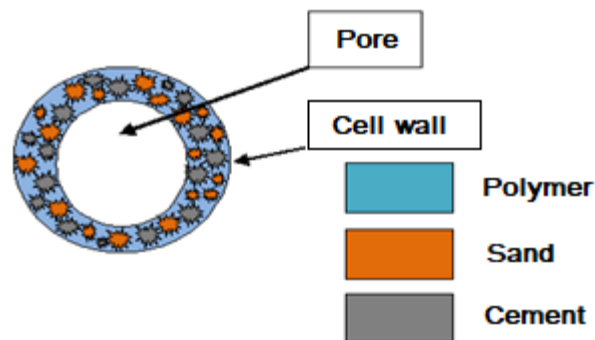


Figure 4. The structure of aerated composite concrete's cell walls.

The use of polymer emulsion and aluminum powder in composite aerated concrete ensures that the communicating pores are closed in space, since the polymer foil creates conditions for their isolation even with a vast release of hydrogen, thereby causing hydrophobic features of the material. Fig. 4 shows a scheme of the cell structure.

The results of determining the compressive strength of traditional and composite aerated concrete are presented in Table 4.

Table 4. Compressive strength of traditional and composite aerated concrete.

Sample	Average density, kg/m ²	Sample's strength in MPa		
		Upper samples	Middle samples	Bottom samples
Traditional aerated concrete	600	2.4	2.9	3.7
		3.5	3.4	3.8
		2.9	3.8	3.1
The average strength	600	2.9	3.4	3.5
The average strength of all samples				3.3
Composite aerated concrete	600	5.1	5.2	5.3
		5.0	5.0	5.3
		4.9	5.1	5.0
The average strength	600	5	5.1	5.2
The average strength of all samples				5.1

The strength properties of aerated concrete were studied in the papers [35]. The experience of studying the strength of samples non-autoclaved aerated concrete shows the result similar to the traditional one in the range from 3 to 3.5 MPa [40].

The strength of traditional aerated concrete is 51 % lower than that of composite. As mentioned above, the reason for this difference in material strength is the quality of the pore structure. One of the essential factors that contribute to reducing the strength of traditional aerated concrete is the saponifier (sodium hydroxide), since it has a strongly alkaline environment, which negatively affects the hardening process. The second factor in reducing strength is the pore walls: the presence of a huge number of micro- and macropores, which are caused by a high water-cement ratio. Rapid loss of moisture in the process of gaining strength during the first days of hardening requires special care of the product, which is an additional technological process.

The explanation for the high strength of composite aerated concrete is the use of a polymer emulsion with a gas-forming agent.

Composite aerated concrete, having water-soluble polymers in its structure, which are also surfactants, plasticizes the solution, positively affecting the process of hydration of the cement binder. The polymer component, forming a foil in the structure of aerated concrete, retains moisture, which positively influences the hardening process of the material, without requiring additional care. This increases the strength by filling micropores and microcracks with a polymer that serves as a binder.

The results of freeze/thaw resistance of traditional and composite aerated concrete are shown in Fig. 5.

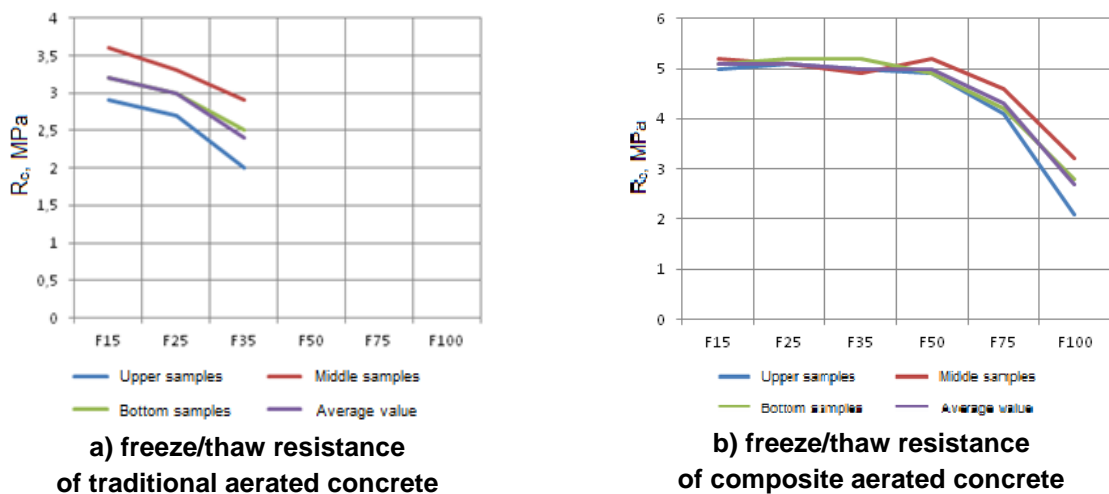


Figure 5. Freeze/thaw resistance of traditional and composite aerated concrete.

The freeze/thaw resistance of non-autoclaved aerated concrete does not contradict the results of the study of traditional aerated concrete, which also varies in the range of 25 to 35 cycles [41].

It is known that in cellular concrete, major pores are not filled with water completely, since due to small capillary forces, water is not retained in them during the extraction of samples from water. In addition, in conventional non-hydrophobized cellular concrete, water is aspirated by capillaries from larger pores. Therefore, the released major pores make up the so-called reserve, i.e. they form a buffer space, which is a damper during the transition of water to ice, which increases the freeze/thaw resistance of cellular concrete. The freeze/thaw resistance of aerated concrete was researched in the works [42].

The mechanism of destructive action is related to the phase transition of water into ice and to the crystallization of salts in process of drying in the concrete pores.

Many authors explain the destruction by hydraulic pressure of water pressed by ice, the crystallization pressure of ice and salts, the specifics of ice segregation in micropores and capillaries, the formation of ice lenses as the concrete freezes layer by layer, and other reasons.

An external sign of concrete failure is an increase in its volume due to the expansion of water in the concrete pores during freezing, as well as shrinkage during thawing and drying. In this case, a system of micro and macro-cracks is formed, and their own structural tensile stresses occur.

Chemical and mineral additives play an important role in giving concrete structural strength and higher freeze/thaw resistance. By introducing various additives, it is possible to improve the properties of concrete mixtures, regulate the time of setting and hardening of concrete, as well as increase its physical and mechanical properties and durability in structures and buildings.

The mechanism of formation and movement of ice in the pores and capillaries of concretes modified with hydrophobizing additives proceeds according to completely different schemes. It is known that ice has

a high adhesion to concrete. Hydrophobization significantly reduces the bonding force of ice with the material, so when it crystallizes, the pressure in the concrete pores is significantly reduced.

Our research on determining the freeze/thaw resistance of composite aerated concrete has also shown their higher resistance in comparison with traditional aerated concrete that does not contain polymer components. Thus, composite aerated concrete withstood 75 cycles of alternating freezing and thawing without external signs of destruction, while traditional concrete withstood only 35 cycles.

The validity of the pore structure and the influence of various factors on it were carried out by many authors, however, all actions were considered from the point of view of raw material activation by adding various kinds of additives that increase the activity of aluminum powder, or cement binder [43]. However, in some cases, given the positive effect of the additive on gas formation, the quality indicator of the binder decreases, or vice versa. The studied work of using sodium hydroxide in the production of non-autoclaved aerated concrete, the gas generation rate of a reasonably high alkaline medium of sodium hydroxide undoubtedly during the chemical reaction, the gas-forming features of aluminum powder significantly increase, but in the process of interaction of strong alkali and cement binder, its strength characteristics significantly decrease its strength characteristics, the material structure begins to peel off. Non-autoclaved composite aerated concrete is primarily focused on the effectiveness of the polymer component on the properties of all raw materials, and for the effective saponification of aluminum powder, both the chemical characteristics of the polymer and the mechanical effects of the rotor-pulsation apparatus were used.

Thus, the emulsion obtained is much safer, since it does not dust during its application, and its effective saponification provides high-quality interconnected pores of the wall, which have a polymer-cement structure. The hydrophobicity of the polymer component provides high freeze/thaw resistance and low water absorption, and the plasticizing effect of the polymer reduces the number of micro and macro pores in the structure of the walls of communicating pores providing high strength.

4. Conclusion

1. Conducted studies of the density difference of traditional aerated concrete on three sections of the material (upper, middle, bottom) samples showed a difference in density from the average density of all samples:

- for upper samples below 0.16 %;
- for middle samples below 0.03 %;
- for bottom samples higher by 0.18 %.

The obtained results indicate that the pore structure of traditional aerated concrete has uneven pores with a certain dynamics of increasing the density of the upper part of the material. However, the density of composite aerated concrete samples showed stability in all sections of the tested block. Indicators of the difference in density of composite aerated concrete from the average density of all samples:

- for upper samples below 0.08 %;
- for middle samples below 0.02 %;
- for bottom samples higher by 0.05 %.

Hence, after analyzing the results, we can conclude that composite aerated concrete has a uniform pore structure that provides a stable density in all areas of the tested block. The density stability of composite aerated concrete in contrast to traditional aerated concrete is 78 % higher.

2. Tests of composite aerated concrete showed an increase in water absorption by 46 %. The dependence of water absorption on changes in the density of the material is also determined. A study on the water absorption of traditional aerated concrete in three sections of the material (upper, middle, bottom samples) showed a difference in the average density of all samples:

- for upper samples with an average density of 616.6, the water absorption difference is higher than 0.8 % of the average water absorption of all samples;
- for average samples with an average density of 617.4, the water absorption difference is less than 0.3 % of the average water absorption of all samples;
- for bottom samples with an average density of 618.7, the water absorption difference is less than 0.7 % of the average water absorption of all samples.

The obtained data indicate that the density of the material does not fully reflect the dependence of the density difference and water absorption. Water absorption of composite aerated concrete is 16 % in all three sections of the tested block, which indicates the stability of the pore structure and the closeness of communicating pores in space.

3. Compressive strength tests of composite aerated concrete showed a 52 % increase in strength. The strength value for three sections (upper, middle, bottom) of the tested material showed the difference in strength from the average value of all samples:

- for upper samples below 12 %;
- for middle samples higher by 3 %;
- for bottom samples higher by 6 %.

These results show the dependence of water absorption and strength of the material, which indicates that the pore communicating structure is closed in space, providing an increase in strength and limiting the spread of water through the structure of the material.

The study of the strength of composite aerated concrete showed a difference in the strength of the material sections (upper, middle, bottom samples) from the average strength of all samples:

- for upper samples below 2 %;
- for average samples it is equal to the average strength of all samples;
- for bottom samples higher by 2 %.

According to the obtained results, it can be concluded that composite aerated concrete on all sections of the block has almost uniform strength, with the exception of an error of ± 2 %.

4. The freeze/thaw resistance of aerated concrete depends directly on the water absorption, strength and density of the material. Composite aerated concrete, having a polymer component in its structure, provides hydrophobicity of cell walls and closeness in the space of the communicating pore structure; in contrast to traditional aerated concrete, it is characterized by an increase in freeze/thaw resistance by 53 %.

5. Acknowledgments

The study was conducted within the framework of grant financing of the Committee of Science of the Ministry of Education and Science of the Republic of Kazakhstan for 2018-2020 under the priority "Rational use of natural resources, including water resources, geology, processing, new materials and technologies, safe products and structures" of the project No. AP05132631 "New composite aerated concrete products on the basis of complex modifiers and industrial wastes".

The authors of the project express their great gratitude to the Research and Production Center of L.N. Gumilyov Eurasian National University ENU-Lab for the provided laboratory base for research work.

References

1. Serdar, M., Bjegović, D., Štímer, N., Banjad Pečur, I., Marijana Serdar, A., Dubravka Bjegović, P. Research challenges for broader application of alternative binders in concrete. DOI: 10.14256/JCE.2729.2019. URL: <https://doi.org/10.14256/JCE.27-29.2019> (date of application: 11.04.2020).
2. Wu, Y., Wang, J.Y., Monteiro, P.J.M., Zhang, M.H. Development of ultra-lightweight cement composites with low thermal conductivity and high specific strength for energy efficient buildings. *Construction and Building Materials*. 2015. 87. Pp. 100–112. DOI: 10.1016/j.conbuildmat.2015.04.004
3. Tonet, K.G., Gorninski, J.P. Polymer concrete with recycled PET: The influence of the addition of industrial waste on flammability. *Construction and Building Materials*. 2013. 40. Pp. 378–389. DOI: 10.1016/j.conbuildmat.2012.09.049
4. Liu, Q., Liu, W., Li, Z., Guo, S., Sun, G. Ultra-lightweight cement composites with excellent flexural strength, thermal insulation and water resistance achieved by establishing interpenetrating network. *Construction and Building Materials*. 2020. 250. DOI: 10.1016/j.conbuildmat.2020.118923
5. Chica, L., Alzate, A. Cellular concrete review: New trends for application in construction. *Construction and Building Materials*. 2019. 200. Pp. 637–647. DOI: 10.1016/j.conbuildmat.2018.12.136. URL: <https://linkinghub.elsevier.com/retrieve/pii/S0950-061818331258> (date of application: 11.04.2020).
6. Kalpana, M., Mohith, S. Study on autoclaved aerated concrete: Review. *Materials Today: Proceedings*. 2020. 22. Pp. 894–896. DOI: 10.1016/j.matpr.2019.11.099. URL: <https://linkinghub.elsevier.com/retrieve/pii/S2214785319337824>
7. Interstate Standard GOST 25485-2019: Cellular concretes. General specifications.
8. Nguyen, T.T., Bui, H.H., Ngo, T.D., Nguyen, G.D., Kreher, M.U., Darve, F. A micromechanical investigation for the effects of pore size and its distribution on geopolymer foam concrete under uniaxial compression. *Engineering Fracture Mechanics*. 2019. 209. Pp. 228–244. DOI: 10.1016/j.engfracmech.2019.01.033
9. Amran, M., Fediuk, R., Vatin, N., Huei Lee, Y., Murali, G., Ozbakkaloglu, T., Klyuev, S., Alabduljabber, H. Fibre-Reinforced Foamed Concretes: A Review. *Materials*. 2020. 13(19). Pp. 4323. DOI: 10.3390/ma13194323. URL: <https://www.md-pi.com/1996-1944/13/19/4323>
10. Sun, H.Y., Gong, A.M., Peng, Y.L., Wang, X. The Study of Foamed Concrete with Polypropylene Fiber and High Volume Fly Ash. *Applied Mechanics and Materials*. 2011. 90–93. Pp. 1039–1043. DOI: 10.4028/www.scientific.net/AMM.90-93.1039. URL: <https://www.scientific.net/AMM.90-93.1039>
11. Fedorov, V., Mestnikov, A. Influence of cellulose fibers on structure and properties of fiber reinforced foam concrete. *MATEC Web of Conferences*. 2018. 143. Pp. 02008. DOI: 10.1051/mateconf/201814302008. URL: <https://www.mateconferences.org/10.1051/mateconf/201814302008>

12. Mahzabin, M.S., Hock, L.J., Hossain, M.S., Kang, L.S. The influence of addition of treated kenaf fibre in the production and properties of fibre reinforced foamed composite. *Construction and Building Materials*. 2018. 178. Pp. 518–528. DOI: 10.1016/j.conbuildmat.2018.05.169. URL: <https://linkinghub.elsevier.com/retrieve/pii/S0950061818312455>
13. Abbas, W., Dawood, E., Mohammad, Y. Properties of foamed concrete reinforced with hybrid fibres. *MATEC Web of Conferences*. 2018. 162. Pp. 02012. DOI: 10.1051/mateconf/201816202012. URL: <https://www.mateconferences.org/10.1051/mateconf/201816202012>
14. Hilal, A.A., Thom, N.H., Dawson, A.R. Failure Mechanism of Foamed Concrete Made with/without Additives and Lightweight Aggregate. *Journal of Advanced Concrete Technology*. 2016. 14(9). Pp. 511–520. DOI: 10.3151/jact.14.511. URL: https://www.jstage.jst.go.jp/article/jact/14/9/14_511/_article
15. Raj, A., Sathyan, D., Mini, K.M. Physical and functional characteristics of foam concrete: A review. *Construction and Building Materials*. 2019. 221. Pp. 787–799. DOI: 10.1016/j.conbuildmat.2019.06.052. URL: <https://linkinghub.elsevier.com/retrieve/pii/S0950061819314771>
16. Hamad, A.J. Materials, Production, Properties and Application of Aerated Lightweight Concrete: Review. *International Journal of Materials Science and Engineering*. 2014. DOI: 10.12720/ijmse.2.2.152-157. URL: <http://www.ijmse.net/index.php?m=content&c=index&a=show&catid=34&id=73>
17. Font, A., Borrachero, M.V., Soriano, L., Monzó, J., Payá, J. Geopolymer eco-cellular concrete (GECC) based on fluid catalytic cracking catalyst residue (FCC) with addition of recycled aluminium foil powder. *Journal of Cleaner Production*. 2017. 168. Pp. 1120–1131. DOI: 10.1016/j.jclepro.2017.09.110
18. Gyurkó, Z., Jankus, B., Fenyvesi, O., Nemes, R. Sustainable applications for utilization the construction waste of aerated concrete. *Journal of Cleaner Production*. 2019. 230. Pp. 430–444. DOI: 10.1016/j.jclepro.2019.04.357. URL: <https://linkinghub.elsevier.com/retrieve/pii/S0959652619314581>
19. Zapotoczna-Sytek, G. Durability of autoclaved aerated concrete based on Polish experience. *ce/papers*. 2018. 2(4). Pp. 53–62. DOI: 10.1002/cepa.850. URL: <http://doi.wiley.com/10.1002/cepa.850>
20. Kalpana, M., Mohith, S. Study on autoclaved aerated concrete: Review. *Materials Today: Proceedings*. 2020. 22. Pp. 894–896. DOI: 10.1016/j.matpr.2019.11.099. URL: <https://linkinghub.elsevier.com/retrieve/pii/S2214785319337824>
21. Narattha, C., Thongsanitgarn, P., Chaipanich, A. Thermogravimetry analysis, compressive strength and thermal conductivity tests of non-autoclaved aerated Portland cement–fly ash–silica fume concrete. *Journal of Thermal Analysis and Calorimetry*. 2015. 122(1). Pp. 11–20. DOI: 10.1007/s10973-015-4724-8. URL: <http://link.springer.com/10.1007/s10973-015-4724-8>
22. Qu, X., Zhao, X. Previous and present investigations on the components, microstructure and main properties of autoclaved aerated concrete – A review. *Construction and Building Materials*. 2017. 135. Pp. 505–516. DOI: 10.1016/j.conbuildmat.2016.12.208.
23. Shuisky, A., Stelmakh, S., Shcherban, E., Torlina, E. Recipe-technological aspects of improving the properties of non-autoclaved aerated concrete. *MATEC Web of Conferences*. 2017. 129. Pp. 05011. DOI: 10.1051/mateconf/201712905011. URL: <http://www.matec-conferences.org/10.1051/mateconf/201712905011>
24. Wang, C., Ni, W., Zhang, S., Wang, S., Gai, G., Wang, W. Preparation and properties of autoclaved aerated concrete using coal gangue and iron ore tailings. *Construction and Building Materials*. 2016. 104. Pp. 109–115. DOI: 10.1016/j.conbuildmat.2015.12.041. URL: <https://linkinghub.elsevier.com/retrieve/pii/S0950061815307145>
25. Chen, Y.-L., Ko, M.-S., Chang, J.-E., Lin, C.-T. Recycling of desulfurization slag for the production of autoclaved aerated concrete. *Construction and Building Materials*. 2018. 158. Pp. 132–140. DOI: 10.1016/j.conbuildmat.2017.09.195. URL: <https://linkinghub.elsevier.com/retrieve/pii/S0950061817320032>
26. Yuan, B., Straub, C., Segers, S., Yu, Q.L., Brouwers, H.J.H. Sodium carbonate activated slag as cement replacement in autoclaved aerated concrete. *Ceramics International*. 2017. 43(8). Pp. 6039–6047. DOI: 10.1016/j.ceramint.2017.01.144. URL: <https://linkinghub.elsevier.com/retrieve/pii/S0272884217301669>
27. EN 771-4:2011+A1:2015 specification for masonry units – Part 4: Autoclaved aerated concrete masonry units.
28. Interstate Standard GOST 12730.1-78: Concretes. Methods of determination of density.
29. EN 772-11:2011 “Methods of test masonry units – Part 11: Determination of water absorption of aggregate concrete, manufactured stone and natural stone masonry units due to capillary action and the initial rate of water absorption of clay masonry units”.
30. EN 772-1:2011 + A1:2015 Methods of test for masonry units – Part 1: Determination of compressive strength.
31. EN772-13:2000: Methods of test for masonry units – Part 13: Determination of net and gross dry density of masonry units (except for natural stone).
32. EN 15304 Determination of the freeze-thaw resistance of autoclaved aerated concrete.
33. Interstate Standard GOST 12730.3-78: Concretes. Method of determination of water absorption.
34. Interstate Standard GOST 25485-89: Cellular concretes. Specifications. Appendix 3 (required).
35. Ramamurthy, K., Narayanan, N. Factors influencing the density and compressive strength of aerated concrete. *Magazine of Concrete Research*. 2000. 52(3). Pp. 163–168. DOI: 10.1680/mac.2000.52.3.163. URL: <http://www.icevirtuallibrary.com/doi/10.1680/mac.2000.52.3.163>
36. Nambiar, E.K.K., Ramamurthy, K. Air-void characterisation of foam concrete. *Cement and Concrete Research*. 2007. 37(2). Pp. 221–230. DOI: 10.1016/j.cemconres.2006.10.009. URL: <https://linkinghub.elsevier.com/retrieve/pii/S0008884606002699>
37. Shabbar, R., Nedwell, P., Wu, Z. Porosity and Water Absorption of Aerated Concrete with Varying Aluminium Powder Content. *International Journal of Engineering and Technology*. 2018. 10(3). Pp. 234–238. DOI: 10.7763/IJET.2018.V10.1065. URL: <http://www.ijetch.org/index.php?m=content&c=index&a=show&catid=93&id=1253>
38. Raj, I.S., John, E. A study on the properties of air-entrained concrete for masonry blocks. *International Journal of Scientific Engineering and Technology*. 2014. 3(11). Pp. 1367–1370. URL: <http://www.indianjournals.com/ijor.aspx?target=ijor-ij-set1&volume=3&issue=11&article=008>
39. Muthu Kumar, E., Ramamurthy, K. Influence of production on the strength, density and water absorption of aerated geopolymer paste and mortar using Class F fly ash. *Construction and Building Materials*. 2017. 156. Pp. 1137–1149. DOI: 10.1016/j.conbuildmat.2017.08.153. URL: <https://linkinghub.elsevier.com/retrieve/pii/S0950061817317610>
40. Narayanan, N., Ramamurthy, K. Structure and properties of aerated concrete: a review. *Cement and Concrete Composites*. 2000. 22(5). Pp. 321–329. DOI: 10.1016/S0958-9465(00)00016-0. URL: <https://linkinghub.elsevier.com/retrieve/pii/S0958-946500000160>

41. Hang, M., Cui, L., Wu, J., Sun, Z. Freezing-thawing damage characteristics and calculation models of aerated concrete. *Journal of Building Engineering*. 2020. 28. Pp. 101072. DOI: 10.1016/j.job.2019.101072. URL: <https://linkinghub.elsevier.com/retrieve/pii/S2352710219315141>
42. Kočí, V., Maděra, J., Jerman, M., Černý, R. Experimental Determination of Frost Resistance of Autoclaved Aerated Concrete at Different Levels of Moisture Saturation. *International Journal of Thermophysics*. 2018. 39(6). Pp. 75. DOI: 10.1007/s107-65-018-2398-8. URL: <http://link.springer.com/10.1007/s10765-018-2398-8>
43. Halyushev, A., Holodnyak, M., Nazhuyev, M. Effect of caustic soda on the intensity of gassing in the production of non-autoclaved aerated concrete. *MATEC Web of Conferences*. 2017. 129. Pp. 05012. DOI: 10.1051/mateconf/201712905012. URL: <http://www.matec-conferences.org/10.1051/mateconf/201712905012>

Contacts:

Yerlan Sabitov, e_sabitov@mail.ru

Duman Dyusseminov, duseminov@mail.ru

Adiya Zhumagulova, zaaskarovna@gmail.com

Daniyar Bazarbayev, phdd84@mail.ru

Rauan Lukpanov, Rauan_82@mail.ru



DOI: 10.34910/MCE.106.6

Porosity of autoclave aerated concrete and foam concrete: origin of porosity and pore size

K.A. Kurochkina^{a*} , L.A. Suleimanova^a , A.S. Kolomatsky^b 

^a V.G. Shukhov Belgorod State Technological University, Belgorod, Russia

^b Belgorod National Research University, Belgorod, Russia

*E-mail: karina200386@yandex.ru

Keywords: porosity, bubble, pore size, autoclaved aerated concrete, foam concrete

Abstract. Porosity in the hardening system consists of air cells, which are the main element of the cellular concrete structure and that formed when gas emission in the mixture or during the foaming. The paper presents the developed models of porous structure formation in autoclaved aerated concrete (AAC) and foam concrete (FC). We elaborated the concept of bubble porosity in fresh concrete by distinguishing three types of bubble pores: microbubble pores, membrane pores and cellular pores. The sizes of such pores are determined and the possibility of pore shape deformation is evaluated. The study revealed that capillary and hydrostatic pressure are the essential factors in the process of bubble system formation. Reducing the size of deformable cellular bubbles and obtaining an increased number of non-deformable membrane bubbles improves the AAC and FC structure. This is a promising method of improving AAC and FC production technology.

1. Introduction

The pore size and the porosity nature are essential for the most hydration hardening materials. By creating a porous structure in production process, highly effective inorganic materials for construction purposes are made from autoclaved aerated concrete (AAC) and foam concrete (FC) non-autoclaved of hardening [1–4].

Three types of pores in hardening systems are distinguished: gel pores, capillary pores and air pores. Air pores called cellular pores, gas pores, or macropores. The concepts of gel porosity were developed in [5]. Gel pores are a space in aggregated growth between highly dispersed hydrated phases. Capillary pores are the space occupied by the mixing water remaining after hydration, minus gel porosity. Gel porosity and capillary porosity mainly depends on the type and amount of binders in the initial mix, as well as the water to binder ratio [6–10]. Such pores will appear in the interbubble septa after matrix crystallization structure formation.

The cellular porosity in the hardening system is created by gas evolution in the mix or by foaming [11–15]. In AAC technology a highly mobile mixture is converted into a raw mass with a coagulation structure due to two quick chemical reactions. In the reaction with dispersed aluminum, hydrogen is emitted and $3\text{CaO} \cdot \text{Al}_2\text{O}_3 \cdot 6\text{H}_2\text{O}$ is formed, and CaO hydrates into $\text{Ca}(\text{OH})_2$, binding part of the mixing water into the solid phase. FC technologies are based on three-phase foam production with air bubbles as a dispersed phase of the system [1].

Raw density, strength, thermal conductivity and other properties of AAC [16, 17] and FC [18, 19] are interrelated. Data on the porous structure of the material are used when cellular concrete of the same

Kurochkina, K.A., Suleimanova, L.A., Kolomatsky, A.S. Porosity of autoclave aerated concrete and foam concrete: origin of porosity and pore size. Magazine of Civil Engineering. 2021. 106(6). Article No. 10606. DOI: 10.34910/MCE.106.6

© Kurochkina, K.A., Suleimanova, L.A., Kolomatsky, A.S., 2021. Published by Peter the Great St.Petersburg Polytechnic University.



This work is licensed under a CC BY-NC 4.0

density have different properties [20], when modeling porosity [21–24], when the nature of the processes in the hardening system is revealed [17, 25] and in other studies. The quantity and quality of bubble pores affects the properties of not only AAC and FC, but also other aerated concretes, for example, gypsum compositions [26–28]. Thermophysical characteristics of AAC and other cellular materials are important for building envelopes in connection with the relevance of energy saving issues for space heating [29–32].

Common to AAC and FC is the formation of their porous structure in a three-phase bubble system. Three-phase foam is both a FC mix and foam stabilized by fine particulate matter, for example [33–36]. The three-phase system of AAC and FC freshly prepared mixes can be reduced to a two-phase system, considering the bubble as a discrete phase, and a concentrated suspension as a carrier, condensed phase. The gas-liquid systems mechanics describes the processes in many modern technologies and is used to consider bubble porosity nature in a cellular concrete mixes [37]. The identification of the types, shapes and sizes of bubble pores in cellular concrete has a significant role for AAC and FC technology. The concept of bubble pores is significant for obtaining scientific data [38–40] and computer modeling of porous systems [41, 42].

According to the above mentioned aspects, the purpose of this study is to develop ideas about the origin of bubble porosity in aerated concrete and pore sizes in AAC and FC. The research tasks included modeling the porosity in AAC and FC, analyzing the bubble porosity taking into account the size of the bubble, and identifying factors that determine the formation of the bubble system. Consideration of the hardening system as a composition consisting of a matrix and bubbles allows one model to characterize the porous structure of different materials hardening AAC and FC. The division of bubble pores into species not only develops the existing understanding of the porosity of hardening systems, but also provides guidance for improving the cellular concrete technology.

2. Materials and Experimental method

2.1. Materials

It was studied FC pressure of the density class of D250 manufactured by LLC «Ecostroymaterials» from samples taken during the installation of monolithic thermal insulation of attic floors of buildings and AAC density class of D500 of CJSC «AEROBEL». The sampling was carried out simultaneously with the routine testing of the material properties by the enterprise. AAC had a dry density of 493 kg/m³, pressure strands 5.54 N/mm², and a coefficient of thermal conductivity of 0.112 W/(mK). FC characteristics: dry density 238 kg/m³, compressive strength 0.64 MPa, coefficient of thermal conductivity 0.057 W/(mK).

2.2. Experimental method

The porous structure was evaluated visually on samples and on photographs on chips and sections. It was used a TESCAN MIRA 3 LMU scanning electron microscope (SEM) scan with an increase from 2 to 1.000.000 and an energy dispersive microanalysis with an attachment to the microscope of the spectrometer.

2.3. Modeling

Processes modeling occurring in porous hardening systems with a change in solid phases composition and ingredients aggregation state was carried out on silicate AAC mix with a density class of 500 kg/m³ (D500). The manufacturing process of AAC according to the criterion of phase transformations is divided into three stages and two phase transformations in the system, which determine the staging (Fig. 1).

The characteristics of the model AAC mix according are given in the table. The lime and aluminum powder activity is taken equal to 100%. For the production of 1 m³ of white AAC, 432.19 l of a AAC mix with a water solid (W/S) ratio W/S = 0.6 is required. The volume fraction of the solid phase in the freshly prepared AAC mix is 0.375, the liquid phase is 0.625. Water in the AAC mix as a dispersion medium ensures the continuity of the hardening system.

Table. Silicate AAC mix characteristic with D500.

Characteristic	Mix ingredients			
	Lime	Quartz sand	Aluminum powder	Water
Proportions (kg on 1 m ³)	112	340	0.5	270
Density (kg/m ³)	3320	2650	2700	1000
Volumetric content of ingredients (l/m ³)	33.7	128.3	0.19	270



Figure 1. Manufacturing AAC process formalization:

□ – stages; ○ – phase transformations;
 S', S'', S''' – solid phases composition, L – liquid phase, G – gas phase.

Bubble porosity of the adobe AAC cake is formed by the released gaseous hydrogen. Based on 1 m³ of AAC we have:

$$V_B + \sum \frac{m_i}{\rho_i} + W^* = 1, \quad (1)$$

where V_B is bubble porosity volume, m³/m³; m_i is solid phases masses, kg; ρ_i is solid phases density, kg/m³; W^* is mixing water volume minus solid phase bound, m³/m³.

The water in the green AAC cake in the second stage of system hardening remains a dispersion medium. Together with silica (SiO₂) and hydrated growth (Ca(OH)₂ and 3CaO·Al₂O₃·6H₂O), water provides stability to membranes and the bubble system as a whole. The contraction porosity estimation during the portlandite formation for the considered model of AAC mix gives the value 5.36·10⁻³ m³/m³.

In the process of green cake autoclave hardening at the second stage of phase transformations (Fig. 1), the physical and mechanical properties of AAC are formed. It is accepted that tobermorite 5CaO·6SiO₂·5H₂O with density 2440 kg/m³ is formed in the model system during hardening. Water at the end of autoclaving exhausts its functions. The volume fraction of the space occupied in green cake water becomes a source of capillary and gel porosity in AAC.

The gas bubbles growth in the freshly prepared mix during the green cake structure formation describes the Rayleigh-Plesset equation [34]:

$$P_G + P_{WV} \geq P_A + \rho_{mix}gH + \rho_{mix} \left(R\ddot{R} + \frac{3}{2}\dot{R}^2 \right) + \frac{2\sigma}{R} + \frac{4\eta\dot{R}}{R} + P_E, \quad (2)$$

where P_G и P_{WV} is gas and water vapor pressure in a bubble; P_A и P_E is atmospheric and excess pressures over the mix; ρ_{mix} is mix density; H is mix column height above the bubble; R is bubble radius; \dot{R} and \ddot{R} is speed and acceleration during bubble growth; σ is surface tension; η is viscosity.

Under conditions of metastable equilibrium for the formed bubble system in the expanded mix from equations (1) and (2) at atmospheric pressure, and also based on the relationship of pressure, volume and temperature of the gas phase, we obtain:

$$\frac{c \cdot K \cdot T_B}{P_A + \rho_{mix} \cdot g \cdot H + 2\sigma / R} + \sum \frac{m_i}{\rho_i} + W^* = 1, \quad (3)$$

where T_B is gas phase temperature in a bubble; c is proportionality coefficient; K is gas constant.

Significant indicators for bubble porosity in the green AAC cake structure formation are gas phase temperature, capillary and hydrostatic pressure.

3. Results and Discussion

Change in phase composition and porosity in a three-stage process according to Fig. 1 for a model AAC mix are presented in Fig. 2. In Fig. 3 a fragment of AAC structure D500 is shown, which according to the main elements corresponds to a model aerated concrete. In hardening systems, when water is bound to the solid phase, chemical shrinkage is observed. The value of the microporosity of the matrix due to chemical shrinkage can only be estimated by calculation according to the reaction equations. When removing water from a hardened cement paste, drying shrinkage takes place. The chemical shrinkage and drying shrinkage (Fig. 2) together give a total shrink of less than 1 % [43, 44]. When considering volumetric phase ratios and porosity in AAC and FC, the phenomena of shrinkage due to their small size can be ignored. Based on the concepts of hardening system porosity, size regions of gel and capillary pores are distinguished, and types, shape and sizes are substantiated for air (bubble) pores.

Five pore areas for AAC and FC were determined by the pore size criterion.

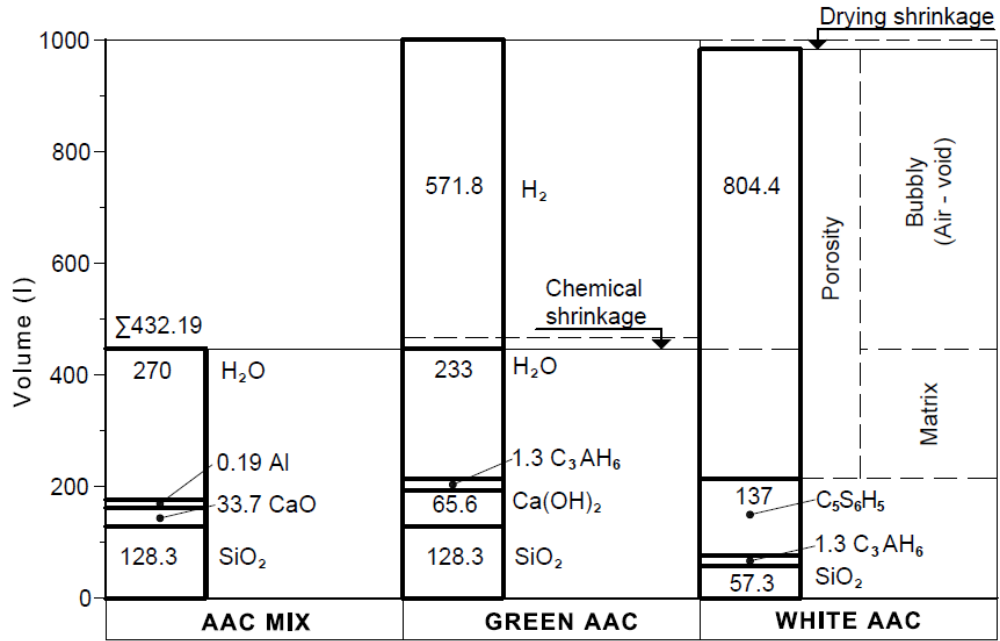


Figure 2. Phase composition and types of porosity per 1 m³ of model freshly mix, green cake and white AAC D500: C₃AH₆ – abbreviated 3CaO·Al₂O₃·6H₂O according to cement as accepted in chemistry; the same, tobermorite C₅S₆H₅.

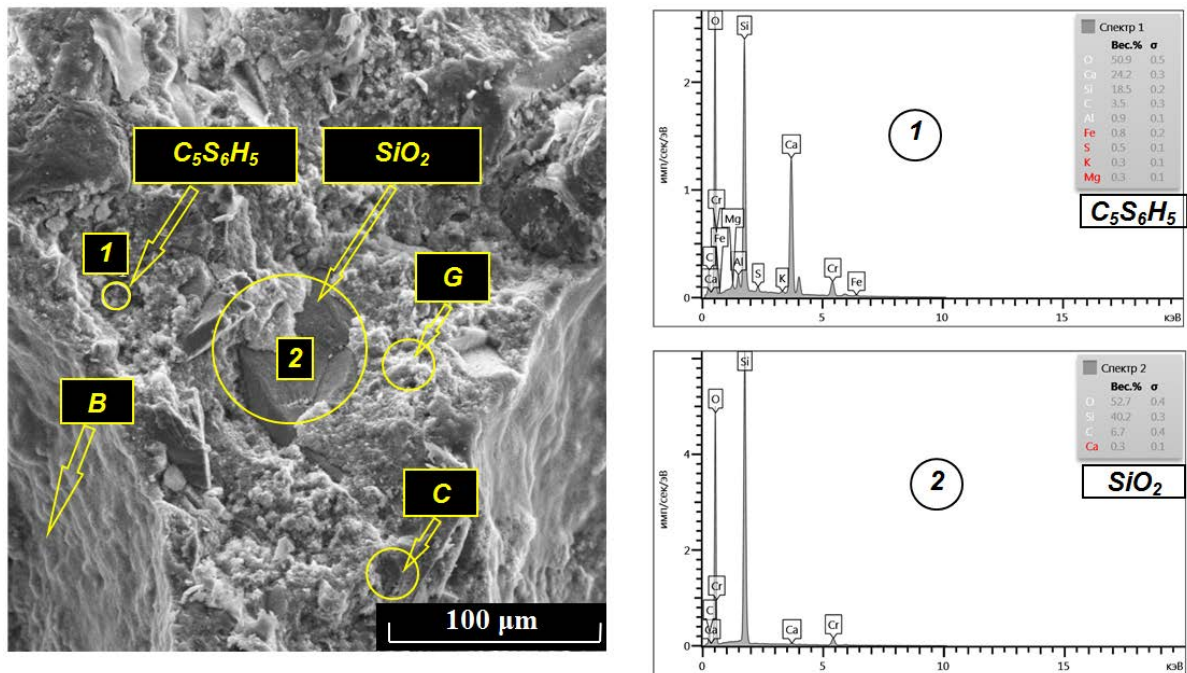


Figure 3. The structure of AAC D500: G – gel pores; C – capillary pores; B – bubbly air pores.

Area 1. Gel pores (Fig. 3, Fig. 4d). The gel porosity of calcium hydrosilicate was calculated according to the data of T. Powers [5] on its value in the gel of hardened systems, equal to 28 %. For the AAC D500 under consideration, a value of 53.3 liters was obtained. The specific volume of tobermorite growth is 0.569, which corresponds to the T. Powers model with a specific gel volume of 0.567. The size for gel pores was determined by IUPAC recommendation and proposal [20]: microgel with pore diameter (d_p) < 2 nm and mesogel with d_p from 2 to 50 nm.

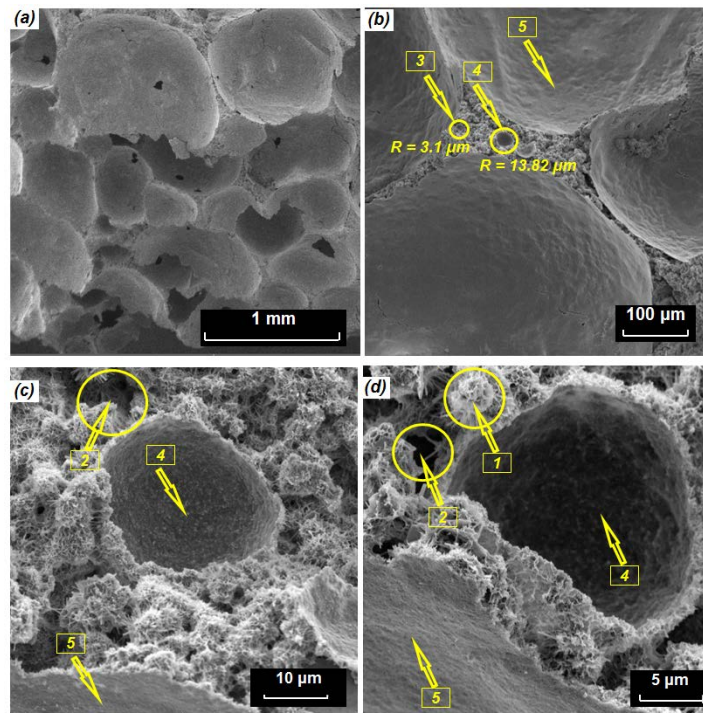


Figure 4. SEM micrographs of FC D250: 1 – gel pores; 2 – capillary pores; 3 – air-micro pores; 4 – air-membrane pores; 5 – air-cellular pores.

The second term in equation (3) for any type of cellular concrete and ingredients composition in the mix allows us to estimate the volume proportion of hydrated phases and to determine the expected value of gel porosity.

Area 2. Capillary pores (Fig. 3; Fig. 4 c, d). The capillary pores presence in concrete is caused by mixing water surplus compared to the quantity of chemically bonded water, as well as contraction phenomena during hardening. It is recommended that contraction porosity not be isolated but added to capillary pores. The equivalent diameter of microcapillary pores (in terminology [20]) is from 50 nm to 1 μm .

Gel pores and capillary pores are formed during hydration in a hardening system. Together with the solid phases of the system, these pores form a hardened matrix in concrete [45, 46]. Gel pores and capillary pores are matrix pores. The properties of AAC and FC, as well as ordinary concrete, depend on the nanostructure and the microstructure of cementitious materials [47, 48], that is, on the matrix structure.

Most pores in AAC and FC are pores of bubble origin. The pores in the structure of the hardened composite AAC, FC, and with entrained air are called air-void [49–53].

An examination of the characteristics of the bubbles in a fresh concrete mix with air-void sizes makes it possible to distinguish three types of bubbles: air-micro bubble, air-membrane bubble and air-cellular bubble. In the structure of AAC and FC, respectively, three areas of air pores formed from vesicles are distinguished.

Area 3. Air-capillary pores (Fig. 4b). The selection of this area is associated with transition in porous system structure from capillary pores to air-micro pores. The diameter of mesocapillary pores according to the terminology [20] and air-micro pores is from 1 to 10 μm . The pressure in the bubble with $R^* = 3.1 \mu\text{m}$ (Fig. 4b), caused by the surface curvature $P_C = 2\sigma/R$, is $R^*_C = 4.7 \cdot 10^4 \text{ Pa}$. Bond number as gravity to surface tension ratio for the bubble under consideration $Bo = 8.7 \cdot 10^{-6} \ll 1$. Therefore, air-micro bubbles in a AAC and FC mixes are spherical and non-deformable.

Area 4. Air-membrane pores (Fig. 4b, c, d). Pores with a diameter from 10 to 100 μm are involved in partitions structure formation between larger air pores. In structural heat-insulating aerated concrete, the shape of bubble membrane pores is close to spherical, but can change to ellipsoidal.

In a hardened matrix, spherical air-micro pores are formed from spherical vesicles.

The binder particle size corresponds to the air-membrane pores size. The spherical air bubbles rise of the considered sizes in water, up to a constant, coincides with the Stokes formula for the solid sphere motion [54]. The geometric factor is the basis on which air bubbles from 10 to 100 μm in size, together with binder, filler and growth particles form the membrane structure in aerated concrete mix. Membrane bubbles

with a diameter less than 60 μm , as will be shown below, are classified as undeformable by the criterion of gravity to surface tension ratio.

Area 5. Air-cellular pores (Fig. 3 and 4) are basic in cellular concrete volume, predetermine the material name and its properties. The pore diameter is from 100 μm to 2 mm.

The air bubbles size upper limit in a cellular concrete mix $D = 2$ mm is determined from equality condition to the Bond number. The value $Bo = 1$ determines the region linear scale in which the surface tension and gravity are comparable and characterized by a capillary constant:

$$b = \sqrt{\frac{\sigma}{g(\rho_L - \rho_G)}} \quad (4)$$

The capillary constant for the most liquids has a value of 1 ... 3 mm [46]. For a bubble in the model AAC mix under consideration, the capillary constant is $b' = 2.11$ mm. For water with $\sigma = 7.27 \cdot 10^{-2}$ J/m², the value of $b'' = 2.72$ mm. When deforming spherical bubbles, it is necessary to use the concept of "equivalent bubble", the volume of which is equal to the volume of the deformed one.

The following estimates are obtained for the lower boundary of the introduced size of air bubbles $D = 0.1$ mm. A air bubble of this size in a model AAC mix with a density of 1670 kg/m³ as a unit cell has a Bond number $Bo = 0.225 \cdot 10^{-2} \ll 1$. Capillary forces exceed the deforming gravitational (Archimedean) forces by more than two orders of magnitude, which corresponds to a gas bubble sphericity condition. Such an assessment is valid for a air bubble located at the AAC mix surface. Gravity forces from the overlying column of aerated concrete mix act on the bubble at the bottom of the form. If the hydrostatic pressures and laplace pressures are equal, the bubble radius according to equation (3) will be $R^* = 2 \cdot \sigma / \rho_{mix} \cdot g \cdot H$.

When a form in the manufacture of AAC with a height of 0.6 m is filled with the model aerated concrete mix under consideration, the filling height is $H = 0.26$ m and the deformable bubbles diameter will be more than 68.3 μm . An array height increase and a decrease in the surface tension in the mix due to surfactants will proportionally reduce the bubble size that is not deformed by calculation. Therefore, in AAC and FC mix, air bubbles with a diameter of 0.1 to 2 mm are stable, but deformable.

Large pores with an effective diameter of more than 2 mm are defects in the structure of AAC and FC. There are two reasons for their appearance in the hardened matrix. The first reason is the coalescence of bubbles in a fresh mix. The second reason is entrained air in a fresh mix. Air-entrained bubbles with $d_p > 2$ mm in AAC and FC take the shape of an inverted drop and retain this shape in the hardened composition.

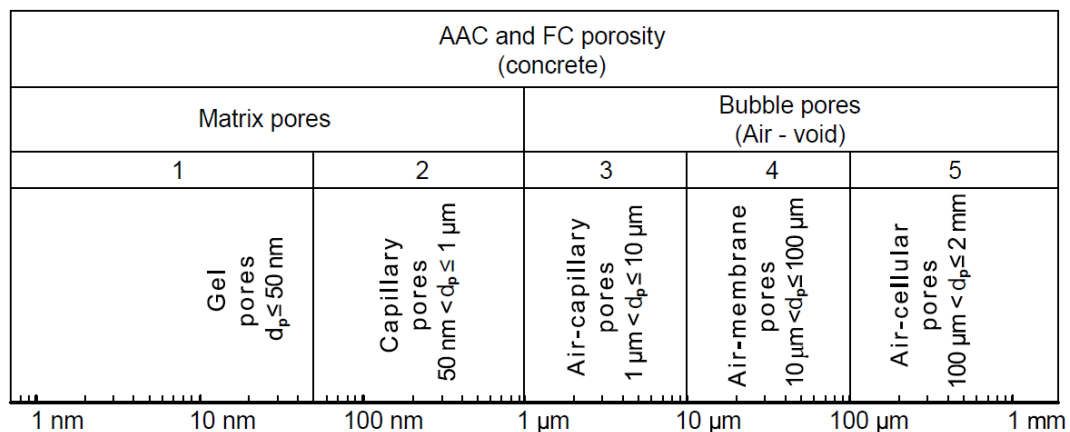


Figure 5. Kinds and sizes of pores in AAC and FC.

Fig. 5 provides information on the separation of vesicular pores into kinds. In this case, the mechanics data of a two-phase system were used for bubbles [37, 54]. An additional criterion for air pores separation by size was the same scale on the pore diameters axis with a logarithmic scale. The concept of gel and capillary pores in hardening systems is generally accepted [1, 7, 20, et. al.]. It is expedient to combine gel and capillary pores with the concept of "matrix pores", as is done in [4, 10]. There are only a few mentions of air-void pores as bubble pores in the literature [4]. The collection of bubble pores, named by origin, is divided into air-capillary, air-membrane and air-cellular pores. Subsequently, the isolated types of vesicular pores can be differentiated. So, air-membrane pores can be divided into formed by their undeformable and deformed bubbles in a fresh concrete mix.

Bubble studies are carried out mainly in cement foams with a bubble diameter of a millimeter size [55, 56]. In [56], the diameter of bubbles in monodispersed cement foams was 0.8 mm. This is close to the upper limit of the air-cellular pores size of 2 mm. In the systems of air-membrane pores with a bubble size from 10 μm to 100 μm , and especially for air-capillary pores with a diameter of 1 to 10 μm , new patterns are predicted. The new properties of such bubbles in solidifying systems with their predominant content in AAC and FC will be associated with the non-deformability of the bubble.

The data obtained and the proposed division by bubble pore sizes indicate the need for future studies of AAC and FC with a significant content, primarily, of non-deformable air-membrane pores.

4. Conclusions

The following conclusions can be made:

1. The main element of AAC and FC structure origin are bubble air pores. The technological process modeling in specific types of aerated concrete manufacture allows us to quantify the size of gel, capillary and bubble porosity in the material. The matrix porosity volume is determined by the mixing water amount remaining in the system after binder hydration, and is a smaller part of the total pore volume. In AAC D500 with $W/S = 0.6$, the matrix pore size is 29 %, and the bubble pore size is 71 %.

2. In porous hardening systems, three types of bubble pores are distinguished, the sizes of the selected pore areas are determined, and the shape of the bubbles is estimated. The air-capillary pores area with a size range from 1 to 10 μm is transitional from shapeless capillary to spherical microair pores. Membrane air pores with a diameter from 10 to 100 μm are comparable in size to the binder particles, and at a size of less than 60 μm , the bubbles in the fresh mix are classified as undeformable, and the pore form is close to spherical. Air-cellular pores with diameters from 100 μm to 2 mm are the main ones in the aerated concrete volume. They are formed from stable, but deformable in a AAC and FC mixture of air bubbles.

3. A perspective technology for aerated concrete is to reduce the maximum and average pore size for membrane and cellular air pores selected areas. A decrease in the bubbles size in hardening system will affect the decrease in the Bond number and increase the capillary forces importance in the AAC and FC pore structure formation.

5. Acknowledgements

This work was realized using the laboratory platform of the High Technology Center at BSTU named after V.G. Shukhov.

References

1. Krämer, C., Schauerte, M., Kowald, T.L., Trettin, R.H.F. Three-phase-foams for foam concrete application. *Materials Characterization*. 2015. 102. Pp. 173–179. DOI: 10.1016/j.matchar.2015.03.004
2. Smolczyk, H.G. Die Ettringit-Phasen im Hochofenzement. *Zement-Kalk-Gips*. 1961. 14. Pp. 277–284.
3. Lyu, K., She, W., Miao, C., Chang, H., Gu, Y. Quantitative characterization of pore morphology in hardened cement paste via SEM-BSE image analysis. *Construction and Building Materials*. 2019. 202. Pp. 589–602. DOI: 10.1016/j.conbuildmat.2019.01.055
4. Zingg, L., Briffaut, M., Baroth, J., Malecot, Y. Influence of cement matrix porosity on the triaxial behaviour of concrete. *Cement and concrete research*. 2016. 80. Pp. 52–59. DOI: 10.1016/j.cemconres.2015.10.005
5. Powers, T.C., Brownyard, T.L. Studies of the physical properties of hardened Portland cement paste. *Journal Proceedings*. 1946. 43(9). Pp. 101–132.
6. Galan, I., Beltagui, H., Garc'ia-Maté, M., Glasser, F.P., Imbabi, M.S. Impact of drying on pore structures in ettringite-rich cements. *Cement and Concrete Research*. 2016. 84. Pp. 85–94. DOI: 10.1016/j.cemconres.2016.03.003
7. Hou, D., Li, D., Hua, P., Jiang, J., Zhang, G. Statistical modelling of compressive strength controlled by porosity and pore size distribution for cementitious materials. *Cement and Concrete Composites*. 2019. 96. Pp. 11–20. DOI: 10.1016/j.cemconcomp.2018.10.012
8. Zhou, S., Sheng, W., Wang, Z., Yao, W., Huang, H., Wei, Y., Li, R. Quick image analysis of concrete pore structure based on deep learning. *Construction and Building Materials*. 2019. 208. Pp. 144–157. DOI: 10.1016/j.conbuildmat.2019.03.006
9. Chung, S.-Y., Elrahman, M.A., Kim, J.-S., Han, T.-S., Stephan, D., Sikora, P. Comparison of lightweight aggregate and foamed concrete with the same density level using image-based characterizations. *Construction and Building Materials*. 2019. 211. Pp. 988–999. DOI: 10.1016/j.conbuildmat.2019.03.270
10. Bharadwaj, K., Glosser, D., Moradillo, M.K., Isgor, O.B., Weiss, W.J. Toward the prediction of pore volumes and freeze-thaw performance of concrete using thermodynamic modelling. *Cement and Concrete Research*. 2019. 124. Pp. 105820. DOI: 10.1016/j.cemconres.2019.105820
11. Chistyakov, B.Z., Mysatov, I.A., Bochkov, V.I. *Proizvodstvo gazobetonnyh izdelij po rezatel'noj tekhnologii* [Aerated concrete products production using cutting technology]. L.: Stroizdat, 1977. p. 240. (rus)
12. Ramamurthy, K., Nambiar, E.K., Ranjani, G., Indu S. A classification of studies on properties of foam concrete. *Cement and Concrete Composites*. 2009. 31(6). Pp. 388–396. DOI: 10.1016/j.cemconcomp.2009.04.006

13. Kumar, E.M., Ramamurthy, K. Effect of fineness and dosage of aluminium powder on the properties of moist-cured aerated concrete. *Construction and Building Materials*. 2015. 95. Pp. 486–496. DOI: 10.1016/j.conbuildmat.2015.07.122
14. Narayan, N., Ramamurthy, K. Structure and properties of autoclaved aerated concrete: a review, microstructural investigations on aerated concrete. *Cement and Concrete Research*. 2000. 22. Pp. 321–329. DOI: 10.1016/S0958-9465(00)00016-0
15. Kurama, H., Topcu, I.B., Karakurt, C. Properties of the autoclaved aerated concrete produced from coal bottom ash. *Journal of materials processing technology*. 2009. 209(2). Pp. 767–773. DOI: 10.1016/j.jmatprotec.2008.02.044
16. Jerman, M., Keppert, M., V'yborn'y, J., Čern'y, R. Hygric, thermal and durability properties of autoclaved aerated concrete. *Construction and building materials*. 2013. 41. Pp. 352–359. DOI: 10.1016/j.conbuildmat.2012.12.036
17. Trong, L.N., Asamoto, S., Matsui, K. Sorption isotherm and length change behavior of autoclaved aerated concrete. *Cement and Concrete Composites*. 2018. 94. Pp. 136–144. DOI: 10.1016/j.cemconcomp.2018.09.003
18. Batool, F., Bindiganavile, V. Quantification of factors influencing the thermal conductivity of cement-based foam. *Cement and Concrete Composites*. 2018. 91. Pp. 76–86. DOI: 10.1016/j.cemconcomp.2018.04.015
19. Raj, A., Sathyan, D., Mini, K.M. Physical and functional characteristics of foam concrete: A review. *Construction and Building Materials*. 2019. 221. Pp. 787–799. DOI: 10.1016/j.conbuildmat.2019.06.052
20. Anders, N. Investigations about porosity analyzing of AAC. 6th International Conference on Autoclaved Aerated Concrete. 2018. 2(4). Pp. 141–145. DOI: 10.1002/cepa.895
21. Wei, S., Yiqiang, C., Yunsheng, Z., Jones, M.R. Characterization and simulation of microstructure and thermal properties of foamed concrete. *Construction and building materials*. 2013. 47. Pp. 1278–1291. DOI: 10.1016/j.conbuildmat.2013.06.027
22. She, W., Zhang, Y., Jones, M.R. Three-dimensional numerical modeling and simulation of the thermal properties of foamed concrete. *Construction and Building Materials*. 2014. 50. Pp. 421–431. DOI: 10.1016/j.conbuildmat.2013.09.027
23. Youssef, M. Ben, Lavergne, F., Sab, K., Miled, K., Neji, J. Upscaling the elastic stiffness of foam concrete as a three-phase composite material. *Cement and Concrete Research*. 2018. 110. Pp. 13–23. DOI: 10.1016/j.cemconres.2018.04.021
24. Pietras, D., Sadowski, T. A numerical model for description of mechanical behaviour of a Functionally Graded Autoclaved Aerated Concrete created on the basis of experimental results for homogenous Autoclaved Aerated Concretes with different porosities. *Construction and Building Materials*. 2019. 204. Pp. 839–848. DOI: 10.1016/j.conbuildmat.2019.01.189
25. Tarasov, A.S., Kearsley, E.P., Kolomatskiy, A.S., Mostert, H.F. Heat evolution due to cement hydration in foamed concrete. *Magazine of concrete research*. 2010. 62(12). Pp. 895–906. DOI: 10.1680/mac.2010.62.12.895
26. Adrien, J., Meille, S., Tadier, S., Maire, E., Sasaki, L. In-situ X-ray tomographic monitoring of gypsum plaster setting. *Cement and Concrete Research*. 2016. 82. Pp. 107–116. DOI: 10.1016/j.cemconres.2015.12.011
27. Jiang, J., Lu, Z., Li, J., Fan, Y., Niu, Y. Preparation and hardened properties of lightweight gypsum plaster based on pre-swelled bentonite. *Construction and Building Materials*. 2019. 215. Pp. 360–370. DOI: 10.1016/j.conbuildmat.2019.04.181
28. Wang, Q., Cui, Y., Xue, J. Study on the improvement of the waterproof and mechanical properties of hemihydrate phosphogypsum-based foam insulation materials. *Construction and Building Materials*. 2020. 230. Pp. 117014. DOI: 10.1016/j.conbuildmat.2019.117014
29. Vatin, N., Korniyenko, S.V., Gorshkov, A.S., Pestryakov, I.I., Olshevskiy, V. Actual thermophysical characteristics of autoclaved aerated concrete. *Magazine of Civil Engineering*. 2020. 96(4). Pp. 129–137. DOI: 10.18720/MCE.96.11
30. Korniyenko, S.V. Thermophysical field testing of residential buildings made of autoclaved aerated concrete blocks. *Magazine of Civil Engineering*. 2016. 4 (64). Pp. 10–25. DOI: 10.5862/MCE.64.2
31. Vatin, N.I., Gorshkov, A.S., Korniyenko, S.V., Pestryakov, I.I. The consumer properties of wall products from AAC. *Construction of Unique Buildings and Structures*. 2016. (1). Pp. 78–101.
32. Gorshkov, A.S., Rymkevich, P.P., Vatin, N.I. Simulation of non-stationary heat transfer processes in autoclaved aerated concrete walls. *Magazine of Civil Engineering*. 2014. 52(8). Pp. 39–49. DOI: 10.5862/MCE.52.5
33. Jones, M.R., Ozlutas, K., Zheng, L. Stability and instability of foamed concrete. *Magazine of Concrete Research*. 2016. 68(11). Pp. 542–549. DOI: 10.1680/mac.15.00097
34. Krämer, C., Schauerte, M., Müller, T., Gebhard, S., Trettin, R. Application of reinforced three-phase-foams in UHPC foam concrete. *Construction and Building Materials*. 2017. 131. Pp. 746–757. DOI: 10.1016/j.conbuildmat.2016.11.027
35. Krämer, C., Kowald, T.L., Trettin, R.H.F. Pozzolanic hardened three-phase-foams. *Cement and Concrete Composites*. 2015. 62. Pp. 44–51. DOI: 10.1016/j.cemconcomp.2015.06.002
36. She, W., Du, Y., Miao, C., Liu, J., Zhao, G., Jiang, J., Zhang, Y. Application of organic-and nanoparticle-modified foams in foamed concrete: reinforcement and stabilization mechanisms. *Cement and Concrete Research*. 2018. 106. Pp. 12–22. DOI: 10.1016/j.cemconres.2018.01.020
37. Suleymanova, L.A., Pogorelova, I.A., Marushko, M.V. Theoretical Basis of Formation Highly Organized Porous Structure of Aerated Concrete. *Materials Science Forum*. 2019. 945. Pp. 309–317. DOI: 10.4028/www.scientific.net/MSF.945.309
38. Yu, Q.L., Brouwers, H.J.H. Microstructure and mechanical properties of β -hemihydrate produced gypsum: An insight from its hydration process. *Construction and Building Materials*. 2011. 25(7). Pp. 3149–3157. DOI: 10.1016/j.conbuildmat.2010.12.005
39. Yu, Q.L., Brouwers, H.J.H. Development of a self-compacting gypsum-based lightweight composite. *Cement and Concrete Composites*. 2012. 34(9). Pp. 1033–1043. DOI: 10.1016/j.cemconcomp.2012.05.004
40. Li, P.P., Yu, Q.L., Brouwers, H.J.H., Chen, W. Conceptual design and performance evaluation of two-stage ultra-low binder ultra-high performance concrete. *Cement and Concrete Research*. 2019. 125. Pp. 105858. DOI: 10.1016/j.cemconres.2019.105858
41. Koenig, A. Analysis of air voids in cementitious materials using micro X-ray computed (μ XCT). *Construction and Building Materials*. 2020. 244. Pp. 118313. DOI: 10.1016/j.conbuildmat.2020.118313
42. Kim, J.-S., Chung, S.-Y., Han, T.-S., Stephan, D., Abd Elrahman, M. Modeling of multiple phase solid microstructures and prediction of mechanical behaviors of foamed concrete. *Construction and Building Materials*. 2020. 248. Pp. 118637. DOI: 10.1016/j.conbuildmat.2020.118637
43. Wong, H.S., Buenfeld, N.R. Determining the water-cement ratio, cement content, water content and degree of hydration of hardened cement paste: Method development and validation on paste samples. *Cement and Concrete Research*. 2009. 39(10). Pp. 957–965. DOI: 10.1016/j.cemconres.2009.06.013
44. Yio, M.H.N., Phelan, J.C., Wong, H.S., Buenfeld, N.R. Determining the slag fraction, water/binder ratio and degree of hydration in hardened cement pastes. *Cement and concrete research*. 2014. 56. Pp. 171–181. DOI: 10.1016/j.cemconres.2014.06.013

45. Qu, X., Zhao, X. Previous and present investigations on the components, microstructure and main properties of autoclaved aerated concrete-A review. *Construction and Building Materials*. 2017. 135. Pp. 505–516. DOI: 10.1016/j.conbuildmat.2016.12.208
46. Liu, L., Qin, G., Qin, S., Tao, G. Simulation of the volumetric deformation and changes in the pore structure of unsaturated cement-based materials subjected to freezing/thawing. *Construction and Building Materials*. 2020. 230. Pp. 116964. DOI: 10.1016/j.conbuildmat.2019.116964
47. Snoeck, D., Pel, L., De Belie, N. Comparison of different techniques to study the nanostructure and the microstructure of cementitious materials with and without superabsorbent polymers. *Construction and Building Materials*. 2019. 223. Pp. 244–253. DOI: 10.1016/j.conbuildmat.2019.06.225
48. Wong, H.S., Poole, A.B., Wells, B., Eden, M., Barnes, R., Ferrari, J., Fox, R., Yio, M.H.N., Copuroglu, O., Gudmundsson, G., others. Microscopy techniques for determining water-cement (w/c) ratio in hardened concrete: a round-robin assessment. *Materials and Structures*. 2020. 53(2). Pp. 1–19. DOI: 10.1617/s11527-020-1458-2
49. Kearsley, E., Visagie, M. Properties of foamed concrete as influenced by air-void parameters. *Concrete Beton*. 2002. 101. Pp. 8–14.
50. Nambiar, E.K.K., Ramamurthy, K. Air-void characterisation of foam concrete. *Cement and concrete research*. 2007. 37(2). Pp. 221–230. DOI: 10.1016/j.cemconres.2006.10.009
51. Aamr-*Daya*, E., Langlet, T., Benazzouk, A., Quéneudec, M. Feasibility study of lightweight cement composite containing flax by-product particles: Physico-mechanical properties. *Cement and Concrete Composites*. 2008. 30(10). Pp. 957–963. DOI: 10.1016/j.cemconcomp.2008.06.002/
52. Sypek, M., Latawiec Rafał and Pichór, W. Gypsum dehydration in cement and its impact on air-void structure in air-entrained concrete. *Construction and Building Materials*. 2019. 220. Pp. 396–402. DOI: 10.1016/j.conbuildmat.2019.06.011
53. Wolter, S., Uhre, F.A.H., Hasholt, M.T., Dahl, V.A., Anton, F. Air void analysis of hardened concrete by means of photogrammetry. *Construction and Building Materials*. 2019. 226. Pp. 953–964. DOI: 10.1016/j.conbuildmat.2019.07.203
54. Labuntsov, D.A., Yagov, V.V. *Mekhanika dvukhfaznykh system [Mechanics of two-phase systems]*. M.: MEI, 2000. 374 p. (rus)
55. Petit, P., Javierre, I., Jézéquel, P.-H., Biance, A.-L. Generation and stability of bubbles in a cement based slurry. *Cement and concrete research*. 2014. 60. Pp. 37–44. DOI: 10.1016/j.cemconres.2014.02.008
56. Feneuil, B., Roussel, N., Pitois, O. Optimal cement paste yield stress for the production of stable cement foams. *Cement and Concrete Research*. 2019. 120. Pp. 142–151. DOI: 10.1016/j.cemconres.2019.03.002

Contacts:

Karina Kurochkina, karina200386@yandex.ru

Lyudmila Suleimanova, ludmilasuleimanova@ya.ru

Alexandr Kolomatsky, kolomatskiy@yandex.ru



DOI: 10.34910/MCE.106.7

Nanomodified rejuvenators and protective materials for asphalt concrete

S.Yu. Shekhovtsova* , E.V. Korolev 

National Research Moscow State Civil Engineering University, Moscow, Russia

*E-mail: ShekhovtsovaSYU@mgsu.ru

Keywords: nanomodification, carbon nanofiber, protection, rejuvenation, asphalt concrete

Abstract. One of the effective methods to prevent the destruction of asphalt concrete pavement is to treat it with protective and rejuvenator materials. This study is aimed at developing an effective composition of the protective material. The proposed method for studying the effect of modification according to the results of rheological tests allows us to determine the conditional elastic modulus of the structured liquids. The influence of the degree of modification on the content of oil-polymer resins in the bitumen binder was evaluated using the developed quality criterion considering the modifier content contribution. We selected a solvent that provides effective dispersion and stability of the resulting suspension. The studied nanomodifier in the composition rejuvenator material had an impact on the properties of asphalt concrete increasing its crack resistance by 49 %, water resistance by 11 %, and shear adhesion by 6.1 %.

1. Introduction

Highways are an important part the country's road infrastructure and significantly affect its socio-economic development. A constant increase in vehicle traffic intensity leads to a significant acceleration in the wear road surfaces, which leads to an increase in the volume repair and restoration work [1, 2].

An effective method for preventing the progressive destruction asphalt concrete pavement is its treatment with protective-reducing rejuvenating compositions [3–4]. The main purpose of using such compositions is the formation a strong protective layer that penetrates deeply into the volume the road composite, which ensures the clogging the pore space, and is resistant to liquid media (water, solutions of various chemical agents) [5].

The first foreign studies of rejuvenator compounds date back to the 70s of the XX century [6]. So, American researchers in the period from 1971–1975 studies have been conducted to establish the penetration depth some rejuvenator compounds in the dense surface asphalt concrete pavement. Depth was estimated by penetration and viscosity of bitumen extracted from asphalt concrete samples. Another independent study [7] showed that the “rejuvenator agent” significantly reduced the complex elastic modulus asphalt concrete samples with a residual porosity of 10–12 %. This result was the basis for recommendations on the prohibition of rejuvenator agents on asphalt pavement with a residual porosity of less than 7–8 %.

C. Chiu and M. Lee [8] studied several different types rejuvenator: traditional impregnations, impregnations based on reconstituted asphalt binder and emulsion impregnations. All studied rejuvenator showed an increase in the ductility “old” binder in the upper layer of asphalt concrete pavement at a depth of 1 cm. The drying speed of the asphalt pavement treated with impregnations also depends on their composition and varies from 2 to 7 hours.

J. Lee and J.R. Kim [9] found that rejuvenator significantly affect the micro- and macro-texture surface of roads and are able, depending on the type modified binder used in the composition, to reduce the adhesion wheel to the road surface by 24 %.

Shekhovtsova, S.Yu., Korolev, E.V. Nanomodified rejuvenators and protective materials for asphalt concrete. Magazine of Civil Engineering. 2021. 106(6). Article No. 10607. DOI: 10.34910/MCE.106.7

© Shekhovtsova, S.Yu., Korolev, E.V., 2021. Published by Peter the Great St.Petersburg Polytechnic University.



This work is licensed under a [CC BY-NC 4.0](https://creativecommons.org/licenses/by-nc/4.0/)

Ambiguous results were obtained by J. Lee et al. [10] according to which the use rejuvenator reduces the complex dynamic elastic modulus and the phase angle of compacted asphalt concrete, increases the track depth and creep strain, and reduces the car tire resistance to sliding along asphalt surface. However, it was also established that the use rejuvenator can effectively resist chipping and “washing out” of individual grains stone material from the road surface.

Summarizing the existing studies, we can conclude that one of the disadvantages existing protective and rejuvenator materials [5–15] used for the surface treatment asphalt concrete coatings is a decrease in the adhesion automobile wheels to the road surface, insufficient resistance to abrasion due to low adhesion, their low fluidity (high viscosity) at operating ambient temperatures, which reduces their penetration rate into the structure asphalt concrete. In this regard, it is currently relevant to use liquid compositions based on bitumen, which use organic solvents with additional modifiers.

Domestic research in this direction is mainly aimed at selecting the optimal ratio the components of the impregnating composition [16–17]. The Russian market of solvent-based protective and reducing rejuvenating materials (RM) is represented by a wide range products: Silcoat (RF), Dorsan (RF), PS-1 (RF), Sanad (RF), Brit-RM-R (RU), Biguma – LDGA (Germany), Surtreat PDC (USA), CRF, Reclamite, CRF Crafcoc (USA) and others, which testifies to the interest of the road industry in these materials and, at the same time, the lack of domestic research aimed at studying the effect component the composition and technological processes for the preparation of RM on the properties of asphalt concrete. Naturally, the accumulation of knowledge and experience will eliminate the existing problems in this area.

This research work is aimed at developing the composition an effective nanomodified rejuvenating material combined action.

2. *Materials and Methods*

The development and optimization of an effective nanomodified rejuvenating material (RM) includes the following steps:

1. Development and optimization of modified bitumen binder (bitumen binder and petroleum polymer resin);
2. Development and optimization of nanomodified suspension (organic solvent and nanofiber);
3. Development and optimization of the control composition of the rejuvenating material (modified bitumen binder prepared according to steps 1 and organic solvent);
4. Nanomodification of the control composition of the rejuvenating material prepared according to steps 3.

The experimental method was used to develop the nanomodified composition RM, the analytical method was used to optimize the composition RM.

For first step was used bitumen BND 90/130, manufactured by LLC Lukoil and petroleum polymers resins (PPR) which are low molecular weight thermoplastic polymer obtained by polymerization aliphatic and aromatic hydrocarbon fractions. Petroleum polymer resins (PPR) were considered as a modifying component for a bituminous binder. Two petroleum polymer resins were considered: PPR Pyroplast-2K which is a product of pyrolysis fraction C9 at 125–200 °C with thermal polymerization containing polycyclopentadiene, polystyrene; PPR Inden-Kumaron which is a product thermal and / or catalytic polymerization the C9 fraction at 120–210 °C hydrocarbon pyrolysis products at a temperature of 240–250 °C, representing a styrene-dicyclopentadiene-indene copolymer with a molecular weight of 600–800, manufactured by the group “Eurohem” companies.

For the second step were used the following solvents which are organic solvents: Solvent No 1 which is a product oil distillation, a mixture liquid aromatic and aliphatic hydrocarbons (not more than 50 % from each group), with a density of not more than 795 kg/m³ (at 20 °C) and with a boiling point not higher than 165 °C, manufactured by CJSC “ARIKON”; Solvent No. 2 which is a direct distillation product the middle distillate oil fraction, with a boiling point in the range of 150-250 °C and density at 20 °C 780–850 kg/cm³, manufactured by CJSC “ARIKON”.

Also for the second step was used following carbon nanofiber (CNF) “Pyrograf III Carbon Nanofiber” which is one-dimensional filiform nanoscale graphite particles that do not have a pronounced cylindrical orientation of graphene layers, as well as an internal cavity manufactured by “Pyrograf Products”, USA. CNF “Pyrograf III Carbon Nanofiber” which is nanomodifying additive.

The composition of the modified bitumen binder was developed based on the assessment of the influence of petroleum polymer resins on the following physical and mechanical properties of bitumen: needle penetration depth at 25 °C; needle penetration depth at 0 °C; softening temperature and adhesion.

The influence petroleum polymer resins on the structurally sensitive properties the bitumen binder was evaluated using a Physica MCR 101 CR-Rheometer (viscometer), in shear rate control mode, using a measuring system such as coaxial cylinders.

For a material that is in a structured liquid state, the rheological curve which is an S-shaped curve located inside the angle formed by tangents that pass through the origin, Fig. 1.

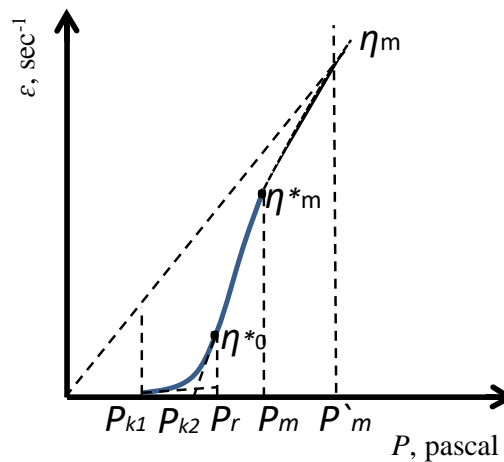


Figure 1. Rheological curve of a system with a conditionally elastic deformation zone.

Based on the rheological curve (Fig. 1) are determined by the rheological parameters elastic-plastic-viscous properties of disperse systems: η^*_0 which is the highest ultimate viscosity of the almost none destructed structure; η_m which is the lowest ultimate viscosity of the extremely destroyed structure; P'_m which is a boundary shear stress corresponding to the ultimate destruction of the structure, η^*_m which is the smallest of the plastic (Bingham) viscosity; P_{k2} which is conditional yield strength corresponding to the ultimate dynamic shear stress; P_{k1} which is conditional yield strength corresponding to the ultimate static shear stress.

Optimization of the composition of the modified bitumen binder was carried out using specific quality criteria describing which is the influence of the percentage of petroleum polymer resin on each quality indicator. Based on the partial quality criteria were calculated a generalized criterions which are showing the degree of modification of the bituminous binder from the content of petroleum polymer resin.

Nano modified suspension was developed by introduced of carbon nanofiber to a solvent. The distribution of carbon nanofibers in the solvent was carried out using an ultrasonic disperser Sonics Vibra-Cell VCX 750. Sound vibrations which are the frequency level of 20 kHz, the dispersion power which is 750 W. The appearance samples dispersed media "solvent – carbon nanofibers" before and after ultrasonic dispersion is shown in Fig. 2.

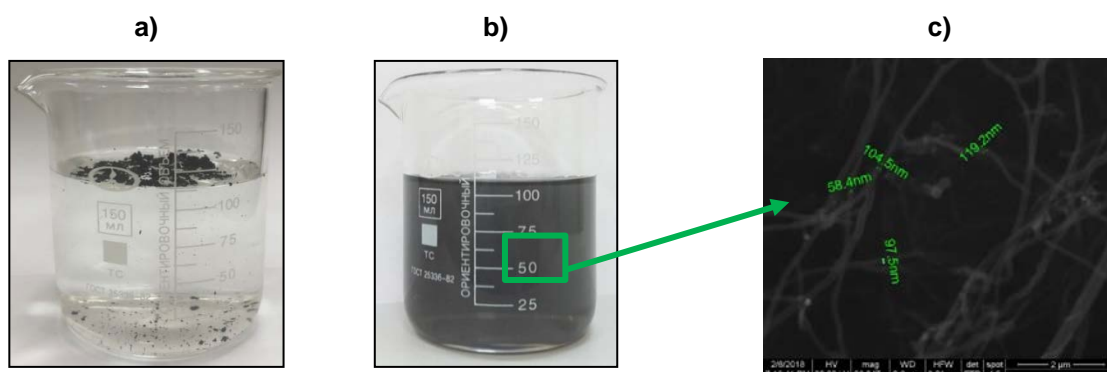


Figure 2. Appearance samples: a – before ultrasonic dispersion; b – after ultrasonic dispersion; c) micrograph carbon nano modifier after ultrasonic dispersion.

In accordance with the preliminary experiment, it was found that the significant effect of nanofiber on the properties of the protective reducing material is in the range from 0.1 to 0.001 % by weight of the solvent.

The size carbon nanofibers were determined on a Zetatract instrument using laser diffraction. Choice the specified carbon nanofibers which are modifier is justified by the following:

1) carbon nanofibers have a high affinity for organic solvents and bitumen binder (this is evidenced by the numerous positive results obtained by domestic and foreign researchers);

2) carbon nanofiber has a lower cost compared to single and multilayer nanotubes, respectively an average 25 and 8 times.

The preparation of the control composition of the protective rejuvenator in laboratory conditions was carried out with sequential multi-stage mixing materials in accordance with third step which is the above. Optimization of the control composition of the protective rejuvenator was carried out in following quality indicators: of drying time, homogeneity and adhesion. The optimal control composition of the rejuvenation material was selected based on the value of the developed generalized quality criterion including particular quality criteria that considered the values of the obtained properties.

The preparation of the nanomodified composition of the rejuvenation and protective material was carried out in accordance with the third step and the addition (which is the above) of a nanomodifier in accordance with the second step (that is, the preliminary introduction of carbon nanofibers into the solvent). Impact research carbon nanofibers on the properties of the protective rejuvenator was carried out in following quality indicators: of drying time, homogeneity and adhesion.

Impact research nano-modified protective and rejuvenator materials on the properties of asphalt concrete was carried out in following quality indicators compressive strength, crack resistance, internal friction coefficient, shear adhesion, and water resistance. The optimal nano-modified protective and rejuvenator materials were selected based on the value of the developed generalized quality criterion including particular quality criteria that considered the values of the obtained properties.

3. Results and Discussion

To select the effective one from the considered petroleum polymer resins, we evaluated their influence on the physic mechanical properties bitumen binders, Fig. 2–7 and their adhesion to the mineral stone (Table 1).

Establishing the influence petroleum polymer resins on the formation a structure was studied by indicators characterizing the greatest resistance to shear in two critical structural states: the highest ultimate viscosity of the almost none destructed structure the bitumen binder; the lowest ultimate viscosity of the extremely destroyed structure a bitumen binder. From the point of view rheology and physical chemistry bitumen binders are colloidal dispersed systems characterized by a sharp change in the structural and mechanical properties temperature. So it is advisable to study them in the temperature range corresponding to the manufacturing and application technology.

The results of the influence of different percentages petroleum polymer resins are presented in Fig. 3.

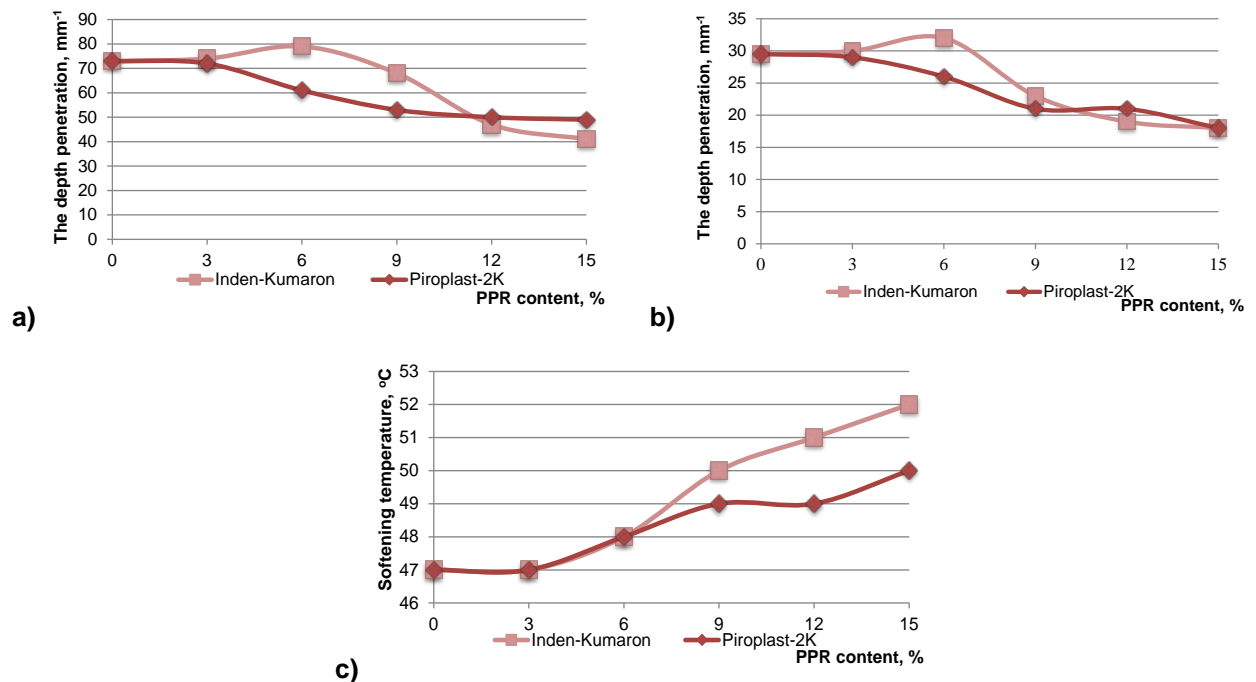


Figure 3. The influence content petroleum polymer resins on the physical and mechanical properties the bitumen binder: a) the depth penetration of the needle at 25 °C; b – the depth penetration of the needle at 0 °C; c – softening temperature.

Table 1. Effect from the content PPR on the adhesion bitumen with mineral stone.

Property	Content PPR, %					
	0	3	6	9	12	15
Inden Kumaron						
Adhesion, point	2	3	4	4	4	4
Piroplast-2K						
Adhesion, point	2	2	3	3	4	4

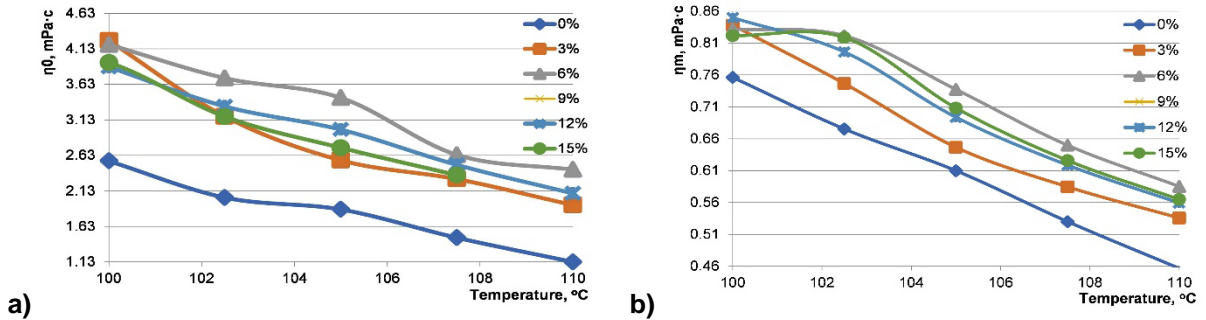


Figure 4. The influence content PPR Inden-Kumaron and temperature:
a – the highest ultimate viscosity of the almost none destroyed structure the bitumen binder;
b – the lowest ultimate viscosity of the extremely destroyed structure a bitumen binder.

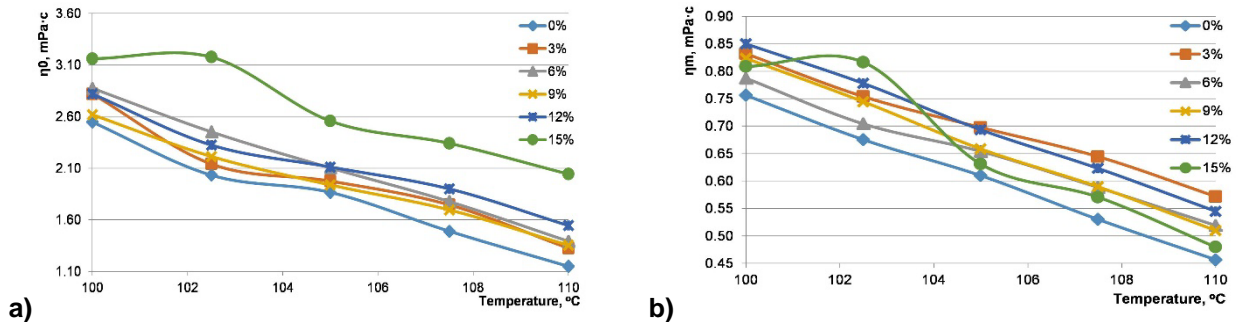


Figure 5. The influence content PPR Piroplast-2K and temperature:
a – the highest ultimate viscosity of the almost none destroyed structure a bitumen binder;
b – the lowest ultimate viscosity of the extremely destroyed structure a bitumen binder.

The numerical value of the ability structured systems at various temperatures to resist shear is expressed by the conditional elastic modulus [18]:

$$E = \frac{\eta_0}{\eta_0 - \eta_m} \cdot P_r, \tag{1}$$

where η_0 which is the highest ultimate viscosity of the almost none destroyed structure a bituminous binder; η_m which is the smallest ultimate viscosity extremely destroyed structure bituminous binder; P_r which is boundary stress corresponding to the almost none destroyed structure bitumen binder, corresponding to the beginning of the process destruction structure.

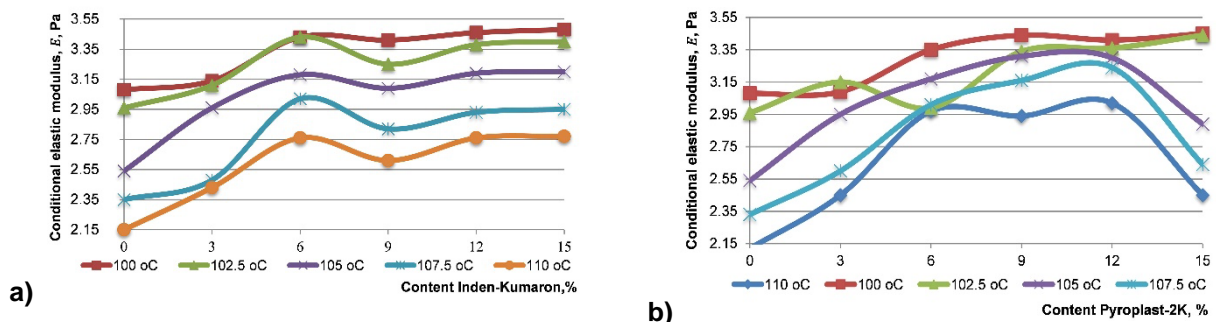


Figure 6. The influence content PPR on the conditional elastic modulus bitumen binder:
a – Inden-Kumaron; b – Piroplast-2K.

The influence content petroleum polymer resins in the modification bitumen binder (Fig. 3–8) was evaluated according to the following developed particular criteria:

- $I_{C_i j}$ which is the criterion characterizing the effect of the content oil-polymer resins on the depth penetration the needle at 0 and 25 °C, softening temperature and adhesion:

$$I_{C_i j} = \left(\frac{I_{j(PPR)} - I_{j(Bitumen)}}{I_{j(Bitumen)}} \right) \cdot \frac{1}{c_i} \cdot 100\% , \quad (2)$$

where $I_{j(PPR)}$ which is the numerical value the property indicator of bitumen with PPR; $I_{j(Bitumen)}$ which is the numerical value the property indicator of bitumen; C_i is the content PPR, % by weight.

- $I_{C_i E_T}$ which is the criterion characterizing the effect content of oil-polymer resins on the relative change in the conditional elastic modulus:

$$I_{C_i E_T} = \left(\frac{I_{E_T(PPR)} - I_{E_T(Bitumen)}}{I_{E_T(Bitumen)}} \right) \cdot \frac{1}{c_i} \cdot 100\% , \quad (3)$$

where $I_{E_T(PPR)}$ which is the numerical value the conditional elastic modulus the bitumen with PPR at a certain temperature; $I_{E_T(Bitumen)}$ which is the numerical value the indicator conditional elastic modulus the bitumen.

The presented particular criteria were also used to calculate the average values the particular criteria in the studied temperature range:

$$I_{C_i E} = \frac{\sum_{i=1}^n I_{C_i E_T}}{n} , \quad (4)$$

$$F_{C_i} = \frac{\sum_{i=1}^n I_{C_i j}}{n} , \quad (5)$$

where n which is the number of particular criteria.

The results calculation, particular criteria and given quality criteria are presented in Tables 2 and 3.

Table 2. Particular criteria characterizing the percentage contribution of a petroleum polymer resins to the modification the bitumen binder.

Private quality criteria	PPR content, %				
	3	6	9	12	15
Inden-Kumaron					
$I_{C_i P25}$	0.46	1.37	–0.76	–2.97	–2.92
$I_{C_i P0}$	0.56	1.41	–2.45	–2.97	–2.60
$I_{C_i T softening}$	0.00	0.35	0.71	0.71	0.71
$I_{C_i Adhesion}$	16.67	16.67	11.11	8.33	6.67
$I_{C_i E}$	2.81	3.64	1.86	1.75	1.44
Pyroplast 2K					
$I_{C_i P25}$	–0.46	–2.74	–3.04	–2.63	–2.19
$I_{C_i P0}$	–0.56	–1.98	–3.20	–2.40	–2.60
$I_{C_i T softening}$	0.00	0.35	0.47	0.35	0.43
$I_{C_i Adhesion}$	0.00	8.33	5.56	8.33	6.67
$I_{C_i E}$	3.34	3.46	2.87	2.26	0.95

Table 3. Average values of particular quality criteria.

Quality criteria	PPR content, %				
	3	6	9	12	15
F_{ci}	Inden-Kumaron				
	4.1	5.0	2.1	1.0	0.7
F_{ci}	Pyroplast 2K				
	0.5	1.5	0.5	1.2	0.7

An analysis the results (Table 3) shows that the greatest modifying effect, estimated by the value he criterion, when introduced into the bitumen binder the considered petroleum polymer resins is observed at their content of 6 %. The indicated content of the PPR was used for further research and development for basic (control) composition.

At the second step the development composition of the nano-modified rejuvenator and protective material. At this step, it is necessary to choose a solvent compatible with the organic bitumen binder, as well as allowing for maximum dispersion the carbon nanofiber and the stability its suspension.

Dispersion of carbon nanofibers were carried out in two solvents. In this case, suspensions were obtained with two concentrations carbon nanofiber C1 = 0.001 % and C2 = 0.01 %. The dispersion quality was estimated by the value reduced diameter of the dispersed phase (carbon nanofiber) in the suspension (Fig. 7).

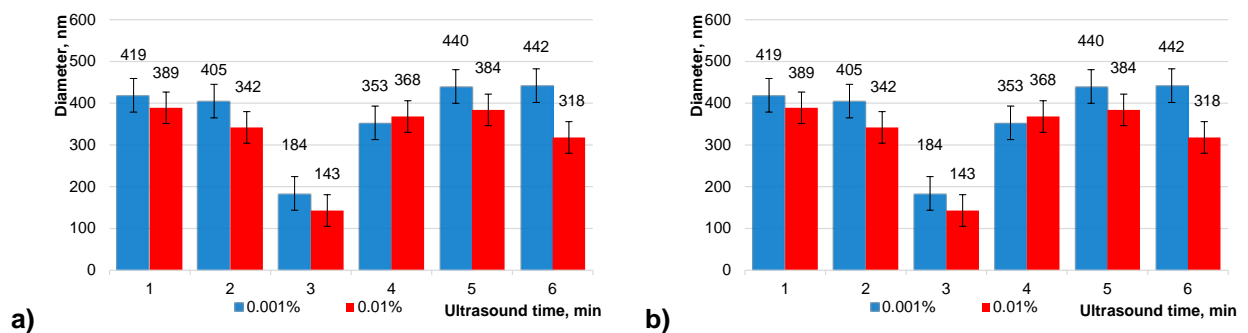


Figure 7. The influence of duration ultrasonic dispersion on the average reduced diameter the carbon nanofibers in suspension: a – Solvent No 1; b – Solvent No 2.

The results obtained (Fig. 7) show that the dependence average reduced diameter the carbon nanofiber in suspension on the duration dispersion is extreme. The smallest value the average diameter of carbon nanofiber in suspension for Solvent No. 1 is observed after 3 minutes dispersion and for Solvent No. 2–4 minutes the dispersion. The average reduced diameter the carbon nanofiber in suspension for Solvent No. 1 is 143–184 nm, and for Solvent No. 2 it is 108–139 nm (depending on the concentration of carbon nanofiber). However, suspensions based on Solvent No. 2 are not stable and precipitation occurs after 7 days of storage. In this regard, in further work, Solvent No. 1 was used as the main medium for the preparation of the suspension.

For RM, ceteris paribus, important quality indicators are: the uniformity the material, which must be maintained for a given period; drying time and adhesion. It is natural that the solvent content will have a significant effect on these properties. Establishing the optimal ratio, the components of the RM and evaluating their compatibility was carried out for 3 formulations (Table 4). The introduction of a lower solvent content into the bitumen binder led to a significant increase in the drying time which was more than 180 minutes, and the introduction of a larger amount of solvent led to an unsatisfactory adhesive adhesion and uniformity the RM.

Table 4. Composition and properties of RM.

Name of components	No. composition		
	1	2	3
	Content of components, %		
Modified binder:			
-Bitumen 90/130 – 100 %	45	55	65
-PPR Inden-Kumaron – 6 %			
Solvent No. 1	55	45	35

Table 5. Technological and operational properties of RM.

Property	Requirements of Russian industry road guidance document (IRGD) 218.3.073-2016	No. composition		
		1	2	3
		Actual results		
Drying time, min	on more 180	55	60	95
Homogeneity after 7 days		uniformly, no clumps or clots		
Adhesion, point	no less 4	3	4	4

Results presented in Table 4 show that the composition No. 1 does not meet the requirements of IRGD 218.3.073-2016 for adhesion. For this indicator, only compositions No. 2 and 3 can be used. Moreover, according to the "Drying Time" indicator, all the studied compositions meet the requirements: composition No. 3 (95 min.) Has a maximum value, and composition No. 1 has a minimum value (55 min). By homogeneity, all compositions also comply with the requirements the normative and technical document. In this regard, the choice of the composition RM can be carried out by a generalized criterion of the form:

$$F_m = 3 \sqrt[3]{\frac{60}{I_t} I_{Adh} I_{Un}}, \quad (6)$$

where I_t is the indicator "Drying time" (60 – normalization coefficient); I_{Adh} is indicator "Adhesion" (when fulfilling the requirements normative-technical document on adhesion $I_{adh} = 1$; if the requirement is not fulfilled, $I_{Adh} = 0$); I_{Un} is indicator "Uniformity" (in the absence of clots and lumps $I_{Un} = 1$; in the presence of clots and lumps $I_{Un} = 0$).

The values generalized criterion F_m for composition No. 1 $F_m = 0$, for composition No. 2 $F_m = 1$, and for composition No. 3 $F_m = 0.86$.

Thus, according to the specified quality indicators, the optimal composition is No. 2, containing the modified bitumen binder – 55 %, Solvent No. 1 – 45 %.

The positive effect of nanoscale modifiers on the properties bitumen materials is widely known, see for example [19, 20]. The introduction nanomodifier in the RM will further structure the maltene component the modified bitumen binder, which will increase its cohesive and adhesive strength.

At the third step development of the nanomodified composition the protective rejuvenation material, the optimal content of the nanomodifier which is carbon nanofiber was selected, Table 5.

Table 5. The composition and properties of nanomodified rejuvenating materials.

Name of components	Without CNFc (control)	No. composition		
		1	2	3
		Content of components, %		
Modified binder:				
-Bitumen 90/130 – 100 %		55		
-PPR Inden-Kumaron – 6 %				
Solvent No. 1		45		
Carbon nanofiber	–	0.001	0.01	0.1
Property		Actual results		
Drying time, min	60	50	43	42
Homogeneity after 7 days		uniformly, no clumps or clots		
Homogeneity after 21 days	sediment		uniformly	
Adhesion, point	4	5	5	5

The results presented in Table 5 show that the introduction of carbon nanofiber in the studied range can improve adhesion by 25 % and shorten the drying time by 16–30 %.

For study the influence of the developed rejuvenator materials on the asphalt concrete quality indicators was selected and tested corresponding in grain composition, to the type mastic asphalt concrete SMA-15. The design of the asphalt mix was carried out in accordance with the requirements of Russian state standard 31015-2002. For a comparative analysis the results the development RM, a comparison was made with

existing industrial analogues the domestic (Brit-RM) and foreign (Surtreat) production, the consumption of which corresponded to the recommended ones from the manufacturer – 1.0 and 0.35 l/m², respectively. The consumption of the developed RM was 0.35 l/m².

The choice of the optimal composition the RM was carried out according to the value of the generalized quality criterion, calculated by the formula:

$$F_k = \sqrt[5]{K_{fm}} = \sqrt[5]{k_{R20} \cdot k_{Rp} \cdot k_{tg} \cdot k_C \cdot k_W}, \quad (7)$$

where k_{R20} is the coefficient taking into account the relative change in compressive strength; k_{Rp} is the coefficient taking into account the relative change in crack resistance during compression; k_{tg} is the coefficient taking into account the relative change in the coefficient of internal friction; k_C is the coefficient taking into account the relative change in adhesion during shear; k_W is the coefficient taking into account the relative change in water resistance during prolonged water saturation.

Table 6. The influence RM on the properties of asphalt concrete.

Property	Actual results					
	Without RM	Asphalt samples processed by RM				
		Surtreat (USA)	Brit-RM (Russia)	No.1	No.2	No.3
Compressive strength, MPa, at a temperature of 20 °C	3.9	4.3	4.2	4.4	4.4	4.4
Crack resistance, MPa, at a temperature of 0 °C	3.1	3.9	4.4	4.2	4.5	4.7
Internal friction coefficient	0.94	0.94	0.94	0.94	0.94	0.94
Shear adhesion at a temperature of 50 °C, MPa	4.24	3.12	3.11	4.20	4.30	4.50
Water resistance with prolonged water saturation	0.89	0.95	0.93	0.98	0.98	0.99

The optimal composition corresponds to the maximum value of the generalized quality criterion. The results of experimental studies the properties of asphalt concrete samples treated with developed RM with different contents the nanofiber and samples treated with analogues are presented in Table 7.

The results calculation of the generalized quality criterion is presented in Table 7.

Table 7. Values of the generalized quality criterion.

Property	Actual results					
	Without RM	With RM				
		Surtreat (USA)	Brit-RM (Russia)	No. 1	No. 2	No. 3
Compressive strength, MPa, at a temperature of 20 °C	1.00	1.10	1.08	1.13	1.13	1.13
Crack resistance, MPa, at a temperature of 0 °C	1.00	1.23	1.39	1.33	1.43	1.49
Internal friction coefficient	1.00	1.00	1.00	1.00	1.00	1.00
Shear adhesion at a temperature of 50 °C, MPa	1.00	0.74	0.73	0.99	1.01	1.06
Water resistance with prolonged water saturation	1.00	1.07	1.04	1.10	1.10	1.11
Generalized quality criteria	1.00	1.01	1.00	1.10	1.12	1.15

From the data of Table 7, it follows that the introduction carbon nanofiber in an amount of 0.001 ... 0.1 % by weight RM provides an increase in the effectiveness of the impregnating composition on the properties asphalt concrete. Nanomodified rejuvenator and protective material the composition No. 3 is characterized by

the maximum value the generalized quality criterion. At the same time, its use allows to increase performance indicators: compressive strength by 12.8 %; crack resistance by 49 %; shear adhesion by 6.1 % and water resistance by 11 %.

It was also established that the existing industrial analogues RM of Russian and foreign production in terms indicators did not demonstrate a significant effect on the properties the asphalt concrete, which makes research aimed at developing effective compositions of RM relevant and promising.

4. Conclusion

1. It was proposed a method for calculating the conditional elastic modulus of structured fluids using the results rheological tests.

2. It was proposed a generalized criterion for calculating the degree of modification bitumen binder with petroleum polymer resins considering the content contribution modifier. It was found that the optimal content of petroleum polymer resin is 6 %.

3. It has been established a solvent which provides disperses carbon nanofiber to a diameter of 143–184 nm and which provides a suspension stability of up to 7 days.

4. It was established the possibility of using one of the by-products in the petrochemical industry which is petroleum polymer resin which is a modifier in rejuvenator and protective materials. This will help to solve the acute problem of waste disposal of chemical and petrochemical production. However, it should be noted that the compositions of RM containing the specified modifier which is petroleum polymer resin, were characterized by low adhesive ability.

The introduction carbon nanofiber in the amount of 0.001...0.1 % by weight of the rejuvenator and protective material allows us to further structure the maltene component the modified bitumen binder, which enhances the modifying effect to increase the performance characteristics of asphalt concrete: compressive strength by 13 %; crack resistance by 49 %; shear adhesion by 6.1 % and water resistance by 11 %.

5. Acknowledgment.

Financial support for this work was obtained from Russian Science Foundation contract numbers: 21-79-00191, <https://rscf.ru/en/project/21-79-00191/>.

References

- Zavyalov, M.A., Kirillov, A.M. Evaluation methods of asphalt pavement service life. Magazine of Civil Engineering. 2017. 2(70). Pp. 42–56. DOI: 10.18720/MCE.70.5
- Bhasin, A., Izadi, A., Bedgaker, S. Three-dimensional distribution of the mastic in asphalt composites. Constr. Build. Mater. 2011. 25. Pp. 4079–4087. DOI: 10.1016/j.conbuildmat.2011.04.046
- Coleri, E., Harvey, J.T., Yang, K., Boone, J.M. A micromechanical approach to investigate asphalt concrete rutting mechanisms. Constr. Build. Mater. 2012. 30. Pp. 36–49. DOI: 10.1016/j.conbuildmat.2011.11.041
- Lin, J., Hon, J., Huang, C., Liu, J., Wu, S. Effectiveness of Rejuvenator Seal Materials on Performance of Asphalt Pavement. Construction and Building Materials. 2014. 55. P. 63. DOI: 10.1016/j.conbuildmat.2014.01.018
- Shekhovtsova, S.Yu., Korolev, Ye.V. Sovremennyy opyt ispolzovaniya reyunivatorov dlya reversinga asfaltobetonnykh pokrytiy [Modern experience in the use of rejuvenation for reversing asphalt pavement] Regional architecture. Construction. 2018. 3 (36). Pp. 5–16. (rus)
- Brown, E.R., Johnson, R.R. Evaluation of rejuvenators for bituminous pavements. AFCEC-TR-76-3. Air Force Civil Engineering Centre. Tyndall Air Force Base. Florida. 1976. 24 p.
- Estakhri, C.K., Agarwal, H. Effectiveness of fog seals and rejuvenators for bituminous pavement surfaces. Report TX-91/1156-1F. Texas Transportation Institute. Texas A&M University. Texas. 1991. 112 p.
- Chiu, C., Lee, M. Effectiveness of Seal Rejuvenators for Bituminous Pavement Surfaces. Journal of Testing and Evaluation. 2006. 34 (5). Pp. 390–394.
- Lee, J., Kim, Y.R. Performance Evaluation of Asphalt Surface Treatments Using MMLS3. Airfield and Highway Pavements. 2006. Pp. 86–97.
- Seong-Hyeok, L., Allistair, B.T., Jun, K., Dae-Wook, P. Evaluation of rejuvenators based on the healing and mechanistic performance of recycled asphalt mixture. Construction and Building Materials. 2019. 220. Pp. 628–636. DOI: 10.1016/j.conbuildmat.2019.05.150
- Inozemtcev, S.S., Korolev, E.V. Increasing the weathering resistance of asphalt by nanomodification. Materials Science Forum. 2018. 945. Pp. 147–157. DOI: 10.4028/www.scientific.net/MSF.945.147
- Weimin, S., Baoshan, H., Xiang S. Influence of warm-mix asphalt technology and rejuvenator on performance of asphalt mixtures containing 50 % reclaimed asphalt pavement. Journal of Cleaner Production. 2018. 192 (10). Pp. 191–198. <https://doi.org/10.1016/j.jclepro.2018.04.269>
- Zhang, Yu., Molenaar, A.A.A., Shaopeng, Wu. Assessment of effectiveness of rejuvenator on artificially aged porous asphalt concrete. Construction and Building Materials. 2016. Pp. 286–292. DOI: 10.1016/j.conbuildmat.2016.02.042
- D'Angelo, G., Lo Prest, D., Thom, N. Optimization of bitumen emulsion properties for ballast stabilisation. Materiales de Construcción. 2017. 67. 327.

15. Song, X., Jianying, Yu., Changbin, H., Defeng, Q., Lihui, X. Laboratory evaluation of rejuvenation effect of reactive rejuvenator on aged SBS modified bitumen. *Materials and Structures*. 2017. 50(6). 233.
16. Xi-dong, W., Zhong T., Liang Z., Lei Y. Application of Slurry Seal Pre-maintenance Technology in Road Maintenance in Cold Region. *The World of Building Materials*. 2011. 01. 418.
17. Maharaj, R., Ramjattan-Harry, V., Mohamed, N. Rutting and Fatigue Cracking Resistance of Waste Cooking Oil Modified Trinidad Asphaltic Materials. *The Scientific World Journal*. 2015. 385013. DOI: 10.1155/2015/385013
18. Abdullin, A.I., Emelyanycheva, E.A. A study of properties of road petroleum bitumen modified with polymer additives. *Journal of Chemical Technology and Metallurgy*. 2018. 53(3). 422–429.
19. Vysotskaya, M.A., Rusina, S.Yu. O perspektivakh ispolzovaniya nanotrubok pri prigotovlenii polimerno-bitumnykh vyazhushchikh [On the prospects of using nanotubes in the preparation of polymer-modified binders]. *Roads and bridges*. 2014. 2 (32). Pp. 171–187. (rus)
20. Shu, B., Wu, S., Pang, L., Javilla, B. The Utilization of Multiple-Walled Carbon Nanotubes in Polymer Modified Bitumen. *Materials*. 2017. 10 (4). 416. DOI: 10.3390/ma10040416

Contacts:

Svetlana Shekhovtsova, SHehovtsovaSYU@mgsu.ru

Evgeniy Korolev, korolev@nocnt.tu



DOI: 10.34910/MCE.106.8

Performance investigation of demolition wastes-based concrete composites

V.S. Lesovik^{a, b} , A.A. Ahmed^a , R.S. Fediuk^{*c} , B. Kozlenko^a , Y.H. Mugahed Amran^d ,
A.Kh. Alaskhanov^e , M.A. Asaad^f , G. Murali^g , V.A. Uvarov^a

^a Belgorod State Technological University, Belgorod, Russia

^b Federal State Budgetary Institution "Central Research and Design Institute of the Ministry of Construction and Housing and Communal Services of the Russian Federation", Moscow, Russia

^c Far Eastern Federal University, Vladivostok, Russia

^d Prince Sattam Bin Abdulaziz University, Alkharj, Saudi Arabia

^e Grozny State Oil Technical University named after Academician M.D. Millionshchikov, Grozny, Chechen Republic, Russia

^f Iraq University College (IUC), Basrah, Iraq

^g SASTRA Demeed to be University, Tamil Nadu, India

*E-mail: roman44@yandex.ru

Keywords: cements, cement-based composites, binders, concretes, durability

Abstract. Due to man-made and natural anomalies occurring on planet Earth, there are a lot of destroyed cities, settlements and houses. The issue is how to rebuild these cities and how to use parts of the destroyed buildings and structures in making greener concrete. This paper aims to study the efficiency and effect of using concrete demolition wastes on the microstructure of greener concrete composites. We prepared demolition wastes-based concrete composite containing a greener supplemental cementing binder (GSCB) and fine aggregates of the previously produced concretes with high mechanical properties. The design of the compositions was determined by taking into account the law of affinity of microstructures of greener concretes. We studied the strengths, microstructural, morphological and thermal properties of raw materials and concretes at 28 days of curing. The dense microstructure was examined via the use of Portland cement and hydration products, which partially included previously unreacted clinker minerals presented in concrete waste and activated during its grinding. Results showed that replacing up to 20 % of Portland cement with the demolition waste of concrete structures as a GSCB improves compressive strength for different concrete applications. This is ensured by the affinity of the microstructure of concrete waste and newly synthesized concrete.

1. Introduction

A review of the scientific literature on the research topic revealed that technical progress in the production of concrete and reinforced concrete requires additional sources of raw materials, in particular, the use of high-quality aggregates [1–10]. According to Bassani et al. [4], the solution to this problem is hindered by an ever-growing shortage of mineral and energy resources, as well as environmental protection requirements [4–7]. Therefore, as reported by Sormunen and Kärki [8], the current task is the integrated

Lesovik, V.S., Ahmed, A.A., Fediuk, R.S., Kozlenko, B., Mugahed Amran, Y.H., Alaskhanov, A.Kh., Asaad, M.A., Murali, G., Uvarov, V.A. Performance investigation of demolition wastes-based concrete composites. Magazine of Civil Engineering. 2021. 106(6). Article No. 10608. DOI: 10.34910/MCE.106.8

© Lesovik, V.S., Ahmed, A.A., Fediuk, R.S., Kozlenko, B., Mugahed Amran, Y.H., Alaskhanov, A.Kh., Asaad, M.A., Murali, G., Uvarov, V.A. 2021. Published by Peter the Great St.Petersburg Polytechnic University.



This work is licensed under a CC BY-NC 4.0

use of deposits of low-quality raw materials and waste from related industries [8–10]. Planned demolition of obsolete buildings and structures, as well as natural and technological disasters, armed conflicts in various countries (including Iraq) produce large volumes of concrete waste [11–15]. According to Sakai [16] and Sharonova et al. [17], first of all, these wastes should be used for repair and restoration work and new construction at the places of their occurrence [16–18]. In this regard, it is relevant to use fragments of destroyed buildings and structures as raw materials for the production of building materials, including “green composites”. Some papers [19–21] are devoted to the study of the possibility of using waste from destroyed buildings. However, the results of these studies are quite contradictory, which is explained by the different composition of waste from destroyed buildings in different countries. The rational use of technogenic products is possible only after their preliminary mechanical treatment, taking into account their chemical and material composition.

The theoretical basis for the design of composites using the specified raw materials is the transdisciplinary science of geomimetics developed by Lesovik et al. [22–23]. It uses the results of studies of natural processes to produce high-strength concrete and new generation building composites. In particular, one of the aspects of this science is the law of affinity of microstructures, which consists in the selection of raw materials with similar physicomaterial characteristics for a composite [24–27]. The law of affinity of microstructures for anisotropic materials involves the multilayered composites design and repair systems at three levels (nano-micro-macro). These systems are identical to the base matrix, which provides a route to a substantial growth in the materials durability [28]. The origin for the formulation of the law was the information obtained in the study of natural analogues of anisotropic and isotropic building composites [22–23]. The results were obtained on the waste of the destroyed buildings and structures of Iraq, which consist mainly of concrete, ceramic bricks and limestone wall blocks. United Nations reported that the demolition of buildings resulted from military and terrorist operations in Al Anbar, Kirkuk, Tikrit, Beiji, Diyal and Baghdad: 80,000 to 100,000 industrial and residential buildings were completely destroyed (Fig. 1). Meanwhile, the country’s natural resources were severely depleted. Thus, the research gaps were related to the fact that concrete components, both binder and aggregate, have limited use and no solid conclusions were drawn. Meanwhile, concrete waste is closest in composition to newly synthesized concrete. The objective of the article is to conduct a performance investigation of demolition wastes-based concrete composite, including the physical and mechanical properties, produced by the use of fragments of destroyed buildings and structures.



Figure 1. Destroyed buildings.

1.1. Research significance

Driven by these facts, this paper scrutinizes the potential of fine-dispersed mineral additives (concrete waste) as a greener supplemental cementing binder (GSCB) and fine aggregate for lightweight and heavyweight concretes. This paper aims to study the effect of the structural patterns of concrete structures wastes on the microstructure of greener concrete composites. To achieve this goal, the following tasks were solved:

- study of the possibility of controlling the processes of microstructure formation in the synthesis of green concrete prepared based on concrete waste;
- develop rational compositions of green concrete using fine-dispersed mineral additives (concrete waste) as a greener supplemental cementing binder (GSCB) and fine aggregate;
- research the properties of modified cement systems for both heavyweight and lightweight concretes.

2. Materials and methods

2.1. Materials

Ordinary Portland cement (OPC) CEM I 42.5 N (Belgorod cement, Russia) was used as a binder. The chemical and mineralogical compositions, as well as the main technical characteristics are given in Tables 1 and 2. The specific surface area of Portland cement was 300–350 m²/kg. The following raw materials were used as natural aggregates: sand of the Kursk deposit (Russia), granite crushed stone of the Erkilya deposit (Russia), and expanded clay fraction of 10–20 mm of the Aleksinsky plant (Russia). Characteristics of sand, gravel and expanded clay are presented in Tables 3-5.

Table 1. Chemical and mineralogical composition of the Portland cement CEM I 42.5 N.

Chemical composition (%)							Mineralogical composition (%)			
CaO	SiO ₂	Al ₂ O ₃	Fe ₂ O ₃	MgO	SO ₃	Alkalis	C ₃ S	C ₂ S	C ₃ A	C ₄ AF
65.73	22.19	4.37	4.30	0.67	0.18	0.70	60.3	16.8	6.9	13.3

Table 2. Physicomechanical properties of the CEM I 42.5 N.

Setting time, h:min		Flexural strength, MPa		Compressive strength, MPa	
start	end	3 d	28 d	3 d	28 d
2:30	3:35	5.8	8.1	33.6	46.6

Table 3. Characteristics of the sand used.

Characteristics	Value
Bulk density, kg/m ³	1400
Fineness modulus	1.8
Content of dusty, clay and silt particles, % wt.	0.7
Specific gravity, kg/m ³	2500
Los Angeles abrasion value	3.64
Absorption capacity, %	9.91
Loss on ignition, % wt.	< 1
Sieve 0.9 mm residue, % wt.	< 1
Sieve 0.5 mm residue, % wt.	> 92

Table 4. Characteristics of gravel used.

Property	Characteristics	Value
	Specific gravity, kg/m ³	2600
	Porosity, % vol.	4.1
Physicomechanical	Compressive strength, MPa:	
	dry	168
	wet	156
	Los Angeles abrasion value	5.50
	Absorption capacity, %	16.5
Mineralogical	Microcline, % wt.	45–60
	Plagioclase, % wt.	15–20
	Quartz, % wt.	25–35
	Biotite, % wt.	2–5

Table 5. Characteristics of expanded clay.

Compressive strength, MPa	Freeze-thaw resistance, cycles	Water absorption, %	Density, kg/m ³
0.3–6	15	10–25	150–800

Table 6 lists the composition of the construction and demolition waste of Iraqi buildings and structures. As it can be seen from Table 6, 99.88% of the waste from construction and demolition because of hostilities in the cities of Iraq consists of rubble and cement concrete. The appearance of the crushed demolition waste is shown in Fig. 2.

Table 6. Composition of demolition waste.

Material	OPC	Crushed stone	Fiber	Wood	Metal	Plastic	Gypsum
Content, %	39.48	60.4	0.04	0.02	0.04	0.01	0.01

**Figure 2. View of demolition waste.**

Visual inspection of crushed stone from concrete waste shows that during crushing by a jaw crusher, intermittent interlayers of mortar component firmly adhered to the rock remain on its grains. Sections of crushed stone surface that do not have such a layer of cement-sand mortar contain thin films of hydrated phases. There is every reason to believe that this will provide increased adhesion of the cement matrix of concrete. The basis for this assumption is the fact that the adhesion of cement paste to various materials grows in a row: quartz < granite < limestone < clinker. These assumptions are based on our previous findings [22–27].

2.2. Methods

Demolition waste was crushed in a jaw crusher to obtain fractions of 2.5–5; 1.25–2.5; 0.63–1.25; 0.315–0.63; 0.16–0.315 and 0–0.16 mm. This raw material was used as a fine aggregate in further studies. To study the demolition waste as supplementary cementitious materials, they were further milled by a VM-20 ball mill (Russia) to sizes comparable to those of Portland cement.

The features of microstructure and compositions of the raw materials and products used as a result of the synthesis of Iraqi materials were studied using theoretical and empirical methods. The morphologies of the raw materials and the small concrete specimens of 15 mm×15 mm×4 mm were examined by scanning electron microscope (MIRA3 TESCAN, Brno, Czech) operated at the accelerating voltage of 8.0 kV. Differential-thermal analysis (DTA) and thermogravimetry (TG) were carried out using a Shimadzu DTG-60H thermogravimetric analyzer (Japan). The mix is poured into a cone 30 cm high, then after removing the cone, the amount of slump is measured. The average density of concrete was determined on specimens-cubes of 100×100×100 mm, dried to constant weight at 105 °C. The compressive strength of concrete specimens (six specimens for each composition) was measured for 10×10×10 cm specimens using a Shimadzu (Kyoto, Japan) tester with a capacity of 200 kN, according to the EN 12390-3. In the experimental work, the methodological foundations of the system-structural approach in building materials science “composition – technology – microstructure – properties” were used.

The chemical composition of the raw materials and the small concrete specimens was analyzed using an ARL 9900 WorkStation X-ray spectrometer (Thermo Fisher Scientific, Waltham, USA) with an integrated diffraction system. X-ray diffraction diagnostics of mineral crystalline phases (qualitative XRD) was carried out using the PDF-2 diffraction database. To determine the quantitative ratios of the crystalline phases, Rietveld full-profile quantitative XRD analysis was used. The calculations were carried out using the DDM v.1.95e program: its Derivative Difference Minimization algorithm makes it possible not to refine the approximation parameters of the complex structured background of the diffraction spectrum. Inorganic Crystal Structure Database (ICSD) data were used as structural models of mineral components for full-profile quantitative XRD analysis.

The error of all the results obtained does not exceed 5 %.

3. Results and Discussion

3.1. SEM images and XRD patterns of various fractions of demolition wastes

As a result of grinding the demolition waste, screenings of fractions of 2.5–5; 1.25–2.5; 0.63–1.25; 0.315–0.63; 0.16–0.315 and 0–0.16 mm were obtained. SEM images of the obtained screenings are shown in Fig. 3. The mineral composition of various fractions of demolition wastes is given in Table 7.

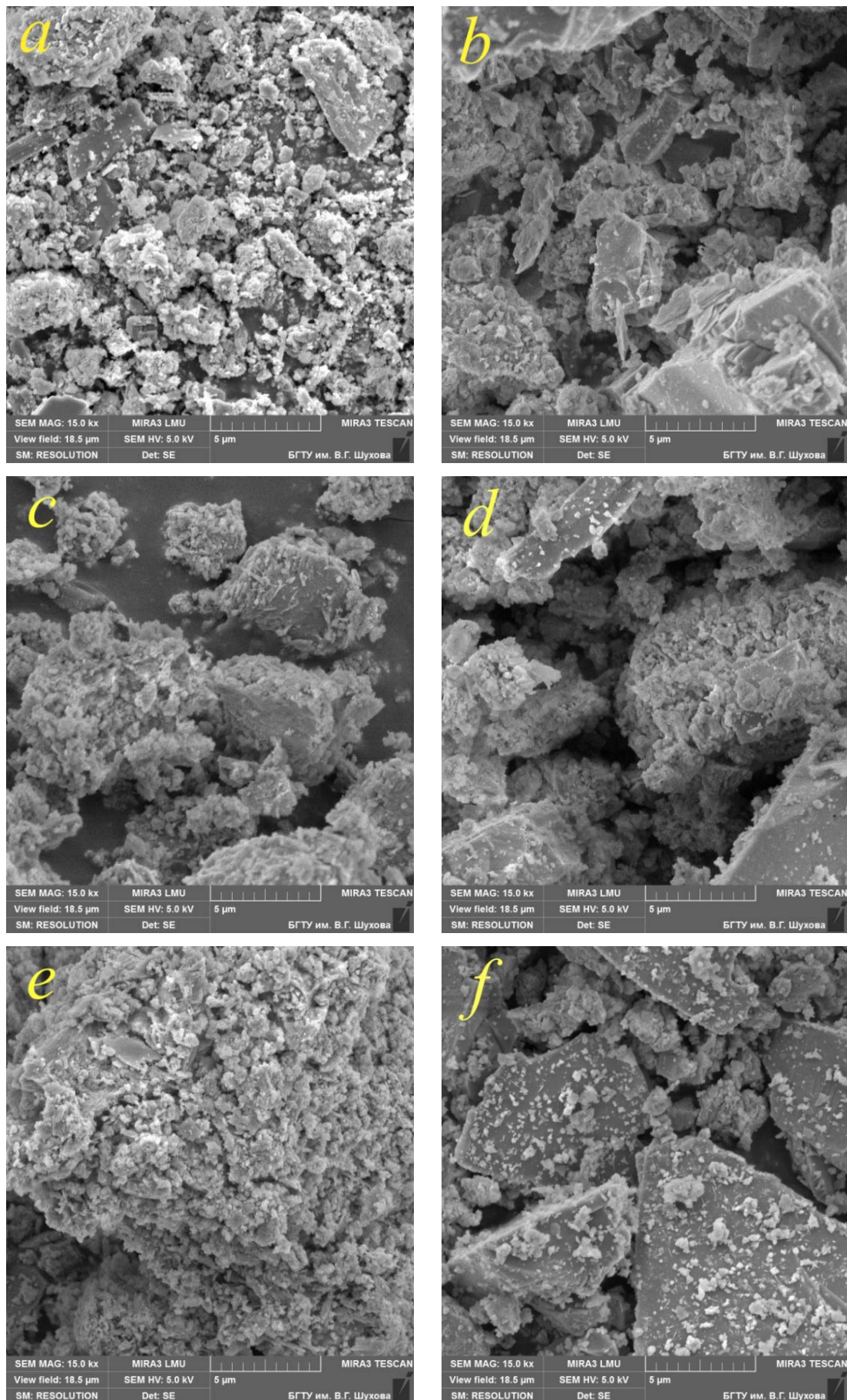


Figure 3. SEM images of demolition waste fractions: 0–0.16 (a); 0.16–0.315 (b); 0.315–0.63 (c); 0.63–1.25 (d); 1.25–2.5 (e) and 2.5–5 (f).

Table 7. The mineral composition of various fractions of demolition wastes (XRD patterns).

Particle sizes, mm	Mineral composition, %					
	SiO ₂	Ca(OH) ₂	CaCO ₃	CSH	C ₃ S	C ₂ S
0.00–0.16	48.4	11.5	10.0	5.8	12.0	12.3
0.16–0.315	55.2	7.4	11.0	4.4	11.0	11.0
0.315–0.63	56.4	11.0	3.9	12.0	6.7	10.0
0.63–1.25	65.1	12.0	6.0	5.9	5.0	6.0
1.25–2.5	64.4	10.5	6.9	3.0	7.6	7.6
2.5–5	62.8	11.0	0	6.0	9.2	11.0

SEM images of various fractions of concrete waste show a significant amount of sharp particles, and this amount increases with decreasing size from 2.5–5 to 0–0.16 mm. This form of aggregate is the most rational, as it provides good adhesion between the aggregate and the cement matrix, thereby strengthening the interfacial transition zone.

The comminuted form of particles, as well as a high content of silica and clinker minerals in them, will contribute to their high activity, which is confirmed by the studies of other authors [2, 4, 6–10]. The crushed particle shape contributes to a large specific surface area, which reacts with the hydration products of the cement clinker. At the same time, the high content of silica and previously unhydrated clinker minerals contributes to the high reactivity of the particles of finely ground concrete waste.

3.2. Compressive strength

The tests were carried out to replace natural sand with artificial crushed sand in expanded clay concrete class C8/10 and heavyweight concrete class C16/20. The tests were carried out with partial and complete replacement of sand with demolition waste with a particle size of 1.8 mm. In this case, concrete mixtures were prepared on natural sand (control composition) and on artificial sand with partial replacement (30 % range) until the replacement was complete (Table 8–9). As the research results showed, the compressive strength of expanded clay concrete with the use of demolition waste increases, which is explained by an increase in adhesion with cement paste.

Table 8. Compositions and properties of expanded clay concretes.

Mix ID	Materials content, kg/m ³					Slump, cm	Average density, kg/m ³	Compress. strength, MPa
	Portland cement	Natural sand	Expanded clay	Demolition waste	Water			
LW-1	225	800	410	–	270	3–4	1670	16
LW-2	225	560	410	240	255	4–5	1600	17.2
LW-3	225	400	410	400	226	3–4	1625	19.8
LW-4	225	240	410	560	243	3–4	1562	17.9
LW-5	225	–	410	800	246	3–4	1564	17.7

Table 9. Compositions and properties of heavyweight concretes.

Mix ID	Materials content, kg/m ³				Water	Slump, cm	Average density, kg/m ³	Compress. strength, MPa
	Portland cement	Natural sand	Crushed stone	Demolition waste				
HW-1	475	600	1350	–	237	4	2360	27
HW-2	475	450	1350	150	237	4	2340	26.9
HW-3	475	300	1350	300	237	4	2365	26.5
HW-4	475	150	1350	450	237	4	2344	27.2
HW-5	475	–	1350	600	237	4	2350	26

Tests to replace natural sand with artificial crushed sand in heavyweight concrete also showed that the strength of concrete does not decrease, but even exceeds the control composition. This indicates that the artificial crushed sand obtained as a result of the classification of screening crushed fragments of destroyed buildings and structures can be used as fine aggregate in concrete. It was found that the obtained results of compressive strength for lightweight concrete exceeded the results of other authors by 12–31 %, and for heavy concrete, by 15–36 % [4, 9–10, 19].

3.3. Microstructure of composite

Fig. 4 shows the contact zone between the cement paste and the aggregate from the waste of destroyed buildings. It is seen that there is a dense intergrowth and germination of concrete waste with the surface of the cement matrix and they look like a single whole. A dense contact zone is ensured by the fact that in the initial period, the aggregate absorbs water from the concrete mix. After the formation of a capillary-porous microstructure, the water from the pores of the aggregate is sucked out by clinker minerals and new growths, thereby increasing the degree of cement hydration without negatively affecting the workability of the concrete mix. If the concrete waste is not large and has not been hydrothermally treated, consequently, it may exhibit secondary (residual) cementitious properties due to the presence of incompletely hydrated particles of belite, as well as portlandite, the amount of which reaches 15–25 % in fresh concrete.

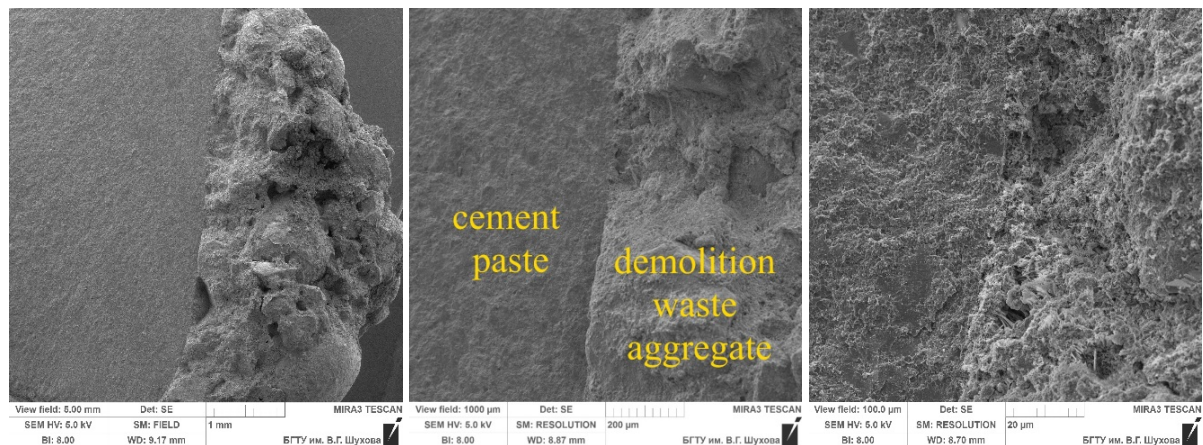


Figure 4. Contact zone between the cement paste and the aggregate from the waste of destroyed buildings.

Consequently, concretes with active fillers and aggregates from concrete wastes are characterized by its increased adhesion to the cement matrix, which provides final products with improved deformability, crack resistance, resistance to dynamic loads, and other properties. These findings, based on the law of affinity of microstructures, were proved by us earlier [22–23].

3.4. Compressive strength for concrete with milled demolition waste

Fig. 5 shows the dependences of the compressive strength on the amount of Portland cement replaced by milled demolition waste. At the same time, in accordance with the law of affinity of microstructures, concrete waste was milled until it reached a specific surface area of Portland cement (300–350 m²/kg). This is confirmed by similar studies by Lesovik et al. [23] carried out for binder composites and aggregates of a different genesis.

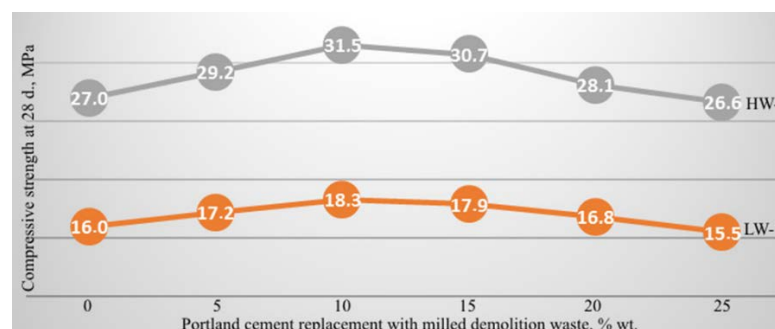


Figure 5. Dependences of the compressive strength on the amount of Portland cement replaced by milled demolition waste.

3.5. SEM images, XRD patterns and DTGA analysis

The addition of chemical and mineral additives to Portland cement leads to a change in the mechanism and rate of reactions of the interaction between clinker cement minerals and water. Mineral additives can interact with new growths of cement stone with the subsequent formation of new phases, which have a different effect on the properties of hardened cement stone. In this regard, the effect of concrete waste on the processes of cement paste hydration was tested using the methods of DTA and XRD.

The DTA pattern of hydrated Portland cement with the addition of milled concrete waste (Fig. 6) has an intense multi-stage endothermic effect with a maximum at a temperature of 101.8 °C, which is explained by the intensive removal of water. The endothermic effect with a maximum at a temperature of 447.6 °C is associated with the dehydroxylation of portlandite. The presence of such a pronounced endo effect of portlandite indicates that the active mineral additive – in this case, concrete waste – did not absorb and bind all calcium hydroxide, so the liquid phase of concrete is saturated with this hydroxide. In a medium of saturated lime solution, it is known that highly basic C-S-H (II) calcium hydrosilicates are stable, and not low-basic C-S-H (I) hydrosilicates. It follows from this that the most important binding component of Portland cement hardening products with the addition of concrete waste are the mentioned fibrous calcium hydrosilicates of the C-S-H (II) group.

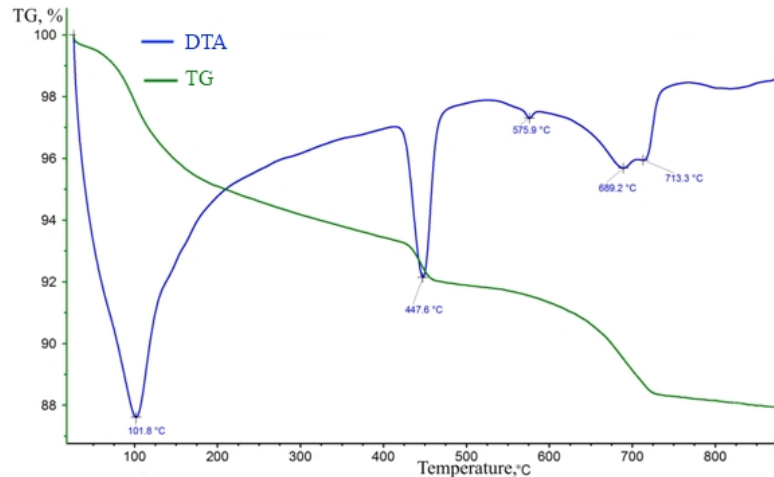


Figure 6. DTGA pattern of hydrated Portland cement with the addition of milled concrete waste.

Weak endo effects at 689.2 °C and 713.3 °C are mainly associated with decarbonization of weakly crystallized metastable forms of calcium carbonate CaCO_3 , which were formed due to partial carbonization of calcium hydroxide. XRD pattern (Fig. 7) fully confirms the results of DTA data. The X-ray diffraction pattern of the same sample of hydrated cement with the addition of milled concrete waste has some peaks of the remains of unhydrated clinker minerals ($d = 4.343$; 4.270 ; 3.357 and 3.198 Å). A small sharp peak with an interplanar distance of 2.637 Å characterizes the presence of portlandite. The same is confirmed by the SEM image of developed concrete at the age of 28 days (Fig. 8). A dense microstructure is noted, provided by both Portland cement products and hydration, and, in part, by hydration products of previously unreacted clinker minerals present in the concrete waste and activated during its milling.

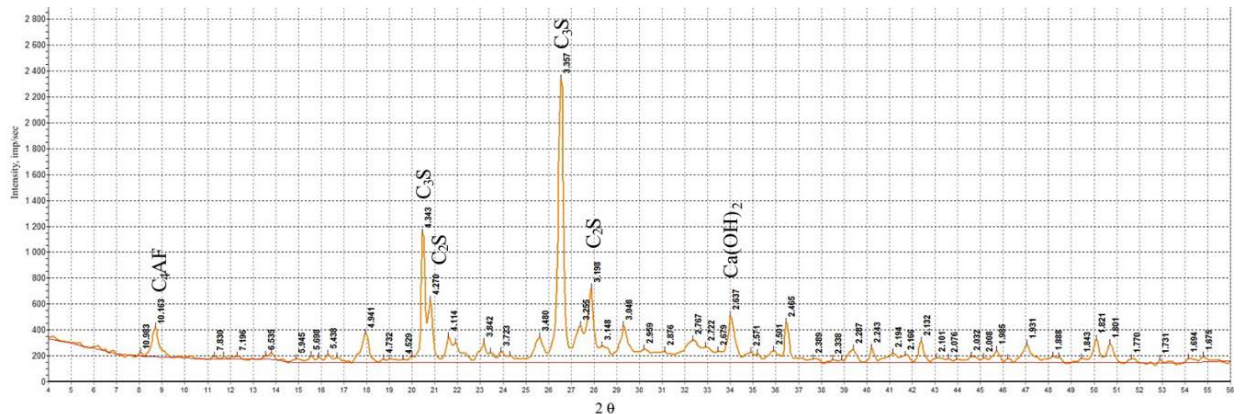


Figure 7. XRD pattern of hydrated Portland cement with the addition of milled concrete waste.

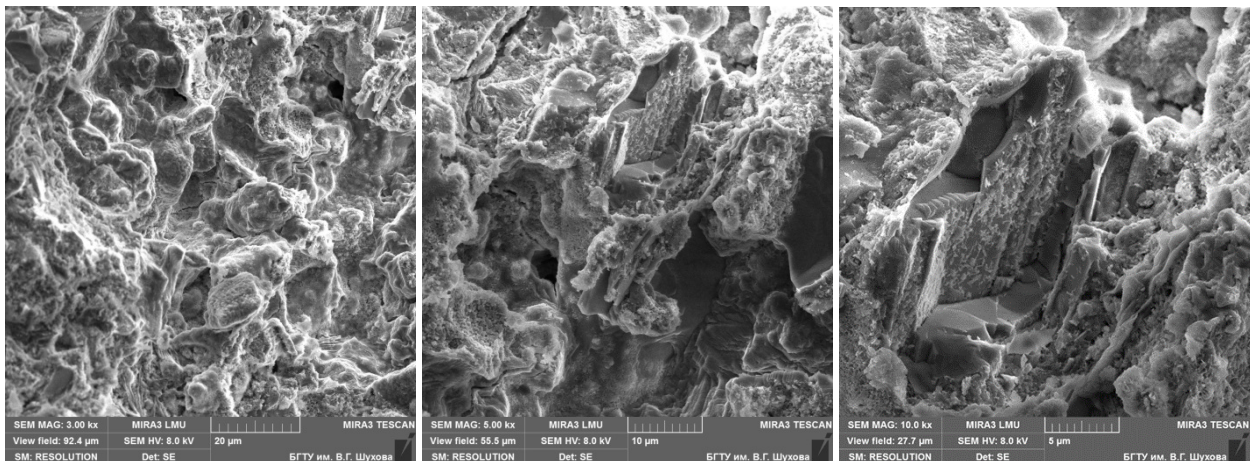


Figure 8. SEM image of developed concrete at the age of 28 days.

4. Conclusion

This article presents the possibility of recycling construction waste to solve two problems: waste disposal and improvement of the physicomaterial properties of concrete by adding recycled waste as a filler or aggregates. The sharp form of particles, as well as the high content of silica and clinker minerals in them, contribute to their high activity. Based on the results obtained, we can draw the following conclusions.

1. The use of demolition waste of buildings and structures as a fine aggregate gives similar results in the mechanical characteristics of heavyweight and lightweight concrete, as when using natural sand. This is due to the dense growth and sprouting of concrete waste to the surface of the cement matrix, as a result of which they look like its integral part.

2. In case of replacing up to 20 % of Portland cement, the demolition waste as a supplementary cementitious material allows obtaining better compressive strength of both heavy and light concrete. This is due to compaction of the microstructure by hydration products of previously unreacted clinker minerals present in concrete waste and activated by milling it. This allows the interfacial transition zone between the cement matrix and the aggregate to be compacted due to the formation of additional hydration products in a constant volume.

5. Prospects for further development of the topic

Further research can be aimed at creating completely cementless binders, using only finely ground concrete waste as a binder.

6. Acknowledgements

This work was financially supported by RFBR grant No. 18-29-24113 "Transdisciplinarity – as a theoretical basis for the rational use of technogenic raw materials for energy-efficient technologies for the production of new generation building composites".

References

1. Abirami, T., Loganaganandan, M., Murali G., Fediuk, R., Vickhram Sreekrishna, R., Vignesh, T., Janupriya, G., Karthikeyan, K. Experimental research on impact response of novel steel fibrous concretes under falling mass impact. *Construction and Building Materials*. 2019. No. 222. Pp. 447–457.
2. Xu, Y. In-situ shear strength of compacted demolition waste. *Powder Technology*. 2019. No. 352. Pp. 72–78.
3. Fediuk, R.S., Lesovik, V.S., Svintsov, A.P., Gladkova, N.A., Timokhin, R.A. et al. Self-compacting concrete using pretreated rice husk ash. *Magazine of Civil Engineering*. 2018. 79(3). Pp. 66–76.
4. Bassani, M., Riviera, P.P., Tefa, L. Short-Term and Long-Term Effects of Cement Kiln Dust Stabilization of Construction and Demolition Waste. *Journal of Materials in Civil Engineering*. 2017. No. 29(5).
5. Kashani, A., Ngo, T.D., Nguyen, T.N., Hajimohammadi, A., Sinaie, S., Mendis, P. The effects of surfactants on properties of lightweight concrete foam. *Magazine of concrete research*. 2020. 72(4), Pp. 163–172. <https://doi.org/10.1680/jmacr.18.00242>
6. Pacheco, J., de Brito, J., Chastre, C., Evangelista, L. Experimental investigation on the variability of the main mechanical properties of recycled aggregate concrete, *Construction and Building Materials*. 2019. No. 201. Pp. 110–120.
7. Xiao, J., Li, W., Fan, Y., Huang, X. An overview of study on recycled aggregate concrete in China (1996–2011). *Construction and Building Materials*. 2012. No. 31. Pp. 364–383.

8. Sormunen, P., Kärki, T. Recycled construction and demolition waste as a possible source of materials for composite manufacturing. *Journal of Building Engineering*. 2019. No. 24. Pp. 100742.
9. Arisha, A.M., Gabr, A.R., El-Badawy, S.M., Shwally, S.A. Performance Evaluation of Construction and Demolition Waste Materials for Pavement Construction in Egypt. *Journal of Materials in Civil Engineering*. 2018. No. 30(2).
10. Xu, Y. Fractal dimension of demolition waste fragmentation and its implication of compactness. *Powder Technology*. 2018. No. 39. Pp. 922–929.
11. Kharrufa, S. Reduction of building waste in Baghdad Iraq. *Building and Environment*. 2007. No. 42(5). Pp. 2053–2061.
12. Qiao, J., Zhang, L., Zhao, J., Zhou, Z. Test Study on Impermeability of Recycled Concrete. *IOP Conf. Series: Mater. Science and Eng.* 2018. No. 423. 012010.
13. Slavcheva, G.S., Artamonova, O.V. Rheological Behavior and Mix Design for 3D Printable Cement Paste. *Key Engineering Materials*. 2019. No. 799. Pp. 282–287. DOI: 10.4028/www.scientific.net/KEM.799.282
14. Xu, L., Deng, F., Chi, Y. Nano-mechanical behavior of the interfacial transition zone between steel-polypropylene fiber and cement paste, *Construction and Building Materials*. 2017. No. 145. Pp. 619–638.
15. Klyuev, S.V., Klyuev, A.V., Vatin, N.I. Fiber concrete for the construction industry. *Magazine of Civil Engineering*. 2018. 84(8). Pp. 41–47. doi: 10.18720/MCE.84.4
16. Sakai, Y. Relationship between water permeability and pore structure of cementitious materials. *Magazine of Concrete Research*. 2019. <https://doi.org/10.1680/jmacr.19.00135>
17. Sharonova, O.M., Yumashev, V.V., Solovyov, L.A., Anshits, A.G. The fine high-calcium fly ash as the basis of composite cementing material. *Magazine of Civil Engineering*. 2019. 91(7). Pp. 60–72. DOI: 10.18720/MCE.91.6
18. Shafaghat, J., Allahverdi, A. Using PC clinker as aggregate-enhancing concrete properties by improving ITZ microstructure. *Magazine of Concrete Research*. 2020. 72(4). Pp. 173–181. <https://doi.org/10.1680/jmacr.18.00134>
19. Wu, H., Zuo, J., Yuan, H., Zillante, G., Wang, J. A review of performance assessment methods for construction and demolition waste management. *Resources, Conservation and Recycling*. 2019. No. 150. 104407.
20. Wu, H., Zuo, J., Zillante, G., Wang, J., Yuan, H. Status quo and future directions of construction and demolition waste research: a critical review. *Journal of Cleaner Production*. 2019. No. 240. 118163.
21. Klyuev, S.V., Khezhev, T.A. Pukhareenko, Yu.V., Klyuev, A.V. Fiber concrete on the basis of composite binder and technogenic raw materials. *Materials Science Forum*. 2018. No. 931. Pp. 603–607.
22. Fediuk, R., Smoliakov, A., Muraviov, A. Mechanical properties of fiber-reinforced concrete using composite binders. *Advances in Materials Science and Engineering*. 2017, 2316347.
23. Lesovik, V.S., Volodchenko, A.A., Glagolev, E.S., Chernysheva, N.V., Lashina, I.V., Fediuk, R.S. Theoretical backgrounds of nonered materials production based on new raw materials. *IOP Conference Series: Materials Science and Engineering*. 2018. No. 327(4). 042064.
24. Fediuk, R. Reducing permeability of fiber concrete using composite binders. *Special Topics and Reviews in Porous Media*. 2018. 9(1). v-vi.
25. Fediuk, R., Pak, A., Kuzmin, D. Fine-Grained Concrete of Composite Binder. *IOP Conference Series: Materials Science and Engineering*. 2017. 262(1). 012025. <https://doi.org/10.1088/1757-899X/262/1/012025>
26. Fediuk, R., Smoliakov, A., Stoyushko, N. Increase in composite binder activity. *IOP Conference Series: Materials Science and Engineering*. 2016. 156(1). 012042.
27. Fediuk, R., Lesovik, V., Mochalov, A., Otsokov, K., Lashina, I., Timokhin, R. Composite binders for concrete of protective structures. *Magazine of Civil Engineering*. 2018. No. 6. Pp. 208–218.
28. Elistratkin, M.Yu., Kozhukhova, M.I. Analysis of the factors of increasing the strength of the non-autoclave aerated concrete. *Construction Materials and Products*. 2018. No. 1(1). Pp. 59–68.
29. Klyuev, S.V., Khezhev, T.A., Pukhareenko, Yu.V., Klyuev, A.V. The fiber-reinforced concrete constructions experimental research. *Materials Science Forum*. 2018. No. 931. Pp. 598–602.
30. Lesovik, V.S., Glagolev, E.S., Popov, D.Y. Textile-reinforced concrete using composite binder based on new types of mineral raw materials. *IOP Conference Series: Materials Science and Engineering*. 2018. No. 327. 032033.
31. Barabanshchikov, Yu.G., Belyaeva, S.V., Arkhipov, I.E., Antonova, M.V., Shkol'nikova, A.A., Lebedeva, K.S. Influence of superplasticizers on the concrete mix properties. *Magazine of Civil Engineering*. 2017. No. 74(6). Pp. 140–146. doi: 10.18720/MCE.74.11
32. Lukutsova, N., Pashayan, A., Khomyakova, E., Suleymanova, L., Kleymenicheva, Y. The use of additives based on industrial wastes for concrete, *International Journal of Applied Engineering Research*. 2016. 11(11). Pp. 7566–7570.

Contacts:

Valeriy Lesovik, naukavs@mail.ru

Anees Alani Ahmed, civileng85@yahoo.com

Roman Fediuk, roman44@yandex.ru

Bogdan Kozlenko, kozlenko@yandex.ru

YH Mugahed Amran, mugahed_amran@hotmail.com

Arbi Alaskhanov, alaskhanov.arbi@mail.ru

Mohammad Ali Asaad, mohamadalsaad@gmail.com

Gunasekaran Murali, murali_220984@yahoo.co.in

Valery Uvarov, asibstu@mail.ru



DOI: 10.34910/MCE.106.9

Analytical approach to stress-strain analysis of right and oblique helicoid structures

E.M. Tupikova*, **M.I. Rynkovskaya**

Peoples' friendship university of Russia, Moscow, Russia

*E-mail: emelian-off@yandex.ru

Keywords: helicoid structure, right helicoid, oblique helicoid, numeric-analytical solution, stress-strain analysis

Abstract. Shell structures with a mid surface of helicoid shape find application in many technical fields, mostly in civil and mechanical engineering. There is a variety of helicoid shells, but the most well-known and used are two types of ruled helicoids: right and oblique. The article is devoted to analytical and numeric-analytical methodologies for shallow right and oblique helicoids. The general approach is based on Kirchhoff–Love linear theory of thin elastic shells. Analytical results can be used for preliminary design and calculations aimed at the understanding of construction physics and regularities of stress-strain state behavior. Two methodologies of stress-strain analysis are presented: the analytical method for shallow right helicoid, and the numeric-analytic method for oblique helicoid (including any special or degenerated case). The numerical results are verified. The results and approach outlined could be of interest to designers and scientists, who want to understand the generalities of thin ruled helicoid shell behavior.

1. Introduction

Shells of helicoidal surface form are permanently in focus among scientists because they have the potential to be applied in the construction [1, 2], architecture [3] and mechanical engineering [4, 5]. The Archimedes screw turbines become popular because of global energy-saving trend [6, 7]. The entrance vehicle and wheelchair ramps are in common use in most objects of urban infrastructure, so the design of such objects is important today. Steel and reinforced concrete helicoid shells of the three most common types – right, oblique and developable, are usually used while designing the objects of different purpose, like parking spaces, transport interchanges, railway junctions, in the most cases the shells are shallow and have small lead of helix. In machine construction, conversely, non-shallow shells of high helix are used. Despite these structures are widely used in very diverse fields [8–12], not so many papers are devoted to mechanics of helicoidal shells and particularly to their stress-strain state [13–17], so the topic seems to be not developed enough. This job is devoted to the design of shallow shells of oblique and right type for structural purposes.

The present study concerns thin elastic shells, which can be calculated in Kirchhoff-Love theoretical model [18]. The models of shells and plates mechanical behaviour are constantly improving, but the Kirchhoff-Love hypothesis remains the basis of the linear elastic shell theory. Such objects have a range of advantages in technical-and-economical indexes, they are light in weight, the minimal thickness of these shells is limited by technological characteristics of erection, like pump-crete machine application. While implementation of special technologies, like concrete pump placing, these limitations can be eliminated.

The research of thin elastic shells has been conducted intensively since the 60-s of 20-s century, the various models and algorithms have been developed [19–22]. All of them can be divided into three main groups: analytical, numeric and numeric analytical methodologies. The right and developable helicoid analyses are more developed comparative to the oblique. Obviously the first two have more simple

Tupikova, E.M., Rynkovskaya, M.I. Analytical approach to stress-strain analysis of right and oblique helicoid structures. Magazine of Civil Engineering. 2021. 106(6). Article No. 10609. DOI: 10.34910/MCE.106.9

© Tupikova, E.M., Rynkovskaya, M.I., 2021. Published by Peter the Great St.Petersburg Polytechnic University.



This work is licensed under a [CC BY-NC 4.0](https://creativecommons.org/licenses/by-nc/4.0/)

expressions of surface equations, and therefore the quadratic forms expressions are simple too. The oblique helicoid equations are defined in general case in non-conjugate non-orthogonal coordinate system, so the expressions are cumbersome.

Among the variety of helicoidal surfaces [23] the most popular and handy are right [24], oblique [25] and developable [26–28] helicoids. At the stage of design study, for comparison and verification of results it is very good to have a standard of reference, some simple example of precise analytical solution that can be used like benchmark before creating detailed complex model. Such an example can be got by analytical approach using modern computer technologies, which give us a powerful software and hardware means of analysis. The analytical methods were popular while designing real objects about 25–30 years ago, and now they are replaced by finite element method. But they are still necessary because of the range of advantages, main of which is obviousness of physical meaning. Due to improvement of both hardware and algorithms, the most of difficulties of computation are resolvable now. If the analytical solution can't be obtained, the equations can be solved by numeric methods. In this case the methodology is called numeric-and-analytic. The accuracy of such methodology is formally lower than the accuracy of analytical methodology and is defined by the numeric method applied, but the results are also valuable [14, 18]. In the present paper analytical and numeric-analytical methods for shallow helicoidal shells are considered for right and oblique helicoids.

2. Methods

2.1. General Methodology

General form of helicoid surface equation can be conceived in vector form:

$$\bar{r}(u, v) = u \cdot \cos(v) \cdot \bar{i} + u \cdot \sin(v) \cdot \bar{j} + (f(u) + c \cdot v) \cdot \bar{k}, \quad (1)$$

Where c is a parameter of helix pitch, if $c = 0$ helicoid degenerates into surface of revolution.

If Oz axis is axis of rotation, then $z = f(u)$ is a generator plane curve equation.

The basic terms of surface theory are coefficients or first quadratic form A, B, F , which characterize the inner geometry of the surface in any point vicinity, and coefficients of second quadratic forms M, N , which characterize the outer geometry of the surface in any point vicinity [30].

Angle between coordinate lines

$$\chi, \cos \chi = \frac{F}{AB}, \quad \operatorname{tg} \chi = \frac{\sqrt{A^2 B^2 - F^2}}{F}, \quad (2)$$

R_u, R_v, R_{uv} are radii of curvature of normal sections along coordinate lines u and v ,

$$\frac{1}{R_v'} = -\frac{N}{B^2}, \quad \frac{1}{R_u'} = -\frac{L}{A^2}, \quad \frac{1}{R_{uv}'} = \frac{M}{AB}, \quad (3)$$

$\bar{u} = u(u, v)$ is a vector of elastic displacement of a point of the middle surface which can be expanded in axis of basic trihedral: $\bar{u} = u_u \frac{\bar{r}_u}{A} + u_v \frac{\bar{r}_v}{B} + u_z \bar{n}$, where u_u, u_v, u_z are displacement components, \bar{n} is normal unit vector.

The Christoffel's symbols of surface coordinates can be expressed in terms of A, B, χ :

$$\Gamma_{11}^1 = \frac{AB^2 \frac{\partial A}{\partial u} + BA^2 \frac{\partial A}{\partial v} - AB \cos \chi \frac{\partial}{\partial u} (AB \cos \chi)}{A^2 B^2 \sin^2 \chi}, \quad (4)$$

$$\Gamma_{11}^2 = \frac{-A^2 B \cos \chi \frac{\partial A}{\partial u} + A^2 \frac{\partial}{\partial u} (AB \cos \chi) - A^3 \frac{\partial A}{\partial v}}{A^2 B^2 \sin^2 \chi},$$

$$\Gamma_{12}^1 = \frac{AB^2 \frac{\partial A}{\partial v} - AB^2 \cos \chi \frac{\partial B}{\partial u}}{A^2 B^2 \sin^2 \chi}, \quad \Gamma_{12}^2 = \frac{A^2 B \frac{\partial B}{\partial u} - A^2 B \cos \chi \frac{\partial B}{\partial v}}{A^2 B^2 \sin^2 \chi},$$

$$\Gamma_{22}^1 = \frac{-AB^2 \cos \chi \frac{\partial B}{\partial v} + B^2 \frac{\partial}{\partial v} (AB \cos \chi) - A^3 \frac{\partial B}{\partial u}}{A^2 B^2 \sin^2 \chi},$$

$$\Gamma_{22}^2 = \frac{A^2 B \cos \chi \frac{\partial A}{\partial v} + AB^2 \cos \chi \frac{\partial A}{\partial v} - AB \cos \chi \frac{\partial}{\partial v} (AB \cos \chi)}{A^2 B^2 \sin^2 \chi}.$$

While designing shell structure the coordinate system choice is crucial. Among the huge variety of any curvilinear coordinates u, v there are some coordinate lines of the important properties, these are: the network of conjugate lines, the network of orthogonal lines, the network of principal curvatures. Any surface can be attributed to curvature lines, which are defined uniquely.

The equations of shell theory can be established in the simplest form if the network of principal curvature is set as coordinate lines of the shell midsurface. The problem is to find analytically curvatures of the surface given. There are some surfaces, which can only be set in curvilinear non-orthogonal non-conjugate coordinate systems.

The classical Kirchhoff-Love thin elastic shell theory is based on the assumptions, the similar to the beam theory. Three-dimensional problem of the theory of elasticity can be reduced to two-dimensional problem because of these assumptions. Stress-strain state of the shell can be presented by functions of two variables, which are coordinates of point on shell midsurface. In this study the non-linear effects are not considered, components of elastic displacement vector and their derivatives are supposed to be so small that the members nonlinear with respect to them, should be neglected.

A.L. Goldenveizer suggested a full system of equations of the thin elastic shell theory, this theory is recognized as a classical [31]. The theory contains several groups of equations: the equilibrium equations, the stress-strain relations, the geometrical relations and continuity equations, (which are not of necessity in the current case). The positive directions of the following inner forces and moments are presented on Fig. 1.

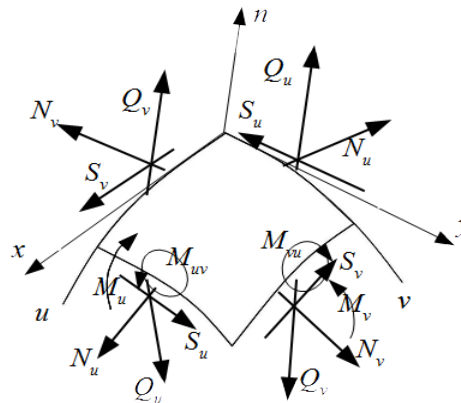


Figure 1. The axis, inner forces and moments.

Equilibrium equations in non-conjugate non-orthogonal (most general type) coordinate system u, v :

$$\frac{1}{\sin \chi} \frac{\partial}{\partial u} (B(N_u + \cos \chi S_u)) - \frac{B^2}{A} \Gamma_{11}^2 \sin \chi S_u - \frac{1}{\sin \chi} \frac{\partial}{\partial v} (A(S_v - \cos \chi N_v)) -$$

$$-B\Gamma_{12}^2 \sin \chi N_v - \sin \frac{AB}{\chi} \left(\frac{Q_u}{R_u} - \frac{Q_v}{R_{uv}} \right) + AB(X + \cos \chi Y) = 0 \quad (5)$$

$$\begin{aligned}
& \frac{1}{\sin \chi} \frac{\partial}{\partial u} \left(B(S_u + \cos \chi N_u) \right) - A \Gamma_{12}^1 \sin \chi N_u + \frac{1}{\sin \chi} \frac{\partial}{\partial v} \left(A(N_v - \cos \chi S_v) \right) + \\
& + \frac{A^2}{B} \Gamma_{22}^1 \sin \chi S_v - \frac{AB}{\sin \chi} \left(\frac{Q_v}{R_v} - \frac{Q_u}{R_{uv}} \right) + AB(Y + \cos \chi X) = 0, \\
& AB \left(\frac{N_u}{R_u} + \frac{N_v}{R_v} + \frac{S_v - S_u}{R_{uv}} \right) + \frac{\partial}{\partial u} (BQ_u) + \frac{\partial}{\partial v} (AQ_v) + AB \sin \chi Z = 0, \\
& \frac{1}{\sin \chi} \frac{\partial}{\partial u} \left(B(M_{uv} + \cos \chi M_u) \right) - \frac{B^2}{A} \Gamma_{11}^2 \sin \chi M_u - \\
& - \frac{1}{\sin \chi} \frac{\partial}{\partial v} \left(A(M_v - \cos \chi M_{uv}) \right) - B \Gamma_{12}^2 \sin \chi M_{vu} + ABQ_v = 0, \\
& \frac{1}{\sin \chi} \frac{\partial}{\partial u} \left(B(M_u + \cos \chi M_{uv}) \right) - A \Gamma_{12}^1 \sin \chi M_{uv} + \\
& + \frac{1}{\sin \chi} \frac{\partial}{\partial v} \left(A(M_{vu} - \cos \chi M_v) \right) + \frac{A^2}{B} \Gamma_{22}^1 \sin \chi M_v - ABQ_u = 0, \\
& \sin \chi (S_u + S_v) + \frac{M_{uv}}{R_u} + \frac{M_{vu}}{R_v} + \frac{M_v - M_u}{R_{uv}} = 0,
\end{aligned}$$

where

N_u, N_v are axial forces along u, v respectively;

M_u, M_v are bending moments around u, v respectively;

$M_{uv} = M_{vu}$ are twisting moments;

Q_u, Q_v are shear forces along u, v respectively;

S_u, S_v are cutting forces along u, v respectively;

(see Fig. 1)

Strain-displacement relations:

$$\begin{aligned}
\varepsilon_v &= \frac{1}{B} \frac{\partial}{\partial v} (u_v + u_u \cos \chi) - \frac{A \sin \chi^2}{B^2} \Gamma_{22}^1 u_u + \frac{u_z}{R_v}, \\
\varepsilon_u &= \frac{1}{A} \frac{\partial}{\partial u} (u_u + u_v \cos \chi) - \frac{B \sin \chi^2}{A^2} \Gamma_{11}^2 u_v + \frac{u_z}{R_u}, \\
\omega_u &= \frac{\sin \chi}{A} \frac{\partial}{\partial u} u_v - \left(\frac{\sin \chi}{B} \Gamma_{12}^1 + \frac{1}{A} \frac{\partial \chi}{\partial v} \right) u_u + \\
& + \cos \chi \left(\frac{B \sin \chi}{A^2} \Gamma_{11}^2 + \frac{1}{A} \frac{\partial \chi}{\partial u} \right) u_v - \frac{1}{\sin \chi} \left(\frac{1}{R_{uv}} + \frac{\cos \chi}{R_u} \right) u_z,
\end{aligned} \tag{6}$$

$$\omega_v = \frac{\sin \chi}{B} \frac{\partial}{\partial v} u_u - \left(\frac{\sin \chi}{B} \Gamma_{12}^2 + \frac{1}{B} \frac{\partial \chi}{\partial v} \right) u_v +$$

$$+ \cos \chi \left(\frac{A \sin \chi}{B^2} \Gamma_{22}^1 + \frac{1}{B} \frac{\partial \chi}{\partial v} \right) u_u - \frac{1}{\sin \chi} \left(\frac{1}{R_{uv}} + \frac{\cos \chi}{R_v} \right) u_z,$$

$$\varepsilon_{uv} = \omega = \omega_u + \omega_v,$$

$$\gamma_u = \frac{1}{A} \frac{\partial}{\partial u} u_z - \frac{u_u}{R_u} + \frac{u_v}{R_{uv}}, \quad \delta = \frac{1}{2} (\omega_v - \omega_u),$$

$$\kappa_u = -\frac{1}{A} \frac{\partial}{\partial u} \left(\frac{\gamma_u - \gamma_v \cos \chi}{\sin \chi} \right) - \frac{\sin \chi}{B} \Gamma_{12}^1 \gamma_v + \frac{\delta}{R_{uv}},$$

$$\kappa_v = -\frac{1}{B} \frac{\partial}{\partial v} \left(\frac{\gamma_v - \gamma_u \cos \chi}{\sin \chi} \right) - \frac{\sin \chi}{A} \Gamma_{12}^2 \gamma_u - \frac{\delta}{R_{uv}},$$

$$\tau^{(1)} = -\frac{1}{A} \frac{\partial}{\partial u} \left(\frac{\gamma_v - \gamma_u \cos \chi}{\sin \chi} \right) - \frac{B \sin \chi}{A^2} \Gamma_{11}^2 \gamma_u + \frac{\delta}{R_u},$$

$$\tau^{(2)} = -\frac{1}{A} \frac{\partial}{\partial v} \left(\frac{\gamma_u - \gamma_v \cos \chi}{\sin \chi} \right) - \frac{A \sin \chi}{B^2} \Gamma_{22}^1 \gamma_u + \frac{\delta}{R_u},$$

$$\tau^{(1)} = \kappa_{uv} - \kappa_u \cos \chi + \frac{1}{R_{uv}} \left(\varepsilon_v \sin \chi - \frac{\varepsilon_{uv} \cos \chi}{2} \right) - \frac{\varepsilon_{uv}}{2R_u},$$

$$\tau^{(2)} = -\kappa_{uv} + \kappa_v \cos \chi - \frac{1}{R_{uv}} \left(\varepsilon_u \sin \chi - \frac{\varepsilon_{uv} \cos \chi}{2} \right) - \frac{\varepsilon_{uv}}{2R_v},$$

where ε_u is relative tension of middle surface along line u ;

ε_v is relative tension of middle surface along line v ;

ε_{uv} is alteration of angle between lines u, v ;

γ_u is angle of rotation of vector \bar{r}_u towards vector n in plane (\bar{r}_u, n) ;

γ_v is angle of rotation of vector \bar{r}_v towards vector n in plane (\bar{r}_v, n) ;

ω_u is angle of rotation of vector \bar{r}_u towards vector \bar{r}_v in tangent plane;

ω_v is angle of rotation of vector \bar{r}_v towards vector \bar{r}_u in tangent plane;

Γ_{ij}^n are Christoffel's symbols (with 3 indexes).

The two subscripts specify derivative variables for $\bar{r} = u(u, v)$ on the left side of the corresponding equality, and the superscript indicates which derivative of $\bar{r} = u(u, v)$ is followed by this coefficient (the digit 1 corresponds to the parameter u , and the digit 2 corresponds to the parameter v).

The stress-strain (physical) relations in accordance with Hooke's law:

$$\begin{aligned}
N_u &= \frac{Eh}{(1-\nu^2)} \left(\frac{\varepsilon_u - \varepsilon_{uv} \operatorname{ctg} \chi + \nu \varepsilon_v}{\sin \chi} \right), \quad N_v = \frac{Eh}{(1-\nu^2)} \left(\frac{\varepsilon_v - \varepsilon_{uv} \operatorname{ctg} \chi + \nu \varepsilon_u}{\sin \chi} \right), \\
S_u = -S_v &= \frac{Eh}{2(1-\nu^2)} \left(\frac{1 + \cos^2 \chi}{\sin^2 \chi} \varepsilon_{uv} - (\varepsilon_u - \varepsilon_v) \operatorname{ctg} \chi \right) - \frac{Eh}{2(1-\nu^2)} \nu (\varepsilon_{uv} - (\varepsilon_u - \varepsilon_v) \operatorname{ctg} \chi), \\
M_u &= -\frac{Eh^3}{12(1-\nu^2)} \left(\frac{\kappa_u + \nu \kappa_v}{\sin \chi} \right), \quad M_v = -\frac{Eh^3}{12(1-\nu^2)} \left(\frac{\kappa_v + \nu \kappa_u}{\sin \chi} \right), \\
M_{uv} &= \frac{Eh^3}{12(1+\nu)} \left(\frac{\kappa_{uv} - \cos \chi \kappa_v}{\sin \chi} \right), \quad M_{vu} = -\frac{Eh^3}{12(1+\nu)} \left(\frac{\kappa_{uv} + \cos \chi \kappa_u}{\sin \chi} \right),
\end{aligned} \tag{7}$$

Where E is modulus of elasticity, h is shell thickness, ν is Poisson's ratio.

These expressions form the system of 20 design equations, which makes possible to define two-dimensional parameters of inner forces and moments.

2.2. Oblique helicoid stress-strain analysis

2.2.1 Theoretical base

The oblique helicoid is a surface arising by moving oblique line along helicoidal line (Fig. 2). The much-used parametrical equation of this surface can be conceived of as [28]:

$$x = u \cdot \cos(\nu), y = u \cdot \sin(\nu), z = k \cdot u + c \cdot \nu, \tag{8}$$

where k is generator's slope ratio.

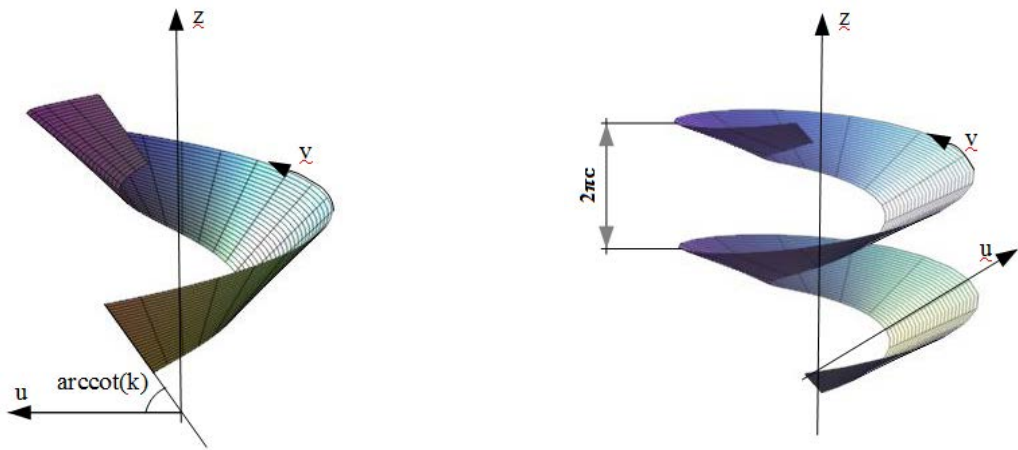
This is the equation in cylindrical coordinate system (Fig. 2, a). Also the oblique helicoid surface equations (5) can be established in oblique axis (Fig. 2, b):

$$x = u \cdot \cos(\varphi) \cdot \cos(\nu), y = u \cdot \cos(\varphi) \cdot \sin(\nu), z = u \cdot \sin(\varphi) + c \cdot \nu, \tag{9}$$

ν coordinate is generator rotation angle, like in cylindrical system, $\varphi = \operatorname{const}$ is the generator obliquity angle.

This coordinate system is non-orthogonal and non-conjugate, but the expressions of quadratic forms would be slightly simpler in comparison to those in cylindrical system:

$$\begin{aligned}
A &= 1, B = \sqrt{u^2 \cdot \cos^2 \varphi + c^2}, F = c \cdot \sin \varphi, \\
M &= -\frac{c \cdot \cos \varphi}{\sqrt{u^2 + c^2}}, N = -\frac{u^2 \cdot \sin 2\varphi}{\sqrt{u^2 + c^2}}, \chi = a \cdot \cos \pm \left(\frac{c \cdot \sin \varphi}{\sqrt{u^2 \cdot \cos^2 \varphi + c^2}} \right).
\end{aligned} \tag{10}$$



a) In cylindrical coordinate system

b) In curvilinear coordinate system

Figure 2. Oblique helicoids.

To simplify the task, assume that the helicoid has many coils, and the stress-strain state does not depend on the boundary conditions along the straight borders, and, consequently, does not depend on v coordinate.

The methodology is well known in shells and plates theory, it is quite straightforward, like brute-force solution. Substituting the strain-displacement relations (6) into the stress-strain equations (7), and after that the forces and moments expressions into the equilibrium equations (5), finally we can obtain a system of 3 ordinary differential equations in displacements. Actually, all parameters are expressed by displacements to get rid of other unknown variables, except three displacements and their derivatives. The main computational problem is to obtain and simplify the coefficients before them, because they are quite cumbersome. The full system of equations is not quoted in this article because of excessive volume, all procedure of dealing with those cumbersome coefficients and their's simplification is computerized. Modern smart software provides an opportunity to process huge symbolic expressions and exclude mistakes of "human element".

The general form of the differential equation system is given below:

$$\begin{aligned} \frac{d^2 u_u}{du^2} &= K_{10} u_u + K_{11} \frac{du_u}{du} + K_{12} u_v + K_{13} \frac{du_v}{du} + K_{14} u_z + K_{15} \frac{du_z}{du} + K_{16} \frac{du_z}{du} + K_{17} \frac{d^2 u_u}{du^2} + K_{1X} X, \\ \frac{d^2 u_v}{du^2} &= K_{30} u_u + K_{31} \frac{du_u}{du} + K_{32} u_v + K_{33} \frac{du_v}{du} + K_{34} u_z + K_{35} \frac{du_z}{du} + K_{36} \frac{du_z}{du} + K_{37} \frac{d^2 u_u}{du^2} + K_{3Y} Y, \\ \frac{d^4 u_z}{du^4} &= K_{70} u_u + K_{71} \frac{du_u}{du} + K_{72} u_v + K_{73} \frac{du_v}{du} + K_{74} u_z + K_{75} \frac{du_z}{du} + K_{76} \frac{du_z}{du} + K_{77} \frac{d^2 u_u}{du^2} + K_{7Z} Z. \end{aligned} \quad (11)$$

The system can be reduced into the first-order system of 8 differential equations by the substitution:

$$u_u = y_0, \frac{du_u}{du} = y_1, u_v = y_2, \frac{du_v}{du} = y_3, u_z = y_4, \frac{du_z}{du} = y_5, \frac{d^2 u_z}{du^2} = y_6, \frac{d^3 u_z}{du^3} = y_7. \quad (12)$$

This is a routine procedure of reduction of order of ordinary differential equation system.

Finally, we can obtain the first-order system of ordinary differential equations $\frac{dy}{dx} = f(x, y)$, or in other terms $y' = f(x, y)$ where:

$$y = \begin{bmatrix} y_0 \\ y_1 \\ y_2 \\ y_3 \\ y_4 \\ y_5 \\ y_6 \\ y_7 \end{bmatrix} = \begin{bmatrix} u_u \\ (u_u)' \\ u_v \\ (u_v)' \\ u_z \\ (u_z)' \\ (u_z)'' \\ (u_z)''' \end{bmatrix}, f(u, y_i) = \begin{bmatrix} f_0 \\ f_1 \\ f_2 \\ f_3 \\ f_4 \\ f_5 \\ f_6 \\ f_7 \end{bmatrix} = \begin{bmatrix} y_1 \\ f_1 \\ y_3 \\ f_3 \\ y_5 \\ y_6 \\ y_7 \\ f_7 \end{bmatrix} = \begin{bmatrix} (u_u)' \\ (u_u)'' \\ (u_v)' \\ (u_v)'' \\ (u_z)' \\ (u_z)'' \\ (u_z)''' \\ (u_z)'''' \end{bmatrix}, \quad (13)$$

$$f_1 = k_{10}y_0 + k_{11}y_1 + k_{12}y_2 + k_{13}y_3 + k_{14}y_4 + k_{15}y_5 + k_{16}y_6 + k_{17}y_7,$$

$$f_3 = k_{30}y_0 + k_{31}y_1 + k_{32}y_2 + k_{33}y_3 + k_{34}y_4 + k_{35}y_5 + k_{36}y_6 + k_{37}y_7,$$

$$f_7 = k_{70}y_0 + k_{71}y_1 + k_{72}y_2 + k_{73}y_3 + k_{74}y_4 + k_{75}y_5 + k_{76}y_6 + k_{77}y_7.$$

The full system of 8 differential equations is not presented in the article because of excessive volume.

The boundary conditions were considered as that: The shell was fixed rigidly along the whole contour. Its calculation model's boundary conditions with this support were supplemented by conditions:

$u_u(u_1) = u_v(u_1) = u_z(u_1) = u_z'(u_1) = 0, u_u(u_2) = u_v(u_2) = u_z(u_2) = u_z'(u_2) = 0$, where u_1 and u_2 are the coordinates of inner and outer curvilinear edges.

These ordinary differential equation systems can be solved by numeric methods [32, 33], particularly by means of sweep method, which is constantly improving and being modified [34, 35]. Differential sweep method of the most simple modification let solve such systems in case of the most simple boundary conditions, that is demonstrated in the present job. Through the sweep method algorithm execution the corresponding Cauchy's problems are solved by Runge-Kutta-Fehlberg 5th order method, that is realized by Giac/Xcas software package for symbolic calculations. In prospect of this job, modified methods of orthogonal successive substitution will make possible to solve similar systems with more complex boundary conditions ensuring the calculation stability.

So that, this method can be called numeric-analytical or semi-analytical, because the faithful and obvious in their physical meaning differential equations are solved by approximate numeric method. With some initial modifications and assumptions the methodology can be applied to shallow or non-shallow shells (the non-shallow variant is more universal, but demands more resources of computer). In the present article the modification for shallow shells was applied.

After calculating the deformations and their derivatives we can calculate internal axial and shear forces and bending and twisting moments.

2.2.2 Numeric experiments

Modern computers and software have high potential for either numerical or symbolic computations, and provide wide opportunities for processing cumbersome expressions. Thus, computational complexities, like stress-strain analysis of thin shells in non-orthogonal non-conjugate system, can be fulfilled and realized. The series of numeric experiments were conducted for helicoidal shells with variable geometrical parameters. Both shallow and non-shallow shells were investigated. In the first series of numeric experiments the influence of the generator obliquity angle on the stress-strain state was analyzed.

The series of numeric experiments were conducted for helicoidal shells with variable geometrical parameters. In the present job the shallow shells were investigated.

The calculation example for the methodology is given for the shell of reinforced concrete material

(Fig. 3). Both edges are fixed, an equally distributed vertical load is applied. The generators obliquity angle $\varphi = 5^\circ$, contour radius $R_1 = 2$ m, $R_2 = 4$ m; thickness of 12 cm and pitch of $0.01 \cdot 2\pi$. The material characteristics: modulus of elasticity $E = 32500$ MPa, Poisson's ratio $\nu = 0.17$. Load intensity is 10 kPa (Fig. 4). The approach is performed by Giac/Xcas software. The test results are shown in Fig. 5.

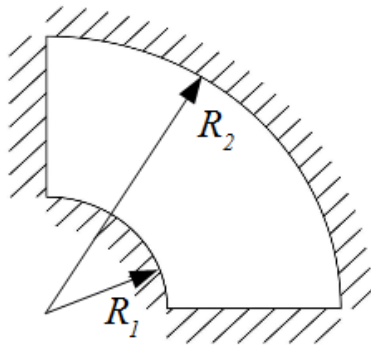


Figure 3. The model scheme.

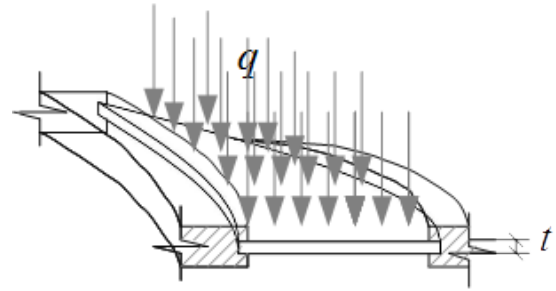


Figure 4. The loading.

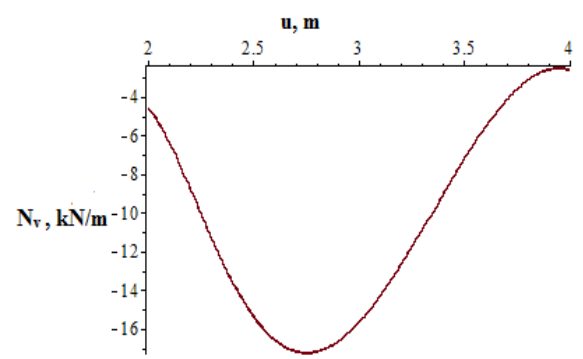
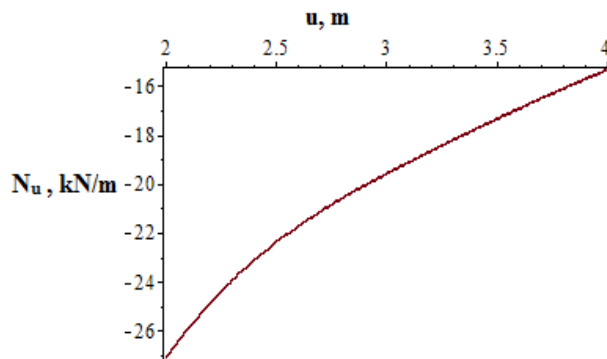


Figure 5. Inner axial forces.

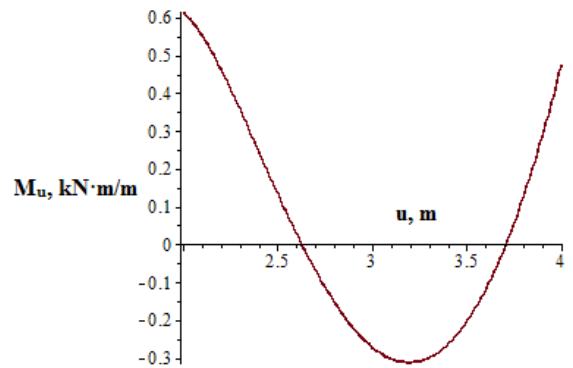
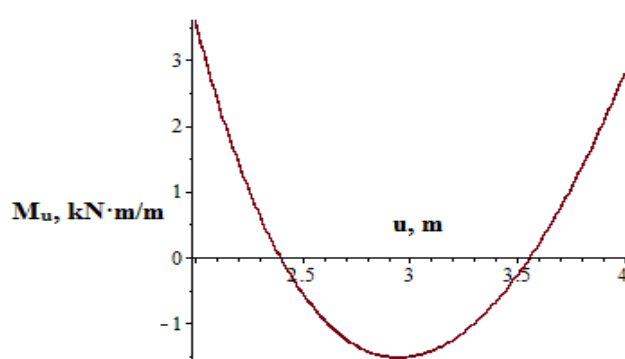


Figure 6. Inner bending moments.

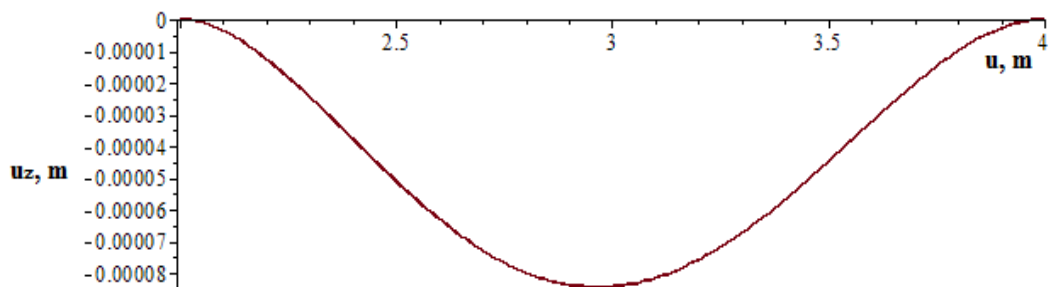


Figure 7. Deflection.

2.3. Right helicoid stress-strain analysis

The right helicoid (Fig. 5) is a surface arising by moving a straight line along helicoidal line when the angle between the straight line and the axis of the surface is equal to 90° . The much-used parametrical equation of this surface can be conceived of as:

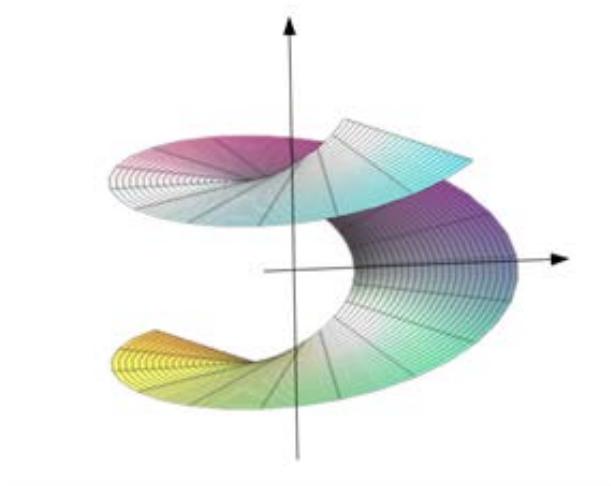


Figure 8. Right helicoid.

$$x = u \cos v \sqrt{b^2 - 4ac}, \quad y = u \sin v, \quad z = cv, \quad (14)$$

where c is displacement of the generator upon its rotation by 1 radian, or the ratio of the translational velocity to the circular velocity;

u, v are curvilinear coordinates of the point C of helicoids;

u is the distance from point C to axis z ;

v is the rotation angle of generator AB from the plane zOx to the point C .

For right helicoids $f(u) = 0$ and coefficients of the first and second quadratic forms are

$$A^2 = 1, \quad B^2 = u^2 + c^2, \quad F = 0, \quad \chi = \pi/2, \quad \cos \chi = 0,$$

$$L = 0, \quad M = -c / \sqrt{u^2 + c^2}, \quad N = 0.$$

If input the first and second quadratic form coefficients into

$$\begin{vmatrix} A^2 du + F dv & F du + B^2 dv \\ L du + M dv & M du + N dv \end{vmatrix} = 0$$

It can be found

$$du^2 = (u^2 + c^2) dv^2, \quad (15)$$

$$du/dv = \pm \sqrt{u^2 + c^2},$$

The angle between direction du/dv and direction $dv = 0$ is α ,

$$\cos \alpha = \frac{A^2 du + F dv}{\sqrt{A^2 du^2 + 2F du dv + B^2 dv^2}} = \frac{du}{\sqrt{du^2 + (u^2 + c^2) dv^2}} du / \sqrt{2 du^2} = \sqrt{2}/2 \quad (16)$$

It means that the angle between every direction and generator $dv = 0$ is 45° .

Main curvatures may be found by the equation

$$\lambda = \frac{1}{R} = \frac{Ldu + Mdv}{A^2 du + Fdv}$$

and for the right helicoid

$$\frac{1}{R_{1,2}} = \mp \frac{c}{u^2 + c^2}, \quad k = k_1 k_2 = -\frac{c^2}{(u^2 + c^2)^2}, \quad k_{cp} = 0. \quad (17)$$

The third equation of (17) shows that right helicoid is a minimal surface, the second equation of (17) shows that the torsion of a helical line passing through a given point of a straight helicoid can be expressed by quantity $\sqrt{-k} = \frac{c}{u^2 + c^2}$.

Shell is considered to be shallow if the following conditions are satisfied: $\frac{l_{\min}}{f} \geq 5, \frac{R_{\min}}{h} \geq 20$.

Where l_{\min} is minimum size of the shell projection f is shell depth, h is shell thickness, R_{\min} is minimum radius.

For shallow shells equilibrium equations can be reduced, and geometrical and physical relations can be essentially simplified. After the transformations finally one equation from equilibrium group and one equation of continuity base the system of mixed-mode method.

Differential operators

$$\begin{aligned} \nabla^2 \dots &= \frac{1}{\sqrt{u^2 + c^2}} \left[\frac{\partial}{\partial u} \left(\sqrt{u^2 + c^2} \frac{\partial \dots}{\partial u} \right) + \frac{1}{\sqrt{u^2 + c^2}} \frac{\partial^2 \dots}{\partial v^2} \right], \\ \nabla_k^2 \dots &= -\frac{2c}{(u^2 + c^2)^{3/2}} \frac{\partial}{\partial v} \left(\frac{\partial \dots}{\partial u} - \frac{u \dots}{u^2 + c^2} \right). \end{aligned} \quad (18)$$

In the case of shallow helicoid analysis c^2 can be neglected in comparison to u^2 , and the first and second quadratic forms coefficients will be:

$$A = 1, \quad B = u, \quad F = 0, \quad L = 0, \quad M = -c/u, \quad N = 0,$$

$$\begin{aligned} \nabla^2 \dots &= \frac{1}{u} \left[\frac{\partial}{\partial u} \left(u \frac{\partial \dots}{\partial u} \right) + \frac{1}{u} \frac{\partial^2 \dots}{\partial v^2} \right], \\ \nabla_k^2 \dots &= -\frac{2c}{u^2} \frac{\partial}{\partial u} \left(\frac{1}{u} \frac{\partial \dots}{\partial v} \right) = -\frac{H}{\pi} \frac{1}{u^2} \frac{\partial}{\partial u} \left(\frac{1}{u} \frac{\partial \dots}{\partial v} \right), \end{aligned} \quad (19)$$

where $H = 2\pi c$. The calculation equations for the shallow helical shells:

$$\nabla^2 \nabla^2 \varphi = -E \cdot h \cdot \frac{H}{\pi} \cdot \frac{1}{r^2} \cdot \frac{\partial}{\partial r} \left(\frac{1}{r} \frac{\partial u}{\partial v} \right), \quad (20)$$

$$\nabla^2 \nabla^2 \phi = -E \cdot h \cdot \frac{H}{\pi} \cdot \frac{1}{r^2} \cdot \frac{\partial}{\partial r} \left(\frac{1}{r} \frac{\partial u_z}{\partial v} \right),$$

which were derived by E. Reissner on the basis of K. Markever's equations for round plates having large deformations. They are solved for a number of particular cases $u_z = u_z(u)$ and $\phi = \phi(u)$, $u_z = kv$ and some others. V.G. Rekach and S.N. Krivoschapko proposed more general cases of solving equations (20). The methodology was developed in [23] and some numeric results were obtained.

Equations (20) are equations of Eulerian type and are reduced to equations with constant coefficients by substitution

$$u = e^t \text{ or } t = \ln u.$$

While using the following relations

$$\begin{aligned} \frac{d\dots}{du} &= \frac{1}{u} \frac{d\dots}{dt}, \\ \frac{d^2 \dots}{du^2} &= \frac{1}{u^2} \left(\frac{d^2 \dots}{dt^2} - \frac{d\dots}{dt} \right), \\ \frac{d^3 \dots}{du^3} &= \frac{1}{u^3} \left(\frac{d^3 \dots}{dt^3} - 3 \frac{d^2 \dots}{dt^2} + 2 \frac{d\dots}{dt} \right), \\ \frac{d^4 \dots}{du^4} &= \frac{1}{u^4} \left(\frac{d^4 \dots}{dt^4} - 6 \frac{d^3 \dots}{dt^3} + 11 \frac{d^2 \dots}{dt^2} - 6 \frac{d\dots}{dt} \right), \end{aligned} \quad (21)$$

Homogenous operators can be obtained:

$$\begin{aligned} \nabla^2 \dots &= \frac{1}{u^2} \left(\frac{\partial^2 \dots}{\partial t^2} + \frac{\partial^2 \dots}{\partial v^2} \right), \\ \nabla^4 \dots &= \frac{1}{u^4} \left(\frac{\partial^4 \dots}{\partial t^4} - 4 \frac{\partial^3 \dots}{\partial t^3} + 4 \frac{\partial^2 \dots}{\partial t^2} - 4 \frac{\partial^3 \dots}{\partial t \partial v^2} + 2 \frac{\partial^4 \dots}{\partial t^2 \partial v^2} + 4 \frac{\partial^2 \dots}{\partial v^2} + \frac{\partial^4 \dots}{\partial v^4} \right), \\ \nabla_k^2 \dots &= \frac{1}{u^4} \frac{\partial}{\partial v} \left(\frac{\partial}{\partial t^2} - 1 \right) \dots, \end{aligned} \quad (22)$$

If switching from coordinates u, v to t, v the (20) will become:

$$\begin{aligned} \nabla^4(t, v) u_z - \frac{H}{\pi D} \nabla_k^2(t, v) \phi &= e^{4t} \frac{Z}{D}, \\ \nabla^4(t, v) \phi + \frac{EhH}{\pi} \nabla_k^2(t, v) u_z &= 0, \end{aligned} \quad (23)$$

where $\nabla^4(t, v) \dots = u^4 \nabla^4 \dots$, $\nabla_k^4(t, v) \dots = u^4 \nabla_k^4 \dots$,

In the case of determination: $\phi = \left(\frac{EhH}{\pi} \right) \nabla_k^2(t, v) \Phi(t, v)$, and $u_z = -\nabla^4(t, v) \Phi(t, v)$ equations (17) can be combined into one equation of eight order:

$$\nabla^8(t, v) \Phi(t, v) + p^2 \nabla_k^4(t, v) \Phi(t, v) = -e^{4t} Z(t, v) / D, \quad (24)$$

$$\text{where } p^2 = \frac{EhH^2}{\pi^2 D} = \frac{12(1-\nu^2)H^2}{\pi^2 h^2}.$$

The solution of equation (24) can be found in trigonometric Fourier series

$\Phi(t, \nu) = \sum_{m=1}^{\infty} \Phi_m(t) \sin mv$ where coefficients of the series may be obtained from differential equations

$$\nabla^8(t, m)\Phi(t) - p^2 \nabla_k^4(t, m)\Phi(t) = 0,$$

$$\text{where } p^2 = \frac{EhH^2}{\pi^2 D} = \frac{12(1-\nu^2)H^2}{\pi^2 h^2}.$$

$$\begin{aligned} \nabla^4(t, m)\dots &= \frac{d^4 \dots}{dt^4} - 4 \frac{d^3 \dots}{dt^3} + 2(2-m^2) \frac{d^2 \dots}{dt^2} + 4m^2 \frac{d \dots}{dt} + m^2(m^2-4)\dots \\ \nabla_k^2(t, m)\dots &= \pm m \left(\frac{d}{dt} - 1 \right) \dots \end{aligned} \quad (25)$$

In this case inner forces and moments are obtained from the following formulas:

$$\begin{aligned} N_u &= \frac{1}{u} \frac{\partial \phi}{\partial u} + \frac{1}{u^2} \frac{\partial^2 \phi}{\partial v^2} = \pm \frac{EhH}{\pi} \frac{1}{u} \sum_{m=1}^{\infty} \left(\frac{d}{du} - \frac{m^2}{u} \right) \nabla_k^2(u, m) \Phi_m(u) \sin mv, \\ N_v &= \frac{\partial^2 \phi}{\partial u^2} = \pm \frac{EhH}{\pi} \frac{d^2}{du^2} \sum_{m=1}^{\infty} \nabla_k^2(u, m) \Phi_m(u) \sin mv, \\ S &= -\frac{\partial}{\partial u} \left(\frac{1}{u} \frac{\partial \phi}{\partial v} \right) = \frac{EhH}{\pi} \frac{1}{u} \left(\frac{d}{du} - \frac{1}{u} \right) \sum_{m=1}^{\infty} m \nabla_k^2(u, m) \Phi_m(u) \sin mv, \\ Q_u &= -D \frac{\partial}{\partial u} \nabla^2 u_z = D \frac{d}{du} \frac{1}{u^2} \sum_{m=1}^{\infty} \nabla^6(u, m) \Phi_m(u) \sin mv, \\ Q_v &= -\frac{D}{u} \frac{\partial}{\partial v} \nabla^2 u_z = \pm \frac{D}{u^3} \sum_{m=1}^{\infty} m \nabla^6(u, m) \Phi_m(u) \sin mv, \\ M_u &= -D \left[\frac{\partial^2 u_z}{\partial u^2} + \frac{\nu}{u} \left(\frac{\partial u_z}{\partial u} + \frac{1}{u} \frac{\partial^2 u_z}{\partial v^2} \right) \right] = \\ &= D \sum_{m=1}^{\infty} \left[\frac{d^2}{du^2} + \frac{\nu}{u} \left(\frac{d}{du} - \frac{m^2}{u} \right) \right] \nabla^4(u, m) \Phi_m(u) \sin mv, \\ M_v &= -D \left[\frac{1}{u} \left(\frac{\partial u_z}{\partial u} + \frac{1}{u} \frac{\partial^2 u_z}{\partial v^2} \right) + \nu \frac{\partial^2 u_z}{\partial u^2} \right] = \\ &= D \sum_{m=1}^{\infty} \left[\frac{1}{u} \left(\frac{d}{du} - \frac{m^2}{u} \right) + \nu \frac{d^2}{du^2} \right] \nabla^4(u, m) \Phi_m(u) \sin mv, \end{aligned} \quad (26)$$

$$M_{uv} = -(1-\nu) \frac{D}{u} \frac{\partial}{\partial v} \left(\frac{\partial u_z}{\partial u} - \frac{u_z}{u} \right) =$$

$$= \mp (1-\nu) \frac{D}{u} \left(\frac{d}{du} - \frac{1}{u} \right) \sum_{m=1}^{\infty} m \nabla^4(u, m) \Phi_m(u) \sin mv.$$

where $\nabla_k^2(u, m) \dots = m \left(u \frac{d}{du} - 1 \right) \dots$,

$$\nabla^2(u, m) \dots = \left(u^2 \frac{d^2}{du^2} + u \frac{d}{du} - m^2 \right) \dots$$

In order to find particular solution, it is possible to use Fourier series $\nabla^2(u, m) \dots = \left(u^2 \frac{d^2}{du^2} + u \frac{d}{du} - m^2 \right) \dots$, expand the right part of the equations (20) in trigonometric series:

$$-\frac{e^{4t}}{D} Z(t, \nu) = -\frac{e^{4t}}{D} \sum_{m=1}^{\infty} Z_m(t) \sin mv, \quad (27)$$

and obtain the solution m member of series

$$\left[\nabla^4 \nabla^4(t, m) - p^2 \nabla_k^2 \nabla_k^2(t, m) \right] \overline{\Phi}(t) = -\frac{e^{4t}}{D} Z_m(t), \quad (28)$$

where $\nabla^4(t, m) \dots$ and $\nabla_k^2(t, m) \dots$ are the same as for a general solution

In the case of the loading applied only along Z axis, two cases can be considered: $Z_m = \frac{4q}{\pi m}$ for

$0 < \nu < \pi$ or $Z_m = -\frac{4q}{\pi m} (-1)^{\frac{m+1}{2}}$ for $-\frac{\pi}{2} < \nu < \frac{\pi}{2}$, when $m = 1, 3, 5, \dots$, and equation (28) can be rewritten as follows:

$$\left[\nabla^4 \nabla^4(t, m) - p^2 \nabla_k^2 \nabla_k^2(t, m) \right] \overline{\Phi}(t) = -\frac{4q}{\pi m} \frac{e^{4t}}{D} \text{ for } 0 < \nu < \pi, \quad (29)$$

$$\left[\nabla^4 \nabla^4(t, m) - p^2 \nabla_k^2 \nabla_k^2(t, m) \right] \overline{\Phi}(t) = \frac{4q}{\pi m} (-1)^{\frac{m+1}{2}} \frac{e^{4t}}{D} \text{ for } -\frac{\pi}{2} < \nu < \frac{\pi}{2},$$

and finally

$$\overline{\Phi}_m(t) = A e^{4t} \text{ for } 0 < \nu < \pi, \quad (30)$$

$$\overline{\Phi}_m(t) = -A (-1)^{\frac{m+1}{2}} e^{4t} \text{ for } -\frac{\pi}{2} < \nu < \frac{\pi}{2},$$

where

$$A = \frac{-4q}{D \pi m \left[4^6 + m^8 - 40m^6 + 528m^4 - 2560m^2 - 9p^2 m^2 \right]}.$$

This method can be considered purely analytical, such solution became possible because of the simplicity of right helicoid quadratic forms. This solution results are precise and so that can be used as a benchmark for comparison to numeric and numeric-analytical solutions.

According to the methodology suggested in part 2.2, it is possible to analyze the stress-strain state of a shallow right helicoid. Several test examples are represented in comparison with results obtained by another methodology (part 2.1) for oblique helicoid in the case when the angle between the plane and the generator is equal to zero.

3. Results and Discussion

The numeric experiments were carried out in present investigation to verify and compare the methodologies given and also to define the border between shallow and non-shallow models.

The first comparison was made for method from chapter 2.1 and finite element method.

The comparison demonstrates close agreement of results, obtained by the numeric-analytic method and those obtained by finite element analysis.

The model is identical to model in example in 2.1.2.

The series of calculations were conducted for shells with different φ angle in limits from 0° to 15° .

Table 1. The results comparison for different angles.

φ	0	3	5	10	15
Maximum deflection along z axis method 1*, m	$8.69 \cdot 10^{-5}$	$8.45 \cdot 10^{-5}$	$8.43 \cdot 10^{-5}$	$7.99 \cdot 10^{-5}$	$4.67 \cdot 10^{-5}$
The same, method 2*, m	$8.7 \cdot 10^{-5}$	$8.6 \cdot 10^{-5}$	$8.0 \cdot 10^{-5}$	$7.4 \cdot 10^{-5}$	$6.6 \cdot 10^{-5}$
Maximum bending moment M_u , method 1*, KN·m/m	3914/ -1663	3805/ -1614	3593/ -1524	2853/ -1191	2076/ -852
The same, method 2*, KN·m/m	3711/ -1667	3689/ -1656	3639/ -1636	3428/ -1532	3108/ -1374

* method 1, – numeric- analytical, method 2 – finite element method

The finite element calculations were carried on by ANSYS APDL 15 software application. The finite element model represents a shell segment of 45° . It was proved that such a segment is sufficient to get the representative deflection and stress shape in the middle section [36]. The finite element SHELL181 was used for the calculation, quadrilateral finite elements were used according to the recommendations of official guideline [37], mesh size of 10 cm was sufficient to obtain the stable results. The loading was applied as gravity (dead load).

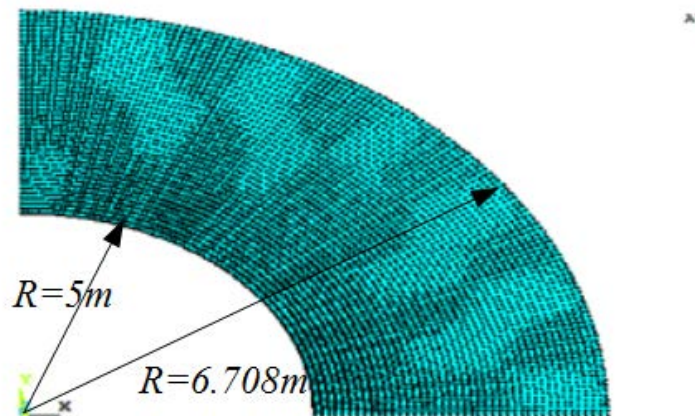


Figure 9. Finite element model.

Because of these results the boundary between shallow and non-shallow model can be determined near 10° generator obliquity angle for shells with a small pitch. This angle approximately corresponds to shell ratio of rise to plane size of 1/5.

The second comparison was made for right helicoid shell, calculated by numeric-analytic method and purely analytic method. The method from chapter 2.1 (for oblique helicoid) is also suitable for stress-strain analysis of shells with middle surface of special and degenerated cases of helicoid: if $\varphi = 0$ then oblique helicoid degenerates into right helicoid, if simultaneously $c = 0$ into flat plate; if $c = 0$, $\varphi \neq 0$ into conus. So we can compare results for right helicoid, calculated as a special case of oblique one, and analytically, directly as it was shown in chapter 2. Thus, the numeric-analytical methodology can be called

the handiest one, combining the advantages of analytical approach and universality of numeric Runge-Kutta solution.

The results obtained by the numeric-analytic method also have close agreement to those obtained by analytical method for right helicoid. The next examples illustrate this.

The shell of right helicoid form is analyzed below. The material characteristics: Young modulus E is $2 \cdot 10^5$ MPa, Poisson's ratio is 0.3. The thickness is 0.02 m, the inner radius R_1 is 5 m, the outer radius R_2 is 6.708 m, the pitch $H = 0.314$ m (or $c = 0.05$), load intensity is 10 KPa. All edges have fixed support.

The results are presented in the Fig. 10.

The maximum deflection is 1.51 mm, analytical method result is 1.48 mm.

The comparison with the results, got by analytical method is given in Table 2.

The results were obtained for analytical and numeric-analytical methodiques. First calculation was carried on for right helicoid as a special case of oblique helicoid by the numeric-analytical metodique, described in 1.1. The second one was conducted for the right helicoid by the analytical metodique, described in 1.2. The graphs were plotted by means of free computer algebra system Giac/Xcas software. The result graphs are overaid on each other compare them visually.

The graphs from Fig. 9 (a-d) were obtained for the central section of long shell, remote enough from the fixed edge, that is considered by one-dimentional model of the corresponding methods. The plots below illustrate that while deflection compared the difference between the values for 2 methodiques is about 0.03 mm, that means the discrepancy is about 2 % (Fig. 9 a). While bending moments M_u or shear forces Q_u compared, the difference is about 1 %, for it M_v is 2.5 %. All these results can be considered close or almost identical with technical accuracy.

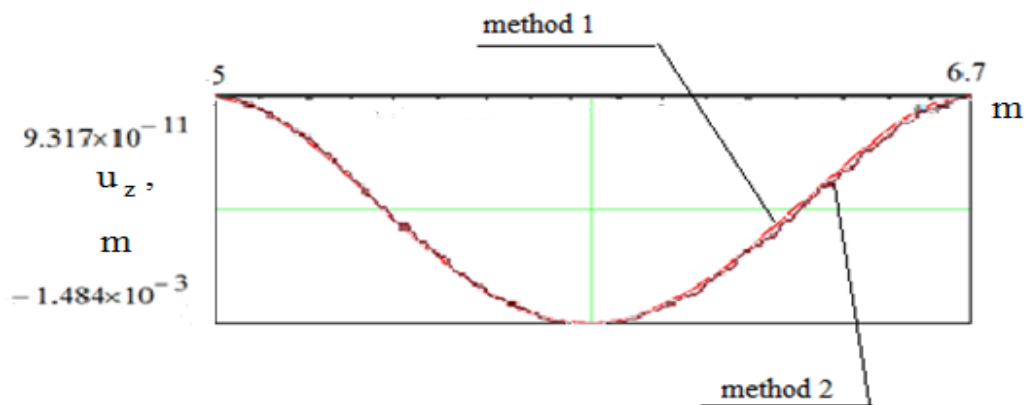


Figure 9 a. Deflection u_z

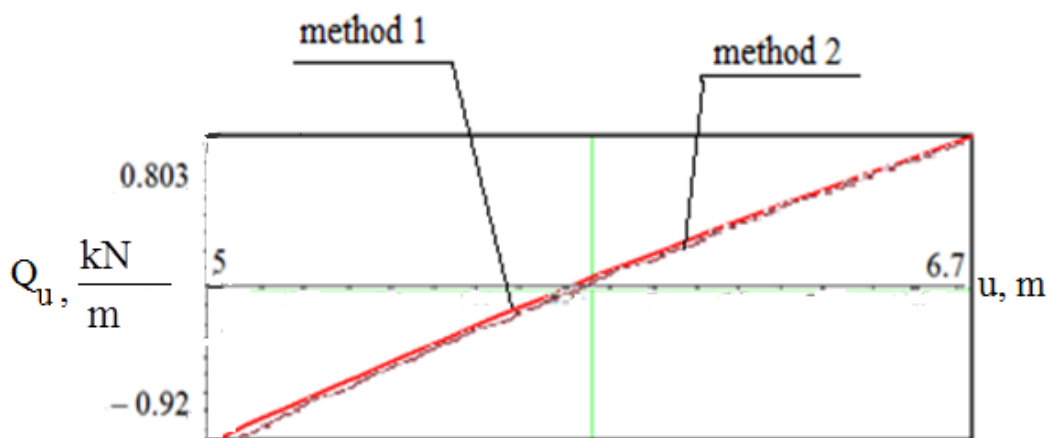


Figure 9 b. Shear force Q_u

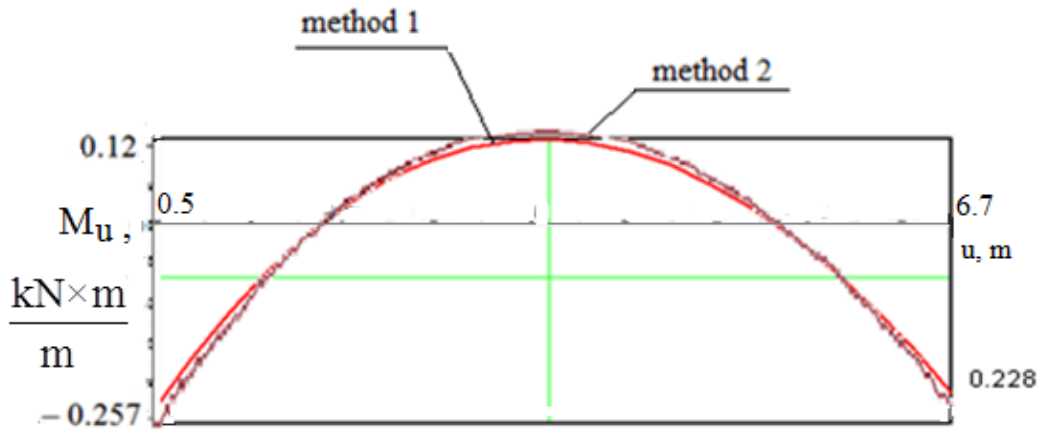


Figure 9 c. Bending moment M_u

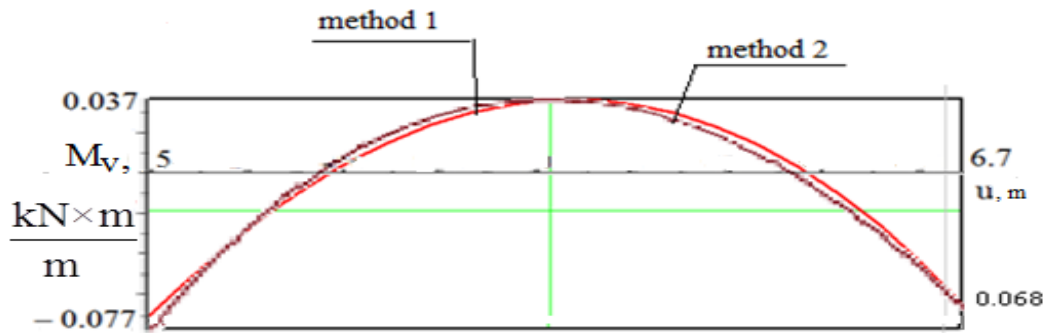


Figure 9 d. Bending moment M_v

All forces, moments and displacements except those which are represented on the graphs are close or equal to zero for shallow shells. These close matching results (see Table 2) show that the numeric-analytical methodology from 1.1 is more universal and can be used for any oblique helicoids including special cases, but the analytical methodology is certainly more accurate.

Table 2. The results comparison for two methods.

Quantity	Method 1	Method 2
Bending moment $M_u, \frac{kN \cdot m}{m}$ First support/midspan/second support	2,57/-1,21/2,289	2,57/-1,20/2,28
Bending moment $M_v, \frac{kN \cdot m}{m}$ First support/midspan/second support	0,77/-0,36/0,68	0,77/-0,37/0,68
Shear force kN First support/second support	-9,208/8,00	-9,208/8,03

Short finite element analysis was also conducted (see Fig. 11) by means of finite element software ANSYS APDL. The analogous calculation for another shell with different parameters was conducted in [38]. The finite element model is represented by one quarter of helicoid coil, because it is sufficient to neglects boundary effects [39]. The model is meshed by quadrilateral elements of 5 cm side length of 'shell 181' type, the element which behaviour is based on Kirghoff-Love linear elastic model. This element size is sufficient for results convergence and appropriate accuracy of the calculation. The distributed load was applied, like own weight. All edges have fixed support. Finite element test also shows close agreement: deflection is 1.516 mm. The isofields of deflections are shown on Fig. 11. Only deflection were compared to avoid coordinate systems mismatch while comparing the inner force factors, because ANSYS has only Cartesian, cylindrical or spherical coordinates, but for corrects comparison curvilinear coordinates needed.

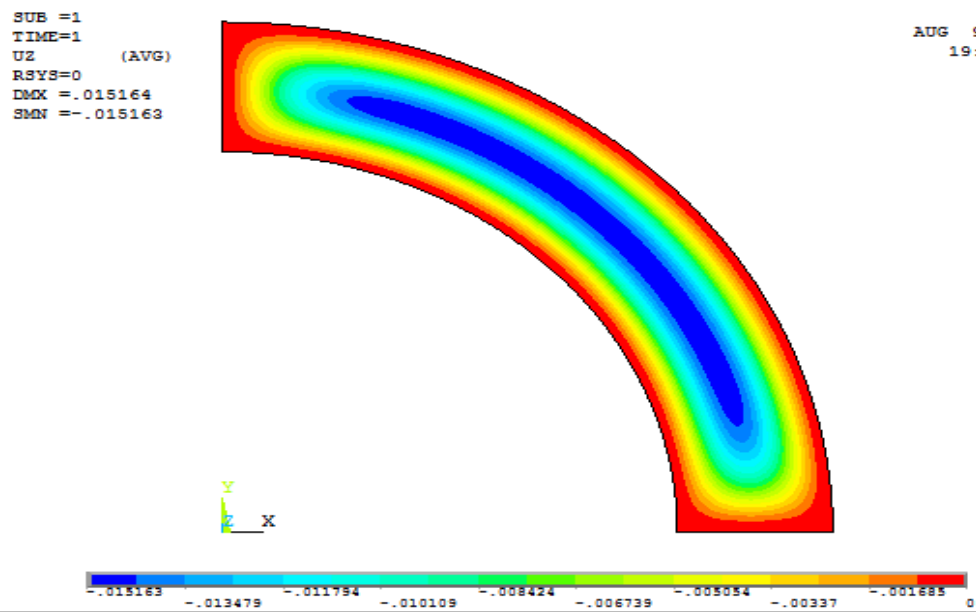


Figure 11. The deflection u_z by FE analysis.

4. Conclusion

In this paper two methodologies of analytical and half-analytical stress-strain state analysis for thin shallow helicoidal structures in the shape of right and oblique helicoids are represented. The analytical approach which is suitable for a right helicoid structure is compared to the half-analytical methodology which is developed by authors for an oblique helicoid structure when the inclination angle of generator is equal to zero (in this case the oblique helicoid turns into the right helicoid). The results which are obtained by two approaches give the appropriate accuracy if compared with each other, as well as if compared with the finite element method results.

The analytical approach for calculation of a right helicoidal structure is realized by the means of computer software based on analytical solutions obtained, while the half-analytical approach for calculation of an oblique helicoidal structure is performed by Giac/Xcas software. The finite element analysis was carried out by the means of Lira SAPR and ANSYS APDL software. The obtained results are also similar to the results obtained by analytical and numeric-analytical methods.

Both methodologies are written in the compact ways and are convenient for a practical engineering application as a means for a preliminary calculation or a deep stress-strain analysis of right and oblique helicoidal structures.

The boundary between shallow and non-shallow model was established approximately at 10^0 generator obliquity, that corresponds to classical recommendations to apply shallow model when h/l (shell depth to span) ratio is less than $1/5$.

All test calculations in this paper are made for cases with simple boundary conditions, mostly fixed supports (rigid restraints), because such cases need less computing time. In prospect this difficulty can be avoided with implementation of superior modifications of sweep method [40]. Another application of the methodology proposed is testing finite element model with the most simple load case and boundary conditions by comparison with the similar analytical model and following application of real loads on it.

To sum up, it may be said, that analytical methodology for right helicoid and numeric-analytic methodology for oblique and right helicoid have an advantages, as transparent physical meaning. The results are valid, the accuracy is appropriate, range of use is defined.

5. Acknowledgments

The paper has been supported by the RUDN University Strategic Academic Leadership Program.

6. Conflicts of Interest

The authors declare no conflict of interest.

References

1. Bradshaw, R., Campbell, D., Gargari, M., Mirmiran A., Tripeny, P. Special structures. Past, present, and future. *Journal of Structural Engineering*. 2002. 128 (6). Pp. 691–709. DOI: 10.1061/(ASCE)0733-9445(2002)128:6(691)
2. Adriaenssens, S., Block, P., Veennendaal, D., Williams, C. *Shell Structures for Architecture – Form finding and Optimization*, Routledge, 2014. 340 p. DOI: 10.4324/9781315849270
3. Fujimoto, K. House in Ashiya. *Jutakutokushu*. 2020. 1. Pp. 119–125.
4. Krivoshapko, S.N., Rynkovskaya, M., Razin, A. Design of a Thin Metal Product with the Developable Middle Surface from a Sheet by Parabolic Bending. *Materials and Technologies in Engineering II, Materials Science Forum*. 2020. 986. Pp. 78–85. DOI: 10.4028/www.scientific.net/MSF.986.78
5. Anisimov, R., Tarapanov, A. Design of the tool for periodic not evolvent profiles. *MATEC Web of Conferences*. 2017. 129 01039.
6. Abdullah, O.S., Khalil, W.H., Kamel, A.H., Shareef, A.J. Investigation of Physical and Numerical Model of Archimedes Screw Turbine. *Journal of Power and Energy Engineering*. 2020. 8. Pp. 26–42. <https://doi.org/10.4236/jpee.2020.810003>
7. Shahverdi, K., Loni, R., Ghobadian, B., Gohari, S., Marofi, S., Bellos, E. Numerical Optimization Study of Archimedes Screw Turbine (AST): A case study. *Renew Energy*. 145. Pp. 2130–2143. DOI: <https://doi.org/10.1016/j.renene.2019.07.124>
8. Nemirovskii, Yu.V., Babin, A.I., Sal'skii, E.A. Termonapryazhennoe sostoyanie mnogoslownykhpoliarmirovannykh gelikoidal'nykh obolochek [Thermo-stressed state of the helicoidalmultilayer polyreinforced shells]. *Doklady Akademii nauk vysshei shkoly Rossiiskoi Federatsii – Proceedings of the Russian higher school Academy of sciences*. 2016, 4 (33). Pp. 7–21. DOI: 10.17212/1727-2769-2016-4-7-21
9. Zhao, Y., Su, D., Wei, W., Dong, X. A meshing principle for generating a cylindrical gear using an Archimedes hob with two degrees of freedom. *Proceedings of the Institution of Mechanical Engineers, Part C: Journal of Mechanical Engineering Science*. 2010. 224 (1). Pp. 169–181. URL: <https://doi.org/10.1243/09544062JMES1535>
10. Akopyan, A.F., Akopyan, V.F., Podolko, K.Yu., Timoshenko, M.S., Boyarskikh, S.A., Litovchenko, T.A. Modelirovaniye raboty svay pri realizatsii prosadki grunta [Modeling of pile operation in the implementation of subsidence]. *Inzhenernyy vestnik Dona*. 2017. 3 (46). Pp. 92–95. URL: <https://cyberleninka.ru/article/n/modelirovanie-raboty-svay-pri-realizatsii-prosadki-grunta>
11. Smulskiy, I.I. Shnekovyye vetrodvigateli i ikh osobennosti [Screw wind turbines and their characteristics]. *Inzhenerno-fizicheskiy zhurnal*. 2001. 74(5). S. 187–195.
12. Jean Paul, V. A review of geometry investigations of helicoids. *IOP Conference Series: Material Science Engineering*. 2018. 371 012029. DOI: 10.1088/1757-899X/371/1/012029
13. Knabbel, J., Lewinski, T. Selected equilibrium problem of thin elastic helicoidal shells. *Arch. Civil Eng.* 1999. 42(2). Pp. 245–257.
14. Shevelev, L.P., Korikhin, N.V., Golovin, A.I. Sostoyaniya polya napryazheniy v gelikoidalnoy obolochke [Field stresses state in the helicoidal shell] *Stroitelstvo unikalnykh zdaniy i sooruzheniy [Construction of Unique Buildings and Structures]*. 2014. 2(17). S. 25–38. DOI: 10.18720/CUBS.17.2
15. Sorokina, A.G., Fomicheva, V.F., Kokoulin, V.G. Raschet napryazhenno-deformirovannogo sostoyaniya elastichnoy lenty gelikoidalnogo konveyera [Calculation of the stress-strain state of the elastic belt of a helical conveyor]. *Inzhenernyy zhurnal: nauka i innovatsii*. 2018. № 12 (84).
16. Savičević, S., Janjić, M., Vukčević, M., Šibalić, N. Stress research of helicoidal shell shape elements. *Machines, technologies, materials*, 2013, 10. URL: http://www.mech-ing.com/journal/Archive/2013/10/42_Savicevic_mtm13.pdf
17. Sorokina, A.G. Raschet formy deformirovannoy sredinnoy poverkhnosti gelikoidalno simmetrichnoy obolochki otkrytogo profilya pri bolshikh peremeshcheniyakh na osnove teorii chistogo izgibaniya [Calculation of the shape of the deformed median surface of a helicoidally symmetric shell of an open profile at large displacements based on the theory of pure bending]. *Izvestiya vysshikh uchebnykh zavedeniy. Mashinostroyeniye*. 2011. 11. S. 8–13.
18. Love, A.E.H. *A treatise on the mathematical theory of elasticity I and II*, Cambridge. 1927.
19. Evkin, A.Yu. Composite spherical shells at large deflections. Asymptotic analysis and applications, *Composite Structures*. 2020. 233 111577. DOI: 10.1016/j.compstruct.2019.111577
20. Zvereyaev, E.M. Saint-Venant – Picard – Banach Method for Integrating the Equations of the Theory of Elasticity of Thin-Walled Systems. *PMM*. 2019. 83(5–6). Pp. 823–833. (rus)
21. Valle, J.M., Martínez-Jiménez, P. Modified Bolle – Reissner Theory of Plates Including Transverse Shear Deformations. *Latin American Journal of Solids and Structures*. 2015. 12(2). Pp. 295–316. <https://dx.doi.org/10.1590/1679-78251275>
22. Michiels, T., Adriaenssens, S., Dejong, M. Form finding of corrugated shell structures for seismic design and validation using non-linear pushover analysis. *Engineering Structures*. 2019. 181. Pp. 362–373. URL: <https://doi.org/10.1016/j.engstruct.2018.12.043>
23. Krivoshapko, S., Rynkovskaya, M. Five Types of Ruled Helical Surfaces for Helical Conveyers. *Support Anchors and Screws. MATEC Web of Conferences*. 2017. 95 06002
24. Rynkovskaya, M., Ivanov, V. Analytical Method to Analyze Right Helicoid Stress-Strain. *Advanced Structured Materials*. 2019. 92. Pp. 157–171. DOI: https://doi.org/10.1007/978-3-319-79005-3_11
25. Tupikova, E. Stress-strain analysis of the shells of the long oblique helicoid form. *Journal of fundamental and applied science*. 2017. 9(7S). Pp. 296–309. DOI: <http://dx.doi.org/10.4314/jfas.v9i7s.28>
26. Romanova, V.A., Rynkovskaya, M., Ivanov, V. Automatic Modeling of Surfaces with Identical Slopes. *Advanced Structured Materials*. 2019. 92. Pp.143–156. DOI: https://doi.org/10.1007/978-3-319-79005-3_10
27. Krivoshapko, S.N., Gbaguidi, A.G. Two methods of analysis of thin elastic open helicoidal shells. *International Journal of Research and Reviews in Applied Sciences*. 2012. 12(3). Pp. 382–390.
28. Krivoshapko, S.N. Geometry and strength of general helicoidal shells. *Applied Mechanics Reviews*. 1999. 52(5). Pp. 161–175.
29. Dekhtyar, A.S. Load carrying capacity of helicoidal shell. *Structural Mechanics and Analysis of Constructions*. 2013. 6. Pp. 1–6. (rus)
30. Abbena, E., Salamon, S., Gray, A. *Modern differential geometry of curves and surfaces with Mathematica*. CRC Press, 2017.
31. Zvereyaev, E.M. Extraction of consistent shell theory equations from 3D theory of elasticity. *Structural Mechanics of Engineering Constructions and Buildings*, 2019.15(2). Pp.135–148. DOI: 10.22363/1815-5235-2019-15-2-135-148
32. Godunov, S.K. A method of orthogonal successive substitution for the solution of systems of difference equations. *USSR Computational mathematics and mathematical physics*. Nov. 1962. 2:6. Pp. 972–982.

33. Abramov, A.A. On the transfer of boundary conditions for systems of ordinary linear differential equations (A variant of the dispersive method). USSR Computational mathematics and mathematical physics. Mar. 1962. 1:3. Pp. 617–622.
34. Toro, E.F. Godunov methods: theory and applications. Springer Science+Business media. LLC, 2001.
35. Abramov, A.A. Numerical stability of a method of transferring boundary conditions. Computational Mathematics and Mathematical Physics. Mar. 2006. Vol. 46: 3. Pp. 382–387.
36. Krivoschapko, S.N. Static analysis of shells with developable middle surfaces. Applied Mechanics Reviews. 1998. 51. Pp. 731–746.
37. Kohnke, P. Ansys: Theory Reference, release 5.6, Ansys, inc. 1999.
38. Tupikova, E.M. Raschet tonkikh uprugikh obolochek v forme dlinnogo kosogo gelikoida. Stroitel'naya mekhanika inzhenernykh konstruksiy i sooruzheniy [Analysis of thin elastic shells in the form of thin oblique helicoid]. 2015. № 3. Pp. 23–27.
39. Aleksandrov, A.V., Kositsyn, S.B., Kositsyn, A.S. Netraditsionnyye modeli konechnykh elementov vysokikh poryadkov [Unconventional high-order finite element models]. Teoreticheskiye osnovy stroitelstva. Warszawa 2.07.96-5.07.96. Moskva: Izd-vo ASV, 1996. Pp. 26–30.
40. Vinogradov, A.Yu. Numerical modeling of boundary conditions in deformation problems of structured material in thin wall constructions. International Symposium Advances in Structured and Heterogeneous Continua II. Moscow, Russia, Book Abstracts. Aug. 1995.

Contacts:

Evgeniya Tupikova, emelian-off@yandex.ru

Marina Rynkovskaya, marine_step@mail.ru



DOI: 10.34910/MCE.106.10

The combination of bamboo grid and concrete pile as soil reinforcement under the embankment

A. Waruwu* , R. Deni Susanti , N. Napitupulu , J. Oges Sihombing 

Institut Teknologi Medan, Medan, Indonesia

*E-mail: azokhiw@gmail.com

Keywords: reinforcement, bamboo grid, concrete pile, design model, embankment, settlement, deflection

Abstract. Material availability and economic price make bamboo a viable option for soil reinforcement. Grids made of split bamboo rods require reinforcement with concrete piles, which are known to have a good bearing capacity under the embankment. The combination of these materials allows reducing the settlement and deflection of the bamboo grid as a subgrade on peat. However, research is needed to get the distance and length of a pile that can provide significant performance in supporting the embankment load. In this research, the pile system with diameters of 2 cm was driven into the peat layer to a certain length and distance. The piles have a length of 15 cm and 25 cm in peat soil layers. The piles were connected monolithically with a bamboo grid using a wire. The pile's distance was 5–20 cm. The peat soil was compacted layer by layer with a total thickness of 50 cm close to the field density. The embankment load was applied in three stages over one day with pressure of 3.02 kPa at each stage. The reinforcement proved to reduce the settlement and the deflection of the bamboo grid. The results showed that the combination of grid bamboo with concrete piles can be used for reinforcement purposes on peat soils on the following conditions: if $L/H = 0.3$, the ratio $s/d \leq 2.5$; if $L/H = 0.5$, the ratio $s/d \leq 7.5$.

1. Introduction

Peat soil has high water content, low specific gravity, low density, and low bearing capacity. Fibrous peat has low ash content, and very high compression. Improvement on peat soils is commonly performed using cement columns, cement, other pozzolanic materials, and preloading method [1–5]. The applying embankment on the peat layer can reduce the compression [6]. The embankment load can lead to lower high and uniform layer of peat. The reinforcement contributes in increasing the stability of the embankment, while strengthening and peat soil shear strength will withstand lateral forces that work [6].

The concrete slab can be used as a reinforcement to the peat to generate uniform settlement under embankment [7]. In addition to a concrete slab, other materials that can be used as soil reinforcement is bamboo. The bamboo is a renewable material and is spread around the world including the Asia-Pacific region, American region as well as African region [8]. The settlement due to embankment load can be reduced with the installation of bamboo grids on the layer of peat [9]. Bamboo grids in the peat soil settlement are able to reduce, increase the modulus of subgrade, and shear modulus. Reinforcement bamboo grids on top of two layers are quite effective in increasing the bearing capacity and reducing the settlement [10]. The use of bamboo grid is effective if the number of layers on top is of two layers, so that it is necessary to consider to use a bamboo grid [11]. Reinforcement bamboo grid is difficult to implement if the peat layer is thick, because it requires the dismantling of the land prior to the installation of the bamboo grids. For that, it needs a combination of mini piles from concrete to increase the stiffness of soil confinement system and inter pile. The reinforcement by sheet pile combined with the nailing is effective

Waruwu, A., Deni Susanti, R., Napitupulu, N., Oges Sihombing, J. The combination of bamboo grid and concrete pile as soil reinforcement under the embankment. Magazine of Civil Engineering. 2021. 106(6). Article No. 10610. DOI: 10.34910/MCE.106.10

© Waruwu, A., Deni Susanti, R., Napitupulu, N., Oges Sihombing, J., 2021. Published by Peter the Great St.Petersburg Polytechnic University.



This work is licensed under a CC BY-NC 4.0

method to reduce the lateral and vertical displacements of clay soil under embankment [12]. The same thing is obtained as a reinforcement for concrete slab on peat soil. The settlement pattern of the concrete slab under embankment on peat soil is similar to that of punching shear [7]. The use of mini piles under the reinforced soil abutments can meet the required bearing capacity value and reducing the settlement [13].

The piles serving to keep the base slab must remain in good contact with the subgrade. Installation of poles on the plate influence the controlling and minimize the damage caused by heave at the ground [14]. Pile foundation system is an effective way to support the pile with minimal reduction in total [15].

There are several advantages of piles as a drag heap of which implementation of embankment construction can be completed in a short time, the pile supporting the embankment can reduce total settlement and the differential settlement was not significantly [16]. Pile on peat soil is able to increase the modulus of subgrade reaction [17]. Installed piles under the slab can increase slab stiffness [18]. The pile under the slab in the nailed slab system is used to resist load, reduce settlement, increase stiffness, and increase stability [19]. Bamboo pile with diameter of 2 cm and a length of 20 cm was used as reinforcement in the bottom of the grid of bamboo on peat soil [20–21]. Pile spacing influences downward pressure and deflection on the ratio $s/d \leq 7.5$. Closer pile distance provides reduction downturn and large deflections. Maulana, et al., [20] stated that bamboo pile and grid are able to reduce settlement and deflection, so that stability of embankment maintained. The ratio of grid bamboo width to pile spacing (B/s) of 15 provides reduction settlement approximately 60 % [21]. Some types of mounting pile as reinforcement on peat soil is end bearing piles, friction piles, settlement reducing piles, tension piles, laterally loaded piles, and piles in fills [7]. The efficiency factors of pile group depend on the distance of piles, number of piles, and the length of the pile [22]. The pile length affects vertical and lateral displacement, and a longer pile shows smaller vertical and lateral displacement [23].

Many researchers investigated the soil reinforcement methods including the use of geosynthetic, geogrid, bamboo grid, concrete-grid, and pile [24–28]. Generally, reinforcement used to support the embankment load is geosynthetic. In this research, reinforcement pile used was bamboo grid combined with the piles from the concrete material. There has been limited research on the model of a small scale in the laboratory. Therefore, this paper is concerned with the performance of bamboo grid-concrete pile system related to the effectiveness of the length and pile spacing to settlement and deflection. This research is part of an ongoing investigation on model of the grid combination of bamboo and concrete piles to support the embankment on the ground. The specific objectives are to determine the ratio of pile spacing to diameter based on the ratio of pile length to peat layer depth and bamboo grid width. In addition, the compression behaviour and the deflection distribution of bamboo grid have been observed. Future work will include the effect of bonding piles with bamboo grids and addition of pile cap to ensure connection with bamboo grids on the behaviours of reinforced concrete pile and bamboo grid.

2. Methods

The research was conducted on peat soil using test box measuring 120 cm×90 cm×90 cm, but with the thickness of peat soils of only 50 cm and this layer was followed by solid layer of 50 cm (Fig. 1). The peat soil was compacted layer by layer as thick as 10 cm with a total thickness of 50 cm. The density of each layer is known from core cutter test with a density close to the field density. The same thing was done to achieve the required thickness of the peat (Fig. 2). To facilitate the drainage of water into the peat layer it is necessary to install pipes in each corner and bottom of the test basin. Ground water levels are modeled to the ground level.

Peat soil used was a fibrous peat soil type and classified as soft soil because it has an undrained shear strength (C_u) value of 6.15 kPa less than 12.5 kPa [24]. Reinforcement of peat soils used 2 cm in diameter (d) concrete piles and 60 cm×30 cm bamboo grids (Fig. 3). The concrete pile was distinguished by the length and distance of the pile. The length of the pile (L) used was 15 cm or L/H of 0.3 and 25 cm or $L/H = 0.5$ with a distance (s) of 5-20 cm or s/d of 2.5-10. The piles were installed in a layer of peat at certain distances and on top of it was laid a bamboo grid.

Embankment load was modeled using the iron bars having dimensions of 1.9 cm×1.9 cm×4 cm as research [12–16]. Load was given gradually every day and each stage was composed of two layers as high as h of 3.8 cm equivalent to the pressure (σ) of 3.02 kPa and a total of three layers of 9.08 kPa (Fig. 4). The settlement of each stage of the load is read at certain times using a dial gauge. In addition to testing the model on a small box, testing was also conducted on a box sized of 2 m×1.5 m (Fig. 5). The lengths of the piles used include 10 cm, 20 cm, 30 cm, and 40 cm with a diameter of 2 cm and a distance of 10 cm. Stages of load are the same as for small box.

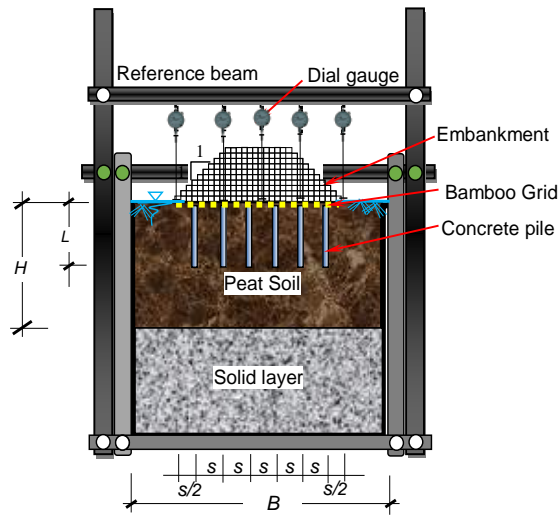


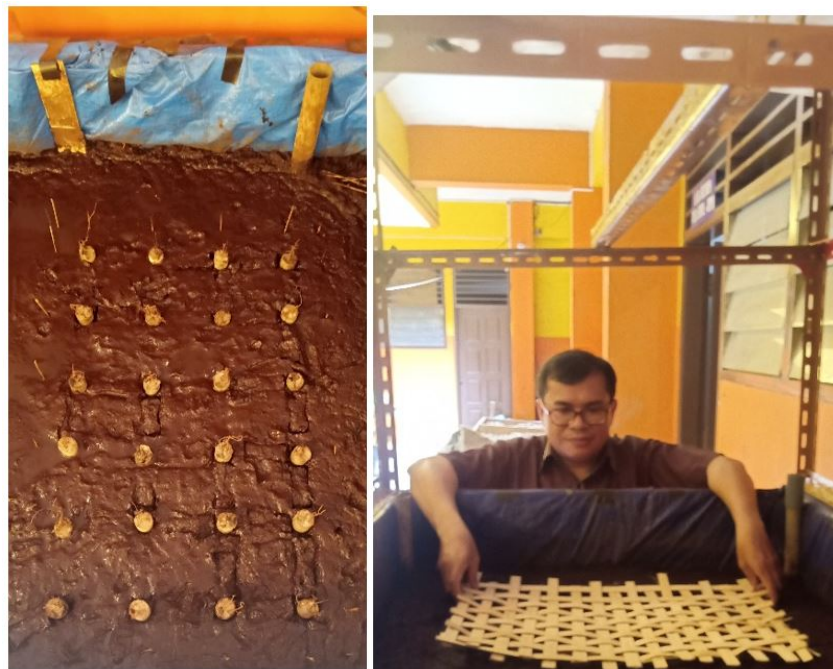
Figure 1. The model test of experimental [24].



(a)

(b)

Figure 2. Photographs of (a). Test box with water drainage pipe; (b). Compacted peat soil.



(a)

(b)

Figure 3. Photographs of (a). Arrangement of piles; (b). Bamboo grid.



Figure 4. Photographs of embankment load test.



Figure 5. Photographs of embankment load test for box sized of 2 m x 1.5 m.

3. Results and Discussion

The results of embankment load on peat soil reinforced by bamboo grid with and without piles can be seen in Fig. 6 and Fig. 7. Load-settlement curves of the study [25], using concrete-grid for reinforcement of subsoil base under foundation, generally reduces the settlement and increases the bearing capacity of

the soil. The piles that reinforced the bamboo grid are seen to influence the peat compression. The longer piles (L of 25 cm) showed a significant effect on behavior change compression of peat (Fig. 7). The shorter piles (L of 15 cm) with a ratio of pile length to peat layer thickness ($L/H < 0.5$) shows relatively small changes in peat compression except for piles with spacing (s) of 5 cm (Fig. 6).

The significant decrease occurs in the ratio of the distance of the piles to the diameter ($s/d \leq 2.5$). This is different if the pile used is longer (L of 25 cm) or equivalent to half the thickness of the peat layer ($L/H \geq 0.5$), as shown in Fig. 7. The friction capacity of the longer pile is noticeably higher than the shorter pile. Long piles showed relatively smaller settlement compared to short piles. Thus, the length of the pile used as a bamboo reinforcement grid on peat soil requires a minimum of half of the thickness of the peat layer ($L/H \geq 0.5$) with the ratio of the distance of the pile to the diameter of the pile ($s/d \leq 7.5$). Relation between pressure and settlement for box sized of 2 m x 1.5 m is shown in Fig. 8.

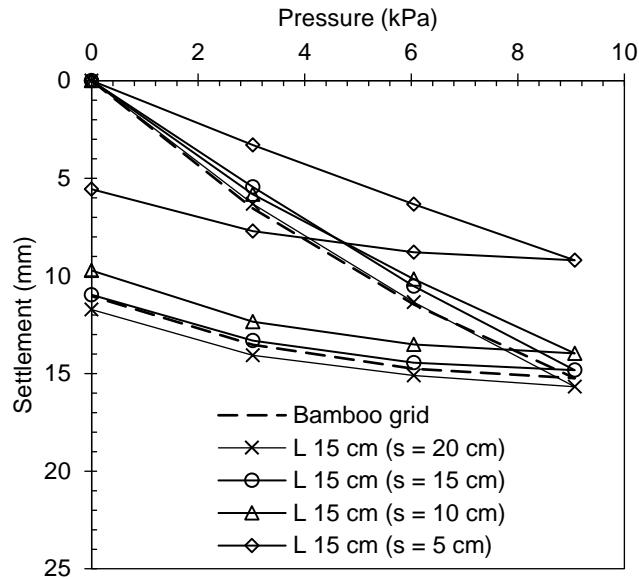


Figure 6. Relation between pressure and settlement for L of 15 cm.

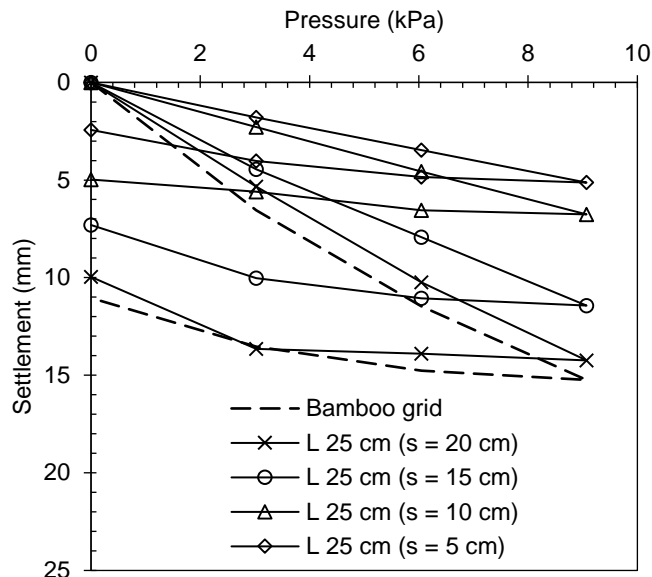


Figure 7. Relation between pressure and settlement for L of 25 cm.

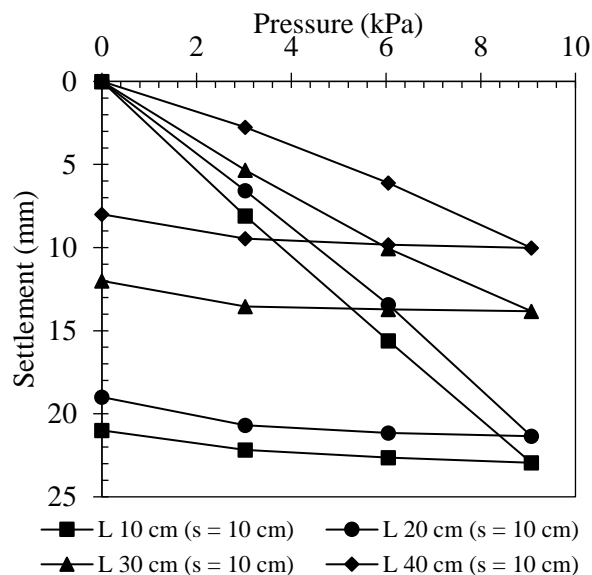


Figure 8. Relation between pressure and settlement for box sized of 2 m×1.5 m.

The results of the embankment load model test conducted in a test box sized of 2 m×1.5 m can be seen in Fig. 8. The compression behavior due to the embankment load shows the same behavior as the load test results from the test box sized 1.2 m×0.9 m (Fig. 6 and Fig. 7). Thus, the size of the larger test box does not have a significant effect on the behavior of the relationship between pressure and settlement. However, the settlement in the box sized of 2 m×1.5 m was relatively higher than the box sized of 1.2 m×0.9 m, this was influenced by the restraint of the test box wall. Further reviews will be made of the further research that is being carried out this year and next.

The load test consists of embankment load modelled from the iron bars having dimensions of 1.9 cm×1.9 cm×4 cm and it is not the form of a plate load test. The result of the embankment load test shows a high compression curve at the beginning of loading and decreases with increasing loading time. The results of this study indicate high compression at the beginning of the study, this is shown that primary compression on peat soil is fast enough at the beginning of the loading. The results of the research of Waruwu, et al. [19] using a test box sized of 7 m×3.5 m, obtained a compression behavior similar to the results of this study.

The relationship of time and settlement of embankment load test can be seen in Fig. 9 and Fig. 10. The addition of the load is done every day both for grid bamboo with pile reinforcement L of 15 cm and L of 25 cm. The relationship of time and settlement on the pile with the length of 15 cm are shown in Fig. 9, while the pile with the length of 25 cm is shown in Fig. 10. The relationship of time and settlement is approaching the same results of research by Waruwu, et al. [24].

Peat soil is known as a soil type with a dominant consolidation settlement and a rapid period of time. Waruwu, et al. [6] stated that the primary consolidation of the peat soil is about 5 minutes and secondary consolidation is about 253 hours. Based on the results of the research model test on a small laboratory scale, it was found that the time of primary consolidation was the first 10-15 minutes. For this reason, the study used one additional load every day for each stage. The results obtained showed that the increase in the settlement after 15 minutes had very little changes. The settlement in a longer time can be analyzed using the hyperbolic method [9].

The shorter pile with spacing of 10-20 cm shows the settlement that is relatively the same as a bamboo grid without piles. This can be caused by the frictional capacity of the pile which does not significantly support the embankment load. The peat compression with bamboo grid looks better compared to short pile at a spacing of 20 cm, which means that the pile does not contribute to bearing the embankment load. To reach a design level it is sometimes necessary to combine reinforcement with stage construction so that the subgrade can have sufficient bearing capacity for the final embankment load [26]. The deduced differential settlement also increased with an increase in the height of the embankment [16].

The longer pile (L of 25 cm) showed a reduction of the settlement better than the shorter pile (L of 15 cm). The spacing of pile affects the settlement, the spacing of pile that is close shows a small settlement [27]. Peat compression is generally greater at the beginning of loading. This can be caused by the primary

compression that occurs in the early minutes and is followed by secondary compression [6]. The compression is becoming lighter along with the length of the pile with a closer distance. Thus, the bamboo grid with the strengthening of the pile has an impact on reducing peat compression.

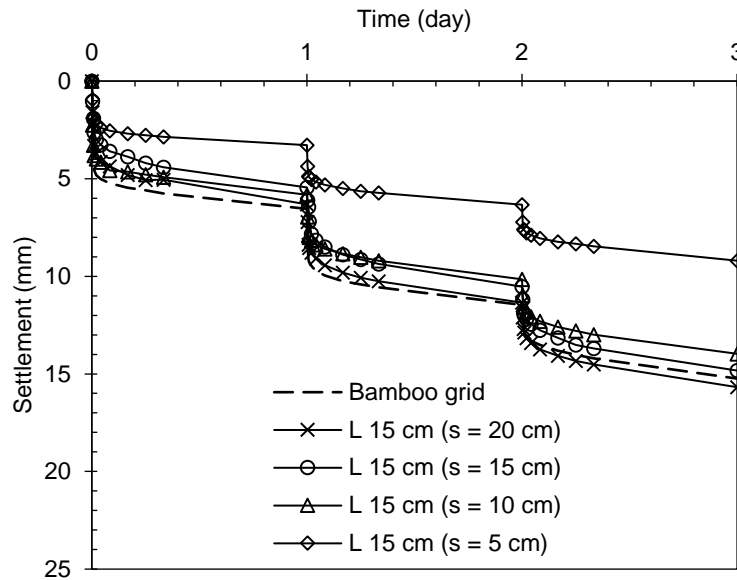


Figure 9. Relation between time and settlement for L of 15 cm.

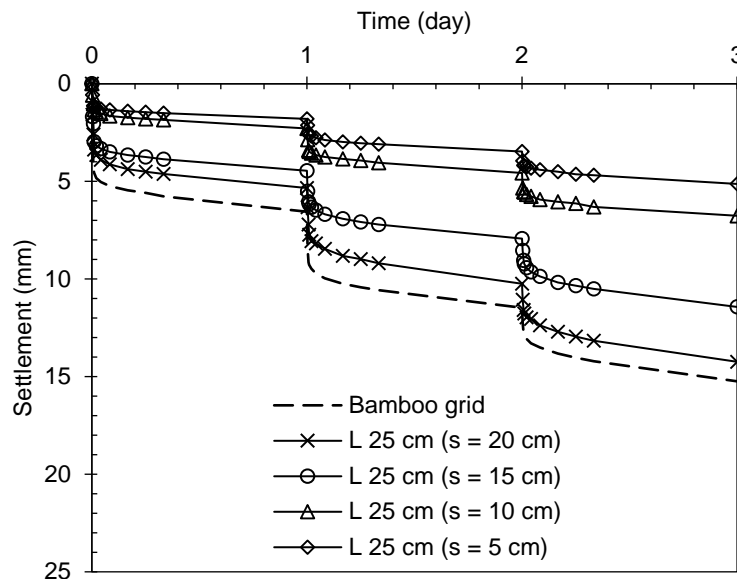


Figure 10. Relation between time and settlement for L of 25 cm.

Effects of embankment load on the behaviour of the deflections of bamboo grid can be seen at Fig. 11 and Fig. 12. The relationship of distance from center of embankment and deflections is approaching the same results of research by Waruwu, et al., [24]. The bamboo grid reinforcement with concrete piles can reduce the deflection of bamboo grid. Longer and denser piles show smaller deflection of bamboo grid compared to shorter piles with longer spacing.

The effect of pile spacing on deflection of bamboo grid for pile with the length L of 15 cm is shown in Fig. 11, while pile length L of 25 cm can be seen in Fig. 12. The deflection of bamboo grids looks smaller at shorter pile spacing, both for shorter pile and for longer piles. But the long piles showed more significant reduction of deflection than the shorter pile. It can be seen that the deflection of a bamboo grid with a short pile spaced 10-20 cm is almost the same as a bamboo grid without a pile except that the pile L of 15 cm with spacing of 5 cm showed deflection that is relatively smaller than a pile with a longer spacing. Whereas on the relatively long pile $L = 25$ cm shows a significant reduction in deflection of the bamboo grid.

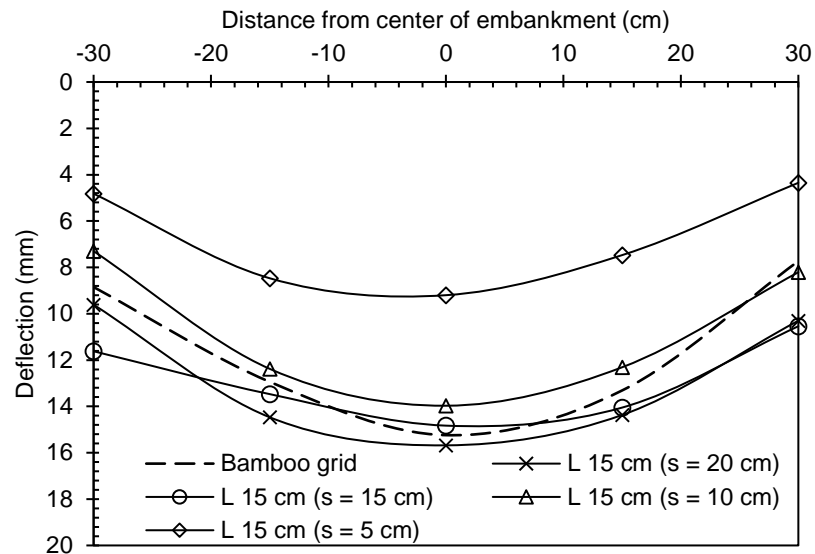


Figure 11. Deflection for L of 15 cm.

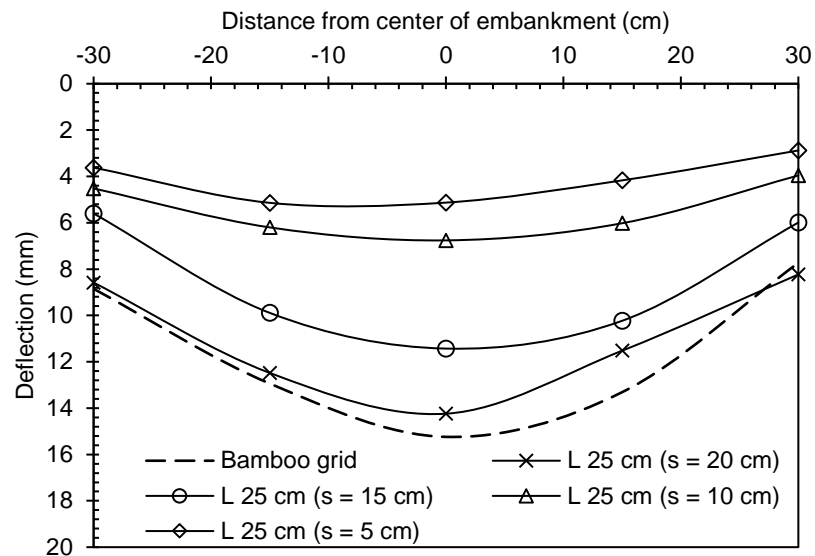


Figure 12. Deflection for L of 25 cm.

The effect of the length of the pile on the deflection of bamboo grid for a pressure of 9.08 kPa can be seen in Fig. 13. Pile with L of 15 cm – spacing of 10-20 cm and pile with L of 25 cm – spacing of 20 cm showed deflection similar to a bamboo grid without a pile. Pile L of 25 cm spacing of 20 cm showed similar deflections to pile L of 15 cm – spacing of 10 cm. The use of bamboo grid and pile concrete reinforcement can increase embankment stability and reduce deflections. Usually, the other reinforcement can increase embankment stability, reduce deformations, improvement of embankment behaviour, cost savings, increase in the feasibility of embankment construction, and the elimination of stage construction [26].

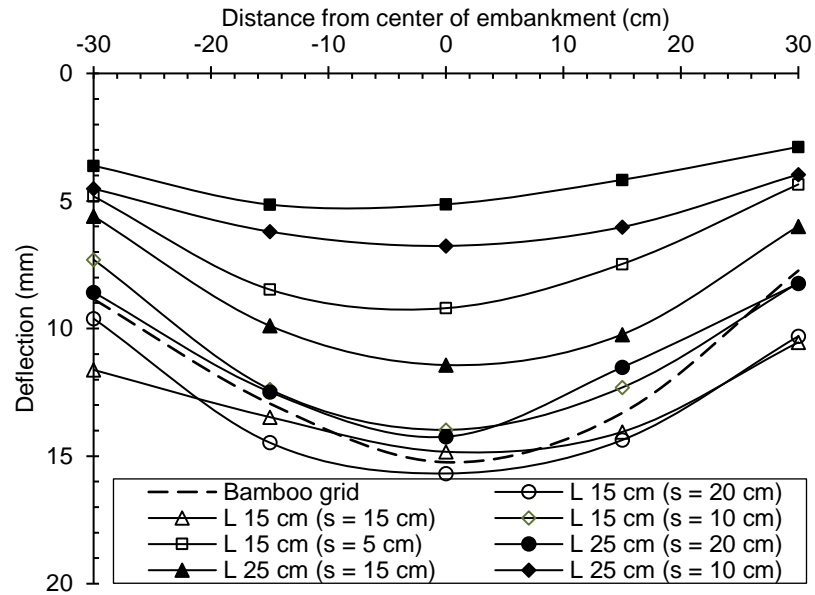


Figure 13. Comparison of deflection L of 15 cm and L of 25 cm.

The performance of concrete pile with bamboo grid as reinforcement on peat soil showed a significant effect on the pile ratio $L/H = 0.3$ with the ratio $s/d \leq 2.5$ and the pile $L/H = 0.5$ with a ratio $s/d \leq 7.5$. This approach is the same as the results of the study Oh and Sin [27], it can be estimated that the geogrid reinforcement is practically ineffective at $s/d \approx 6-7$. The pile with ratio $s/d \approx 5$ gives a significant effect on the settlement reduction [20]. The relationship between L/H and s/d can be described in Fig. 14. This relationship can be approximated by Equation (1). Where s of pile spacing, d of pile diameter, L of the pile length, and H = peat layer thickness. If the soil layer is relatively thick, then the ratio = pile spacing to the pile diameter can be determined from the ratio of the length to the width of the bamboo grid with piles (L/B) as shown in Fig. 15 and Equation (2). This relationship is a maximum limit to obtain the influence of the installation of pile on a bamboo grid. Better results are obtained at a relatively longer pile with a shorter spacing.

$$\frac{s}{d} \leq \frac{100}{3} \left(\frac{L}{H} \right)^2 - \frac{5}{3} \left(\frac{L}{H} \right) \tag{1}$$

$$\frac{s}{d} \leq 48 \left(\frac{L}{B} \right)^2 - 2 \left(\frac{L}{B} \right) \tag{2}$$

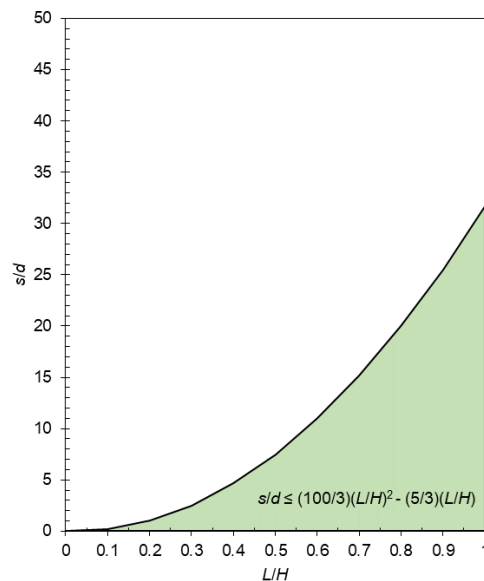


Figure 14. Relation between L/H and s/d .

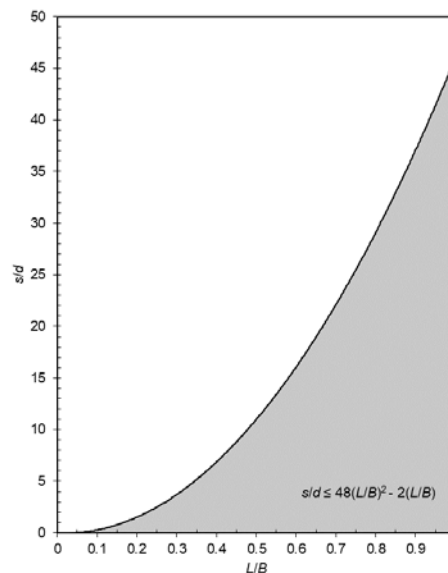


Figure 15. Relation between L/B and s/d .

4. Conclusion

The following conclusions are based on the results and discussions of this study:

1. Changes in peat soil compression behavior are found on piles with a length of more than half the thickness of the peat layer. Short piles exert less influence on peat compression. Long piles have a higher friction capacity so that decreases are smaller.
2. All types of tests show high peat compression in the initial minutes of loading and are followed by constant compression changes. Compaction of peat becomes smaller as the length of the pile grows closer. Bamboo grids reinforced with concrete piles have an impact on reducing peat compression.
3. Deflection of the bamboo grid is found to be getting smaller at a tight pile spacing, both for the short and long pile. However, the longer pile shows more significant reduction of deflection than the shorter pile. Piles with a length of more than half the thickness of the peat showed a significant effect on reducing the deflection of the bamboo grid.
4. Performance of bamboo grids with concrete piles as reinforcement on peat soil showed a significant effect on the pile ratio $L/H = 0.3$ or $L/B = 0.25$ with a ratio of $s/d \leq 2.5$ and pile $L/H = 0.5$ or $L/B = 0.42$ with a ratio $s/d \leq 7.5$. Performance of reinforcement is influenced by the ratio of the length of the piles to the thickness of the peat, the ratio of the length of the pile to the width of the bamboo grid, and the ratio of the pile spacing to the diameter of the pile. The length and spacing of the pile affect the settlement, compression, and deflection.

5. Acknowledgement

The authors would like to express thanks to the Ministry of Research, Technology and Higher Education of The Republic of Indonesia for financial support. The authors would like to thank the head and the technicians of the Soil Mechanics Laboratory – Medan Institute of Technology for their help during the experimental work.

References

1. Yan, S.W., Chu, J. Soil improvement for a storage yard using the combined vacuum and fill preloading method. *Canadian Geotechnical Journal*. 2005. 42(4). Pp. 1094–1104. DOI: 10.1139/t05-042
2. Duraisamy, Y., Huat, B.B.K., Muniandy, R. Compressibility behavior of fibrous peat reinforced with cement columns. *Geotech Geol Eng*. 2009. 27(5). Pp. 619–629. DOI: 10.1007/s10706-009-9262-3
3. Huat, B.B.K., Kazemian, S., Prasad, A., Barghchi, M. A study of the compressibility behavior of peat stabilized by dmm: lab model and FE analysis. *Academic Journals*. 2011. 6(1). Pp. 196–204. DOI: 10.5897/SRE10.790
4. Kazemian, S., Huat, B.B.K., Moayedi, H. Undrained shear characteristics of tropical peat reinforced with cement stabilized soil column. *Geotech Geol Eng*. 2012. 30(4). Pp. 753–759. DOI: 10.1007/s10706-012-9492-7
5. Boobathiraja, S., Balamurugan, P., Dhansheer, M., Adhikari, A. Study on strength of peat soil stabilised with cement and other pozzolanic materials. *International Journal of Civil Engineering Research*. 2014. 5(4). Pp. 431–438.

6. Waruwu, A., Hardiyatmo, H.C., Rifa'i, A. Compressive behavior of Bagansiapiapi-Riau peat in Indonesia. *Electronic Journal of Geotechnical Engineering*. 2016. 21(16). Pp. 5217–5227.
7. Zainorabidin, A., Abdurahman, M.N., Kassim, A., Azlan, M.F.M.D. Settlement behaviour of parit nipah peat under static embankment. *International Journal of GEOMATE*. 2019. 17(60). Pp. 151–155. DOI: 10.21660/2019.60.8263
8. Bonivento Bruges, J.C., Vieira, G., Revelo Orellana, D.P., Togo, I. Parameter of thermal resistance of bamboo multilayer wall. *Magazine of Civil Engineering*. 2018. 83(7). Pp. 92–101. DOI: 10.18720/MCE.83.9
9. Waruwu, A., Maulana, Halim, H. Settlement estimation of peat reinforced with bamboo grid under embankment. *International Review of Civil Engineering (I.R.E.C.E.)*. 2017. 8(6). Pp. 299–306. DOI: 10.15866/irece.v8i6.13130
10. Waruwu, A., Halim, H., Nasution, T., Hanova, Y. Bamboo grid reinforcement on peat soil under repeated loading. *Journal of Engineering and Applied Sciences*. 2018. 13(8). Pp. 2190–2196. DOI: 10.36478/jeasci.2018.2190.2196
11. Waruwu, A., Susanti, R.D., Buulolo, J.A.P. Effect of dynamic loads on the compressibility behaviour of peat soil reinforced by bamboo grids. *Journal of Applied Engineering Science*. 2019. 17(2). Pp. 157–162. DOI: 10.5937/jaes17-16937
12. Isobe, Y., Shahin, H.M., Nakai, T. Effectiveness of reinforcement in embankment ground subjected to repeated shear deformation. *International Journal of GEOMATE*. 2014. 7(2). Pp. 1111–1116.
13. Bukowski, M., Lysiak, P., Oleszek, R., Trochymiak, W. Modeling and analysis of ground settlement between a flyover and reinforced soil embankment. *Archives of Civil Engineering*. 2018. 64(4). Pp. 77–100. DOI: 10.2478/ace-2018-0064
14. Diana, W., Hardiyatmo, H.C., Suhendro, B. Effect of pile connections on the performance of the nailed-slab system on the expansive soil. *International Journal of GEOMATE*. 2017. 12(2). Pp. 134–141. DOI: 10.21660/2017.32.42773
15. Reinaldo, V.M., Shao, Y. Geogrid-reinforced and pile-supported roadway embankment. *Proceedings of Contemporary Issues in Foundation Engineering*. New York: ASCE Publications. 2005. Pp. 26–28. DOI: 10.1061/40777(156)9
16. Liu, H.L., Ng, C.W.W., Fei, K. Performance of a geogrid-reinforced and pile-supported highway embankment over soft clay: case study. *Journal of Geotechnical and Geoenvironmental Engineering*. 2007. 13(12). Pp. 1483–1493. DOI: 10.1061/(ASCE)1090-0241(2007)133:12(1483)
17. Waruwu, A., Hardiyatmo, H.C., Rifa'i, A. Deflection behavior of the nailed slab system-supported embankment on peat soil. *Journal of Applied Engineering Science*. 2017. 15(4). Pp. 556–563. DOI: 10.5937/jaes15-15113
18. Puri, A., Hardiyatmo, H.C., Suhendro, B., Rifa'i, A. Validating the curve of displacement factor due to full scale of one pile row nailed-slab pavement system. *International Journal of GEOMATE*. 2019. 17(59). Pp. 181–188. DOI: 10.21660/2019.59.65815
19. Waruwu, A., Hardiyatmo, H.C., Rifa'i, A. The Performance of the nailed slab system-supported embankment on peat soil. *International Review of Civil Engineering (I.R.E.C.E.)*. 2019. 10(5). Pp. 243–248. DOI: 10.15866/irece.v10i5.15757
20. Maulana, Azwar, Susanti, R.D., Waruwu, A. Potential of bamboo pile as reinforcement of peat soil under embankment. *ARPJ Journal of Engineering and Applied Sciences*. 2018. 13(1). Pp. 52–56.
21. Maulana, M., Hanova, Y., Waruwu, A., Putra, E.R. Simplified method for prediction of settlement in bamboo piles-reinforced peat under embankment. *Journal of Applied Engineering Science*. 2019. 17(1). Pp. 35–42. DOI: 10.5937/jaes17-18793
22. Yudiawati, Y., Mochtar, I.B., Mochtar, N.E. Group capacity and efficiency of full friction piles on very soft soil. *International Journal of GEOMATE*. 2019. 16(57). Pp. 201–208. DOI: 10.21660/2019.57.68950
23. Ibrahim, Y.E-H., Nabil, M. Risk of surface blast load on pile foundations. *Magazine of Civil Engineering*. 2019. 90(6). Pp. 47–61. DOI: 10.18720/MCE.90.5
24. Waruwu, A., Susanti, R.D., Endriani, D., Hutagaol, S. Effect of loading stage on peat compression and deflection of bamboo grid with concrete pile. *International Journal of GEOMATE*. 2020. 18(66). Pp. 150–155. DOI: 10.21660/2020.66.62072
25. Boiko, I.L., Alhassan, M., Adejumo, T.W. Load-settlement test of full-scale foundation on concrete-grid reinforced soil. *Academic Journal. Journal of Civil Engineering and Construction Technology*. 2013. 4(6). Pp. 211–216. DOI: 10.5897/JCECT2013.0277
26. Rowe, R.K., Li, A.L. Geosynthetic-reinforced embankments over soft foundations. *Geosynthetics International*. 2005. 12(1). Pp. 50–85. DOI: 10.1680/gein.2005.12.1.50
27. Oh, Y.I., Shin, E.C. Reinforcement and arching effect of geogrid-reinforced and pile-supported embankment on marine soft ground. *Marine Georesources & Geotechnology*. 2007. 25(2). Pp. 97–118. DOI: 10.1080/10641190701359591
28. Farsakh, M.Y.A., Chen, Q. Evaluation of geogrid base reinforcement in flexible pavement using cyclic plate load testing. *International Journal of Pavement Engineering*. 2011. 12(3). Pp. 275–288. DOI: 10.1080/10298436.2010.549565

Contacts:

Aazokhi Waruwu, azokhiw@gmail.com

Rika Deni Susanti, razzanrikadeni@yahoo.com

Nurtiani Napitupulu, napitupulunurtiani@gmail.com

Jaya Oges Sihombing, jayanababan15050@gmail.com



DOI: 10.34910/MCE.106.11

Layer model of elasticity modulus prediction for lightweight concretes

A.S. Korolev^a , N. Vatin^b ^aSouth Ural State University, Chelyabinsk, Russia^bPeter the Great St. Petersburg Polytechnic University, St. Petersburg, Russia

*E-mail: korolev@sc74.ru

Keywords: light concretes, modulus of elasticity/deformation of concrete, concrete deformability, relative elastic and plastic deformations, layer calculation model

Abstract. Reducing the structures' weight is one of the basic approaches to improving the efficiency of construction. There are many developments in this area, especially with lightweight concretes. One of the problems for structural lightweight concrete is a fairly low modulus of elasticity and increased plastic deformations in extreme conditions due to the high porosity of the lightweight aggregates. Therefore, the assessment and prediction of the deformative properties of lightweight concretes is an urgent scientific task on a par with heavy concretes. Our previous work proved the performance of the layer calculation model for heavy concretes. In this research, we attempted to test the layer model when calculating the deformative properties of concretes containing lightweight aggregates.

1. Introduction

Developing a calculation model of the heavy concretes deformative properties, the dependence of the elastic modulus on the layer model with the number of layers $i=n$, the elastic modulus of the layer E_i and the relative thickness of the layer δ_i was proposed

$$E_c = \frac{E_1 E_2 \dots E_n}{\sum_{i=1}^n \delta_i \frac{E_1 \dots E_n}{E_i}} \quad (1)$$

Consideration of the graphic dependence of the heavy concrete elastic modulus with strength class B25 (Fig. 1) allows us to assess the non-additivity of the elastic modulus of concrete. It depends on the moduli of structural layers and the fundamentally high importance of both the elastic modulus of the aggregate and the elastic modulus of the contact zone "cement paste-aggregate" (ITZ) in the formation of the composite structure modulus. As seen in Fig.1 modulus calculated as the weighted average of the modulus of the layers is significantly higher than the actual one, which indicates that a decrease or increase in the elastic modulus of one of the layers leads to a disproportionate decrease or increase in the modulus of the entire structure. Therefore, the low modulus of elasticity of porous light aggregates leads to an intense decrease the modulus of elasticity of structural concrete. For example, the elastic modulus of heavyconcrete class B15 is about $2.3 \cdot 10^4$ MPa, and the elastic modulus of light concrete D1600 of the same class B15 is $1.4 \cdot 10^4$ MPa.



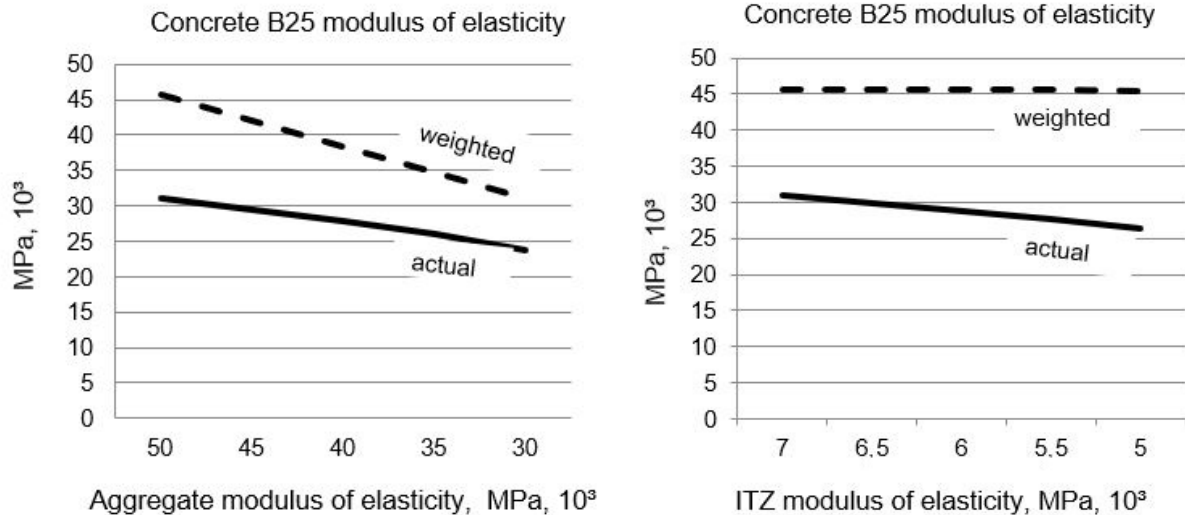


Figure 1. Relations of the concrete B25 elastic modulus to the elastic modulus of layers.

In heavy concretes, hydrated cement paste [1–2], aggregate [3–6], and the contact zone between them were used as layers [6–8]. In concretes with lightweight aggregate, at the initial stage of the hardening process, capillary pumping out the closing water from the binder layer, the structure of the cement hydrated paste in the layer and the contact zone is compact due to the above effect [9–12]. This is confirmed by the features of deformation under a load of heavy concretes in comparison with light ones on porous aggregates. If heavy concretes have significant plastic deformations when sustained at loading stages, then concretes on porous aggregates have almost no such plastic deformations [13–21]. As shown in previous studies, the main cause of plastic deformation of heavy concrete when withstood at loading stages is increased porosity and deformability of the cement hydrated paste and aggregate contact zone ITZ. Self-sealing of the contact zone with a light aggregate, leads to the absence of such plastic deformations.

In this regard, and connection with the different density and, as a consequence, the different modulus of small and large aggregates in the calculated layer model of concrete on a light aggregate, we propose to consider cement hydrated paste, fine and coarse aggregates as layers (Fig. 2).

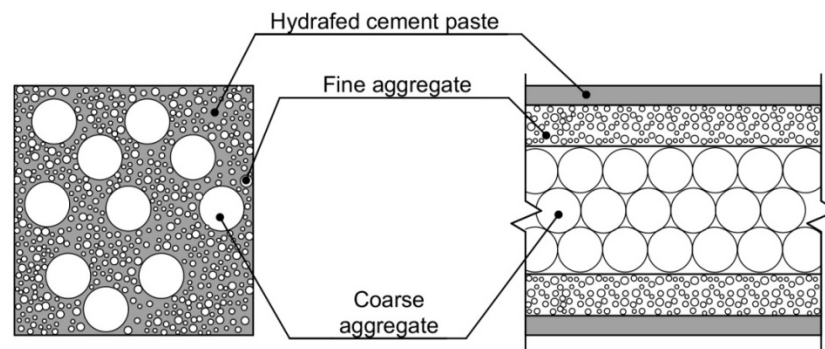


Figure 2. Calculated layer model of concrete deformability on a light aggregate.

A special feature of light concretes can be the use of both lightweight aggregate, and a combination of heavy and light aggregates, often fine heavy and coarse light. In the case of a combination of heavy and light aggregates, it is theoretically necessary to evaluate the modulus of the mortar part using the heavy concrete model, followed by an additional calculation using the two-layer "mortar–coarse aggregate" model. At the same time, it is possible to assume that in the process of pumping out the mix's water with a coarse light aggregate, the contact zone ITZ in the heavy mortar part is also compacted and its influence on the module is disappeared. Therefore, we will test the proposed model "cement hydrated paste–aggregate1–aggregate2".

2. Materials and Methods

The analytical method was used to select and evaluate the composites layer model calculation method.

Standard methods of Russian State Standards GOST 24452-80 "Concretes. Methods of prismatic, compressive strength, modulus of elasticity and Poisson's ratio determination" and GOST 22690-2015

“Concretes. Determination of strength by mechanical methods of nondestructive testing” were used to determine the modulus of elasticity and compressive strength of concrete of various classes. Each classes series of 3 samples were tested under compression on the Matest press with determination of longitudinal elastic and plastic deformation using digital deformation sensors on every sides of sample. Compression was made by 10 % of cracking stress stages to the 40 % of cracking stress (Fig.2). The elasticity modulus has been determined as a relation of 30 % cracking stress to the sum of elastic relative deformation except plastic on stages delay by standard. Compressive strength was determined on 6 samples series by standard.

To define the fact concrete elasticity modulus in our experiment, we used local producers' materials:

1. The keramzite gravel with an elastic modulus of $E_{ag2}=5 \cdot 10^3$ MPa;
2. The perlite sand with the $E_{ag1}=7 \cdot 10^3$ MPa;
3. The granite coarse aggregate and quartz sand with a strength of $R_{agg}=1000$ MPa and an elastic modulus of $E_{ag1}=50 \cdot 10^3$ MPa;
4. The Portland cement B42.5 CEM I with a water requirement of normal density of 25 % and the compressive strength of hydrated cement paste with W/C of normal density in standard age $R_{cem}=100$ MPa and an elastic modulus of $E_{cem}=50 \cdot 10^3$ MPa;
5. The Portland cement B27.5 CEM III with a water requirement of normal density of 27 % and the compressive strength of hydrated cement paste with W/C of normal density in standard age $R_{cem}=700$ MPa and an elastic modulus of $E_{cem}=30 \cdot 10^3$ MPa.

The contents of various classes mixture components are presented in Table 1.

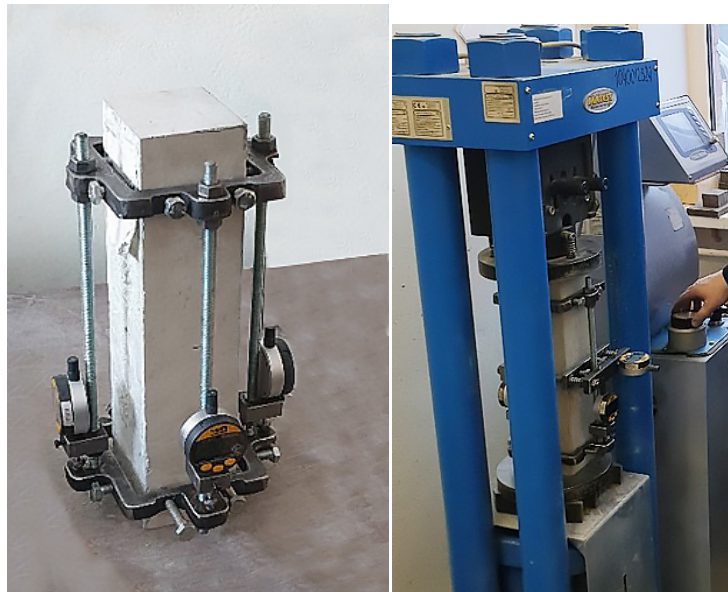


Figure 3. Concrete sample modulus of elasticity under compression testing.

3. Results and Discussion

Existing calculations of lightweight concrete elasticity modulus by M.Z Simonov, G.D. Zhiskrely, O.Y. Berg, A.L. Ambartsumyan and others used as a factors: concrete strength, aggregate elasticity modulus, average density, but not all components modulus together. It makes difficult to use these equation for modulus definition depending on mix components containing. Our calculation is determining the relative thicknesses of layers in first case, and these factors are most important in elasticity forming.

According to the proposed calculation model [22], the light concrete elastic modulus equation is

$$E_c = \frac{E_{cem} E_{ag1} E_{ag2}}{cem E_{ag1} E_{ag2} + ag1 E_{cem} E_{ag2} + ag2 E_{cem} E_{ag1}}, \quad (2)$$

E_{cem} is the modulus of elasticity of the cement hydrated paste layer;

E_{ag1} is the modulus of elasticity of the layer "fine aggregate";

E_{ag2} is the elastic modulus of the layer "coarse aggregate";

$cem, ag1, ag2$ are the relative thickness of the layers of cement, fine and coarse aggregates.

The relative thicknesses are determined from the condition of surface areas in the contact zones between the layers S_{itz} with the thicknesses δ equality

$$cem = \frac{\delta_{cem}}{\delta_{mv}} = \frac{S_{itz} \delta_{cem}}{S_{itz} (\delta_{cem} + \delta_{agg})} = \frac{V_{cem}}{V_{cem} + V_{agg}} = \frac{V_{cem}}{V_c}, \quad (3)$$

V_{cem} is a volume of cement paste;

V_c is a volume of concrete.

The relative thickness of the aggregate layers is determined by the same principle

$$ag1 = \frac{V_{ag1}}{V_c};$$

$$ag2 = \frac{V_{ag2}}{V_c}.$$

For testing the model lightweight concrete was produced in different versions:

1. Coarse aggregate is the keramzite gravel, fine aggregate is the quartz sand;
2. Coarse aggregate is the keramzite gravel, fine aggregate is the perlite sand with Portland cement B42,5 and B27,5;
3. Coarse aggregate is the granite, fine aggregate is the perlite sand.

Working compositions of light concrete mixes of our own concrete mixing plant of classes B5...B15, D800...D1600 were used for testing. Table 1 shows data for the sequential calculation of the elastic modulus of light concretes by the layer model based on the parameters of the modulus of components and composition of the light concrete mix - relative thicknesses $cem, ag1, ag2$. To assess the accuracy, the standard values of the elastic modulus for classes according to Russian Building Norms SNiP 2.03.01-84* (1996) "Concrete and reinforced concrete structures" were used.

Table 1. Calculated and standard characteristics of the lightweight concrete elastic modulus.

$Ag1$	B	D	E_{cem} , MPa, 10^3	E_{ag1} , MPa, 10^3	E_{ag2} , MPa, 10^3	C , kg/m ³	$Ag1$, kg/m ³	$Ag2$, kg/m ³	cem	$Ag1$	$Ag2$	E_c , MPa, 10^3	E_{st} , MPa, 10^3	E_{fact} , MPa, 10^3
	7,5	1200				330	650	250	0.18	0.32	0.50	8.9	8.7	9.0
Quartz	10	1400	50	40	5	360	720	210	0.24	0.35	0.41	10.5	11.0	10.9
	15	1600				540	940	100	0.28	0.45	0.27	14.1	14.0	15.1
	5	800				440	55	110	0.15	0.65	0.20	7.3	6.3	6.9
Perlite	7,5	1000	50	7	5	520	50	130	0.18	0.60	0.22	7.5	7.2	7.5
	10	1200				880	35	165	0.30	0.40	0.30	8.8	9.5	9.0
Perlite/ PC B27.5	5	1000	30	7	5	520	50	130	0.18	0.60	0.22	7.4	7.2	7.2
Perlite/ Granite	10	1400	30	7	50	540	55	510	0.18	0.65	0.17	10.0	11.0	9.5

As can be seen from the data in Table 1, the method provides good convergence in predicting the modulus of elasticity, calculated and actual values difference is not more than 15 %.

It is noticeable that with equal density classes, the moduli of elasticity of concretes on heavy and light fine aggregates with the very different elasticity moduli are the same but strength of perlite concrete is higher. It causes due to the greater relative thickness of the layer of the most modular component that is cement hydrated paste.

If, in order to economical efficiency, a part of the cement is replaced with micro additives, the subsequent decrease in the activity and elastic modulus of this cement hydrated paste slightly affects the light concrete elastic modulus. In this case, the more significant factor is the thickness of the cement hydrated paste layer. As can be seen from the dependence (Fig. 4) of lightweight concrete elastic modulus on hydrated cement paste elasticity modulus, even over 50 % decrease of cement paste modulus result in less than 10 % modulus decrease.

The task of structural lightweight concrete D1400...D1800 producing can be equally achieved by using of heavy fine/light coarse and light fine/heavy coarse aggregates. Second version surprisingly provided homogeneous structure of concrete. This method realizing made possible to test additively layer model, but also it's useful in technology. Method's choose depends on composition's economical parameters.

Providing and improving the deformative properties of structural lightweight concrete can result in characteristics close to the levels of heavy concrete. With the slightly lower level of the elasticity modulus ($15 \dots 18 \cdot 10^3$ MPa) plastic deformations of lightweight concrete under prolonged loading are much less, and the weight of structures can be reduced by 30...50 % and more with a significant economic effect on the level of the entire building or structure.

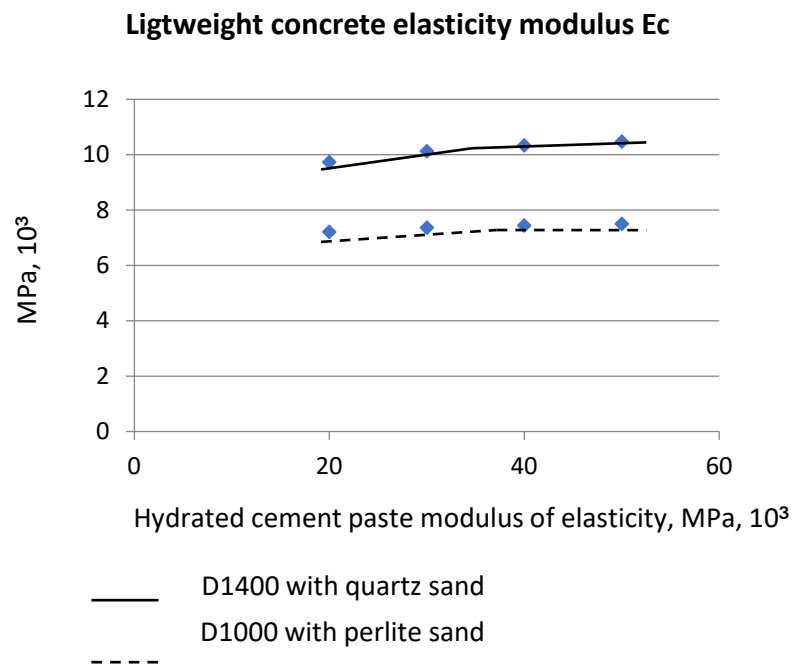


Figure 4. Lightweight elasticity modulus relation in cement hydrated paste elasticity modulus.

Analysis of the layer model result in principles of lightweight concrete elasticity modulus regulation:

1. The thickness of the layer of the binder component with the lowest content in the structure is of greater significance in the lightweight concrete deformation properties than the activity and modulus of its elasticity. It makes a great reserve of cement saving by cement class decreasing with elasticity level providing. Thus to increase the elastic modulus of lightweight concrete more efficiently increase the consumption of cement while reducing its activity and cost than increasing cement's activity.

2. Elastic modulus of aggregates, components with the highest content in light concrete, are determining for the concrete modulus of elasticity. And compositioning of light and heavy fine and coarse aggregates provides great possibilities for lightweight concrete modulus of elasticity regulation and providing.

4. Conclusion

As a result of analytical and experimental work, the suitability of the layer model for estimating the elastic modulus of lightweight cement composites was confirmed. The calculation model based on the layer

model operates on 6 factors: elastic modulus and relative thicknesses of the structural layers "cement hydrated paste", "fine aggregate", "coarse aggregate".

On the base of this model received the method of lightweight cement composites elasticity modulus calculation depending on mix components properties and containing. The method allows to solve two basic technological problems: 1) to ensure the normative deformability of the given density class concrete; 2) to identify ways to increase elastic properties within a given composition and raw materials.

5. Acknowledgment

The work was performed within the framework of the state task of the Ministry of science and higher education of the Russian Federation FENU-2020-0019.

References

1. Odelson, J.B., Kerr, E.A., Vichit-Vadakan, W. Young's modulus of cement paste at elevated temperatures. *Cement and Concrete Research*. 2007. Vol. 37. No. 2. Pp. 258–263. <https://doi.org/10.1016/j.cemconres.2006.11.006>
2. Sanahuja, J., Dormieux, L., Chanvillard, G. Modelling elasticity of a hydrating cement paste. *Cement and Concrete Research*. 2007. Vol. 37. No. 10. Pp. 1427–1439. <https://doi.org/10.1016/j.cemconres.2007.07.003>
3. Itskovich, S.M., Chumakov, L.D., Bazhenov, Yu.M. *Tekhnologiya zapolnitelej betona [Concrete aggregate technology]*. Vysshayashkola. Moskva, 1991. (rus)
4. Varlamov, A.A., Rimshin, V.I., Tverskoi, S.Y. The modulus of elasticity in the theory of degradation. *IOP Conference Series: Materials Science and Engineering*. 2018. 463. 022029. <https://doi.org/10.1088/1757-899X/463/2/022029>
5. Jurowski, K., Grzeszczyk, S. The influence of concrete composition on Young's modulus. *Procedia Engineering*. 2015. Vol. 108. Pp. 584–591. DOI: 10.1016/j.proeng.2015.06.181
6. Akhverdov, I.N. *Osnovy fiziki betona [Concrete physics fundamentals]*. Strojizdat, 1981. (rus)
7. Xingyi, Z., Gao, Y., Dai, Z., Corr, D., Shah, S. Effect of interfacial transition zone on the Young's modulus of carbon nanofiber reinforced cement concrete. *Cement and Concrete Research*. 2018. 107. Pp. 49–63. DOI: 10.1016/j.cemconres.2018.02.014.
8. Li, G., Zhao, Y., Pang, S.S. Four-phase sphere modeling of effective bulk modulus of concrete. *Cement and Concrete Research*. 1999. 29. Pp. 839–845. DOI: 10.1016/S0008-8846(99)00040-X.
9. Topçu, İ.B., Bilir, T., Boğa, A.R. Estimation of the modulus of elasticity of slag concrete by using composite material models. *Construction and Building Materials*. 2010. Vol. 24. No. 5. Pp. 741–748. <https://doi.org/10.1016/j.conbuildmat.2009.10.034>.
10. Young's modulus of fiber-reinforced and polymer-modified lightweight concrete composites. Kurugöl, Sedat, Tanaçan, Leyla iErsoy, HalitYaşa. 2008. *Construction and Building Materials*. DOI: 10.1016/j.conbuildmat.2007.03.017
11. Usanova, K., Barabanshchikov, Y.G. Cold-bonded fly ash aggregate concrete. *Magazine of Civil Engineering*. 2020. Pp. 104–118. https://doi.org/10.1007/978-3-030-33342-3_10
12. Silva, R.V., De Brito, J., Dhir, R.K. Establishing a relationship between modulus of elasticity and compressive strength of recycled aggregate concrete. *Journal of Cleaner Production*. 2016. Vol. 112. Part 4. Pp. 2171–2186. DOI: 10.1016/j.jclepro.2015.10.064
13. Brooks, J.J. *Elasticity of Concrete*. Concrete and Masonry Movements. 2015.
14. Noguchi, T., Nemati, K.M. Relationship between compressive strength and modulus of elasticity of high-strength concrete. *Proceedings of the 6th International Conference on Fracture Mechanics of Concrete and Concrete Structures*. 2007. 9780415446174.
15. Sprince, A., Pakrastins, L., Gailitis, R. Long-Term Parameters of New Cement Composites. 3rd International Conference on the Application of Superabsorbent Polymers (SAP) and Other New Admixtures Towards Smart Concrete. 2020. Vol. 24. Pp. 85–94. https://doi.org/10.1007/978-3-030-33342-3_10
16. Salman, M.M., Al-Amawee, A. The Ratio between Static and Dynamic Modulus of Elasticity in Normal and High Strength Concrete. *Journal of Engineering and Development*. 2006. Vol. 10. No. 2.
17. Sideris, K.K., Manita, P., Sideris, K. Estimation of ultimate modulus of elasticity and Poisson ratio of normal concrete. *Cement and Concrete Composites*. 2004. Vol. 26. No. 6. Pp. 623–631. DOI: 10.1016/S0958-9465(03)00084-2
18. Wongpa, J., Kiattikomol, K., Jaturapitakkul, C., Chindapasirt, P. Compressive strength, modulus of elasticity, and water permeability of inorganic polymer concrete. *Materials and Design*. 2010. Vol. 31. No. 10. Pp. 4748–4754. DOI: 10.1016/j.matdes.2010.05.012
19. Yildirim, H., Sengul, O. Modulus of elasticity of substandard and normal concretes. *Construction and Building Materials*. 2011. Vol. 25. No. 4. Pp. 1645–1652. DOI: 10.1016/j.conbuildmat.2010.10.009
20. Alsalman, A. Dang, C.N., Prinz, G.S., Hale, W.M. Evaluation of modulus of elasticity of ultra-high performance concrete. *Construction and Building Materials*. 2017. Vol. 153. Pp. 918–928. DOI: 10.1016/j.conbuildmat.2017.07.158
21. Bahr, O., Schaumann, P., Bollen, B., Bracke, J. Young's modulus and Poisson's ratio of concrete at high temperatures: Experimental investigations. *Materials & Design*. 2013. Vol. 45. Pp. 421–429. DOI: 10.1016/j.matdes.2012.07.070
22. Korolev, A.S., Vatin, N.I. Elasticity modulus of cement composites predicting using layer structure model. *Magazine of Civil Engineering*. 2021. 104(4). Article No. 10413. DOI: 10.34910/MCE.104.13

Contacts:

Alexander Korolev, korolev@sc74.ru

Nikolai Vatin, vatin@mail.ru



DOI: 10.34910/MCE.106.12

Impact of elevated temperature on the behavior of strengthened RC beams with CFRP

R. Al-Rousan 

Jordan University of Science and Technology, Irbid, Jordan

E-mail: rzalrousan@just.edu.jo

Keywords: reinforced concrete, elevated temperature, flexural strength, fiber reinforced polymer, experimental

Abstract. Elevated temperatures (beyond 500°C) severely deteriorate concrete structures due to vapor pressure, decomposition of cement hydration products, inhomogeneous volume changes of concrete's ingredients. Carbon fiber-reinforced polymer (CFRP) composite materials provide the most significant retrieval of the structural performance to severely heat-damaged structural concrete members. Therefore, an experimental study investigated the influence of elevated temperatures on the flexural behavior of reinforced concrete (RC) beams strengthened externally with CFRP. For this purpose, thirty-two reinforced concrete beams were cast. Twenty-four beams were externally strengthened with CFRP, and eight beams were unanchored and left as a control. The beams then were tested under four-point bending to assess their structural performance in terms of failure modes and load-displacement relations. The experimental results have clearly shown that the control beams suffered from ductile failure. The CFRP strengthened beams failed by debonding the CFRP sheets after yielding the flexural steel reinforcement. The strengthened beams showed an increase in the ultimate load-carrying capacity accompanied by an enhancement in mid-span deflection in different percentages concerning the control beam. The CFRP sheets' ability in the bridging of the crack increased with the increase of CFRP length by providing more development length in catching the two sides of the major flexural crack. The load-deflection curve can be divided into two stages; the first portion is nearly a straight line, and the second stage with slope experienced a slight increase in the load with a large increase in deflection. The second stage formed after the yielding of steel reinforcement and formation of the main flexural crack where the applied load was carried by the CFRP sheet. Finally, the influence of the exposure temperature on the ductility, energy absorption, and ultimate load reduction percentage increases with the increase of temperature.

1. Introduction

Nowadays, the primary rehabilitation and strengthening composite materials of flexure or shear deficient reinforced concrete (RC) structures are carbon-fiber-reinforced polymer materials (CFRP). The CFRP external strengthening of the concrete structure increased the shear or flexural capacity. This composite material's integrity depends on the bond condition and how it can transfer stress from the concrete debonding surface to CFRP composite materials. The reliability of the bond between the concrete surface to CFRP composite materials determines the accomplishment of externally strengthening of deficient RC members. The significant considerations consist of CFRP composite material type, the number of CFRP composite, surface preparation, bonded length, laminate, and epoxy quality application.

CFRP materials are frequently used in structural engineering applications for the repair and strengthening of existing concrete structures. Externally bonded FRP composite is used to strengthen concrete beams in flexure and shear. Many experimental observations indicated that the debonding at the interface between concrete and FRP is a typical failure mode of reinforced concrete beams strengthened with externally bonded CFRP [1, 2]. CFRP composite materials have come to the forefront as promising

Al-Rousan, R. Impact of elevated temperature on the behavior of strengthened RC beams with CFRP. Magazine of Civil Engineering. 2021. 106(6). Article No. 10612. DOI: 10.34910/MCE.106.12

© Al-Rousan, R., 2021. Published by Peter the Great St.Petersburg Polytechnic University.



This work is licensed under a CC BY-NC 4.0

materials and systems for structural retrofit. Glass fiber reinforced polymer (GFRP) and carbon fiber reinforced polymer (CFRP) have higher tensile strength but its strength is not fully utilized due to debonding problem and brittle tensile behavior. The general influence is clearly an increase in the peak loads of the specimens [3, 4].

Elevated temperatures cause severe damage for reinforced concrete (RC) structures, such as RC beams. RC beams have been reported to loss strength and stiffness with relatively large permanent deformations because of exposure to high temperatures [5]. These harmful effects could be attributed to the deterioration of mechanical characteristics of concrete and steel rebars and the redistribution of stresses within the beam due to the elevated temperatures [5, 6]. Currently, the most commonly used technique to repair the heat-damaged RC beams is using CFRP composites. These sheets are advanced materials that can be easily applied to the structures and characterized by outstanding mechanical and corrosion resistance characteristics. Various studies were performed to investigate the flexural behavior of RC beams wrapped with CFRP. The results showed that externally bonded CFRP sheets and laminates enhance the beams' flexural behavior and recover, to a specific limit, the flexural strength of heat-damaged beams. Strengthening level of recovery depends on several factors such as fire resistance [7], elevated temperature [8, 9], fiber type [10–13], analysis type [14–18], energy integrity resistance [19], anchored system [20], heating condition [21, 22], degree of beam's damage and geometry and type of fiber sheet [23], and safety factors for CFRP strengthening of bridges [24].

Reinforcing concrete structures are often subjected to heating cycles–cooling such as in chimneys, concrete foundations for launching rockets carrying spaceships, concrete near to the furnace, clinker silos, and nuclear power plants, or those subjected to fire then extinguished using water. Temperature cycles are critical to the stability of concrete structures and require considerations upon design [25, 26]. As well stipulated, the mechanical properties of concrete are preserved for exposure temperatures below 300 °C, yet are decreased considerably as the temperature exceeds 500 °C [27]. Additional damage results from rapid cooling such as in the case of distinguishing of fire with cool water due to creation of temperature gradient between concrete core and its surface. This results in tensile stresses on the concrete surface that are high enough to crack concrete, and this is considered as another source of damage results from incompatible expansion and contraction of aggregate and surrounding cement paste. The magnitude of damage is influenced by many factors such as the size of concrete members, the type of cement and aggregate, the concrete moisture content, and the predominant environmental factors, those are represented in heating exposure time, and rate, type of cooling, and maximum temperature attained [28]. Different types of materials and techniques were used in strengthening and retrofitting existing concrete structures, such as steel plate bolting, reinforced concrete jackets, prestressed external tendons, and most recently, CFRP composite which has been used on a large scale in different countries. CFRP composites have many advantages over conventional methods represented in ease of application, high strength-to-weight ratio, excellent mechanical strength, and good resistance to corrosion, especially that most structures are damaged due to dynamic loads, corrosion of steel, and freeze-thaw cycles as well as the CFRP composites have disadvantages such as the low ductility of CFRP compared to steel, low fire resistance, problematic bonding to the structure [29–31].

This research will be useful for retrofitting the existing buildings, mainly for buildings exposed to elevated temperatures. Furthermore, the ACI 440 guideline [30] concluded that the behavior and endurance of FRP-reinforced concrete structures under exposure to high heat is still not well understood. Therefore, essential issues to produce effective, economical, and successful CFRP strengthening were needed. Also, the impact of CFRP external strengthening on the behavior of flexural deficient reinforced concrete beams exposed to elevated temperature must receive miniature consideration. The scientific problem considered in the study is indeed one of the problems in the modern theory of flexural deficient reinforced concrete beams. A lack of literature regarding flexural behavior of deficient beams exposed to elevated temperature necessitated conducting the present investigation. In this study, experimental program was carried out to find the improvements in the strength and ductility behavior of RC beams confined externally with CFRP. The main parameters studied were the length of CFRP sheets (400, 600, and 800 mm) and elevated temperature (23 °C, 150 °C, 250 °C, and 500 °C).

2. Methods

2.1. Experimental Work

Thirty-two (two beams were made from each type) beams were casted and tested as simply supported under four points' loading, as shown in Fig. 1. The tested beams were 1100 mm long with cross-sectional dimensions of 150×250 mm. The investigated parameters in this study are the length of CFRP sheets (400, 600, and 800 mm) and elevated temperature (23 °C, 150 °C, 250 °C, and 500 °C) as shown in Table 1. The designation and steel reinforcement (yielding stress of 420 MPa) of the tested beams are summarized in Table 1 and Fig. 1, respectively.

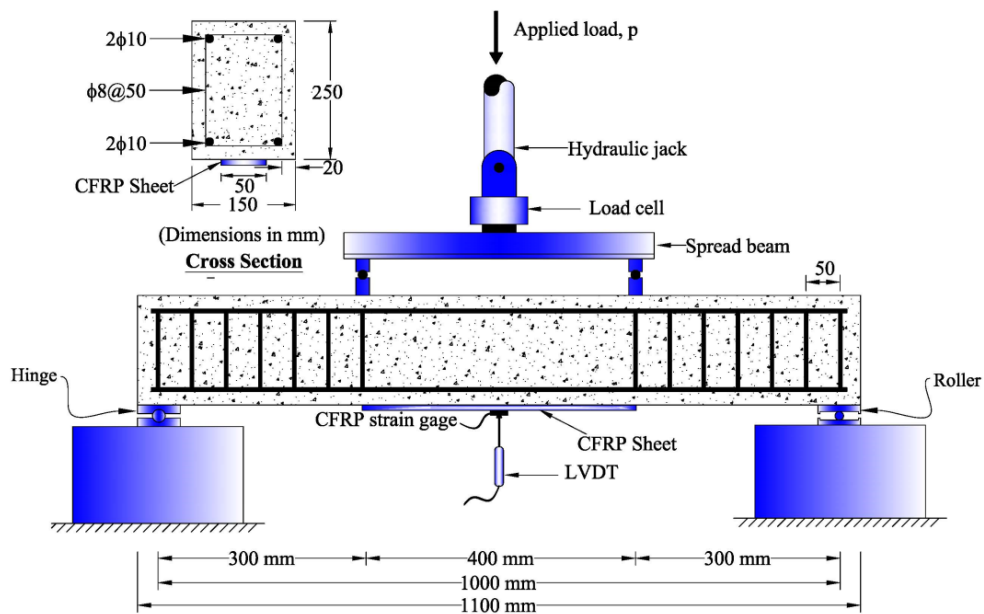


Figure 1. Setup and reinforcement details of the beams.

Table 1. The details of failure of tested shear beams.

Group	Specimen	T , °C	CFRP Configuration	P_u , kN	Δ_u , mm	ε_f , $\mu\varepsilon$	$\varepsilon_f / \varepsilon_{fu}$, %
1	FBT23-0	23	None	101.1	10.8	---	---
	FBT23-400		CFRP sheet (length of 400 mm and width of 50 mm)	113.8	12.5	4685	0.28
	FBT23-600		CFRP sheet (length of 600 mm and width of 50 mm)	121.7	14.0	5750	0.34
	FBT23-800		CFRP sheet (length of 800 mm and width of 50 mm)	132.2	15.8	6858	0.41
2	FBT150-0	150	None	95.3	10.5	---	---
	FBT150-400		CFRP sheet (length of 400 mm and width of 50 mm)	108.7	11.6	4279	0.26
	FBT150-600		CFRP sheet (length of 600 mm and width of 50 mm)	117.4	12.1	5285	0.32
	FBT150-800		CFRP sheet (length of 800 mm and width of 50 mm)	128.8	13.2	6326	0.38
3	FBT250-0	250	None	82.7	9.9	---	---
	FBT250-400		CFRP sheet (length of 400 mm and width of 50 mm)	95.5	10.7	3817	0.23
	FBT250-600		CFRP sheet (length of 600 mm and width of 50 mm)	103.1	11.2	4323	0.26
	FBT250-800		CFRP sheet (length of 800 mm and width of 50 mm)	113.1	12.1	5163	0.31
4	FBT500-0	500	None	62.7	9.3	---	---
	FBT500-400		CFRP sheet (length of 400 mm and width of 50 mm)	72.6	9.9	3334	0.20
	FBT500-600		CFRP sheet (length of 600 mm and width of 50 mm)	79.6	10.4	3890	0.23
	FBT500-800		CFRP sheet (length of 800 mm and width of 50 mm)	87.3	10.6	4343	0.26

Note: The values between parentheses are normalized with respect to the control, T: Temperature, P_u : Ultimate Load, Δ_u : Ultimate deflection, ε_f = CFRP strain, ε_{CFRP} is the strain in CFRP strips and ε_{fu} is the ultimate strain in CFRP strips of 16700 $\mu\varepsilon$.

2.2. Mix design

Table 2 shows the design of concrete mixture with the proportions by weight of water to cement ratio (w/c) of 0.59:1.00(cement (Ordinary Type I Portland cement)):2.98(Crushed limestone coarse aggregates

with the absorption of 2.3 %, a maximum aggregate size of 12.5 mm, and a specific gravity of 2.62):2.62 (fine aggregates with the absorption of 1.9 %, fineness modulus of 2.69, and specific gravity of 2.65). The superplasticizer as a percent of the cement weight was used to improve the concrete mixture's workability and result in a slump of about 50 mm.

Table 2. Mix design proportions.

Ingredient	Quantity (kg/m ³)
Cement	269
Water	158
w/c	0.59
Super- plasticizer	8
Coarse aggregate	891
Fine aggregate	834

The beams are casted using a tilting drum mixer with a capacity of 0.15 m³ (Fig. 2). Firstly, the tilting drum mixer inner surface was wetted. During the tilting drum mixer running, all the crushed limestone coarse aggregates with portion of the used water were added (Fig. 2). After that, the fine aggregates, cement, and water were added gradually. Finally, the superplasticizer with the last amount of used water was added to the concrete mixture. Lastly, all the concrete mixture ingredients were mixed for five minutes before pouring into wooden molds with inner dimensions of (100×150×1100 mm) and compacted with an electrical vibrator (Fig. 2). After twenty-four hours from the beams casting, all beams were de-molded and then cured in lime-saturated water tank for 28 days (Fig. 2).



Preparing the ingredients of mixture



Mixing concrete by tilting drum mixer



Wooden mold for casting beams



Casting concrete into molds



Casting concrete into cylinders



Water-cured tank for 28 days

Figure 2. The mixing, casting, and curing of reinforced concrete beams.

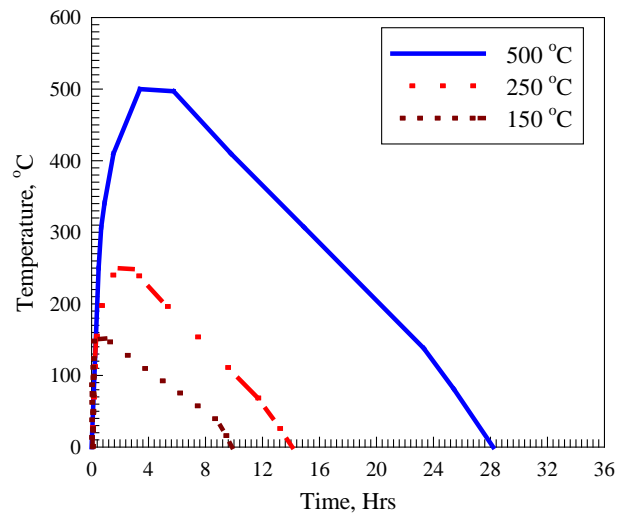


Figure 3. The time-temperature schedule.

2.3. Heat treatment Method

The average 28-day splitting compressive and tensile strengths of the tested cylinders were 25.0 MPa and 3.0 MPa, respectively. Cylindrical specimens and blocks were subjected to heat treatment for two hours at temperatures from 150-500 °C before allowing them to cool inside the special electrical furnace. The furnace is equipped with an electronic panel to automatically control the time of exposure and the temperature (maximum of 1200 °C). Fig. 3 shows the time-temperature schedule for the furnace. The expected temperature inside the beam during the heat treatment method is 28 % of the applied temperature on the exposed surface [30].

The effect of exposing specimens to elevated temperatures is demonstrated in Fig. 4, which depicts the residuals for compressive and splitting strength versus temperature. The curves followed almost similar trend behavior represented in a slight decrease at a temperature of 150 °C followed by a significant reduction at higher temperatures. The detrimental effect of high temperatures greater than 250 °C on both strengths can be referred to as thermally induced cracks and/or decomposition of cement binding materials (beyond 250 °C) [27]. The damage by heating caused map type cracking, which increased with elevated temperature without being accompanied by an apparent surface alteration. The reduction in residual strengths (compressive, splitting) which is (98 %, 97 %) at 150 °C to (61 %, 60 %) at 500 °C, are similar to reported values by Haddad et al. [27] as can be deduced from Fig. 4.

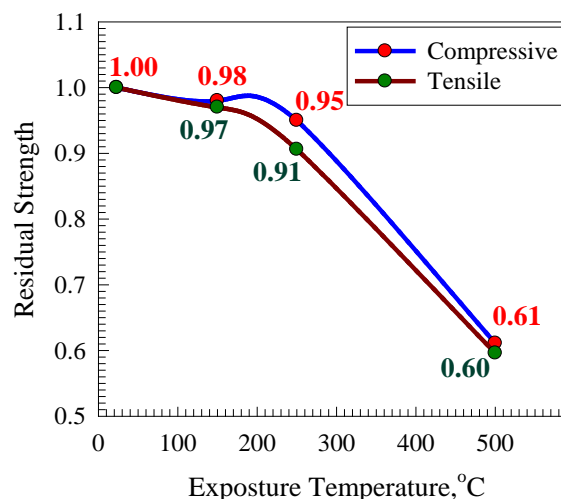


Figure 4. Residuals for compressive and splitting strengths versus exposure temperature.

2.4. Bonding of CFRP sheets to the concrete beams

The concrete beams were demolded after 24 hours of casting and cured in a lime-saturated water tank for 28 days. Firstly, the concrete bonded area was roughened and brushed with steel wire cup brush to provide leveled contact between CFRP sheets and concrete (Fig. 5). Secondly, any dust and loose particles were removed from the bonded area by using the air vacuum cleaner, and then the bonded area

was marked while the un-bonded area was covered with plastering tape to be free of epoxy (Fig. 5). Based on investigated parameters, the CFRP composite sheets are cut into sheets with a width of 50 mm and different lengths. Thirdly, the epoxy compounds (parts A and B) were prepared using a low-speed electric drill for at least 3 minutes to get a homogenous epoxy mixture. Fourthly, the epoxy first layer was applied uniformly over the bonded area and then the CFRP composite sheet (the tensile strength of 4900 MPa, thickness of 0.166 mm, elongation at break of 2.1 %, elastic modulus of 230 GPa) was placed onto the epoxy. Plastic roller was used along the fiber direction in order to remove any entrapped air bubbles. Finally, the epoxy second layer was applied over the CFRP sheet bonded area to make sure epoxy homogeneous distribution (Fig. 5).



Marking the area of CFRP sheets bonded using plastering tape



Concrete bonded area were roughened and brushed with steel wire cup brush



Applying the first layer of epoxy onto CFRP sheets surface



Applying the two layers of epoxy onto CFRP sheets surface

Figure 5. Bonding of CFRP sheets to reinforced concrete beams.

2.5. Testing Setup

All beams were tested under four-point loading with a simply supported span of 1000 mm (Fig. 1). The two supports are one roller, and the other one is a hinge, as well as the loading points were made from steel to make sure zero deformation. A hydraulic testing machine is used to apply the load with a displacement loading rate of 0.1 mm/sec. The vertical linear variable displacement transducer (LVDT) is used to record the mid-span deflection which is placed at the bottom of the beam (Fig. 1). Also, one strain gauge was placed in a position such that to record the CFRP tensile strain. The tested results (load-deflection curves and the CFRP strain) were collected using the data acquisition system, while the failure modes and cracks pattern were obtained visually.

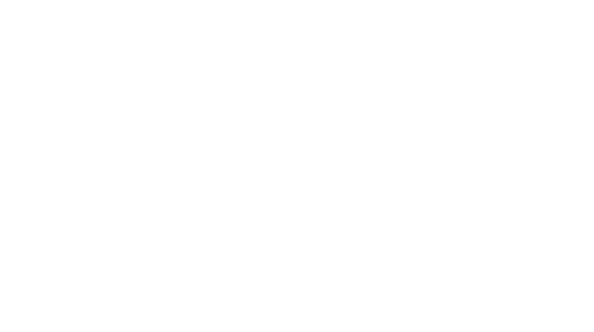
3. Results and Discussion

3.1. Failure Mode

The crack patterns and mode of failure developed during testing of all RC beams are shown in Fig. 6. In control beam, the first crack appeared in the middle of the constant moment region followed by formation of additional nearby flexural cracks (Fig. 6(a)). In all beams, the first flexural crack developed in the middle of the beam and at the tension side (within the constant moment region) (Fig. 6(b)).



23 °C



150 °C



250 °C

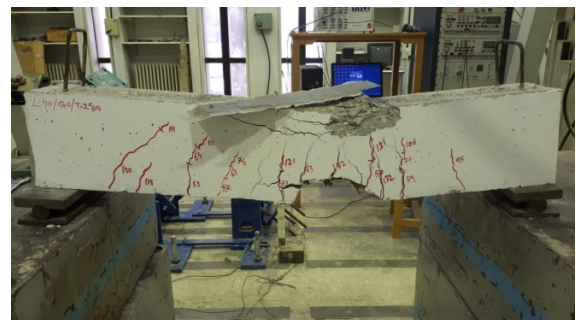


500 °C

(a) Effect of elevated temperature



0 mm (Control)



400 mm



600 mm



800 mm

(b) Effect of CFRP bonded length

Figure 6. The typical failure mode of tested beams.

The failure in the control beams (conventionally reinforced) occurred by yielding steel reinforcement followed by the crushing of the concrete in the beams' compression zone in the constant moment region. As load approached failure, local concrete crushing under the loading points was observed, as shown in Fig. 6(a). The strengthened beams failed by debonding the CFRP sheets after yielding the flexural steel reinforcement except the ductile flexure failure shown in Fig. 6(b). Upon yielding the steel reinforcement, the CFRP sheet picked up more strains and contributed to the beams' further load carrying capacity. After

failure, the CFRP sheet partially delaminated and it was observed that the sheet had adhered well to the concrete. The additional strength provided by the CFRP sheet delayed cracking and increased the load carrying capacity of the beams after yielding of steel occurred. It was noticed that the cracks numbers, distribution and length visibly depends on the CFRP sheet length (Fig. 6(b)). Inspection Fig. 6 reveals that crack distribution and numbers increased with the increase of elevated temperature (Fig. 6(a)) and length CFRP sheet length (Fig. 6(b)). As a matter of fact, Ahmed et al. [32] reported all the beams failed by flexural failure mode and the tested beams reveal a dramatic effect and spalling in the concrete cover, especially at temperature of 500 °C and more as well as at the end of the testing some crushing cracks caused by compression failure appeared at the top surface. But the crack from the tension side up to top of the cracking section neutral axis decreased with the increase of the elevated temperature (Fig. 6(a)) and length CFRP sheet length (Fig. 6(b)). The increase in crack width and the reduction in beam capacity after the elevated temperature is due to the residual concrete strength after elevated temperature exposure, which is much lower than that at room temperature [32]. This is due to the CFRP sheets ability in the bridging of the flexural cracks by providing adequate development length in catching the two sides of the major flexural crack.

3.2. CFRP strain

Fig. 7 shows the typical load-CFRP strain curve for all tested beams. Fig. 7 reveals that the tensile stresses develop in the CFRP composites after the yielding of the steel reinforcement. Furthermore, the maximum tensile stresses occurred close to the middle of the CFRP composite that intersects the first flexural crack to the beam's mid-span, as shown in Fig. 7. Also, it is noticed that all tested beams had CFRP strain below the maximum value of 16700 $\mu\epsilon$ as shown in Table 1 as the percentage of CFRP ultimate strain. Inspection of Table 1 reveals that the length of CFRP sheets had a substantial immct on the efficiency of CFRP sheets for beams exposed to 23°C with a percentage concerning ultimate strain of CFRP sheet of 28 %, 34 %, and 41 % for 400 mm, 600 mm, and 800 mm, respectively. While, the percentage of beams exposed to 150°C with a percentage concerning the ultimate strain of CFRP sheet of 26 %, 32 %, and 38 % for 400 mm, 600 mm, and 800 mm, respectively, and this equivalent to 0.93 of the beams strains exposed to 23 °C. The percentage of beams exposed to 250 °C with a percentage for the ultimate strain of CFRP sheet of 23 %, 26 %, and 31 % for 400 mm, 600 mm, and 800 mm, respectively, and this equivalent to 0.76 of the beams strains exposed to 23 °C. Finally, the percentage of beams exposed to 500 °C with a percentage for the ultimate strain of the CFRP sheet of 20 %, 32 %, 26 % for 400 mm, 600 mm, and 800 mm, respectively, and this equivalent to 0.63 of the beams strains exposed to 23 °C.

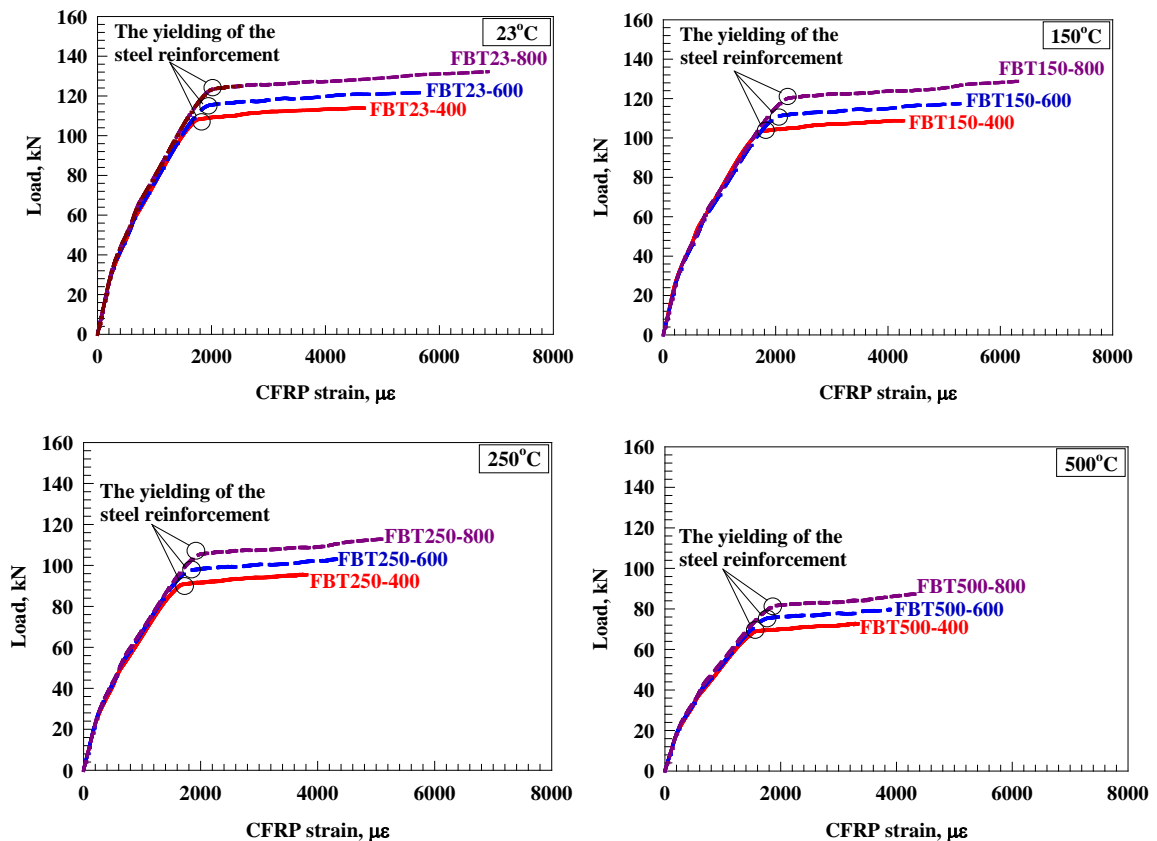


Figure 7. Typical load-CFRP strain curve.

CFRP strain development was less than $2000 \mu\epsilon$ (12 % of the ultimate strain of CFRP sheet) before the steel reinforcement yielding. After the steel reinforcement yield, the CFRP strain increased rapidly and continued to increase until the beam failure, as shown in Fig. 7. It can be observed that the strain in the CFRP developed at a high rate as the applied load increases.

3.3. Load-deflection behavior

The load versus mid-span deflection curves for typically tested beams are shown in Fig. 8. The mid-span deflection curves are plotted in a way that allows for comparing the effect of CFRP sheet length for beams in terms of elevated temperature. Inspection of Fig. 8 reveals that the load-deflection curve can be divided into two stages; the first stage is from zero loadings up to yielding of steel reinforcement (Stabilization of the behavior) with nearly a straight line with rapidly increasing in load and slightly increasing in deflection. Then after the yielding of steel reinforcement (indicating a reduction in the beam stiffness and the CFRP sheets handled the applied load), the slope of the curve experienced a slight increase in the load with a large increase in deflection, and this is based on investigated parameters. At ultimate load, the load was dropped suddenly to zero after crashing of the compression zone. The load versus mid-span deflection curves for control and damaged beams showed similar trend behavior, as depicted in Fig. 8: curves were linear up to a certain point before became nonlinear. A limited linear portion can be clearly noticed for damaged beams because of concrete's thermal cracking. Similar trend behavior was noticed by Haddad and Almomani [33] in which the curves showed linear behavior at the initial stages of loading before turned nonlinear behavior thereafter. The degradation in mechanical properties and softening in damaged beams is referred to as the reduction in (a) the yield strength of steel reinforcing bars; (b) bond strength between steel reinforcement and concrete; and (c) concrete compressive strength, which was reduced by about 61 % of its intact value. Inspection of Fig. 8 reveals that the load-deflection curve was extensively affected by elevated temperature and CFRP bonded length in terms of ultimate load, ultimate deflection, toughness, and stiffness reflected either limited improvement and even degradation in the mechanical response of strengthened damaged, as compared to un-damaged control beams, as depicted in Fig. 8. In addition, the larger CFRP bonded length showed better performance than those with a small CFRP bonded length. Besides, the curve's performance decreased with the increase of exposed temperature, as shown in Fig. 8.

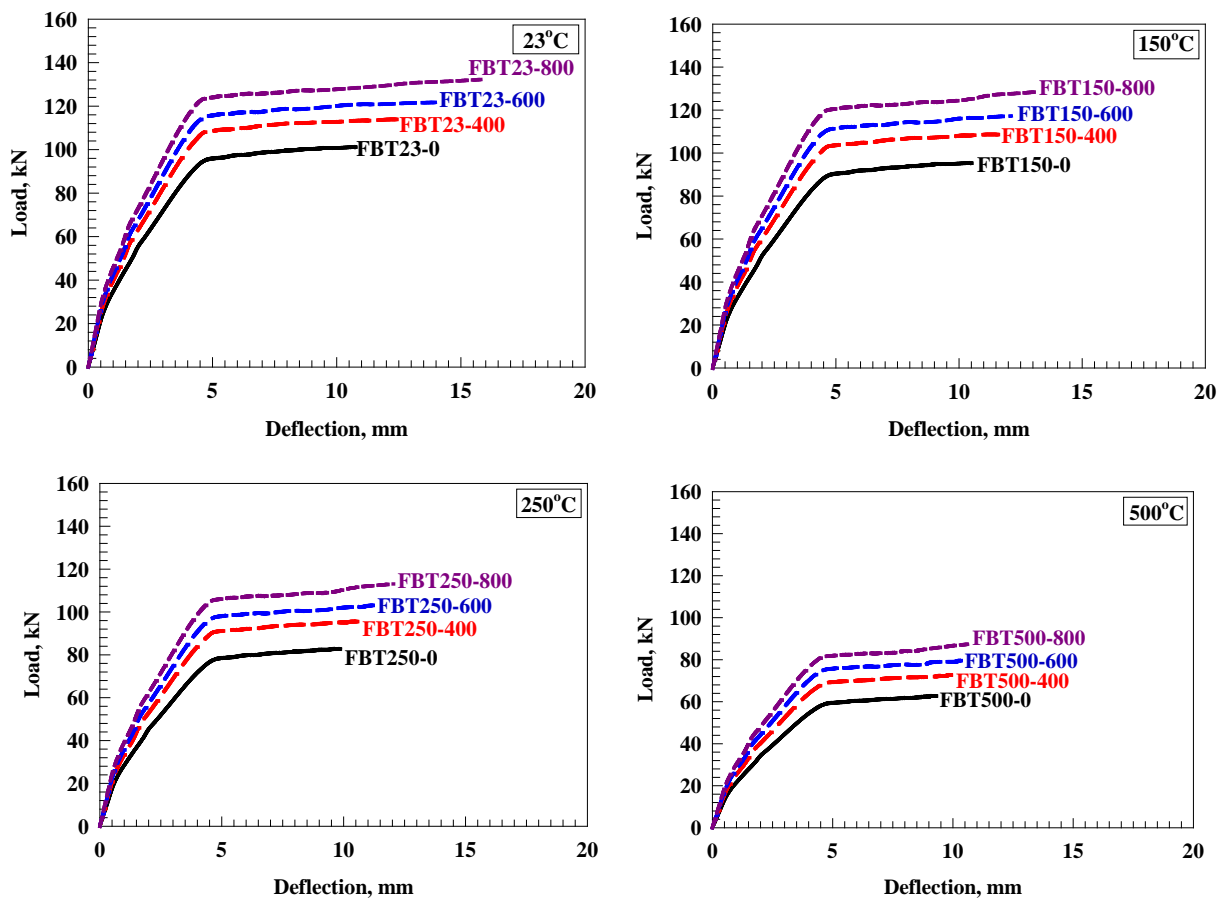


Figure 8. Load-deflection curves for the tested beam.

3.4. Ultimate load capacity and corresponding deflection

Table 3 shows the characteristics of the load-deflection curves for tested beams. The assessment of beams for load capacity and corresponding deflection shows the excellent performance of RC members. For strengthened RC members, deflection and ultimate load capacity can be related to the serviceability, and ultimate load limit states, respectively, as shown in Table 3. The load capacity and deflection percentages are defined as the ultimate load capacity and deflection, respectively, of CFRP strengthened beam divided by the ultimate deflection and load capacity of the un-strengthened beam (undamaged beam) as shown in Fig. 9. The strength ratio also predicts the increase of load that the model can sustain. Inspection of Fig. 9 reveals that the strength percentage increased significantly with the increase of the length of CFRP sheets. The average ultimate load enhancement percentage (Fig. 9) for tested beams with respect to the control beam is 14 %, 24 %, and 35 % for 400 mm, 600 mm, and 800 mm, respectively. Whereas, the average ultimate load reduction percentage (Fig. 9) for tested beams with respect to beams exposed to 23 °C is 4 %, 16 %, and 36 % for 150 °C, 250 °C, and 500 °C, respectively. Thus, it is possible to regain the 96 %, 84 %, and 64 % of the initial capacity of un-damaged beam (23 °C) 150 °C, 250 °C, and 500 °C, respectively. Therefore, the regaining percentage of the initial capacity is decreased with the increase of exposed temperature.

Table 3. Characteristics of load-deflection behavior.

Group	Specimen	T, °C	Elastic stiffness (kN/mm)	Toughness (kN.mm ²)	SF	DF	PF
1	FBT23-0	23	29.0	871	2.26	1.06	2.40
	FBT23-400		34.6	1187	2.69	1.26	3.40
	FBT23-600		37.3	1438	2.99	1.50	4.48
	FBT23-800		40.3	1783	3.43	1.79	6.12
2	FBT150-0	150	27.4	799	2.21	1.04	2.30
	FBT150-400		33.1	1033	2.49	1.23	3.08
	FBT150-600		35.9	1172	2.59	1.47	3.80
	FBT150-800		39.3	1413	2.87	1.75	5.02
3	FBT250-0	250	23.7	640	2.08	0.97	2.02
	FBT250-400		29.0	818	2.29	1.16	2.65
	FBT250-600		31.6	938	2.40	1.38	3.31
	FBT250-800		34.5	1109	2.61	1.64	4.28
4	FBT500-0	500	18.0	451	1.96	0.92	1.80
	FBT500-400		22.1	570	2.14	1.09	2.33
	FBT500-600		24.4	657	2.22	1.30	2.88
	FBT500-800		26.6	734	2.30	1.55	3.56

Note: SF: strength factor, DF: Ductility factor, PF: Performance Factor = SF×DF

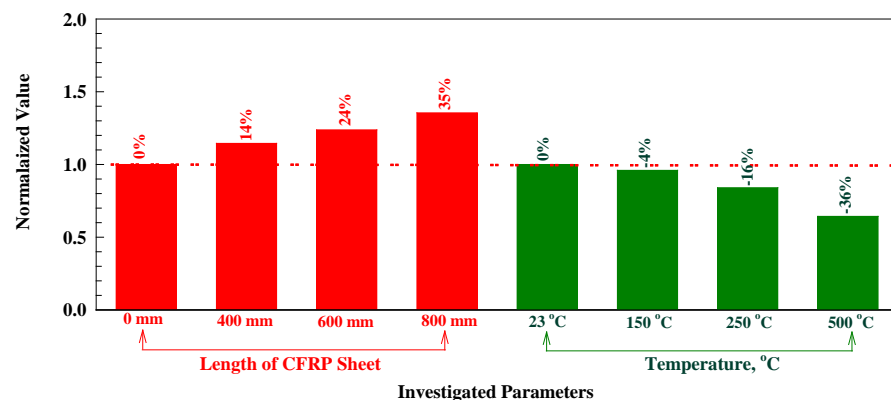


Figure 9. Normalized ultimate load capacity for control beam.

The deflection indicates how much the strengthened RC beams can sustain deformations without failure. The deflection percentage is defined as the ratio of the strengthened beam's ultimate deflection to the ultimate deflection of the control beam (undamaged beam), as shown in Fig. 10. Fig. 10 shows that the ductility percentage also significantly increased with the increase in the length of CFRP sheets and decreased with exposed temperature. The average ultimate deflection enhancement percentage (Fig. 10) for tested beams with respect to control beam is of 10 %, 18 %, and 27 % for 400 mm, 600 mm, and 800 mm, respectively, and this equal to 0.71 times the enhancement percentages in ultimate load. Whereas, the average ultimate deflection reduction percentage (Fig. 10) for tested beams with respect to beams exposed to 23 °C is 10 %, 17 %, and 23 % for 150 °C, 250 °C, and 500 °C strips, respectively, and this equal to 0.64 times the reduction percentages in ultimate load.

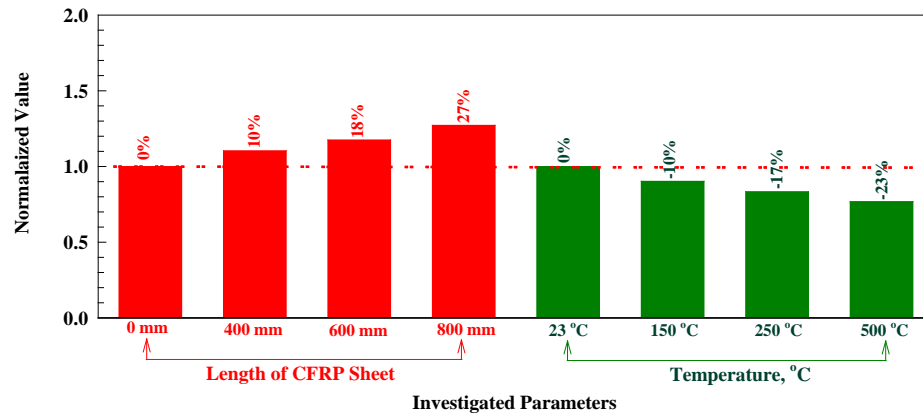


Figure 10. Normalized ultimate deflection for control beam.

3.5. Elastic stiffness

The elastic stiffness determines the crystal's response to an externally applied strain (or stress) and provides information about the bonding characteristics, mechanical and structural stability. The elastic stiffness represents the first stage of the load-deflection curve's slope before initiation of the first main flexural crack. For comparison, each strengthened beam's elastic stiffness with CFRP sheets was normalized for the control beam without CFRP sheets, as shown in Fig. 11. Fig. 11 reveals that the elastic stiffness percentage increased significantly with the increase of length of CFRP sheets. The average elastic stiffness enhancement percentage (Fig. 11) for tested beams with respect to control beam is of 21 %, 32 %, and 44 % for 400 mm, 600 mm, and 800 mm, respectively. Whereas, the average elastic stiffness reduction percentage (Fig. 11) for tested beams with respect to beams exposed to 23 °C is 7 %, 15 %, and 37 % for 150 °C, 250 °C, and 500 °C strips, respectively.

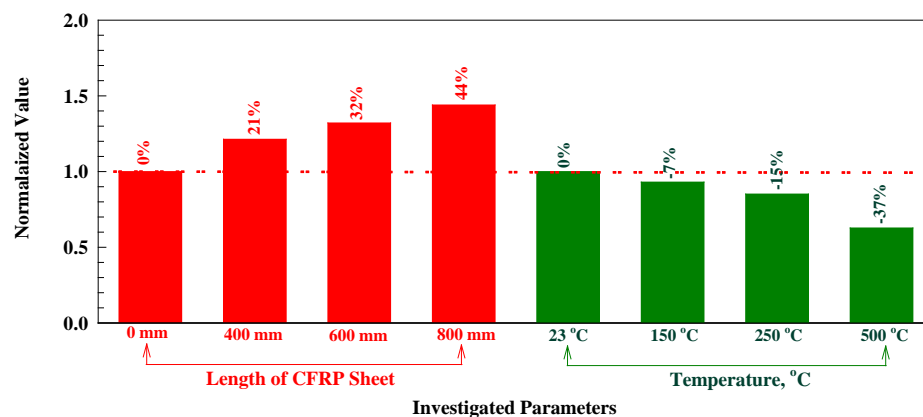


Figure 11. Normalized stiffness for control beam.

3.6. Toughness

In materials science and metallurgy, toughness is the ability to absorb energy and plastically deform without fracturing. One definition of material toughness is the amount of energy per unit volume that a material can absorb before rupturing. Toughness is calculated as the entire area under the load-deflection curve. In addition, the toughness of each strengthened beam with CFRP sheets was normalized with respect to the control beams without CFRP sheets as shown in Fig. 12. Inspection of Fig. 12 reveals that the toughness percentage increased significantly with the increase of length of CFRP sheets. The average toughness enhancement percentage (Fig. 12) for tested beams with respect to control beam is of 30 %,

51 %, and 79 % for 400 mm, 600 mm, and 800 mm, respectively. Whereas, the average toughness reduction percentage (Fig. 12) for tested beams with respect to beams exposed to 23 °C is 15 %, 33 %, and 53 % for 150 °C, 250 °C, and 500 °C strips, respectively.

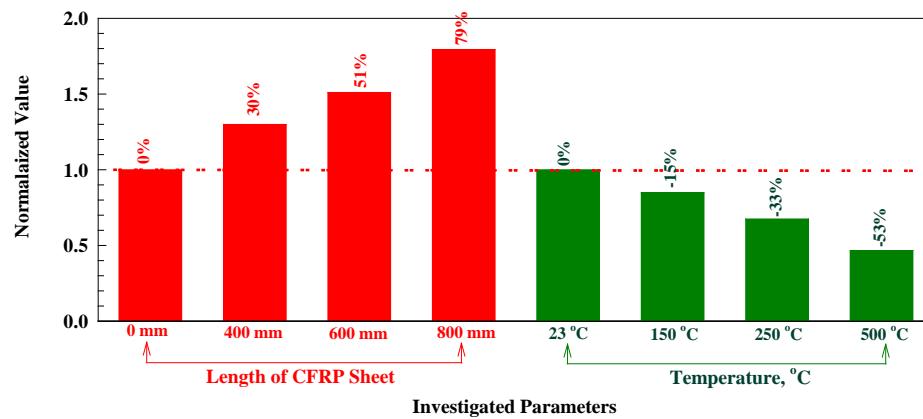


Figure 12. Normalized toughness with respect to control beam.

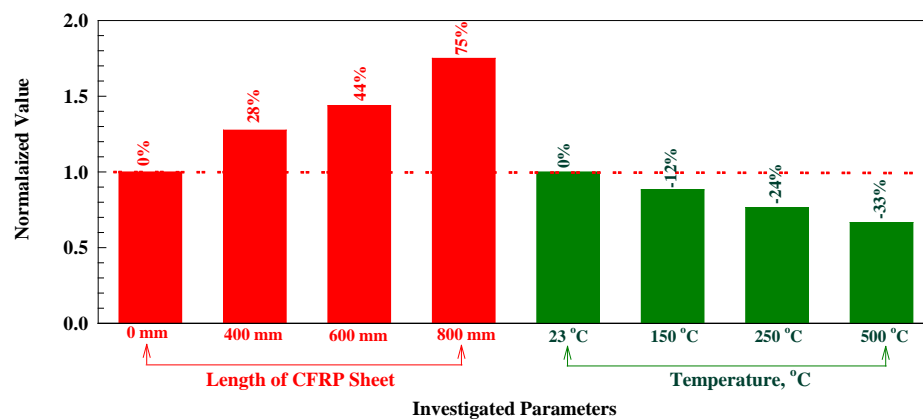


Figure 13. Normalized performance factor for control beam.

3.7. Evaluation of Performance of Experimental Results

The terms deformability factor (DF) and strength factor (SF) can then be defined as the deflection and the ultimate load capacity, respectively, of the strengthened beam, compared with the control beam. The strengthened composite beam's overall structural performance can thus be evaluated by a performance factor (PF), defined as DF multiplied by SF. Performance factor is a combination of the strength factor and the deformability factor to generate an overall structural performance as shown in Table 3 and Fig. 13. Based on Fig. 13 the PF increased as the length of CFRP sheets (bonded area of CFRP) increased and decreased with elevated temperature. Inspection of Fig. 13 reveals that the performance factor percentage increased significantly with the increase of the length of CFRP sheets. The average performance factor enhancement percentage (Fig. 12) for tested beams with respect to the control beam is 28 %, 44 %, and 75 % for 400 mm, 600 mm, and 800 mm, respectively. The average performance factor reduction percentage (Fig. 12) for tested beams for beams exposed to 23 °C is 12 %, 24 %, and 33 % for 150 °C, 250 °C, and 500 °C strips, respectively.

3.8. Comparison of experimental results with the ACI model

For comparison, the experimental results are compared with the ACI model [30]. The general design guidance is derived from the experimental data and is only applicable to external FRP reinforcement. Fig. 14 shows a comparison of the results predicted by the ACI model (P_f , experimental / P_f , ACI [30]). Note that the ACI model was calibrated for CFRP should be used with caution for other types of composites, as shown in Fig. 14. The overall predictions by ACI model [30] appear to be overestimated for beams strengthened with 400 mm, 600 mm, and 800 mm with a mean P_f , experimental / P_f , ACI value of 1.02, 1.06 and 1.09, respectively, and a coefficient of variation (COV) of 13 %. It is also important to consider that all the ACI model are semi-empirical, with important governing parameters derived from test data for beams strengthened with FRP sheets. In contrast, the ACI model cannot be applied in certain cases. Also, a careful inspection of Fig. 14 will show that the ACI model [30] has a much more comprehensive range of experimental/theoretical failure load ratios of 1.02 to 1.09.

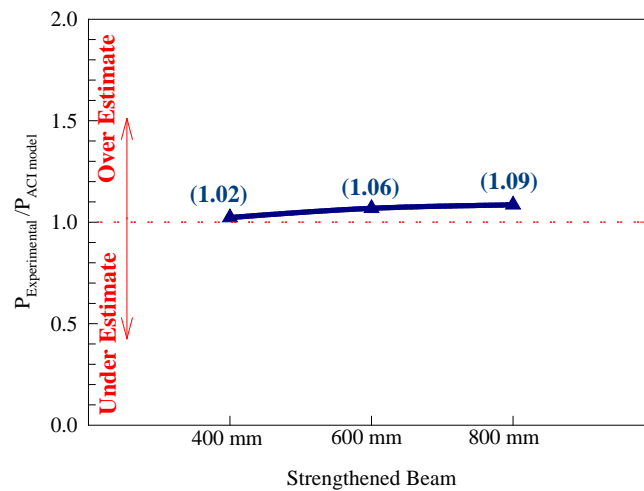


Figure 14. The normalized experimental FRP flexural force with respect to ACI model [30].

4. Conclusions

1. The CFRP sheet bridged the flexural cracks by providing adequate development length in catching the two sides of the major flexural crack.
2. The load-deflection curve can be divided into two stages; the first portion is nearly a straight line and the second stage with slope experienced a slight increase in the load with a large increase in deflection. The second stage is formed after steel reinforcement and the primary flexural crack formation, where the CFRP sheet carries the applied load.
3. The influence of the number of CFRP strips on the ductility, energy absorption, and ultimate load improvement percentage is significant.
4. The influence of the exposed temperature on the ductility, energy absorption, and ultimate load reduction percentage is significant and increased with the increase of temperature.
5. It is encouraging advantage of using the CFRP sheets along the bottom face of the beam to enhance the beam integrity before and after cracking (ductile failure mode), external arresting the flexural cracks, and improving the structural performance and serviceability of tested beam.
6. The ACI model [30] appears to be overestimated with a coefficient of variation (COV) of 13 %.

5. Acknowledgment

The author gratefully acknowledges the financial support from Deanship of Scientific Research at Jordan University of Science and Technology under Grant number 2019/507.

References

1. Al-Rousan, R.Z. Empirical and NLFEA prediction of bond-slip behavior between DSSF concrete and anchored CFRP composites. *Construction and Building Materials*. 2018. 169(1). Pp. 530–542. DOI: 10.1016/j.conbuildmat.2018.03.013
2. Al-Rousan, R.Z. Behavior of macro synthetic fiber concrete beams strengthened with different CFRP composite configurations. *Journal of Building Engineering*. 2018. 20(1). Pp. 595–608. DOI: 10.1016/j.job.2018.09.009
3. Al-Rousan, R.Z. Isra'a, A.-M. Bending and Torsion Behaviour of CFRP Strengthened RC Beams. *Magazine of Civil Engineering*. 2019. 92(8). Pp. 62–71. DOI: 10.18720/MCE.92.8
4. Travush, V.I., Konin, D.V., Krylov, A.S. Strength of reinforced concrete beams of high-performance concrete and fiber reinforced concrete. *Magazine of Civil Engineering*. 2018. 77(1). Pp. 90–100. DOI: 10.18720/MCE.77.8
5. Kodur, V., Agrawal, A. An approach for evaluating residual capacity of reinforced concrete beams exposed to fire. *Engineering Structures*. 2016. 110(1). Pp. 293–306. DOI: 10.1016/j.engstruct.2015.11.047
6. Al-Ostaz, A.M., Irshidat, B., Tenkhoff, P.S. Ponnappalli. Deterioration of bond integrity between repair material and concrete due to thermal and mechanical incompatibilities. *Journal of Materials in Civil Engineering*. 2010. 22(2). Pp. 136–144. DOI: 10.1061/(ASCE)0899-1561(2010) 22:2(136)
7. Nedviga, E., Beresneva, N., Gravit, M., Blagodatskaya, A. Fire Resistance of Prefabricated Monolithic Reinforced Concrete Slabs of "Marko" Technology. *Adv. Intell. Syst. Comput.* 2018. 692(1). Pp. 739–749. DOI: 10.1007/978-3-319-70987-1_78
8. Hezhev, T.A., Zhurto, A.V., Tsipinov, A.S., Klyuev, S.V. Fire resistant fibre reinforced vermiculite concrete with volcanic application. *Magazine of Civil Engineering*. 2018. 80(1). Pp. 181–194. DOI: 10.18720/MCE.80.16
9. Goremikins, V., Blesak, L., Novak, J., Wald, F. Experimental investigation on SFRC behaviour under elevated temperature. *Journal of Structural Fire Engineering*. 2017. 8(1). Pp. 287–299. DOI: 10.1108/JSFE-05-2017-0034

10. Goremikins, V., Blesak, L., Novak, J., Wald, F. To testing of steel fibre reinforced concrete at elevated temperature. *Applications of Structural Fire Engineering*. 2017. 1(1). Pp. 48–54. DOI: 10.14311/asfe.2015.055
11. Blesak, L., Goremikins, V., Wald, F., Sajdlova, T. Constitutive model of steel fibre reinforced concrete subjected to high temperatures. *Acta Polytechnica*. 2016. 56(1). Pp. 417–424. DOI: 10.14311/AP.2016.56.0417
12. Korsun, V., Vatin, N., Franchi, A., Korsun, A., Crespi, P., Mashtaler, S. The strength and strain of high-strength concrete elements with confinement and steel fiber reinforcement including the conditions of the effect of elevated temperatures. *Procedia Engineering*. 2015. 117(1). Pp. 970–979. DOI: 10.1016/j.proeng.2015.08.192
13. Goremikins, V., Blesak, L., Novak, J., Wald, F. Experimental method on investigation of fibre reinforced concrete at elevated temperatures. *Acta Polytechnica*. 2016. 56(1). Pp. 258–264. DOI: 10.14311/AP.2016.56.0258
14. Selyaev, V.P., Nizina, T.A., Balykov, A.S., Nizin, D.R., Balbalin, A.V. Fractal analysis of deformation curves of fiber-reinforced fine-grained concretes under compression. *PNRPU Mechanics Bulletin*. 2016. 1(1). Pp. 129–146. DOI: 10.15593/permech/2016.1.09
15. Bily, P., Fladr, J., Kohoutkova, A. Finite Element Modelling of a Prestressed Concrete Containment with a Steel Liner. *Proceedings of the Fifteenth International Conference on Civil, Structural and Environmental Engineering Computing*. Civil-Comp Press. 2015. DOI: 10.4203/ccp.108.1
16. Bílý, P., Kohoutková, A. Sensitivity analysis of numerical model of prestressed concrete containment. *Nuclear Engineering and Design*. 2015. 295(1). Pp. 204–214. DOI: 10.1016/j.nucengdes.2015.09.027
17. Al-Rousan, R. Behavior of two-way slabs subjected to drop-weight. *Magazine of Civil Engineering*. 2019. 90(6). Pp. 62–71. DOI: 10.18720/MCE.90.6
18. Al-Rousan, R. The impact of cable spacing on the behavior of cable-stayed bridges. *Magazine of Civil Engineering*. 2019. 91(7). Pp. 49–59. DOI: 10.18720/MCE.91.5
19. Krishan, A., Rimshin, V., Erofeev, V., Kurbatov, V., Markov, S. The energy integrity resistance to the destruction of the long-term strength concrete. *Procedia Engineering*. 2015. 117(1). Pp. 211–217. DOI: 10.1016/j.proeng.2015.08.143
20. Korsun, V., Vatin, N., Korsun, A., Nemova, D. Physical-mechanical properties of the modified fine-grained concrete subjected to thermal effects up to 200°C. *Applied Mechanics and Materials*. 2014. 633–634. Pp. 1013–1017. DOI: 10.4028/www.scientific.net/AMM.633-634.1013
21. Korsun, V., Korsun, A., Volkov, A. Characteristics of mechanical and rheological properties of concrete under heating conditions up to 200°C. *MATEC Web Conference*. 2013. 6(1). Pp. 07002. DOI: 10.1051/mateconf/20130607002
22. Petkova, D., Donchev, T., Wen, J. Experimental study of the performance of CFRP strengthened small scale beams after heating to high temperatures. *Construction and Building Materials*. 2014. 68(1). Pp. 55–61. DOI: 10.1016/j.conbuildmat.2014.06.014
23. Ji, G., Li, G., Alaywan, W. A new fire resistant FRP for externally bonded concrete repair. *Construction and Building Materials*. 2013. 42(1). Pp. 87–96. DOI: 10.1016/j.conbuildmat.2013.01.008
24. Trentin, C., Casas, J.R. Safety factors for CFRP strengthening in bending of reinforced concrete bridges. *Composite Structures*. 2015. 128(1). Pp. 188–198. DOI: 10.1016/j.compstruct.2015.03.048
25. Ferrari, V.J., Hanai, J.B. de, Souza, R.A. de. Flexural strengthening of reinforcement concrete beams using high performance fiber reinforcement cement-based composite (HPFRCC) and carbon fiber reinforced polymers (CFRP). *Construction and Building Materials*. 2013. 48(1). Pp. 485–498. DOI: 10.1016/j.conbuildmat.2013.07.026
26. Attari, N., Amziane, S., Chemrouk, M. Flexural strengthening of concrete beams using CFRP, GFRP and hybrid FRP sheets. *Construction and Building Materials*. 2012. 37(1). Pp. 746–757. DOI: 10.1016/j.conbuildmat.2012.07.052
27. Rami, H. Haddad, Rajai Al-Rousan, Ashraf Almasry. Bond-slip behavior between carbon fiber reinforced polymer sheets and heat-damaged concrete. *Composites Part B: Engineering*. 2013. 45(1). Pp. 1049–1060. DOI: 10.1016/j.compositesb.2012.09.010
28. Kara, I.F., Ashour, A.F., Köroğ'lu, M.A. Flexural behavior of hybrid FRP/steel reinforced concrete beams. *Composite Structures*. 2015. 129(1). Pp. 111–121. DOI: 10.1016/j.compstruct.2015.03.073
29. Kolchunov, V.I., Dem'yanov, A.I. The modeling method of discrete cracks in reinforced concrete under the torsion with bending. *Magazine of Civil Engineering*. 2018. 81(5). Pp. 160–173. DOI: 10.18720/MCE.81.16
30. ACI Committee 440. Design and Construction of Externally Bonded FRP Systems for strengthening Concrete Structures. *ACI440.2R-02. 2002. American Concrete Institute, Farmington Hills, Mich.: 45 p. DOI: 10.1061/40753(171)159. ISBN: 978-0-870312854
31. Roberto Pagani, Massimiliano Bocciarelli, Valter Carvelli, Marco Andrea Pisani. Modelling high temperature effects on bridge slabs reinforced with GFRP rebars. *Engineering Structures*. 2014. 81(1). Pp. 318–326. DOI: 10.1016/j.engstruct.2014.10.012
32. Ahmed Hassan, Faisal Aldhafairi, L.M., Abd-EL-Hafez, A.E.Y. Abouelezz. Retrofitting of different types of reinforced concrete beams after exposed to elevated temperature. *Engineering Structures*. 2019. 194(1). Pp. 420-430. DOI: 10.1016/j.engstruct.2019.05.084
33. Haddad Rami, H., Almomani Oubaida, A. Recovering flexural performance of thermally damaged concrete beams using NSM CFRP strips. *Construction and Building Materials*. 2017. 154(1). Pp. 632–643. DOI: 10.1016/j.conbuildmat.2017.07.211

Contacts:

Rajai Al-Rousan, rzalrousan@just.edu.jo



DOI: 10.34910/MCE.106.13

Corrosive behavior of low-alloy structural steels

V.G. Kiselev , A.A. Kalyutik* 

Peter the Great St. Petersburg Polytechnic University, St. Petersburg, Russia

*E-mail: AA_Kalyutik@spbstu.ru

Keywords: construction, corrosion of structural materials, mechanical safety, mechanical properties, strength of materials, corrosive tests, fatigue of materials

Abstract. Increasing the corrosion resistance of low-alloy steels containing less than 2.5% of doping components (except carbon), which are actively used in the construction of various buildings and structures, is one of the priorities in the development of the modern construction industry. This problem becomes especially urgent during operation of stressed elements of various structures, which are used in the conditions of possible surface exposure to moisture. As part of the research, the results of which are presented in this article, we have examined the possible reduction in the rate of electrochemical corrosion of low-alloy steels in a natural corrosive environment. The purpose of the study was to establish the effect of the composition of steels on their corrosive properties. The main method chosen was a method of thermodynamic potentials, used in conjunction with model ideas about ideal gas and free energy of diffusion of liquid, solid and gaseous solutions. The present study analyzes the process of formation of ideal binary alloy, based on which the relationship between the thermodynamic characteristics of its original components and the corrosive behavior of the alloy was established. In order to verify the detected corrosion mechanism, the process of amalgam anode dissolution was considered, which fully confirmed the results obtained earlier. Based on the analysis conducted, it can be concluded that the equilibrium potential of the ideal binary alloy in the electrolyte in no way depends on the process of its formation from the pure original components. It is determined solely by the ratio of energy characteristics of metal ions actually in the alloy, as well as the energy characteristics of the same ions in the solution of electrolyte, which comes into contact with the alloy.

1. Introduction

Buildings, with the exception of temporary ones, are designed for a very long service life in the presence of significant adverse conditions associated with simultaneous effects of various aggressive factors. Such factors include: mechanical load, solar radiation, as well as chemical, electrochemical and microbiological activity of the environment, etc. [1–4], which in turn contribute to the intensification and localization of corrosive processes that occur to varying degrees on the metal parts of almost all modern architectural objects. Hence, there is a need for long-term forecasting of the behavior of the materials used, especially metals and their alloys. A significant role in this case is played by their corrosive resistance, in the water solutions of electrolytes in particular, as that is where soil and atmospheric corrosion, characteristic of such structures, occurs.

Due to the fact that in modern industrial construction we almost always use only alloys (not pure metals), the study and prediction of their corrosive behavior is a priority for the relevant construction industry and the part of material science that serves it, as well as the study of metal corrosion, which shows the extreme relevance of this problem in the realities of today.

The main method used to solve the problem of corrosion of alloys in active state is the analysis and synthesis of methods of chemical kinetics and thermodynamics. Here the key role is played, on the one hand, by the method of thermodynamic potentials, and on the other hand, by the theory of electrochemical

Kiselev, V.G., Kalyutik, A.A. Corrosive behavior of low-alloy structural steels. Magazine of Civil Engineering. 2021. 106(6). Article No. 10613. DOI: 10.34910/MCE.106.13

© Kiselev, V.G., Kalyutik, A.A., 2021. Published by Peter the Great St.Petersburg Polytechnic University.



This work is licensed under a [CC BY-NC 4.0](https://creativecommons.org/licenses/by-nc/4.0/)

kinetics. We should note that thermodynamic research methods are in high demand today. References to them are found not only in articles in academic publications, but also in books and journals specializing in publications of pronounced applied nature. In this case, it is appropriate to recall a series of articles related to metal corrosion in electrolyte (soil) in the presence of an additional factor of aggressiveness due to the presence of an alternating stray current in the system. Thermodynamic analysis of the corrosion process of such objects is usually carried out using the Pourbaix diagrams [5–7]. The second area where thermodynamics techniques are actively used is the cathode protection of underground metal structures from corrosion [8–11]. In this case, it is appropriate to recall the technique for measuring potentials (stationary and polarization), which is based on the theory and practice of using non-polarizable reference electrodes [12], usually copper-sulfate ones.

In all these cases, kinetic methods for studying anodic dissolution of metals are also used. However, almost all of these works do not analyze the process of obtaining alloys, and, consequently, its effect on their corrosive behavior. This fact speaks about the extreme relevance of research devoted to this subject. The exception to this rule is the works of I.K. Marshakov [13]. We need to note that the traditional approach to thermodynamic analysis of corrosive behavior of alloys considers the process of their formation, primarily, as ideal solid solutions and connects this phenomenon with the corresponding change in free energy and entropy. Due to the fact that the formation of the alloy occurs spontaneously, it is automatically accepted that this event is accompanied by a decrease in Gibbs free energy (at constant pressure and temperature) of the system [13, p. 89], which, in its turn, can be transformed into the appropriate amount of electrical work described by the following formula:

$$G_i^M = \bar{G}_i - G_i^0 = RT \ln N_i = -z_i F E_i^M, \quad (1)$$

where G_i^M is relative partial molar free energy of the i^{th} component; \bar{G}_i is partial molar free energy of the i^{th} component; G_i^0 is molar free energy of the i^{th} component (pure matter); R is the Universal gas constant; T is absolute temperature; N_i is molar fraction of the i^{th} component in a solid solution; z_i is valence of the i^{th} component (i^{th} metal); F is the Faraday constant; E_i^M is potential difference corresponding to electrical work due to the presence of the relative partial molar free energy of the i^{th} component.

From the last formula, I.K. Marshakov [13, p. 89] has obtained the value of the partial relative electrode potential of the i^{th} component for standard conditions, namely E_i^M :

$$E_i^M = \bar{E}_i - E_i^0 = -\frac{RT}{z_i F} \ln N_i, \quad (2)$$

where \bar{E}_i is equilibrium partial electrode potential of the i^{th} component in the alloy, determined by the equilibrium between the component in the alloy and the ions of this component in the electrolyte solution; E_i^0 is equilibrium standard potential of the pure i^{th} component.

Since the molar (atomic) fraction $N_i < 1$, then $E_i^M > 0$ always. Thus, alloy formation leads to a shift of potential in a positive direction ($\bar{E}_i > E_i^0$). Therefore, if the anode dissolution of the alloy occurs in conditions close to equilibrium, then there should be an inhibition of the anode reaction for any component [13, p. 89]. We should note that this view is broadcast by a number of subsequent authors, for example, N.I. Isaev.

However, based on the article of one of the co-authors of this publication [14], it is possible to show some illogicality of the last thesis stated by I.K. Marshakov and supported by a number of his followers. In the last paper listed [14], on the example of the ideal gas it was shown that the mixing process (the formation of the ideal solution) is indeed accompanied by a change in Gibbs (Helmholtz) energy. However, this change in no way affects the energy state of the components of the alloy (ideal solution), in other words, the energy of the substance molecules' communication with each other is the same, both in the alloy, which is an ideal solid solution, and in the pure matter. Indeed, as it does, however, directly follow from the definition of the concept of the ideal solid solution, the following conditions should be observed in its formation:

1. When pure components are mixed, there is no change in the volume of the system;
2. The heat of the mixing is zero, i.e. there is no interaction between the components of the solution;

3. The vapors of components above the solution behave like ideal gases and at all concentrations of the solution the Raoult's law is fulfilled:

$$P_i = P_i^0 N_i, \quad (3)$$

where P_i is partial pressure of the ideal gas consisting of the i^{th} component of the alloy above its surface, and P_i^0 is pressure of the ideal gas consisting of the i^{th} component of the alloy above the surface of the alloy.

This definition is enough to show the invariability of the energy state of individual molecules in the formation of ideal solid solutions, which, however, is mentioned by I.K. Marshakov himself [13, pp. 41–44]. Moreover, in [14] this thesis is confirmed in various ways, including using the method of thermodynamic potentials. Therefore, on the basis of these data, we can state that the process of forming an ideal alloy is not accompanied by changes in the energy state of the molecules of substances involved in the process under consideration and, therefore, at least some adjustment of the formulas (1) and (2) above is necessary. Indeed, the ratio (2), due to the energy equality of molecules involved in the subsequent electrochemical process of anode dissolution of the alloy, can no longer be recognized as fair, which leads to its degeneration, which, in its turn, can be illustrated by the following:

$$E_i^M = \bar{E}_i - E_i^0 = 0. \quad (4)$$

However, the equation (1), at least, its left part, due to the spontaneity of the process of alloy formation cannot be recognized as incorrect. This circumstance automatically raises the question of the legality of its use to obtain the ratio (2). At the same time, there arises a problem of interpreting the physical meaning of the equation (1), which, in particular, is the subject of this study. In other words, the purpose of this work is to perform thermodynamic analysis of the process of binary ideal alloy formation and to establish the mechanism of its effect on electrochemical corrosive processes occurring on their surfaces.

To achieve this goal, we will have to solve the following two problems:

1. Conducting a thermodynamic analysis of the process of ideal binary alloy formation.
2. Establishing a relationship between the thermodynamic characteristics of the original components of the ideal binary alloy and its corrosive behavior.

In the following sections of this work, we will focus on solving these problems in some more detail.

2. Materials and Methods

The work uses one of the most widespread analytical methods of research in modern thermodynamics, which is called the method of thermodynamic potentials (or characteristic functions). The main advantages of this method include its suitability for analysis of non-cyclical processes, such as chemical reactions, diffusion processes, mixing processes (formation of solutions), etc. Its essence is included in almost any book on thermodynamics and lies in the fact that the basic thermodynamic equation allows for a quasi-static thermodynamic system to derive some state functions, called thermodynamic potentials, the change of which with a change in the state of the system is a complete differential. Based on this circumstance, it is possible to write down the corresponding mathematical equations suitable for describing the process under consideration, which we will demonstrate in this article.

3. Results and Discussion

3.1. The formation of the ideal solid solution

The main method that we will use to solve the problem outlined in the introduction to this article is the method of thermodynamic potentials. To simplify the analysis of the process, let us assume that our system consists of a number of ideal gases, which are to be mixed. Without loss of generality, we will assume that there are two such gases (first and second). Replacing the ideal solid solution with the ideal gas from a thermodynamic point of view is quite acceptable, as in this case all the energy characteristics of the systems under consideration are equal to each other up to a constant. This fact for the ratios aimed at studying the changes taking place in the quasi-static systems under consideration practically indicates their equivalence.

A more detailed examination of the stated thesis will be based on a specific example. For greater visibility, the analysis will be carried out using the energy characteristics of this object, which include, first of all, the free energies of Gibbs and Helmholtz. In addition, without loss of generality, let us accept that the

volume in which each of the two types of ideal gas to be mixed is originally located, is V_1 and V_2 accordingly, and the total volume of the mixture, after their mixing is equal to $V = V_1 + V_2 = 1$. However, the invariance of the initial pressure P during mixing of two portions of ideal gases (identical or different) directly follows from the thermal equation of the state of ideal gases [14].

Of course, the stated thesis is valid only if the mixture is still an ideal gas and the number of molecules in it remains the same. After the introductory remarks have been made, we proceed to a direct examination of the process of combining two generally different portions of different ideal gases.

3.2. *Mixing two portions of different ideal gases*

We will briefly return again to the system consisting of two generally different portions of different first and second ideal gases, placed in two volumes, V_1 and V_2 respectively, so that the following ratio is observed: $V = V_1 + V_2 = 1$. At the same time, between them there is some partition, which can be removed, and ideal gases differ from each other, for example, there can be a small difference in the size of molecules. When this partition is removed, they are mixed in the volume V . Let us assume that the total amount of first and second gases is equal to one mole, i.e. in other words, the following ratio is observed:

$$G_m = N_1 \overline{G_1} + N_2 \overline{G_2}, \quad (5)$$

where G_m is the Gibbs molar energy of the mixture of the ideal gases; $\overline{G_1}$ and $\overline{G_2}$ are the partial Gibbs molar free energies, respectively, of the 1st and 2nd components of the mixture of two ideal gases; N_1 and N_2 are molar fractions of the 1st and 2nd components in a mixture of two ideal gases.

In addition, it is clear that, according to the conditions imposed, the following ratios must be satisfied:

$$N_1 = \frac{n_1}{n_1 + n_2}, \quad (6)$$

$$N_2 = \frac{n_2}{n_1 + n_2}, \quad (7)$$

$$n_1 + n_2 = 1, \quad (8)$$

where n_1 and n_2 are the number of moles of the 1st and 2nd components in the mixture of two ideal gases.

We need to note that if the last ratio is satisfied, the following is also true: $N_1 = n_1$ and $N_2 = n_2$. When two identical ideal gases are mixed, there is no change in any macroscopic parameters of the system, namely temperature, pressure and its total volume remain unchanged. In this case, for the Gibbs free energy of the combined system [14], we can write the following ratio:

$$G_m = G_1 + G_2, \quad (9)$$

where G_1 and G_2 are the Gibbs free energies of the 1st and 2nd initial components of the two ideal gases.

Therefore, based on the latest formula, the change in the Gibbs free energy ΔG when mixing two portions of the same ideal gas, provided the gas mixture is also ideal, will be equal to:

$$\Delta G = G_m - G_1 - G_2 = 0. \quad (10)$$

However, in the system under consideration, consisting of n_1 and n_2 moles of two different ideal gases located in two generally not in equal volumes, divided by an impenetrable partition, there is, at least still one more energy component. It is the of Gibbs free energy of diffusion inherent in this system as a whole. Its very existence in this case is inextricably linked to the fact that our object has some practical or theoretical possibility of mixing existing different ideal gases. This mixing can occur in equilibrium (getting third-party work using semi-permeable membranes) or nonequilibrium (removal of an impenetrable partition between the two ideal gases) ways.

In this case, it is appropriate to recall the monograph of L.I. Antropov, in which he during thermodynamic analysis of the properties of ideal and real solutions in particular considered the behavior

of the diffusion component of the Gibbs free energy. The fact that is relevant for us is that in his work he used a differential from the Gibbs free energy of diffusion G , which was defined by him as follows:

$$dG = \sum_i n_i d\mu_i, \quad (11)$$

where n_i is the number of moles of the i^{th} substance participating in the process, and μ_i is the chemical potential of this i^{th} substance.

In the case of one mole of the i^{th} ideal gas, its Gibbs energy G_i , equal to its chemical potential μ_i , as we know [13, p. 20], equals:

$$G_i = G_i^0 + RT \ln P_i, \quad (12)$$

where G_i^0 is the standard Gibbs energy value equal to a constant.

If there are two different ideal gases, based on the previous ratio, the equation (11) can be rewritten as follows:

$$dG = RT \sum_{i=1}^2 n_i d(\ln P_i). \quad (13)$$

After differentiation and trivial transformation of the right part of the last ratio, we get

$$dG = n_1 RT \frac{dP_1}{P_1} + n_2 RT \frac{dP_2}{P_2}. \quad (14)$$

At the same time, the Gibbs free energy of the original state of the system under consideration G_n is known to be an additive function of its constituent subsystems, namely:

$$G_n = G_{1n} + G_{2n}, \quad (15)$$

where G_{1n} and G_{2n} are, respectively, the Gibbs initial free energies of the first and second ideal gas, which in turn are determined by the following ratios [13, p. 20]:

$$G_{1n} = n_1 (G_1^0 + RT \ln P_{1n}), \quad (16)$$

$$G_{2n} = n_2 (G_2^0 + RT \ln P_{2n}), \quad (17)$$

where G_1^0 and G_2^0 are, accordingly, the standard values of Gibbs initial free energies of the first and second ideal gases, which are known to be constant, but in general are not equal to each other, which is confirmed by the presence of at least different values of heat capacities of different ideal gases; P_{1n} and P_{2n} are, respectively, the initial pressures of the first and second ideal gases initially located in volumes V_1 and V_2 .

We will mix two original portions of ideal gases while maintaining the total volume of the system $V = 1$. In this case, the final free energy of each of these gases, G_{1k} and G_{2k} , by reducing their partial pressures and lack of interaction between them, will be characterized by the following values of Gibbs energy:

$$G_{1k} = n_1 (G_1^0 + RT \ln P_{1k}), \quad (18)$$

$$G_{2k} = n_2 (G_2^0 + RT \ln P_{2k}), \quad (19)$$

where P_{1k} and P_{2k} are, respectively, the partial pressures of the first and second ideal gases after they mix in the volume $V = 1$.

Now we will determine the values P_{1n} and P_{2n} , as well as P_{1k} and P_{2k} . To do this, we will use thermal equations of the state of the ideal gas

$$PV = nRT, \quad (20)$$

where n is the number of moles of the ideal gas.

The last ratio for the first and second ideal gas taking part in the mixing process, characterizing their initial state in the system, can be rewritten in the following form:

$$P_{1n} V_1 = n_1 RT, \quad (21)$$

$$P_{2n} V_2 = n_2 RT, \quad (22)$$

where P_{1n} and P_{2n} are initial pressures of the first and second ideal gas respectively.

In this case, for the characteristics P_{1n} and P_{2n} , we obtain:

$$P_{1n} = RT \frac{n_1}{V_1}, \quad (23)$$

$$P_{2n} = RT \frac{n_2}{V_2}. \quad (24)$$

The resulting values for the initial pressures of ideal gases in the system P_{1n} and P_{2n} make it possible to rewrite ratios (16) and (17) in the following way:

$$G_{1n} = n_1(G_1^0 + RT \ln RT \frac{n_1}{V_1}), \quad (25)$$

$$G_{2n} = n_2(G_2^0 + RT \ln RT \frac{n_2}{V_2}). \quad (26)$$

Equations (21) and (22) characterize the system in question after the mixing process. In this case, taking into account the fact that both gases will be in the same volume $V = 1$, the following statement will be fair for them:

$$P_{1k} = n_1 RT, \quad (27)$$

$$P_{2k} = n_2 RT. \quad (28)$$

The resulting final values of ideal gas pressures in the system P_{1k} and P_{2k} make it possible to write the ratios (18) and (19) as follows:

$$G_{1k} = n_1(G_1^0 + RT \ln n_1 RT), \quad (29)$$

$$G_{2k} = n_2(G_2^0 + RT \ln n_2 RT). \quad (30)$$

This allows to integrate the expression (14), which determines the change in free diffusion energy when two different ideal gases are mixed, from the initial to the final value of that energy. Thus, the change in the value of the Gibbs free energy of diffusion ΔG_d will be determined by the following:

$$\Delta G_d = G_{1k} + G_{2k} - G_{1n} - G_{2n}. \quad (31)$$

After substituting previously obtained ratios for G_{1n} , G_{2n} , G_{1k} and G_{2k} , and making elementary algebraic transformations, we can get the value of characteristic change of Gibbs free energy ΔG_d caused by the diffusion process in the system under consideration, namely:

$$\Delta G_d = n_1 RT \ln V_1 + n_2 RT \ln V_2. \quad (32)$$

We need to note that in this equation both V_1 and V_2 are less than one, which automatically leads to $\Delta G_d < 0$, in other words, it indicates the spontaneity of the diffusion process, which is observed in

practice. However, the diffusion equalization of chemical potentials has no effect on the energy of particle interaction, as the ideality of the system in question (a mixture of ideal gases, ideal solid or liquid solutions) does not get violated according to the definition of such systems above, which means that the energy of their chemical interaction is invariable.

Thus, we can argue that the original state of the system in question is characterized by some integral amount of free energy, including, among other things, free energy of diffusion G_d . The latter, as is obvious from the previous text, does not refer to the individual components of the system under consideration, but to it as a whole. This circumstance allows us to write the following equation:

$$G_n = G_{1n} + G_{2n} + n_1 RT \ln V_1 + n_2 RT \ln V_2. \quad (33)$$

When we include the values of G_{1n} and G_{2n} and carry out elementary algebraic transformations, we get:

$$G_n = n_1 G_1^0 + n_2 G_2^0 + n_1 RT \ln n_1 RT + n_2 RT \ln n_2 RT. \quad (34)$$

At the same time, we can argue that the final state of the system in question is characterized by the following amount of free energy G_d (free diffusion energy in this case is zero):

$$G_k = G_{1k} + G_{2k}. \quad (35)$$

When we substitute the values of G_{1n} and G_{2n} , and perform elementary transformations accordingly, we get:

$$G_k = n_1 (G_1^0 + RT \ln n_1 RT) + n_2 (G_2^0 + RT \ln n_2 RT). \quad (36)$$

So, for the change in the Gibbs free energy $\Delta G_{1,2}$ when mixing two different ideal gases, we get:

$$\Delta G_{1,2} = G_{1k} + G_{2k} - G_{1n} - G_{2n}. \quad (37)$$

Substituting the values G_{1k} , G_{2k} , G_{1n} and G_{2n} , as well as making elementary algebraic transformations, taking into account the comments made by us earlier, allows us to finally write down:

$$\Delta G_{1,2} = n_1 RT \ln V_1 + n_2 RT \ln V_2. \quad (38)$$

Concluding this subsection of the article, we need to emphasize that the latest formula describes the change in the Gibbs energy when two not necessarily identical portions of different ideal gases are mixed. This also takes into account the change of free energy of diffusion, inherent to the system under consideration as a single whole.

3.3. Discussion of the results and their verification

The calculations carried out in the two previous subsections of this work allow us to draw a completely unambiguous conclusion that when two portions of ideal gases are mixed, there is no change in their molar characteristics. In turn, taking into account the free diffusion energy, inherent to the system in question with two different ideal gases as a single whole, leads to a decrease in this type of energy. In other words, the amount of change in the energy characteristics of the object in question, such as, for example, low-alloy carbon steel, depends on their starting point of reference, i.e. the presence (or lack of) free diffusion energy, inextricably linked to the system being considered as a single whole, and not its individual parts.

Now we will demonstrate that the results are well consistent, at least, with some features of corrosive behavior of alloys. For this purpose, we will consider the process of electrochemical interaction of amalgams of different metals with the environment. In this case, according to the ideas developed in particular by H. Kaesche [15, pp. 36–49], the equilibrium potential of the liquid alloy is determined by the following ratios:

$$E = E_{Hg/Hg_2^{2+}}^0 + \frac{RT}{2F} \ln \frac{C_{Hg_2^{2+}}}{1 - \gamma_{Me}} = E_{Me/Me^{z+}}^0 + \frac{RT}{zF} \ln \frac{C_{Me^{z+}}}{\gamma_{Me}}, \quad (39)$$

where: E is the equilibrium electrode potential of the amalgam; $E_{Hg/Hg_2^{2+}}^0$ is the standard value of the mercury electrode's potential; $E_{Me/Me^{z+}}^0$ is the standard value of the potential of the metal (not mercury)

electrode, which is part of the amalgam in question; $C_{Hg_2^{2+}}$ is the concentration of mercury ions in the electrolyte solution; $C_{Me^{z+}}$ is the concentration of metal (not mercury) ions in the electrolyte solution; γ_{Me} is molar fraction of metal in the amalgam.

It is obvious that for the liquid binary alloy (metal amalgam) in question, the ratio between the molar fraction of mercury γ_{Hg} and metal γ_{Me} in amalgam can be written as:

$$\gamma_{Hg} = 1 - \gamma_{Me} \quad (40)$$

A simple analysis of the equation (39) shows that the equilibrium potential of the amalgamated electrode is achieved at a double equilibrium [15, p. 49]. In this case, with the set of molar and atomic fractions γ_{Hg} and γ_{Me} in the amalgam, in the solution there is a fully defined ratio of activities or concentrations of mercury ions and ions of the metal dissolved in it a_{Hg} / a_{Me} . We can find similar equations in the works of other authors, for example, L.I. Antropov, where he is considering the behavior of amalgam electrodes. Thus, we should note that the change in the energy state of the system associated with the formation of the alloy (ideal system), which is represented by ratios (1) and (2), in no way affects its equilibrium potential and the speed of its anode dissolution. In general, this situation seems quite logical. This is due to the fact that the thermodynamics of the transition of ions across the boundary of the phase section of binary alloy–electrolyte, which is actually responsible for establishing a state of equilibrium in the system in question, is determined solely by the strength (energy) of the connections of ions under consideration in these systems, naturally, with equal energy of their solvation (hydration). We should note that under ideal conditions, the process of alloy formation has no effect on the process of transition of ions, i.e. a kind of "diffusion component of potential" presented by equations (1) and (2) of course should be absent. However, this is indirectly confirmed by I.K. Marshakov himself. Indeed, he does not use the conclusions of one of the sections of his monograph [13, pp. 89–91] dedicated to the thermodynamic preconditions of alloy formation in any way. This fact indicates, at least, the lack of verification process. On the other hand, the formation of real alloys, for example, high-alloy steels as opposed to ideal alloys, is already associated with changes in the chemical energy. This becomes especially noticeable in the case of the formation of new chemical bonds, for example, in the formation of intermetallic compounds, which is usually accompanied by the release or absorption of heat in the process under consideration [16, p. 67]. This fact unequivocally will affect the strength of chemical bonds in a solid solution (alloy), which is noted, for example, in the paper [14], and, consequently, will change the equilibrium potential of the real binary alloy, which, in its turn, significantly affects the kinetics of electrochemical corrosion and, consequently, the rate of its anode dissolution. A more detailed analysis of the problem under consideration can be conducted based on the Terrace Ledge Kink model, which is used in practice during consideration of electrochemical dissolution of metals, which, in particular, was successfully demonstrated by K. Fetter in his classic monograph [17, pp. 313–354]. However, in our fairly simple case of anode dissolution of binary alloys, it is quite possible to limit ourselves to the illustration of this process, given in the book by N.D. Tomasov and G.P. Chernova.

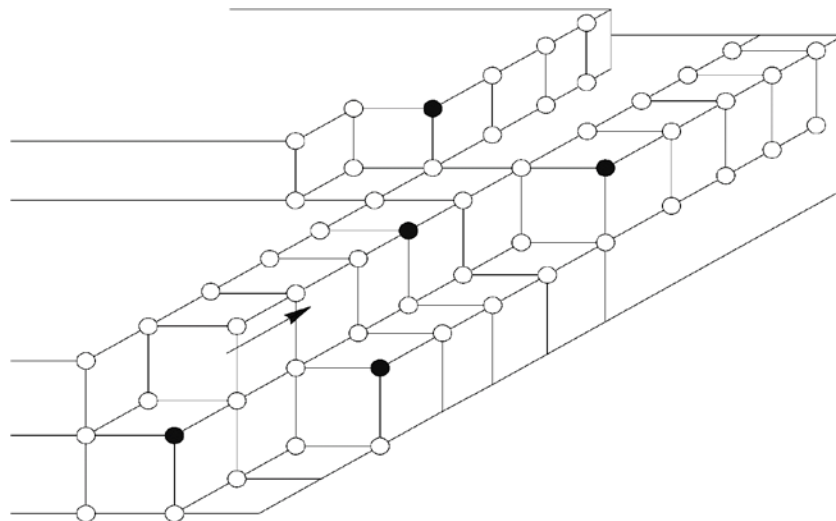


Figure 1. Scheme of anode dissolution of cubic crystal lattice of binary alloy of the solid solution type. Dark dots are the atoms of the doping component.

In this case, within the framework of the scheme proposed by Kossel and Stranski, dissolution of metals that make up, for example, the cubic crystal lattice of the binary alloy (the system forms a substitutional solid solution) is carried out from different energy points of its crystal lattice, at the same time [16, p. 69] "the lesser the number of the adjacent atoms with which the atom is associated, the bigger it is energy opportunities, and therefore the more negative its electrochemical potential and the more likely its ionization and transition into the solution." This picture becomes even more prominent if we have, for example, a binary substitutional solution illustrated in Fig. 1, where the dark dots represent the atoms of the doping component. In this case, during dissolution according to the scheme presented by the arrow in the mentioned figure, more resistant atoms (the doping component) will gradually appear "in more active places", namely in the corners of the edges of the crystal lattice and thus slow down the overall rate of anode dissolution of the alloy. On the other hand, if we assume that the energy characteristics of all atoms are identical and in the formation of the ideal solid solution remain unchanged, which, however, directly follows from its definition, then the only changing parameter, in addition to the existing concentration changes in the alloy, is the energy of solvation (hydration) of the atoms of the system in question. Thus, the kinetic analysis of the process of anode dissolution of low-doped binary alloys in the approximation of ideal solid solutions clearly demonstrates the independence of its electrochemical behavior (the rate of anode dissolution) from the process of its formation from the pure original components. However, taking into account the experimental data on the reduction of free energy in the formation of non-ideal alloys such as solid solutions [16, p. 67], the value of which is estimated to be about a thousand calories (4187 joules) per gram-atom, "which corresponds to a change in the electrochemical potential of the components in a positive direction by about 20 mV." We should note on our own that it is fair for divalent metals, for monovalent metals this value will already equal approximately 40 mV. At the same time, it is known that "The decrease in free energy during corrosion reactions for technical (base) metals can amount to tens and hundreds of thousands of calories per gram-atom, i.e. it will correspond to the EMF corrosion process of about 200–2000 mV" [16, p. 67], which corresponds to approximately the interval from 41870–418700 joules. It would seem that the contribution of "ideality" in the formation of an alloy (approximately 20–40 mV) in its corrosive behavior, caused by the alloy-electrolyte relationship (200–2000 mV) is extremely small, i.e. ranges from one to twenty percent. However, this impression is deeply misguided. Very often, especially in atmospheric and soil corrosion, corrosive vapors are formed, EMF of which can be compared with the values under consideration [18]. Figure 2 illustrates this statement.

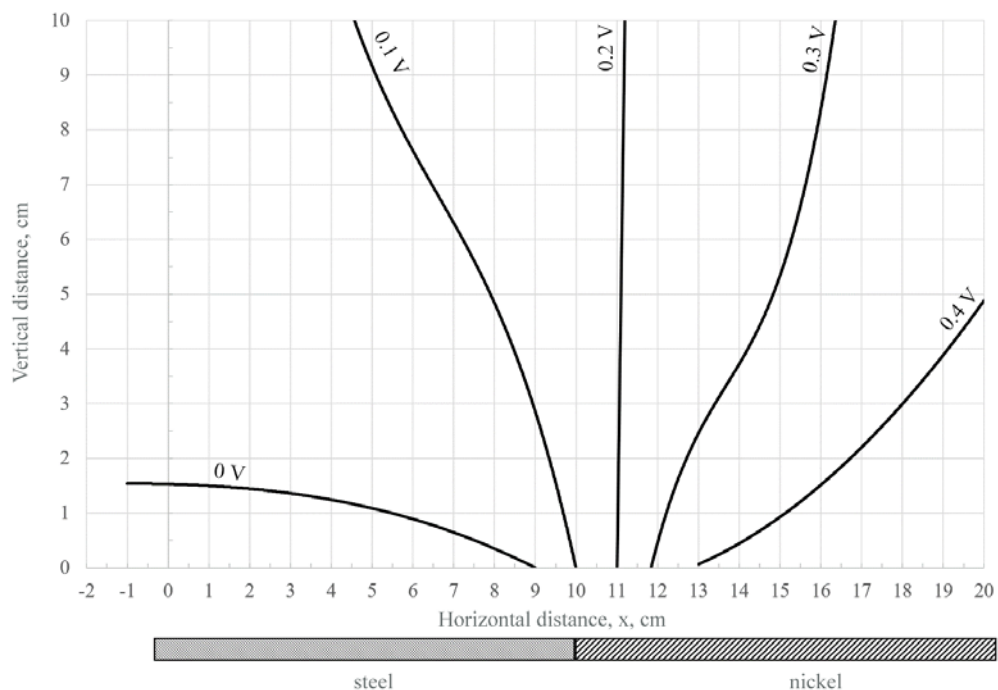


Figure 2. Potential field over a flat short-circuited element with a steel anode and a nickel cathode in tap water. The potential is related to the potential of corrosion of the anode.

It is appropriate to compare the given data on the "inediality" of a solid solution with the change in the free energy, which is observed in the formation of ideal solutions. In this case, as we have established earlier, the formula (38) "works", which for the case under consideration is more convenient to present in the following form [13, p. 30–31].

$$\Delta G_{1,2} = N_1 RT \ln N_1 + N_2 RT \ln N_2 \quad (41)$$

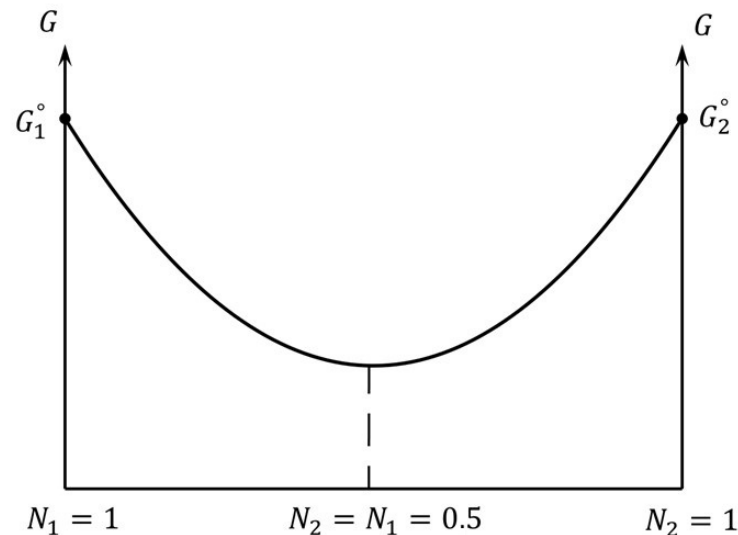


Figure 3. Dependence of the Gibbs free energy (diffusion component) of the ideal binary alloy from its chemical composition in the ideal solid solution approximation.

Where N_1 and N_2 are molar fractions of respectively the first and second components of the alloy, and $\Delta G_{1,2}$, as before, refers to one mole of the solution (alloy); Accordingly, $\Delta G_1 = N_1 RT \ln N_1$ and $\Delta G_2 = N_2 RT \ln N_2$.

A respective graph of change of the "ideal" Gibbs free energy (diffusion component) is presented on the Figure 3 and represents some curve with a minimum [13, p. 22].

Table 1. Changes in Gibbs free energy (diffusion component) in the formation of the ideal binary alloy (solid solution) as a function of changing the molar fractions of the alloy components.

Indicators	1	2	3	4	5
N_1	0.5	0.1	0.01	0.001	0.0001
N_2	0.5	0.9	0.99	0.999	0.9999
ΔG_1	- 844.20	- 561.01	-112.18	- 16.83	-2.24
ΔG_2	- 844.20	- 231.08	- 24.12	- 2.43	- 0.24
$\Delta G_{1,2}$	- 1688.40	- 792.09	- 136.30	-19.26	-2.48

Values of the $\Delta G_{1,2}$ are listed in joules per mole of the alloy, and the partial molar values $\Delta G_1 = N_1 RT \ln N_1$ and $\Delta G_2 = N_2 RT \ln N_2$, listed in joules, are normalized by their molar fractions in the alloy.

However, due to the fact that this dependence shows only trends of changes in $\Delta G_{1,2}$, and therefore does not allow to determine the specific values of the change of free energy, for the subsequent comparative analysis we will have to present them in a table form. We will do this for five different cases of the ratio of the molar fractions of the initial components in the alloy, numbered from 1 to 5 (during the calculations, the conventional temperature of the solution formation was chosen equal to 20 °C).

The simplest analysis, of the both graphical dependence and table data, shows that firstly the change in molar free energy formation of the ideal alloy even at its maximum absolute value (equal original alloy components, column 1) is relatively small compared to the experimentally observed magnitudes of the formation of real alloys and in this case the ratio is approximately equal to 0.04 ($1688.40/41868 \approx 0.04$), and secondly, when the molar fraction of one of the components (in our case, N_1) begins to decrease even more markedly in the absolute value of this indicator and, for example, for the column 5 it is already a small fraction, namely 0.00006 ($2.48/41868 \approx 0.00006$). We should note that for the calculations carried out in the latter case, we used the minimum possible value of the "chemical" component of the free energy, equal,

as we have established earlier, to 41870 joules. The data obtained are undoubtedly an additional and very strong argument in favor of the practical absence of the effect of the process of formation of the ideal binary alloy on the nature of its possible further anode dissolution.

We should note that in the modern construction industry and the industries that serve it, a lot of attention is paid to the actual problem of materials science [19–22], as well as the issues of preserving the strength characteristics of the materials used. A logical continuation of this trend is the presented work on the study of corrosive behavior of low-alloy steels. This material-scientific problem is also in the trend of modern science, as evidenced by the numerous publications on this topic [23–30], which argues for the relevance of the research presented in this paper. This article is, to some extent, a continuation and development of previous publications [14, 31–36] devoted to the consideration of the process of mixing ideal gases and in no way contradicts them. At the same time, it aims to address the very specific and extremely important problem of increasing the corrosion resistance of carbon and low-alloy steels, which play a very important role in almost every area of human activity, especially in the field of construction and architecture. This research, focused primarily on the study of ideal binary alloys that are models of real carbon and low-alloy steels, allows us to draw conclusions presented below.

4. Conclusions

1. The equilibrium potential of the ideal binary alloy in the electrolyte is by no means dependent on the process of its formation from the pure raw components, but is determined solely by the ratio of energy characteristics of the ions of metals located actually in the alloy, as well as the energy characteristics of the same ions in the electrolyte solution that comes into contact with the alloy.

2. The presence of the Gibbs free energy, which characterizes the diffusion behavior of two generally different portions of different components of the ideal binary alloy and, accordingly, the process of its formation, in no way affects the speed of its anode dissolution.

References

1. Yusuf, M.O. Microstructure and strength of iron-laying Portland cement paste and mortar. *Magazine of Civil Engineering*. 2019. 90(6). Pp. 28–36. DOI: 10.18720/MCE.90.3
2. Adewumi, A.A., Ismail, M., Ariffin, M.A.M., Yusuf, M.O., Maslehuiddin, M., Mohamed, H.D. Strength and microstructure of alkali-activated natural pozzolan and limestone powder mortar. *Magazine of Civil Engineering*. 2019. 92(8). Pp. 36–47. DOI: 10.18720/MCE.92.3
3. Urkhanova, L.A., Lkhasaranov S.A., Buyantuyev S.L., Fedyuk R.S., Taskin A.V. Reducing alkaline corrosion of basalt fiber in concrete. *Magazine of Civil Engineering*. 2019. 91(7). Pp. 112–120. DOI: 10.18720/MCE.91.10
4. Strokova, V.V., Nelubova, V.V., Rykunova, M.D. Resistance of cement stone in sanitation solutions. *Magazine of Civil Engineering*. 2019. 90(6). Pp. 72–84. DOI: 10.18720/MCE.90.7
5. Houban, M. Beurteilung von wechselstrom-korrosionsgefährdeten kathodisch geschützten Stahlrohrleitungen. 3R - Fachzeitschrift für sichere und effiziente Rohrleitungssysteme. 2017. No. 6. Pp. 66–74.
6. Bette, U., Buchler, M. Taschenbuch für den kathodischen Korrosionsschutz. Vulkan-Verlag, Essen, 2017. 335 p.
7. Yan, L., Arafin, M., Gravel, J.-P. Penetration of Cathodic Protection into Pipeline Coating Disbondment. *Corrosion Conference & Expo 2017*. NACE International, Publications Division, 2017
8. Kiselev, V.G., Kalyutik, A.A., Makoev, S.O., Fedyukhin, A.V. Main trends in increasing technical and economic efficiency of underground power pipelines cathodic protection. *IOP Conference Series: Earth and Environmental Science* 2019. Pp. 012098. DOI: 10.1088/1755-1315/288/1/012098
9. Kiselev, V., Kalyutik, A., Rouzich, E. Influence of the soil electrical conductivity in the area of the underground pipeline on energy efficiency of the cathodic protection. *International Scientific Conference on Energy, Environmental and Construction Engineering (EECE-2018) electronic edition*. MATEC Web of Conferences. 2018. Pp. 07015. DOI: 10.1051/mateconf/201824507015
10. Kalyutik, A., Kiselev, V., Rouzich, E. Impact of the underground metal construction cover layer on the cathode protection efficiency. *V sbornike: International Multi-Conference on Industrial Engineering and Modern technologies electronic edition*. IOP Conference Series: Materials Science and Engineering. 2018. Pp. 022057. DOI: 10.1088/1757-899X/463/2/022057
11. Kalyutik, A., Kiselev, V., Ruzich, E., Kibarin, A. Features of Russian regulatory framework governing cathodic protection of heating networks against external corrosion in the ground. *E3S Web of Conferences*. 2019. DOI: 10.1051/e3sconf/201914005004
12. Buchler, M., Joos, D. The effectiveness of cathodic corrosion protection under shielding conditions: Disbonded factory applied coatings. *3R- Technical journal for piping system integrity and efficiency*. 2018. No. 1. Pp. 36–51
13. Marshakov, I.K. Thermodynamics and corrosion of alloys: monograph. Voronezh: Voronezh University publishing House, 1983. 168 p.
14. Kiselev, V.G. The Gibbs paradox and its solution. *News of higher educational institutions. Energy Problem*. 2016. No. 11-12. Pp. 129–137. DOI: 10.30724/1998-9903-2016-0-11-12-129-137
15. Keshe, G. Corrosion of metals: a monograph. Moscow: "Metallurgy" publishing house, 1984. 400 p.
16. Tomashov, N.D., Chernova, G.P., Theory of corrosion and corrosion-resistant structural alloys: a monograph. Moscow: "Metallurgy" publishing house, 1986, 358 p.
17. Fetter, K. Electrochemical kinetics: a monograph. Moscow: "Chemistry" publishing house, 1967, p. 856
18. Copson, H.R. Distribution of galvanic corrosion. *Transactions of The Electrochemical Society*. 1943. Vol. 84. No. 1.
19. Mukhametrakhimov, R.Kh., Lukmanova, L.V. Structure and properties of mortar printed on a 3D printer. *Magazine of Civil Engineering*. 2021. 102(2). Article No. 10206. DOI: 10.34910/MCE.102.6

20. Erofeev, V.T., Rodin, A.I., Bochkina, V.S., Ermakov, A.A. Properties of porous glass ceramics based on siliceous rocks. Magazine of Civil Engineering. 2021. 102(2). Article No. 10202. DOI: 10.34910/MCE.102.2
21. Galishnikova, V.V., Kharun, M., Koroteev, D.D., Chidiyghikaobi, P.C. Basalt fiber reinforced expanded clay concrete for building structures. Magazine of Civil Engineering. 2021. 101(1). Article No. 10107. DOI: 10.34910/MCE.101.7
22. Aniskin, N.A., Nguyen, T.C. The effect of formworks on the temperature regime in the mass concrete. Magazine of Civil Engineering. 2020. 99(7). Article No. 9911. DOI: 10.18720/MCE.99.11
23. Chen, X., Li, X.G., Du, C.W., Cheng, Y.F. Effect of cathodic protection on corrosion of pipeline steel under disbonded coating. Corrosion Science. 2017. Vol. 51. Pp. 2242–2245.
24. Qian, S., Cheng, Y.F. Accelerated corrosion of pipeline steel and reduced cathodic protection effectiveness under direct current interference. Construction and Building Materials. 2017. Vol. 148. Pp. 675–685.
25. Xu, L.Y., Cheng, Y.F. Experimental and numerical studies of effectiveness of cathodic protection at corrosion defects on pipelines. Corrosion Science. 2014. Vol. 78. Pp. 162–171.
26. Gadala, I.M. Numerical simulations of soil physicochemistry and aeration influences on the external corrosion and cathodic protection design of buried pipeline steels. Materials and Design. 2016. No. 97. Pp. 287–299.
27. Mitolo, M. Interactions between cathodically protected pipelines and grounding systems. IEEE Transactions On Industry Applications. 2016. No. 52(5). Pp. 3694–3698.
28. Kiselev, G., Kalyutik, A., Derevianko, O. Optimization of the amount of coke filling usage in cathodic protection systems for an anode grounding model in the form of a hemisphere. IOP Conference Series: Materials Science and Engineering, 2018. 463(4), 042059
29. Kiselev, V.G., Sergeev, V.V., Rouzich, E.N. Influence of the electric double-layer capacitance at the rate of corrosion at the phase interface. Corrosion Reviews. 2017. DOI: 10.1515/correv-2016-0049
30. Kiselev, V.G., Alimov, E.V. Manufacture of grounding rods for cathode protection of metal structures. Litejnoe Proizvodstvo. 1997.
31. Ihnatovych, V. Study of the possibility of eliminating the Gibbs paradox within the framework of classical thermodynamics. Preprint at <http://arxiv.org/pdf/1306.5737>.
32. Ihnatovych, V. The logical foundations of Gibbs' paradox in classical thermodynamics. Preprint at <http://arxiv.org/pdf/1305.0742>. 2014.
33. Ihnatovych, V. On the incorrectness of the proof of the Gibbs theorem on the entropy of a mixture of ideal gases, which was given by J. W. Gibbs. Preprint/ 2018. at <http://arxiv.org/pdf/1804.08721>.
34. Ihnatovych, V. Explanation of the Gibbs paradox. URL: <https://zenodo.org/record/2908285>.
35. Ihnatovych, V. Explanation of the Gibbs paradox. Zenodo. 2019. DOI: 10.5281/zenodo.2908285.

Contacts:

Vladimir Kiselev, kis_vg@mail.ru

Aleksandr Kalyutik, AA_Kalyutik@spbstu.ru



DOI: 10.34910/MCE.106.14

Performance of composite connections strengthened with CFRP laminate

M. Ramezani 

University of Alabama at Birmingham, Birmingham, Alabama, USA

E-mail: mramezani@uab.edu

Keywords: finite element method, reinforced concrete, stiffness, bending strength, fiber reinforced plastics, composite materials, retrofitting

Abstract. This paper presents the development of a three-dimensional non-linear finite element model to predict the moment-rotational response of partial depth endplate composite connections. A parametric study is performed to evaluate the influence of utilizing various sizes (i.e., length, width, and thickness) of external Carbon Fiber Reinforced Polymer (CFRP) laminates on the composite connection performance. The numerical analysis reveals that the flexural resistance of the retrofitted CFRP strengthened composite connection increases by up to around 20% and the rotation capacity decreases by approximately 60%. Moreover, the results indicate that applying CFRP laminate to the tension face of the composite slab can reduce the amount of rebar needed for the bending capacity of steel-concrete composite beam-to-column connections.

1. Introduction

Steel and concrete are the two widely used building materials in the construction industry [1], [2]. Each of these materials imparts certain strengths and weaknesses. For example, concrete exhibits low tensile strength and fracture toughness resulting in cracking [3], [4]. Structural steel elements, on the other side, are susceptible to buckling and exhibits poor fire resistance performance. The undesirable properties of these materials can be neutralized when they are combined to form a composite structure. The composite connection may be perceived as the addition of a reinforced concrete slab to the bare steel connection by providing an appropriate mechanism of shear transfer in between the concrete slab and the steel beams [5]. This mechanism is provided using shear studs that are welded to the top flange of the steel beam and embedded in concrete in order to act as a single unit. The key characteristics of composite connections (i.e., moment capacity, rotation capacity and rotational stiffness) are considerably affected by many factors such as joint type, slab depth, reinforcement bar ratio, the degree of shear interaction and load application procedure [6]–[14].

In addition, to maintain the favorable performance of composite connections during their service life, the flawless performance of the steel and concrete components should be continuously provided. In this regard, steel and concrete need special modification and rehabilitation schemes to withstand their primary properties for a long period of time when exposed to service environments. As for instance, it is estimated that developed countries assign approximately 40% of their total construction industry budget for repair and maintenance purposes of the existing infrastructures [15]. In case of a reinforced concrete (RC) structures, the main detrimental factors are the increase in applied loads, corrosion of steel reinforcing bars and unexpected events such as earthquakes. The retrofit of RC elements can be achieved by adding steel or Fiber Reinforced Polymer (FRP) materials including rods [16], [17], plates [18] and innovative systems [19] to the damaged RC element. In the case of retrofitting plates, steel or FRP plates are attached to the surface of the concrete element in such a way that the slip between the connected materials is prevented and they act compositely in carrying the load. The FRP materials are more attractive than steel, primarily due to higher strength-to-weight ratio, resistance to many chemicals and metal-corrosive agents as well as easier

Ramezani, M. Performance of composite connections strengthened with CFRP laminate. Magazine of Civil Engineering. 2021. 106(6). Article No. 10614. DOI: 10.34910/MCE.106.14

© Ramezani, M., 2021. Published by Peter the Great St.Petersburg Polytechnic University.



This work is licensed under a CC BY-NC 4.0

handling and installation. Thus, external bonding of FRP plates has become a widely popular method for the strengthening of different RC structural members such as beams, columns and slabs [20], [21].

An abundance of tests over the last two decades have shown that the bending capacity of flexural members such as RC beams and slabs to be enhanced by applying FRP overlays to their tension face [22], [23]. Parvin and Granata [24], Mosallam [25] and Gergely et al. [26] carried out experimental and numerical studies on the behavior of RC joints strengthened with FRP laminates. The authors reported the increase in the flexural capacity and decrease in the ultimate rotation of joints as a result of FRP strengthening of RC connections. Esfahani et al. [27] and Almusallam et al. [28] examined the effect of reinforcement bar ratio on the behavior of beams strengthened with FRP laminates. They pointed out the enhancement in bending capacity and stiffness of the retrofitted beams. On the other hand, a significant absence of literature exists on the behavior of endplate composite connections strengthened with FRP laminates.

The main objective of this study is to evaluate the moment-rotational response of endplate composite connections including strengthening of the slab using different sizes and thickness of Carbon Fiber Reinforced Polymer (CFRP) laminates attached to the tension face of the slab. To this end, a three dimensional (3D) non-linear finite element model is developed in ANSYS software to perform a parametric study. In addition, various values of reinforcement bar ratio in the slab is considered to investigate the possibility of decreasing the rebar in the presence of the CFRP laminate. This will reduce rebar congestion in the composite joint resulting in cost and time savings in rehabilitation projects.

2. Methods

The Finite Element Method (FEM) is a numerical technique that can be used to solve complicated problems in engineering by breaking down a complex problem into a large number of simple problems. In this section, a short description of the experimental program that was used as the calibration basis for the numerical studies is initially presented. The finite element models are then used in parametric analyses of partial depth endplate composite connections.

The specimen SCJ10 tested by Xiao [13], [14] at The University of Nottingham serves as the base model (un-strengthened model) to compare with those finite element models strengthened with CFRP laminates. The specimen SCJ10 is depicted in Figure 1. Two 305×165×UB40 (beam element) of 1.6 m in length and one 203×203×UC52 (column element) of 1.2 m in height are connected to form the cruciform configuration. The beams are connected to the column flanges at a height of 500 mm by means of partial-depth endplates (190×150×10 mm) welded to the steel beam and bolted to the column flange with two rows of M20 Grade 8.8 bolts. A 120 mm deep slab with RMF CF46 profiled metal decking is used. The slab rebar ratio is 0.8%. Two point loads of the same magnitude are applied symmetrically to each cantilever at 1.5 m from the column flange.

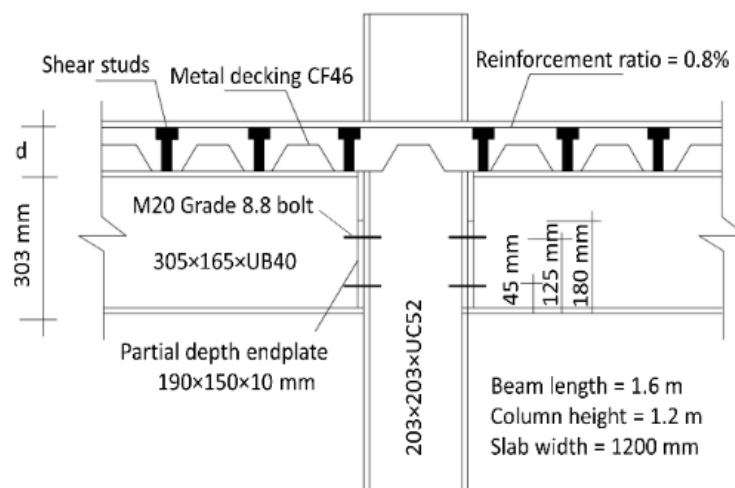


Figure 1. Cruciform arrangement of partial depth endplate composite connection (SCJ10).

In this study, the advantage of the symmetry is used to model the composite connections in order to reduce the problem size. Therefore, it is essential to address the problem with proper boundary conditions. To define the support condition or to establish symmetry, appropriate restraints on nodes or node sets are required. Regarding symmetry about two axes of the cross-section, the concrete-steel composite connections are modeled with half-length (see Figure 2). All nodes on the line of symmetry are restrained against both translation and rotation in the z-axis direction.

The metal deck and beams are modeled with eight-node thin shell elements (SHELL281) and the concrete slab is modeled using a solid element (SOLID185). The SOLID185 element has eight nodes with three degrees of freedom at each node. The element has plasticity, hyper-elasticity, stress stiffening, creep, large deflection and large strain capabilities. The reinforcement bars are modeled using the link element (LINK8) and shear studs are idealized by twenty-node solid elements (SOLID95). The eight-node solid elements (SOLID45) is used to model the column, endplate and bolts.

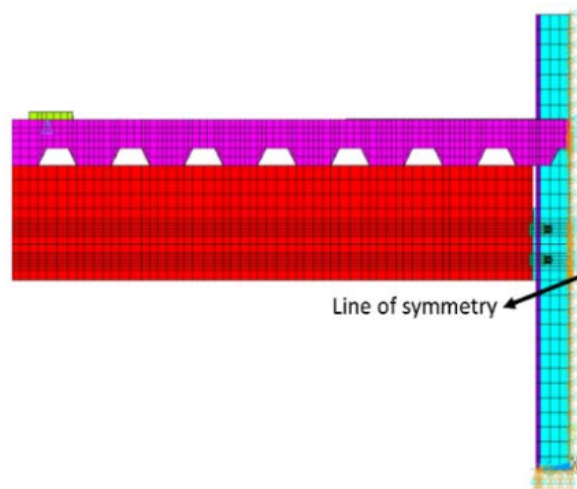


Figure 2. Typical finite element model with Boundary conditions.

The interaction between the metal deck and steel beams is not fully bonded. Thus, surface-to-surface contact elements are used as the interface element between the metal deck and the steel beam to prevent any penetration of steel decking into the steel beam. To model this behavior, the surface-to-surface contact elements, CONTA174 and TARGE170 are superimposed on the surface of the solid or shell elements which form the interface. Each of these “contact pairs” is also capable of representing the slide between the two surfaces activated by defining a friction coefficient. The surface-to-surface contact model also defines the complex interfaces between the endplate and the column flange, the shear studs and concrete as well as the column flange and concrete. The coefficient of friction is assumed equal to 0.45 in this research.

For the material properties, ANSYS requires input of the modulus of elasticity, yield stress and Poisson's ratio. In this study, Poisson's ratio values of 0.3 and 0.2 are used for steel and concrete, respectively. The relationship between the compressive strength of concrete and its tensile strength and modulus of elasticity is expressed as shown in Equations (1) and (2), respectively [29]:

$$f_r = 0.632\sqrt{f'_c} \quad (1)$$

$$E_c = 4700\sqrt{f'_c} \quad (2)$$

where f_r , f'_c and E_c are the tensile strength, compressive strength and modulus of elasticity of concrete, respectively. The compressive uniaxial stress-strain relationship for concrete in the ascending branch to compute the multi-linear isotropic stress-strain curve is calculated using Equations (3) to (5) [30]:

$$f = \frac{E_c \varepsilon}{1 + \left(\frac{\varepsilon}{\varepsilon_0}\right)^2} \quad (3)$$

$$\varepsilon_0 = 2 \frac{f'_c}{E_c} \quad (4)$$

$$E_c = \frac{f}{\varepsilon} \quad (5)$$

where ε is the strain, f is the stress at any strain and ε_0 is the strain at the ultimate compressive strength. The stress-strain behavior adopted for concrete is shown in Figure 3.

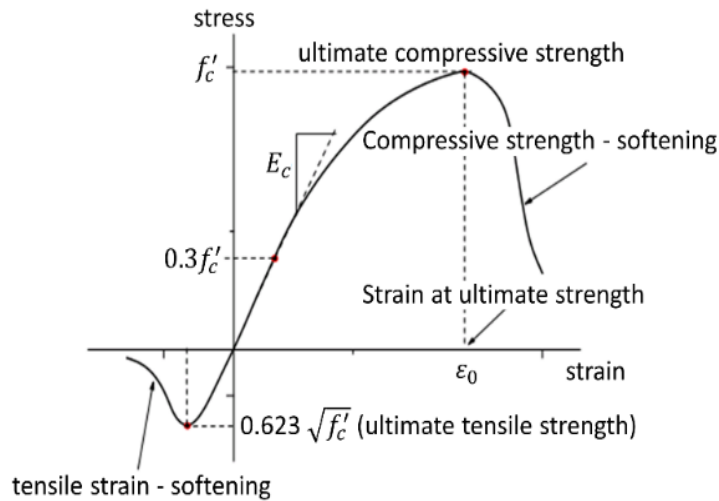


Figure 3. Uniaxial stress-strain curve adopted for concrete.

The shear studs and metal deck are modeled using a bilinear stress-strain curve with the bilinear isotropic hardening option (BISO). The bilinear stress-strain curve is capable of representing elastic-perfectly plastic material behavior with equal yield stresses in tension and compression as well as with the hardening option.

The steel reinforcement is modeled for nonlinear analysis as an elastic-plastic material using a three linear stress-strain law symmetrical in tension and compression (see Figure 4 (a)). An increase of deformation over the elastic limit leads to the exhibition of a yielding plateau phase. After the perfectly plastic branch, strain-hardening behavior initiates. The plastic strain deformation at the end of the yielding plateau (ϵ_{st}) and the modulus of elasticity in the hardening phase (E_{st}) for steel reinforcement bars are obtained using Equations (6) and (7), respectively [31], [32]:

$$\epsilon_{st} = 3\epsilon_{sy} \tag{6}$$

$$E_{st} = 0.02E_y \tag{7}$$

where ϵ_{sy} and E_y are the yield strain and the modulus of elasticity, respectively.

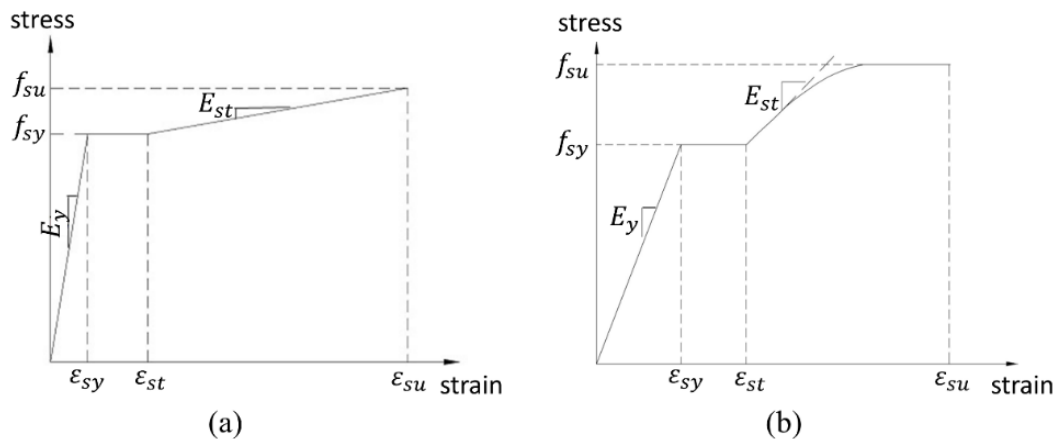


Figure 4. Stress-strain curve for (a) steel reinforcement bars (b) beam, column, bolts and steel deck.

In line with Gattesco [33], other structural steel parts are modeled using a stress-strain relationship that incorporates multi-linear isotropic hardening (see Figure 4 (b)). Amadio and Fragiaco [32] have proposed Equations (8) and (9) for the plastic strain deformation at the end of ϵ_{st} and E_{st} , respectively.

$$\epsilon_{st} = 15\epsilon_{sy} \tag{8}$$

$$E_{st} = 0.015E_y \tag{9}$$

In this research, a 3-D layered structural element (SOLID46) with three degrees of freedom at each node is used to model the CFRP laminates. The element allows up to 250 layers and translation in the x,

y, and z directions. The element is defined by eight nodes, layer thickness, layer material direction angles and orthotropic material properties. This study assumes that the strength of the epoxy used to attach the CFRP laminates to the surface of concrete was sufficiently high to support the full bonded assumption. In line with similar studies [34], [35], the CFRP laminate "MBRACE® laminate 460/1500" with a 71% volume fraction of carbon fiber is adopted for this research. The material properties of the CFRP material are given in Table 1.

Table 1. Material properties of CFRP laminate.

CFRP laminate	Tensile modulus (GPa)	Poisson's ratio	Tensile strength (MPa)	Elongation at break (%)	Thickness (mm)
MBRACE® LAMINATE 460/1500	478.730	0.36	1607	0.36	1.45

3. Results and Discussion

In this section, the moment-rotation curves are plotted using the obtained numerical results. From this curve, the ultimate moment and rotation capacities are determined and compared with the existing experimental test data [13], [14] in order to validate the finite element results. Then, a direct comparison between the strengthened and un-strengthened composite connections are made and the effect of implementing CFRP external reinforcing laminates is studied.

3.1. Model validation

The experimental and numerical moment-rotation curves for the un-strengthened specimen (SCJ10) are compared in Figure 5. The experimental values of ultimate moment and rotation capacities were 147.8 kN.m and 16.5 mRad, respectively [13], [14]. The ultimate moment and rotation capacities obtained from FEM model for SCJ10 are 146.5 kN.m and 16.1 mRad, respectively, which are very close to the experimental test data. Note that both the experimental and FEM curves follow a similar trend. In the initial phase, the connection behaves linearly which is then followed by nonlinear behavior where the connection gradually loses its rotational stiffness as rotation increases.

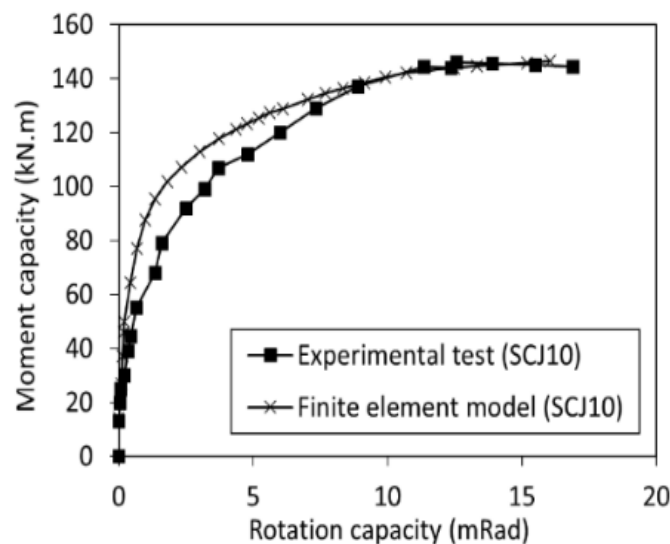


Figure 5. Comparisons between experimental and FEM results.

Also, The failure mode for SCJ10 using FEM shows good correlation with the experimental test results [13]; both experimental and FEM models failed due to the column web buckling (see Figure 6 (a) and 6 (b)). The deformation of the partial depth endplate due to the applied load can also be seen in Figure 6 (c). These confirm the accuracy of the developed finite element model.

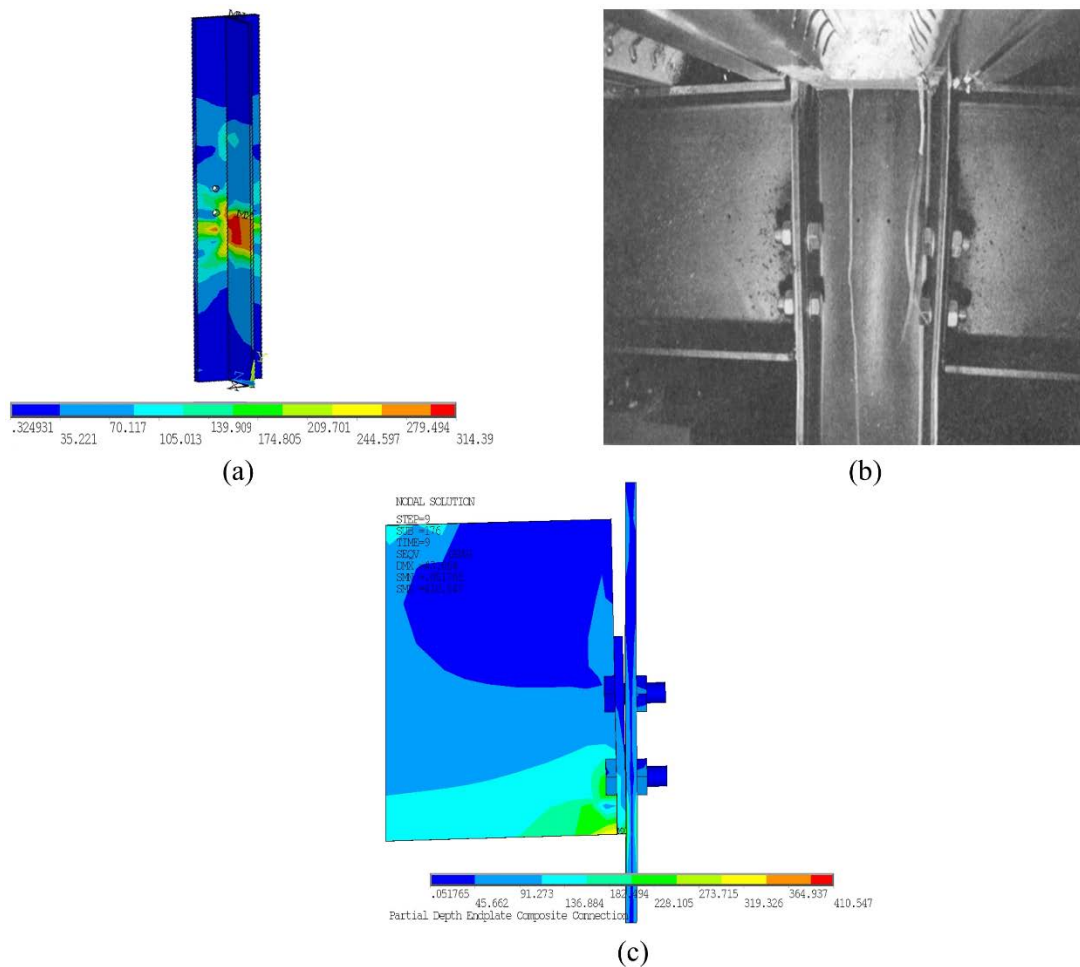


Figure 6. (a) FEM failure mode (b) experimental failure mode (c) deformation of partial depth endplate after FE simulation.

3.2. Parametric study

3.2.1. Effect of CFRP length and width

To investigate the effect of the CFRP laminate dimensions, five models with different widths and lengths are developed. Table 2 shows the configurations of these models. A composite connection without a CFRP laminate is analyzed to serve as a reference model to comparison with those models reinforced with CFRP laminates. In this research, the CFRP laminate have width values between 30% and 60% of the slab width. The length of the CFRP laminate is varied from 20% to 40% of the length of the composite slab. The thickness of the laminates is 1.45 mm.

Table 2. CFRP laminate dimensions.

Test ID	CFRP laminate configuration		
	Width (%slab width)	Length (%slab length)	Thickness (mm)
CFRP W30xL30	30		1.45
CFRP W45xL30	45	30	
CFRP W50xL20	50	20	
CFRP W60xL30	60	30	
CFRP W60xL40		40	

Figure 7 shows a typical FE model of a CFRP laminate applied to the tension face of the partial depth endplate composite connection. A finer mesh is used around the shear studs due to the stress concentration in their vicinities.

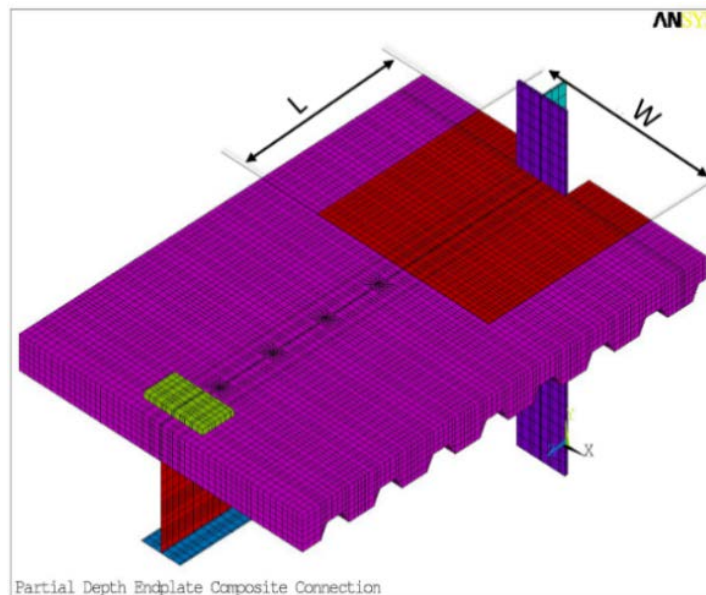


Figure 7. Typical FE model of a composite connection strengthened with CFRP laminate.

The ultimate moments and rotation capacities for un-strengthened and strengthened models with different CFRP laminate configurations is shown in Table 3. Also, the moment-rotation curves for the FE models are presented in Figure 8. The results show that applying CFRP laminate to the tension face of the composite connection will increase the ultimate moment and rotational stiffness of the connection compared with the un-strengthened model. The rotation capacity of the CFRP strengthened connection is considerably lower than the un-strengthened specimen (SCJ10). Moreover, it is clear that the length of the CFRP laminate has greater influence on the moment capacity than its width. For example, the ultimate moment and rotation capacity for test ID CFRP W60xL40 is increased by 8.2% and 9.5% compared with CFRP W60xL30, respectively. In addition, test ID CFRP W50xL20 with the smallest length exhibits the smallest moment capacity amongst all the FE models.

Table 3. FEM results of partial depth composite connections with and without CFRP laminate.

Test ID	Ultimate Moment (kN.m)	Rotation capacity (mRad)
Un-strengthened model (SCJ10)	146.47	16.05
CFRP W30xL30	150.34	6.910
CFRP W45xL30	158.10	6.747
CFRP W50xL20	149.08	7.573
CFRP W60xL30	162.63	6.631
CFRP W60xL40	175.92	7.264

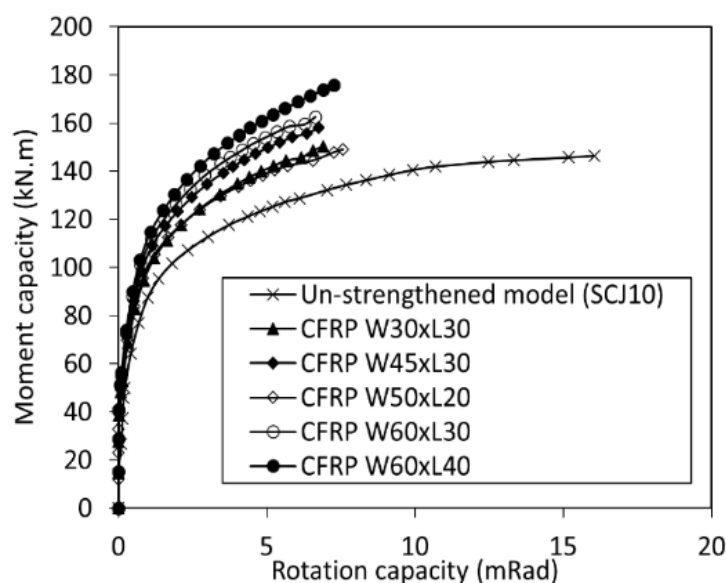


Figure 8. Moment-rotation curves for un-strengthened and strengthened models.

3.2.2. Effect of CFRP thickness

To investigate the effect of the CFRP laminate thickness on the moment-rotation curve of the composite connection, CFRP W60xL40 is modeled with different sheet thicknesses. Table 4 shows the configurations and moment/rotation capacities of the considered models. From the FE results, it can be seen that by increasing the thickness of CFRP sheets, the moment capacity of the composite connection is slightly increased. By increasing the CFRP laminate thickness from 2 mm to 5 mm, the moment and rotation capacities are increased by only 5.5% and 4.5%, respectively.

Table 4. FEM results of various configurations of CFRP reinforced composite connections.

Test ID	CFRP laminate configuration			Moment capacity (kN.m)	Rotation capacity (mRad)
	Width (%slab width)	Length (%slab length)	Thickness (mm)		
CFRP W60xL40			1.45	175.92	7.264
CFRP W60xL40xT2	60	40	2	176.16	6.378
CFRP W60xL40xT5			5	185.82	6.665

3.3. Effect of reinforcement bar ratio

To investigate the influence of the reinforcement bars on the composite connection, test IDs SCJ10xR0.2 and SCJ10xR0.4 with identical joint details but different areas of reinforcement bar from SCJ10 are considered. The reinforcement bar ratios for SCJ10xR0.2 and SCJ10xR0.4 are 0.2 % and 0.4 %, respectively. The results obtained from these finite element models are shown in Table 5. The FEM results indicate that by decreasing the reinforcement bar ratio, the moment capacity is decreased. The moment capacity of SCJ10xR0.4 and SCJ10xR0.2 reduces by 13.6 % and 22.2 %, respectively, compared with test ID SCJ10 (reinforcement bar ratio of 0.8%). However, the rotation capacity of SCJ10xR0.2 is slightly higher than SCJ10xR0.4 (5.8% higher).

As stated previously, one of the main objectives of this study is to investigate the feasibility of decreasing the reinforcing bars in the presence of CFRP laminate at the tension face of the composite connection. Two models of CFRP W60xL40xR0.2 and CFRP W60xL40xR0.4 are therefore considered. The specifications and moment/rotation capacities of these models are shown in Table 5. The moment capacity of test ID CFRP W60xL40xR0.2 is increased by 25.3 % and the rotation capacity is decreased by 64.5 % (rotational stiffness is increased) compared with test ID SCJ10xR0.2. Also, the moment capacity of test ID CFRP W60xL40xR0.4 is 18.5 % more than the moment capacity of its un-strengthened model (SCJ10xR0.4). From the FEA results, it is obvious that CFRP laminate can reduce the amount of reinforcement bars needed to provide the required bending strength of a composite connection.

Table 5. FEM results of various reinforcement bar ratios with and without CFRP laminate.

Test ID	CFRP laminate configuration			Reinforcement bar ratio (%)	Moment capacity (kN.m)	Rotation capacity (mRad)
	Width (%slab width)	Length (% slab length)				
SCJ10xR0.2				0.2	113.93	9.110
SCJ10xR0.4	-	-		0.4	126.60	8.612
SCJ10				0.8	146.47	16.05
CFRP W60xL40xR0.2				0.2	142.77	3.233
CFRP W60xL40xR0.4	60	40		0.4	149.97	3.688

4. Conclusions

The full scale testing of composite connections to obtain the mechanical properties such as the strength and stiffness requires expensive and time-consuming experiments. A straightforward alternative method is to use finite element analysis, yet the numerical results must be verified by available experimental data. In this paper, a three-dimensional nonlinear finite element analysis is carried out using ANSYS software to investigate the influence of various parameters on the moment-rotational response of partial depth endplate composite connections. The comparison between the experimental and finite element results proves that finite element analysis could precisely predict the complex behavior of composite connections. The following conclusions can be drawn:

- The results show that the application of CFRP laminate to the tension face of the slab leads to significant enhancements in flexural strength and stiffness of the partial depth endplate composite connections. Under identical loading conditions, applying external CFRP laminate exhibits 20.1% increase in the ultimate moment and 58.7% decrease in joint rotation, compared with the un-strengthened case.
- Increasing the CFRP laminate thickness can slightly improve the performance of composite beam-to-column connections by reducing the joint rotation and increasing the moment capacity. The increase in the CFRP laminate thickness from 2 to 5 mm results in a slight increase in the flexural strength of the composite connection.
- Applying CFRP laminate to the tension face of the slab can reduce the amount of reinforcement bars needed for flexural capacity of the composite beam-to-column connections by contributing to the tensile force. This will alleviate rebar congestion in the joint and make the whole structure more cost effective.

References

1. Bakis, C.E., Bank, L.C., Brown, V.I., Cosenza, E., Davalos, J.F., Lesko, J.J., Machida, A., Rizkalla, S.H., Triantafyllou, T.C. Fiber-reinforced polymer composites for construction—State-of-the-art review. *Journal of composites for construction*. 2002. 6(2). Pp. 73–87. DOI: 10.1061/(ASCE)1090-0268(2002)6:2(73).
2. Ramezani, M. Design and predicting performance of carbon nanotube reinforced cementitious materials: mechanical properties and dispersion characteristics. *Electronic Theses and Dissertations*. Paper 3255. DOI: 10.18297/etd/3255.
3. Ramezani, M., Kim, Y.H., Sun, Z. Modeling the mechanical properties of cementitious materials containing CNTs. *Cement and Concrete Composites*. 2019. 104. Pp. 1–21 (103347). DOI:10.1016/j.cemconcomp.2019.103347.
4. Ramezani, M., Kim, Y.H., Sun, Z. Mechanical Properties of Carbon Nanotube Reinforced Cementitious Materials: Database and Statistical Analysis. *Magazine of Concrete Research*. 2019. Pp. 1–25. DOI: 10.1680/jmacr.19.00093.
5. Ramezani, M. Finite element model of composite connections strengthened with CFRP laminates. DOI: 10.31224/osf.io/sfkwv.
6. Ahmed, B., Nethercot, D.A. Prediction of initial stiffness and available rotation capacity of major axis composite flush endplate connections. *Journal of Constructional Steel Research*. 1997. 41(1). Pp. 31–60. DOI: 10.1016/S0143-974X(96)00053-3.
7. Anderson, D., Najafi, A.A. Performance of composite connections: Major axis end plate joints. *Journal of Constructional Steel Research*. 1994. 31(1). Pp. 31–57. DOI: 10.1016/0143-974X(94)90022-1.
8. Thai, H.T., Uy, B. Rotational stiffness and moment resistance of bolted endplate joints with hollow or CFST columns. *Journal of Constructional Steel Research*. 2016. 126. Pp. 139–152. DOI: 10.1016/j.jcsr.2016.07.005.
9. Song, Y., Uy, B., Wang, J. Numerical analysis of stainless steel-concrete composite beam-to-column joints with bolted flush endplates. *Steel and Composite Structures*. 2019. 33(1). Pp. 143–162. DOI: 10.12989/scs.2019.33.1.143.
10. Waqas, R., Uy, B., Thai, H.T. Experimental and numerical behaviour of blind bolted flush endplate composite connections. *Journal of Constructional Steel Research*. 2019. 153. Pp. 179–195. DOI: 10.1016/j.jcsr.2018.10.012.
11. Guo, L., Wang, J., Wang, W., Wang, C. Cyclic tests and analyses of extended endplate composite connections to CFST columns. *Journal of Constructional Steel Research*. 2020. 167. Pp. 1–22 (105937). DOI: 10.1016/j.jcsr.2020.105937.
12. Davari, M., Ramezani, M., Hayatdavoodi, A., Nazari, M. Finite Element Analysis of Precast Concrete Connections under Incremental load. *Australian Journal of Basic and Applied Sciences*. 2012. 6(12). Pp. 341–350.
13. Xiao, Y., Choo, B.S., Nethercot, D.A. Composite connections in steel and concrete. I. Experimental behaviour of composite beam-column connections. *Journal of Constructional Steel Research*. 1994. 31(1). Pp. 3–30. DOI: 10.1016/0143-974X(94)90021-3.
14. Xiao, Y., Choo, B.S., Nethercot, D.A. Composite connections in steel and concrete. Part 2—Moment capacity of end plate beam to column connections. *Journal of Constructional Steel Research*. 1996. 37(1). Pp. 63–90. DOI: 10.1016/0143-974X(95)00015-N.
15. Mehta, K., Monteiro, P. *Concrete: Microstructure, Properties, and Materials*. 3rd edn. McGraw-Hill Inc. New York, 2006.
16. Almassri, B., Al Mahmoud, F., Francois, R. Behaviour of corroded reinforced concrete beams repaired with NSM CFRP rods, experimental and finite element study. *Composites Part B: Engineering*. 2016. 92. Pp. 477–488. DOI: 10.1016/j.compositesb.2015.01.022.
17. Almassri, B., Barros, J.A.O., Al Mahmoud, F., Francois, R. A FEM-based model to study the behaviour of corroded RC beams shear-repaired by NSM CFRP rods technique. *Composite Structures*. 2015. 123. Pp. 204–215. DOI: 10.1016/j.compstruct.2014.12.043.
18. Napoli, A., Bank, L.C., Brown, V.L., Martinelli, E., Matta, F., Realfonzo, R. Analysis and design of RC structures strengthened with mechanically fastened FRP laminates: A review. *Composites Part B: Engineering*. 2013. 55. Pp. 386–399. DOI: 10.1016/j.compositesb.2013.06.038.
19. Mosallam, A., Elsanadedy, H.M., Almusallam, T.H., AL-Salloum, Y.A., Alsayed, S.H. Structural evaluation of reinforced concrete beams strengthened with innovative bolted/bonded advanced frp composites sandwich panels. *Composite Structures*. 2015. 124. Pp. 421–440. DOI: 10.1016/j.compstruct.2015.01.020.
20. Huang, L., Yan, B., Yan, L., Xu, Q., Tan, H., Kasal, B. Reinforced concrete beams strengthened with externally bonded natural flax FRP plates. *Composites Part B: Engineering*. 2016. 91. Pp. 569–578. DOI: 10.1016/j.compositesb.2016.02.014.
21. Yuan, X., Zhu, C., Zheng, W., Hu, J., Tang, B. Flexure Performance of Externally Bonded CFRP Plates-Strengthened Reinforced Concrete Members. *Mathematical Problems in Engineering*. 2020. 2020. Pp. 1–15. DOI: 10.1155/2020/2604024.
22. Banjara, N.K., Ramanjaneyulu, K. Investigations on behaviour of flexural deficient and CFRP strengthened reinforced concrete beams under static and fatigue loading. *Construction and Building Materials*. 2019. 201. Pp. 746–762. DOI: 10.1016/j.conbuildmat.2019.01.010.
23. Rashid, K., Li, X., Deng, J., Xie, Y., Wang, Y., Chen, S. Experimental and analytical study on the flexural performance of CFRP-strengthened RC beams at various pre-stressing levels. *Composite Structures*. 2019. 227. Pp. 1–12 (111323). DOI: 10.1016/j.compstruct.2019.111323.

24. Parvin, A., Granata, P. Investigation on the effects of fiber composites at concrete joints. *Composites Part B: Engineering*. 2000. 31(6–7). Pp. 499–509. DOI: 10.1016/S1359-8368(99)00046-3.
25. Mosallam, A.S. Strength and ductility of reinforced concrete moment frame connections strengthened with quasi-isotropic laminates. *Composites Part B: Engineering*. 2000. 31(6–7). Pp. 481–497. DOI: 10.1016/S1359-8368(99)00068-2.
26. Gergely, J., Pantelides, C.P., Reaveley, L.D. Shear strengthening of RCT-joints using CFRP composites. *Journal of Composites for Construction*. 2000. 4(2). Pp. 56–64. DOI: 10.1061/(ASCE)1090-0268(2000)4:2(56).
27. Esfahani, M.R., Kianoush, M.R., Tajari, A.R. Flexural behaviour of reinforced concrete beams strengthened by CFRP sheets. *Engineering Structures*. 2007. 29(10). Pp. 2428–2444. DOI: 10.1016/j.engstruct.2006.12.008.
28. Almusallam, T.H., Elsanadedy, H.M., Al-Salloum, Y.A. Effect of longitudinal steel ratio on behavior of RC beams strengthened with FRP composites: Experimental and FE study. *Journal of Composites for Construction*. 2015. 19(1). Pp. 1–18. DOI: 10.1061/(ASCE)CC.1943-5614.0000486.
29. ACI Committee 318. *Building Code Requirements for Structural Concrete*. Detroit, MI, 2014.
30. MacGregor, J.G., Wight, J.K. *Reinforced concrete: mechanics and design*. 3rd edn. Prentice Hall Inc. Upper Saddle River, New Jersey, 2009.
31. Gil, B., Bayo, E. An alternative design for internal and external semi-rigid composite joints. Part II: Finite element modelling and analytical study. *Engineering Structures*. 2008. 30(1). Pp. 232–246. DOI: 10.1016/j.engstruct.2007.03.010.
32. Amadio, C., Fragiaco, M. Analysis of rigid and semi-rigid steel-concrete composite joints under monotonic loading - Part I: Finite element modelling and validation. *Steel and Composite Structures*. 2003. 3(5). Pp. 349–369. DOI: 10.12989/scs.2003.3.5.349.
33. Gattesco, N. Analytical modeling of nonlinear behavior of composite beams with deformable connection. *Journal of Constructional Steel Research*. 1999. 52(2). Pp. 195–218. DOI: 10.1016/S0143-974X(99)00026-7.
34. Wu, C., Zhao, X., Duan, W.H., Al-Mahaidi, R. Bond characteristics between ultra high modulus CFRP laminates and steel. *Thin-Walled Structures*. 2012. 51. Pp. 147–157. DOI: 10.1016/j.tws.2011.10.010.
35. Wu, C., Zhao, X.L., Chiu, W.K., Al-Mahaidi, R., Duan, W.H. Effect of fatigue loading on the bond behaviour between UHM CFRP plates and steel plates. *Composites Part B: Engineering*. 2013. 50. Pp. 344–353. DOI: 10.1016/j.compositesb.2013.02.040.

Contacts:

Mahyar Ramezani, mramezani@uab.edu



DOI: 10.34910/MCE.106.15

The dependence of the gathering characteristics of nanocarbon cement on the parameters of its production process

A.V. Cherkashin* , A.E. Radaev , Y.A. Olekhovich , K.S. Sulatskiy

Peter the Great St. Petersburg Polytechnic University, St. Petersburg, Russia

*E-mail: jizm@mail.ru

Keywords: building materials, carbon nanostructures, nanotubes, nanofibers, nanocement, approximation, optimization model

Abstract. The article covers issues connected to the justification of the relationship between gathering characteristics of structure-modified materials and parameters of technological processes connected to the materials' production. On the basis of preliminary analysis of experimental data, the procedure has been proposed for formation of analytical dependence of weight gain values for carbon nanotubes and nanofibres on cement particles (with the use of gas-phase synthesis applied to carbon nanostructures) on time parameters of reduction of iron oxide and synthesis of nanostructures directly on the matrix surface. As a base of the mentioned-above dependence, it has been proposed to use a superposition of two components: the linear component defined by the reduction parameter and a logistic component defined by the synthesis parameter. It has been proposed to use optimization modeling tools for the determination of parameters of analytical dependence. On the basis of the results of the procedure, the conclusion has been made about the adequacy of the obtained results and, as a sequence, high practical importance of the proposed analytical dependence. As part of the further stage of the research, it is planned to carry out laboratory experiments and form the corresponding analytical dependences to assess the effect of synthesis modes on the characteristics of the resulting product for alternative matrix cement materials, such as sulfate-resistant cement, magnesia, slag Portland cement, alumina, pozzolanic.

1. Introduction

Modern conditions for the development of the construction industry define the need for the development and application of innovative technologies for obtaining of more efficient construction materials in terms of their operational characteristics [1–3], as well as the cost of manufacturing and installation [4, 5]. At the same time, one of the most promising directions of operational properties improvement for the materials of building structures is modification of cement structure by means of carbon nanostructures integration [6, 7] into it to increase radar absorption capacity and strength of building material [6–8]. In this regard, one of the most important tasks is to determine the relationship between the operational characteristics of structurally modified nanocarbon cement and the parameters of the creation process for the specified construction material. At the same time, the results of scientific works analysis in the corresponding research field showed the limitations of existing tools used for the determination of adequate forecast values of material's operational characteristics on the basis of regulated values of the technological parameters for the material's creation process [9–11, 14–17].

That circumstance determined the feasibility of the research, which aim is to develop tools for determination of the operating characteristics for structurally modified cement on the basis of the

Cherkashin, A.V., Radaev, A.E., Olekhovich, Y.A., Sulatskiy, K.S. The dependence of the gathering characteristics of nanocarbon cement on the parameters of its production process. Magazine of Civil Engineering. 2021. 106(6). Article No. 10615. DOI: 10.34910/MCE.106.15

© Cherkashin, A.V., Radaev, A.E., Olekhovich, Y.A., Sulatskiy, K.S., 2021. Published by Peter the Great St.Petersburg Polytechnic University.



This work is licensed under a CC BY-NC 4.0

technological parameters of the material's creation. To achieve the specified aim, the following tasks have been formulated:

1. Carry out the analysis of the scientific works related to the justification of the relationship between obtained characteristics of structure-modified materials and parameters of technological processes connected to the materials' production.
2. Conduct a series of laboratory experiments to obtain structurally modified cement M500D0 (CEM I 42.5 N) with different characteristics of the technological process connected to the material's creation.
3. Propose an analytical dependence of the acquired characteristics values of the structurally modified material on the values of the technological process parameters connected to the material's production.
4. Propose and implement on the basis of conducted experiments results a procedure for formation of the analytical dependence of acquired characteristics values of the structurally modified material on the values of the parameters for the technological process connected to the material's production.

In this case the research object is the process of creation of the structurally-modified cement (by integration of carbon nanostructures on its particles) as the building material's element providing the improvement of corresponding physical and mechanical properties (in comparison with materials without nanocarbon cement). The research subject is the relationship between the values of the acquired characteristics of the structurally-modified cement and parameters of technological process connected to the material's creation.

The scientific novelty of the research is determined by the composition of considered parameters of the material and technological process for its creation, and also by specific structure of the proposed analytical dependence based on the superposition of linear and non-linear components.

At the initial stages of the research the analysis of the scientific works connected to the research field has been carried out. Detailed description of the main scientific developments is presented in Table 1.

Table 1. The results of the review of scientific papers on the research topic

No	The name of development	The content and features of development
1	Determination of the characteristics of the thermal catalytic steam decomposition (CVD) system for the growth of carbon nanotubes [14]	description of the process of synthesis of carbon nanofibers growth using the Taguchi matrix design using nitrogen as a transport gas; analysis of factors that have the influence on the growth of nanostructures; identification of the factor that has the greatest influence on the growth of nanostructures on the basis of the experiments' results; synthesis with medium temperature
2	Determination of characteristics for the carrier gas to ensure the maximum yield of carbon nanotubes during synthesis with the use of CVD method [15]	analysis of the influence of the flow rate, the composition of the carrier gas (H ₂ , N ₂ , and Ar), and the amount of benzene on the quality and yield of carbon nanotubes created by catalytic vapor decomposition; identification of the carrier gas variant that provides the maximal (most preferred) values of the yield characteristics and the best qualities of carbon nanotubes on the basis of the results obtained during conducted experiments
3	Analysis of the effect of ferrocene on the structure of carbon nanotubes synthesized on the basis of Si / SiO ₂ / Al ₂ O ₃ [16]	analysis of the growth process for multilayer carbon nanotubes under the following conditions: silicon aluminum substrate is used as the matrix base; ethylene is selected as the gas used for nucleation of nanostructures.
4	Direct synthesis of carbon nanofibers on cement particles [17]	identification of ferrocene as a catalyst that provides high purity characteristics of carbon structures on the basis of the experiments' results. analysis of processes connected to the direct synthesis of carbon nanotubes and nanofibers on cement particles; C ₂ H ₂ , CO ₂ , and CO are used as carbon carrier gases; the method of low-temperature and high- performance synthesis that provides a significant increase (in comparison with previously proposed methods) of the characteristics of compressive strength and electrical conductivity for the created structurally modified material.

On the basis of the information presented in Table 1, it has been concluded that scientific works do not include mathematical description (approximation dependence, tendency, extrapolation formula, etc.) of the patterns revealed within conduction of laboratory experiments. Therefore corresponding scientific results cannot be directly used for more complex tasks connected to prediction and optimization. That circumstance confirmed the necessity for the research being conducted.

At the further stages of the research, a series of laboratory experiments assuming the analysis of the operational properties of structurally modified cement of grade M500D0 (CEM I 42.5 N) (by integration of carbon nanostructures on its particles) in conditions of different values of parameters of the technological process connected to the material's creation – growth of carbon nanostructures on the surface of cement powder with the use of the gas-phase synthesis method [9, 14] – has been conducted. The mentioned-above technological process included the following main steps:

1. Preliminary heating of a certain volume of pure cement powder in the furnace in the atmosphere of argon at the temperature of 650 °C.
2. Reduction of iron oxide in cement structure by addition of hydrogen [15] in the argon atmosphere for a certain time – controlled value, hereinafter referred to as reduction parameter.
3. Synthesis of carbon nanostructures on the surface of cement powder by replacement of argon-hydrogen atmosphere with acetylene-hydrogen mixture with ratio of hydrogen to acetylene 8.3:1 within a certain time period [16] – controlled value, hereinafter referred to as synthesis parameter.
4. Creation of fine-grained concrete on the basis of pure cement in combination with nanocarbon cement by mixing with fine aggregate and water.
5. Creation of prototype samples by the placement of produced concrete into mold with subsequent holding of material for several days till its complete hardening and carrying out of physical and mechanical tests with subsequent analysis [7, 13].

It's necessary to note that during the described-above technological process the initial material's weight increase or IMWI (%), caused by the growth of carbon nanotubes and nanofibers, has been considered as one of the key operational characteristics. The corresponding calculation formula is the following:

$$y = \frac{M_1 - M_0}{M_0}, \quad (1)$$

where M_0 , M_1 are the masses of the sample obtained on the basis of pure and modified cement, respectively (g).

The results of the experiments in the form of a three-dimensional plot (surface) of the IMWI value dependence on the reduction and synthesis parameters' values is shown in Table 2 and Fig. 1. It's also necessary to note that the mentioned surface is based on the results of 25 experiments performed with various combinations of values for the reduction and synthesis parameters.

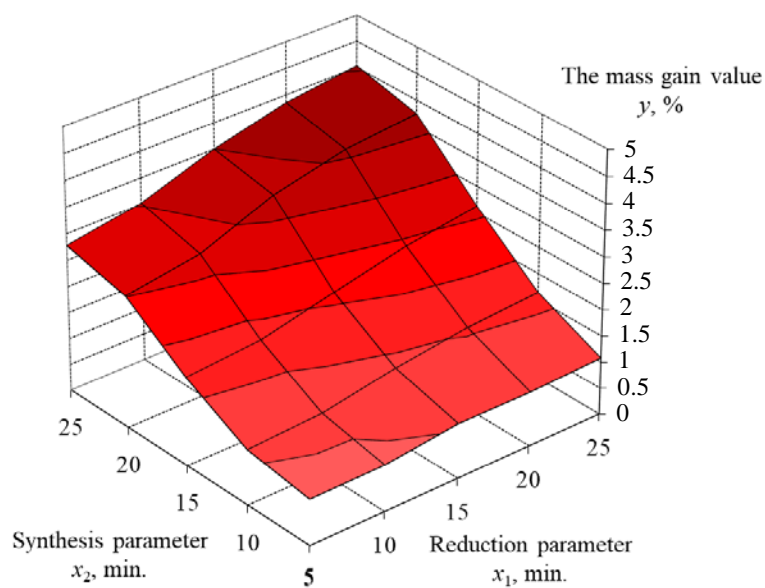
2. Methods

During the next stage of the research the procedure has been proposed for the formation of analytical dependence [14–16] of the IMWI value on the reduction and synthesis parameters' values. The main provisions for the implementation of the procedure are the following:

1. The parameters of reduction and synthesis are considered as the most significant factors determining the IMWI (the influence of the other parameters of the technological process connected to the material's creation on the specified increase value is either absent or negligible).
2. The two-dimensional dependence of IMWI value on the reduction and synthesis parameters' values is monotonically increasing (confirmed by the data presented in Table 2 and Fig. 1).
3. The IMWI value is linearly depends on the reduction parameter value and nonlinearly depends on the synthesis parameter value (confirmed by the data presented in Table 2 and Fig. 1); in the latter case, the corresponding relationship in the Cartesian coordinate system "IMWI – synthesis parameter" is described by an s-shaped curve containing an inflection point (argument values, that are smaller and larger than the abscissa of the inflection point, indicate concavity and convexity, respectively).

Table 2. The results of experiment, shown in analytical form

Experiment number	Value of parameter of the process connected to the creation of the structurally modified material		Initial material's weight increase (IMWI)
	reduction parameter	synthesis parameter	
1	5	5	0.87
2	10	5	0.88
3	15	5	1.04
4	20	5	1.03
5	25	5	1.08
6	5	10	1.05
7	10	10	1.12
8	15	10	1.37
9	20	10	1.55
10	25	10	1.64
11	5	15	1.68
12	10	15	1.79
13	15	15	2.11
14	20	15	2.42
15	25	15	2.62
16	5	20	2.51
17	10	20	2.73
18	15	20	3.28
19	20	20	3.60
20	25	20	3.74
21	5	25	2.78
22	10	25	3.02
23	15	25	3.50
24	20	25	3.85
25	25	25	4.03

**Figure 1. The results of experiments (shown in graphic form).**

4. The analytical dependence of the IMWI value on the reduction and synthesis parameters' values is proposed to be described in the form of a superposition of two components: linear, determined by the value of the reduction parameter, and so-called logistic, determined by the value of the synthesis parameter; the corresponding formula is the following:

$$\tilde{y}(x_1, x_2) = \tilde{y}_1(x_1) + \tilde{y}_2(x_2) = a_0 + a_1 \cdot x_1 + \frac{a_2}{1 + b_2 \cdot e^{-c_2 \cdot x_2}}, \quad (2)$$

where x_1 is the value of reduction parameter (min);

x_2 is the value of synthesis parameter (min);

\tilde{y} is the theoretical IMWI value determined by the reduction and synthesis parameters' values (%);

\tilde{y}_1 is the value of the linear component of the analytical dependence of the IMWI value on the reduction and synthesis parameters' values (%); the component value is determined only by the reduction parameter value;

\tilde{y}_2 is the value of the logistic component of the analytical dependence of the IMWI value on the reduction and synthesis parameters' values (%); the component is determined only by the value of the synthesis parameter;

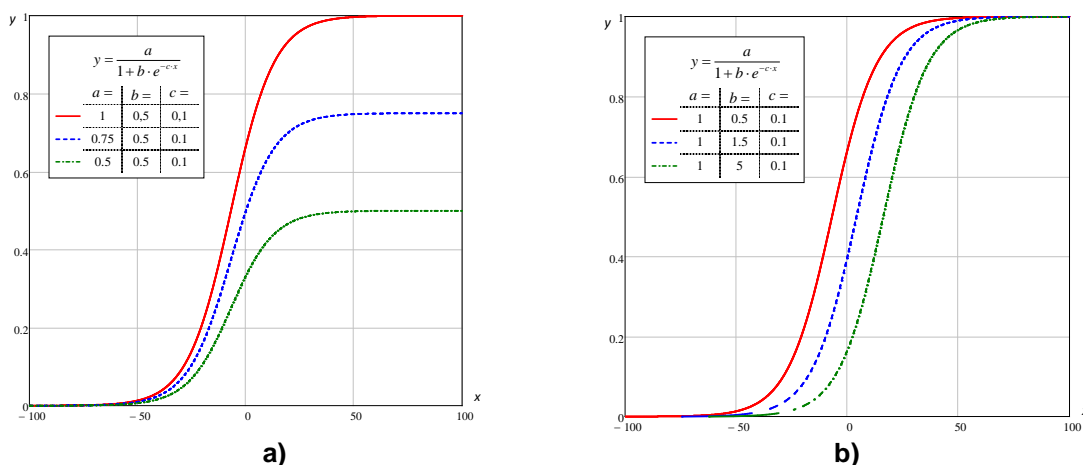
Description of other elements of the formula is given in Table 2 (lines 2.1–2.5); the purpose of parameters a_2, b_2, c_2 of the logistics component of the analytical dependence is illustrated in Fig. 2.

5. The analytical dependence formation of the IMWI value on the reduction and synthesis parameters' values is based on the determination of values for parameters a_0, a_1, a_2, b_2, c_2 of linear and logistical components (see formula (2)) as part of the nonlinear approximation procedure and is performed by building and implementation of the optimization model based on minimization of the sum of squares for deviations of the calculated (theoretical) IMWI values from the respective actual (experimental) values.

6. In order to evaluate the adequacy of the formed analytical dependence, i.e. the degree of compliance of calculated (theoretical) IMWI values obtained on the basis of the specified dependence with the actual values obtained by experiments, it is proposed to use the determination index R ; formed analytical dependence will be able to be used for the calculation of predicted IMWI values on the basis of known values of reduction and synthesis parameters in case of fulfillment of the following condition [21]

$$R \geq 0.9. \quad (3)$$

The description of the source data for the implementation of the proposed procedure, as well as unknown variables of the corresponding optimization model (see paragraph 5 of the main provisions), is given in Table 2. The description of the calculated characteristics enumerated during the procedure's implementation is given in Table 3.



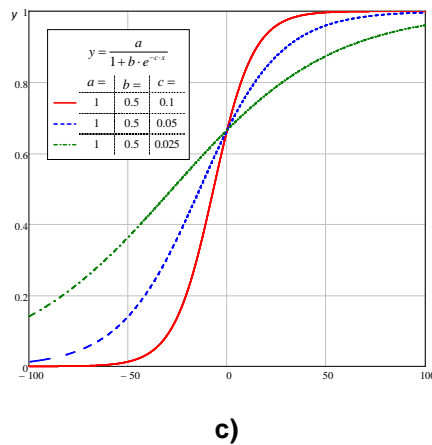


**Figure 2. Main parameters of the logistic function and their purposes:
a) – scale parameter; b) – offset parameter; c) – form parameter**

Table 3. Source data required for the implementation of the procedure and unknown variables of the corresponding optimization model

No	Name of the initial data element / of the unknown variable	Measure unit	Designation / formula
1	Initial data (input parameters)		
1.1	Basic initial data		
1.1.1	Number of measurements	units	m
1.1.2	The share of the actual IMWI value determined by value of reduction parameter [†]	-	Δ_1
1.1.3	The share of the actual IMWI value determined by value of synthesis parameter [†]	-	Δ_2
1.2	Indexes		
1.2.1	Index of experiment	-	$i = 1, 2, \dots, m$
1.3	Characteristics of each experiment i ($i = 1, 2, \dots, m$)		
1.3.1	Reduction parameter value	min.	x_{1i}
1.3.2	Synthesis parameter value	min.	x_{2i}
1.3.3	IMWI value	%	y_i
1.4	Initial values of unknown variables		
1.4.1	Value of the form parameter for the logistic component of the formed analytical dependence ^{**}	min^{-1}	c_2^0
2	Unknown variables ^{***} (output parameters)		
2.1	Value of the offset parameter for the linear component of the formed analytical dependence	%	a_0
2.2	Value of the scale parameter for the linear component of the formed analytical dependence	$\frac{\%}{\text{min}}$	a_1
2.3	Value of the scale parameter for the logistic component of the formed analytical dependence	%	a_2
2.4	Value of the offset parameter for the logistic component of the formed analytical dependence	-	b_2
2.5	Value of the form parameter for the logistic component of the formed analytical dependence	min^{-1}	b_2

Note: [†] – the values of the source data elements must meet the following conditions: $\Delta_1, \Delta_2 \geq 0$; $\Delta_1 + \Delta_2 = 1$; ^{**} – the value of the source data element is determined by the actual IMWI values depending on the values of the reduction and synthesis parameters; ^{***} – in the names of variables, the formed analytical dependence means the dependence of the IMWI value on the reduction and synthesis parameters' values.

Table 4. Calculated characteristics enumerated during the proposed procedure's implementation

No	Name of calculated characteristic	Measure unit	Formula
1	Calculated characteristics for each experiment i ($i = 1, 2, \dots, m$)		
1.1	Actual IMWI value determined by the reduction parameter value	%	$y_{1i} = y_i \cdot \Delta_1$
1.2	Actual IMWI value determined by the synthesis parameter value	%	$y_{2i} = y_i \cdot \Delta_2$
1.3	Theoretical IMWI value determined by the reduction parameter value	%	$\tilde{y}_{1i} = a_0 + a_1 \cdot x_{1i}$
1.4	Theoretical IMWI value determined by the synthesis parameter value	%	$\tilde{y}_{2i} = \frac{a_2}{1 + b_2 \cdot e^{-c_2 \cdot x_{2i}}}$
1.5	The total theoretical IMWI value	%	$\tilde{y}_i = \tilde{y}_{1i} + \tilde{y}_{2i}$
1.6	The share of the calculated IMWI value (in total theoretical value), determined by the value of the reduction parameter*	-	$\tilde{\Delta}_{1i} = \frac{\tilde{y}_{1i}}{\tilde{y}_i}$
1.7	The share of the calculated IMWI value (in total theoretical value), determined by the value of the synthesis parameter*	-	$\tilde{\Delta}_{2i} = \frac{\tilde{y}_{2i}}{\tilde{y}_i}$
2	Generalized calculated characteristics for the entire set of experiments		
2.1	Minimal reduction parameter value	min.	$x_1^{\min} = \min_i \{x_{1i}\}$
2.2	Maximal reduction parameter value	min.	$x_1^{\max} = \max_i \{x_{1i}\}$
2.3	Minimal synthesis parameter value	min.	$x_2^{\min} = \min_i \{x_{2i}\}$
2.4	Maximal synthesis parameter value	min.	$x_2^{\max} = \max_i \{x_{2i}\}$
2.5	Minimal actual IMWI value determined by the reduction parameter value	%	$y_1^{\min} = \min_i \{y_{1i}\}$
2.6	Maximal actual IMWI value determined by the reduction parameter value	%	$y_1^{\max} = \max_i \{y_{1i}\}$
2.7	Minimal actual IMWI value determined by the synthesis parameter value	%	$y_2^{\min} = \min_i \{y_{2i}\}$
2.8	Maximal actual IMWI value determined by the synthesis parameter value	%	$y_2^{\max} = \max_i \{y_{2i}\}$
2.9	The average (among the experiments) share of the calculated IMWI value determined by the reduction parameter value*	-	$\tilde{\Delta}_1 = \frac{\sum_{i=1}^m \tilde{\Delta}_{1i}}{m}$
2.10	The average (among the experiments) share of the calculated IMWI value determined by the synthesis parameter value*	-	$\tilde{\Delta}_2 = \frac{\sum_{i=1}^m \tilde{\Delta}_{2i}}{m}$
3	Initial values of unknown variables		
3.1	Value of the offset parameter for the linear component of the formed analytical dependence**	%	$a_0^0 = y_1^{\min} - a_1^0 \cdot x_1^{\min} =$ $= y_1^{\max} - a_1^0 \cdot x_1^{\max}$
3.2	Value of the scale parameter for the linear component of the formed analytical dependence	$\frac{\%}{\text{min.}}$	$a_1^0 = \frac{y_1^{\max} - y_1^{\min}}{x_1^{\max} - x_1^{\min}}$

No	Name of calculated characteristic	Measure unit	Formula
3.3	Value of the scale parameter for the logistic component of the formed analytical dependence***	%	$a_2^0 = y_2^{\min} \cdot \left(1 + b_2^0 \cdot e^{-c_2^0 \cdot x_2^{\min}}\right) =$ $= y_2^{\max} \cdot \left(1 + b_2^0 \cdot e^{-c_2^0 \cdot x_2^{\max}}\right)$
3.4	Value of the offset parameter for the logistic component of the formed analytical dependence	–	$b_2^0 = -\frac{y_2^{\min} - y_2^{\max}}{e^{-c_2^0 \cdot x_2^{\min}} \cdot y_2^{\min} - e^{-c_2^0 \cdot x_2^{\max}} \cdot y_2^{\max}}$
4	The adequacy indicators for the formed analytical dependence of the IMWI value on the reduction and synthesis parameters' values		
4.1	The sum of squared values of deviations of the theoretical IMWI values from the actual IMWI values	–	$\Delta^\Sigma = \sum_{i=1}^m (\tilde{y}_i - y_i)^2$
4.2	Determination index****	–	$R = \sqrt{1 - \frac{\Delta^\Sigma}{\sum_{i=1}^m \left(y_i - \frac{\sum_{i=1}^m y_i}{m} \right)^2}}$

Note: * – the calculated characteristic is used to assess the deviations of the final share characteristics $\tilde{\Delta}_1$ и $\tilde{\Delta}_2$ (lines 2.9 and 2.10 of Table 3, respectively) for the theoretical IMWI values with the corresponding share characteristics Δ_1 и Δ_2 (lines 1.1.2 and 1.1.3 of Table 2, respectively) for the actual IMWI values; ** – enumeration of the calculated characteristic is based on the results of the calculation of the characteristic described in the line 3.2 of Table 3;*** – enumeration of the calculated characteristic is based on the results of the calculation of the characteristic described in the line 3.4 of Table 3; **** – the calculated characteristic takes values in the interval $[0;1]$ and is used to assess the adequacy of the formed analytical dependence of the IMWI value on the reduction and synthesis parameters' values: the closer the value of the characteristic to the value 1, the greater is the degree of compliance for the actual and theoretical IMWI values.

The structure of the proposed procedure is described by the block-scheme shown in Fig. 3 and has the following distinctive features:

- on the basis of the prepared source data (stage 1) and the generated characteristics (stage 2), the optimization model is constructed and implemented (stage 4), which provides approximation of experimental data (growth rates for carbon nanotubes / nanofibers by the weight of the initial material for different combinations of the values of the reduction and synthesis parameters) on the basis of component analytical dependence (expression (2)); since the mentioned-above optimization model is nonlinear, its implementation with application of standard software (such as "Microsoft Excel", "Mathcad", "Matlab", etc.) assumes the use of the generalized reduced gradient (GRG) method, which requires preliminary setting of the correct initial values for unknown variables of the model – the corresponding operation is performed as part of stage 3 of the procedure;
- based on the results of the optimization model's implementation, the degree of compliance of the theoretical IMWI values with the actual IMWI values is verified (stage 5) in accordance with the condition (3). In case the calculated values are not adequate, the initial data are adjusted in terms of the number of experiments and the corresponding results – the actual IMWI values.

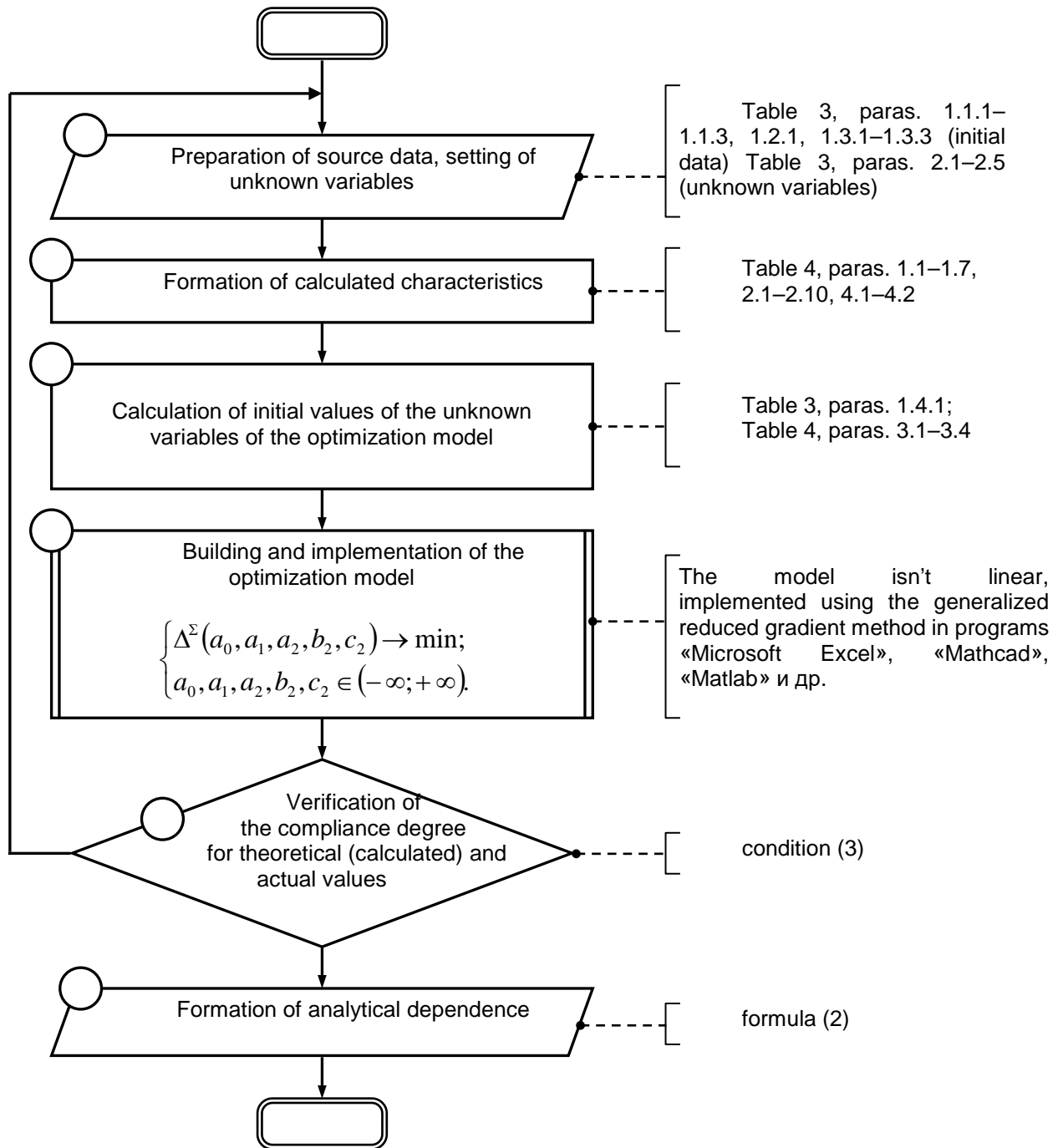


Figure 3. The block-scheme of the proposed procedure for the formation of the analytical dependence of the value of initial material's weight increase (IMWI) on the values of the reduction and synthesis parameters.

3. Results and Discussion

During the final stage of the research, the proposed procedure has been implemented on the basis of the experimental data obtained at the initial stage (see Table 1, Fig. 1). Corresponding process assumed the use of the software "Microsoft Excel" (a workbook has been created, within which one worksheet has been used) and the add-in "Solver" [24] for the direct implementation of the optimization model in accordance with step 4 of the procedure (see the block-scheme in the Fig. 3). The general view of the "Microsoft Excel" worksheet, as well as the principles for filling in the corresponding cells are presented in Fig. 4 and Table 5, respectively. Values of "Solver" add-in parameters used for the implementation of the optimization model are shown in Table 6. The resulting analytical dependence of the IMWI value on the values of the reduction and synthesis parameters' values is determined by the following expression:

$$\tilde{y}(x_1, x_2) = 0.265 + 0.0454 \cdot x_1 + \frac{2.5493}{1 + 222.5493 \cdot e^{-0.3525 \cdot x_2}} \quad (4)$$

A graphical description of the dependence (for the experiments' characteristics in terms of the values of the reduction and synthesis parameters indicated in Table 1) is presented in Fig. 5.

The calculated value of the determination index is $R \approx 0.987$, which satisfies the condition (3) and indicates a high degree of the theoretical IMWI values compliance with the corresponding actual values, and, therefore, the high practical significance of the formed dependence as a tool.

	A	B	C	D	E	F	G	H	I	J	K	
1	Table 1. Initial data connected to the components of the formed analytical dependence											
2	Parameter name			Value for the parameter								
3				reduction parameter	synthesis parameter							
4												
5												
6				Δ_{1j}	Δ_{2j}							
7				-	-							
8	The share of the actual value of gain of UT/UV on the mass of initial cement determined by value of the parameter			0.5	0.5							
9												
10												
11	Table 2. Initial data and calculated characteristics describing the measurement results											
12	Index of measurement	Value of the parameter connected to the process of the creation of structurally modified material		Value for the growth of UT/UV on the mass of initial material						The share of the actual value of the growth of UT/UV on the mass of initial material, determined by the parameter		
13				actual			theoretical					
14				component, determined by the value of the parameter		component, determined by the value of the parameter						
15	reduction parameter	synthesis parameter	total	reduction parameter	synthesis parameter	total	reduction parameter	synthesis parameter	reduction parameter	synthesis parameter		
16												
17												
18												
19	i	x_{1i}	x_{2i}	y_i	y_{1i}	y_{2i}	y_{-i}	y_{-1i}	y_{-2i}	Δ_{-1i}	Δ_{-2i}	
20	-	мин.	мин.	%	%	%	%	%	%	-	-	
21	1	5	5	0.87	0.435	0.435	0.558	0.492	0.066	0.8812	0.1188	
22	2	10	5	0.88	0.44	0.44	0.785	0.719	0.066	0.9156	0.0844	
23	3	15	5	1.04	0.52	0.52	1.012	0.946	0.066	0.9345	0.0655	
24	4	20	5	1.03	0.515	0.515	1.239	1.173	0.066	0.9465	0.0535	
25	5	25	5	1.08	0.54	0.54	1.466	1.400	0.066	0.9548	0.0452	
26	6	5	10	1.05	0.525	0.525	0.836	0.492	0.344	0.5885	0.4115	
27	7	10	10	1.12	0.56	0.56	1.063	0.719	0.344	0.6764	0.3236	
28	8	15	10	1.37	0.685	0.685	1.290	0.946	0.344	0.7333	0.2667	
29	9	20	10	1.55	0.775	0.775	1.517	1.173	0.344	0.7732	0.2268	
30	10	25	10	1.64	0.82	0.82	1.744	1.400	0.344	0.8027	0.1973	
31	11	5	15	1.68	0.84	0.84	1.715	0.492	1.223	0.2869	0.7131	
32	12	10	15	1.79	0.895	0.895	1.942	0.719	1.223	0.3702	0.6298	
33	13	15	15	2.11	1.055	1.055	2.169	0.946	1.223	0.4361	0.5639	
34	14	20	15	2.42	1.21	1.21	2.396	1.173	1.223	0.4895	0.5105	
35	15	25	15	2.62	1.31	1.31	2.623	1.400	1.223	0.5337	0.4663	
36	16	5	20	2.51	1.255	1.255	2.671	0.492	2.179	0.1842	0.8158	
37	17	10	20	2.73	1.365	1.365	2.898	0.719	2.179	0.2481	0.7519	
38	18	15	20	3.28	1.64	1.64	3.125	0.946	2.179	0.3028	0.6972	
39	19	20	20	3.6	1.8	1.8	3.352	1.173	2.179	0.3500	0.6500	
40	20	25	20	3.74	1.87	1.87	3.579	1.400	2.179	0.3912	0.6088	
41	21	5	25	2.78	1.39	1.39	3.008	0.492	2.516	0.1636	0.8364	
42	22	10	25	3.02	1.51	1.51	3.235	0.719	2.516	0.2223	0.7777	
43	23	15	25	3.5	1.75	1.75	3.462	0.946	2.516	0.2733	0.7267	
44	24	20	25	3.85	1.925	1.925	3.689	1.173	2.516	0.3180	0.6820	
45	25	25	25	4.03	2.015	2.015	3.916	1.400	2.516	0.3575	0.6425	
46	Minimum value	5	5	0.87	0.435	0.435	0.558	0.492	0.066	0.164	0.045	
47	Maximum value	25	25	4.03	2.015	2.015	3.916	1.400	2.516	0.955	0.836	
48	Average value	-	-	-	-	-	-	-	-	0.53	0.47	
49												
50	Table 3. Parameters of the formed analytical dependence											
51	Name of the component for the analytical dependence	Name of the parameter	Designation	Measure units	Value							
52					initial	optimal						
53	Linear component	offset parameter	a_0	%	0.04	0.2650						
54		scale parameter	a_1	%/мин.	0.079	0.0454						
55	Logistic component	scale parameter	a_2	-	4.6698	2.5993						
56		offset parameter	b_2	-	16.0505	222.5493						
57		form parameter	c_2	-	0.1	0.3525						
58												
59	Table 4. Characteristics of the adequacy for the formed analytical dependence											
60	Name of the characteristic			designation	Measure units	Value						
61	The total difference of the squared deviations of the theoretical values of the growth of UT/UV on the mass of initial material from the actual			Δ^2	-	0.700051135						
62												
63												
64	Index of determination			R	-	0.986807002						

Figure 4. General view of the worksheet of the "Microsoft Excel" workbook during the implementation of the proposed procedure.

Table 5. The principles of filling of the cells for the worksheet of the "Microsoft Excel" workbook during the implementation of the proposed procedure

Worksheet cell addresses	Formula / comment	Element of procedure	
Table 1			
E8;F8	Cells with the initial data values	Table 2, para 1.1.2, 1.1.3	
Table 2			
A21:A45	Cells with the initial data values	Table 2, paras. 1.2.1	
B21:B45		Table 2, paras. 1.3.1	
C21:C45		Table 2, paras. 1.3.2	
D21:D45		Table 2, paras. 1.3.3	
E21(:F45)		=D21*E\$8	Table 3, paras. 1.1–1.2
G21(:G45)		=H21+I21	Table 3, para. 1.5
H21(:H45)		=\$H\$53+\$H\$54*B21	Table 3, para. 1.3
I21(:I45)		=\$H\$55/(1+\$H\$56*EXP(-\$H\$57*C21))	Table 3, para. 1.4
J21(K45)		=H21/\$G21	Table 3, paras. 1.6, 1.7
B46[:C46;E46;F46]		=MIN(B21:B45)	Table 3, paras. 2.1, 2.3, 2.5, 2.7
D46		=MIN(D21:D45)	-
G46(:G46)		=MIN(G21:G45)	-
B47[:C47;E47;F47]		=MAX(B21:B45)	Table 3, paras. 2.2, 2.4, 2.6, 2.8
D47	=MAX(D21:D45)	-	
G47(:K47)	=MAX(G21:G45)	-	
J48(:K48)	=AVERAGE(J21:J45)	Table 3, paras. 2.9, 2.10	
Table 3			
G53	=E46-G54*B46	Table 3, para. 3.1	
G54	=(E47-E46)/(B47-B46)	Table 3, para. 3.2	
G55	=F46*(1+G56*EXP(-G57*C46))	Table 3, para. 3.3	
G56	=(F46-F47)/(EXP(-G57*C46)*F46-EXP(-G57*C47)*F47)	Table 3, para. 3.4	
G57	the cell with the initial data values	Table 2, para. 1.4.1	
H53:H57	cells with the values of variables into which the calculated values from cells G53:G57 are copied before launching the "Solver" add-in	-	
Table 4			
G61	=SUMXMY2(D21:D45;G21:G45)	Table 3, para. 4.1	
G64	=SQRT(1-G61/(VAR.P(D21:D45)*ROWS(A21:A45)))	Table 3, para. 4.2	

Note: the designation with abstract addresses of cells X1 (:Y10) means that in the cell X1 it is necessary to enter the formula indicated in the corresponding column of table 5, after which the result "stretch" to cell Y10; the designation with abstract addresses of cells X1 [: Y2; Z3] means that in the cell X1 you need to enter the formula indicated in the corresponding column of table 5, then copy the contents of cell X1 and paste it into cells Y2 and Z3 one by one.

Table 6. Parameters of the "Solver" add-in of the "Microsoft Excel" software for the implementation of the optimization model assumed by the proposed procedure for the formation of analytical dependence

No.	Parameter name	Parameter value
1	General parameters	
1.1	Set Objective	\$G\$61
1.2	To:	Min
1.3	By Changing Variable Cells:	\$H\$53:\$H\$57
1.4	Make Unconstrained Variables Non-Negative	[disabled]
1.5	Select a Solving Method	GRG Nonlinear
2	Solving method options	
2.1	Convergence	0,0001
2.2	Derivatives	Forward
2.3	Multi-start Options for Global Optimization	
2.3.1	Use Multi-start	[disabled]
2.3.2	Population Size	100
2.3.3	Random Seed	0
2.3.4	Require Bounds on Variables	[enabled]

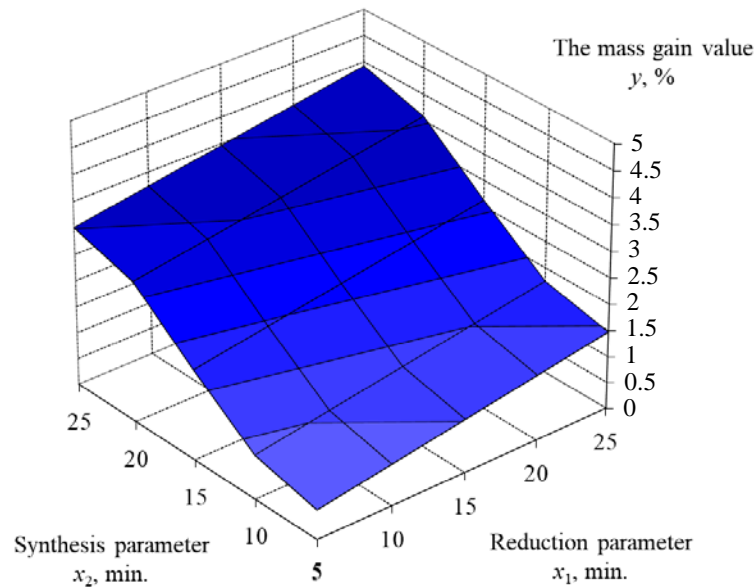


Figure 5. Graphic description of the formed analytical dependence

However, it should be noted that the share indicators $\{\tilde{\Delta}_{1i}\}$ for the calculated IMWI, determined by the reduction parameter value (Table 3, line 1.6), in comparison with the similar rate Δ_1 but for the actual IMWI value, differ from each other by experiments and vary in a relatively wide range – from 0.164 to 0.955 (see Fig. 4). A similar statement (with a slight difference at the borders of the range) is true for share indicators $\{\tilde{\Delta}_{2i}\}$ and Δ_2 , which are related to the synthesis parameter (Table 3 line 1.7 and Table 2 line 1.1.3, respectively). That circumstance is connected to the nonlinear nature of the analytical dependence (Expression (2)) with respect to the synthesis parameter and does not negatively affect the adequacy of the results of the proposed procedure, since the values of fractional indicators Δ_1 and Δ_2 , fixed by measurements, are used only to calculate the initial values of unknown variables of the optimization model with a relatively simple structure of the objective function.

It's also important to note that as there is no description of scientific developments (in published literature related to the research topic) in the field of nonlinear two-dimensional approximation of the experimental results on structurally modified cement in terms of the dependence of IMWI value on the reduction and synthesis parameters' values, the results of the study cannot be compared with the results of other studies in the field of structurally modified building materials.

4. Conclusions

During the performed research the following results have been obtained:

1. Laboratory experiments have been carried out to create structurally modified cement of the initial grade M500D0 (CEM I 42.5 N) with the measurement of the operational characteristics of the final material for various values of characteristics for the technological process of the material's creation.
2. The analytical dependence of the value of weight increase of the initial material from the values of the time parameters connected to the reduction of iron oxide and synthesis of carbon nanostructures has been formed; the dependence includes two components – linear, defined by the time parameter connected to the reduction of iron oxide and logistic, defined by the time parameter connected to the synthesis of carbon nanostructures;
3. Based on the results of the experiments, the procedure for formation of analytical dependence of the value of weight increase of the initial material from the values of the time parameters connected to the reduction of iron oxide and synthesis of carbon nanostructures has been proposed and implemented on a practical case. The obtained results of the procedure's implementation indicate the high adequacy of the formed analytical dependence, and, as a result, the high practical significance of the developed tool.

However, it is important to note that the formation of this dependence has been made on the basis of initial data, which includes a relatively small number of weight increase measurements with unique

combinations of the controlled parameters' values ($m = 25$ units) due to the difficulty of conduction of the corresponding experiments. The specified amount of initial data was sufficient to assess the nature of the dependence and correctly select the structure of the approximating function (Expression (2)). However, the statement that the dependence obtained at the current stage of research (Expression (4)) is a reference for all, without exception, brands of cement obtained by modification of the pure cement on the basis of carbon nanostructures is incorrect due to the insufficient number of experiments.

At the further stages of the research the following measures are planned to be implemented:

- carrying out of additional experiments to increase the number of corresponding measurements and possible clarification of the values of the parameters of the final analytical dependence (formula (4)) based on the results of repeated execution of the proposed procedure for formation of the dependence (block-scheme in Fig. 3).
- analysis of changes in the adequacy of the formed analytical dependence when its structure becomes more complex by adding an additional linear component determined by the value of the synthesis parameter;
- carrying out of laboratory experiments and formation of the corresponding analytical dependences to assess the effect of synthesis modes on the characteristics of the resulting product for alternative matrix cement materials, such as sulfate-resistant cement, magnesia, slag portland cement, alumina, pozzolanic.

5. Acknowledgements

The research is partially funded by the Ministry of Science and Higher Education of the Russian Federation as part of World-class Research Center program: Advanced Digital Technologies (contract No. 075-15-2020-934 dated 17.11.2020).

References

1. Yusuf, M.O. Synergistic-effect of iron-filing and silica-fume on the absorption and shrinkage of cement paste. *Magazine of Civil Engineering*. 2019. 91(7). Pp. 16–26. DOI: 10.18720/MCE.91.2.
2. Shakhov, S.A., Rogova, E.V. Factors affecting the ultrasonic disaggregation of powders. *Magazine of Civil Engineering*. 2019. 88(4). Pp. 14–24. DOI: 10.18720/MCE.88.2
3. Rassokhin, A.S., Ponomarev, A.N., Figovsky, O.L. Silica fumes of different types for high-performance fine-grained concrete. *Magazine of Civil Engineering*. 2018. 78 (2). Pp. 151–160. DOI: 10.18720/MCE.78.12
4. Frolov, A.V., Chumadova, L.I., Cherkashin, A.V., A.L.I. Ekonomichnost ispolzovaniya i vliyaniye nanorazmernykh chastits na svoystva legkikh vysokoprochnykh betonov. *Stroitelstvo unikalnykh zdaniy i sooruzheniy*. 2014. 4 (19). Pp. 51–61. URL: http://unistroy.spbstu.ru/index_2014_19/5_frolov_19.pdf
5. Mastalygina, E.E., Ovchinnikov, V.A., Chukhlanov, V.Y. Light heat-resistant polymer concretes based on oligooxyhydridesilomethylensiloxysilane and hollow spherical fillers. *Magazine of Civil Engineering*. 2019. 90 (6). Pp. 37–46. DOI: 10.18720/MCE.90.4
6. Zhdanok, S.A., Polonina, E.N., Leonovich, S.N., Khroustalev, B.M., Koleda, E.A. Influence of the Nanostructured-Carbon-Based Plasticizing Admixture in a Self-Compacting Concrete Mix on Its Technological Properties. *Journal of Engineering Physics and Thermophysics*. 2019. 92 (2). Pp. 376–382. DOI: 10.1007/s10891-019-01941-7
7. Ponomarev, A.N., Guskov, V.D., Vorontsov, V.V., Ageyev, I.V., Kemenov, L.A., Romanov, A.V., Shegelman, I.R. A new high performance neutron-absorbing materials based on the mineral binder and polymer components. *Magazine of Civil Engineering*. 2012. (9). Pp. 9–13. DOI: 10.5862/MCE.35.1.
8. Lesovik, R.V., Klyuyev, S.V., Klyuyev, A.V., Ntrebenko, A.V., Durachenko, A.V. High-strength fiber-reinforced concrete containing technogenic raw materials and composite binders with use of nanodispersed powder. *Research Journal of Applied Sciences*. 2014. 9. Pp. 1153–1157. DOI: 10.3923/rjasci.2014.1153.1157. URL: <http://docsdrive.com/pdfs/medwelljournals/rjasci/2014/1153-1157.pdf>
9. Cherkashin, A.V., Pykhtin, K.A., Begich, Y.E., Sherstobitova, P.A., Koltsova, T.S. Mechanical properties of nanocarbon modified cement. *Magazine of Civil Engineering*. 2017. 72(4). DOI: 10.18720/MCE.72.7
10. Cherkashin, A.V., Golubkov, A.G., Firsenskov, A.A., Koltsova, T.S. Radar-absorbent composite material for construction applications and method for production thereof. RU2655187C1. 2017.
11. Ziari, H., Amini, A., Goli, A., Mirzaeiyan, D. Predicting rutting performance of carbon nano tube (CNT) asphalt binders using regression models and neural networks. *Construction and Building Materials*. 2018. 160. Pp. 415–426. DOI: 10.1016/j.conbuildmat.2017.11.071
12. Sun, X., Zhao, W. Prediction of stiffness and strength of single-walled carbon nanotubes by molecular-mechanics based finite element approach. *Materials Science and Engineering A*. 2005. 390(1–2). Pp. 366–371. DOI: 10.1016/j.msea.2004.08.020
13. Tang, X., Yan, X. Acoustic energy absorption properties of fibrous materials: A review. *Composites Part A: Applied Science and Manufacturing*. 2017. 101. Pp. 360–380. DOI: 10.1016/j.compositesa.2017.07.002.
14. Nasibulin, A.G., Koltsova, T., Nasibulina, L.I., Anoshkin, I. V., Semench, A., Tolochko, O. V., Kauppinen, E.I. A novel approach to composite preparation by direct synthesis of carbon nanomaterial on matrix or filler particles. *Acta Materialia*. 2013. 61(6). Pp. 1862–1871. DOI: 10.1016/j.actamat.2012.12.007.

15. Barde, A.A., Klausner, J.F., Mei, R. Solid state reaction kinetics of iron oxide reduction using hydrogen as a reducing agent. *International Journal of Hydrogen Energy*. 2016. 41(24). Pp. 10103–10119. DOI: 10.1016/j.ijhydene.2015.12.129.
16. Kraynova, K.A., Yeroshkina, N.A., Korovkin, M.O. Issledovaniye vozmozhnosti primeneniya syrya otechestvennykh proizvoditeley v tekhnologii sukhikh stroitelnykh smesey dlya nalivnogo pola [Investigation of the possibility of using raw materials from domestic manufacturers in the technology of dry building mixtures for self-leveling floors]. *Mezhdunarodnyy nauchno-tekhnicheskiy zhurnal «TEORIYA. PRAKTIKA. INNOVATSI»*. 2017. 5 (17). Pp. 100–105. (rus)
17. Cherkashin, A., Begich, Y., Sherstobitova, P., Semencha, A., Doroshin, I. Heat-resistant properties of construction composites based on nanocarbon cement (nCMC). *E3S Web of Conferences*. 2019. 91. Pp. 3–8. DOI: 10.1051/e3sconf/20199102029
18. Levensov, V., Radaev, A., Salkutsan, S. Mathematic model of production technology transformation. *SHS Web of Conf.* 2018. 00054(44 (2018)). Pp. 1–8.
19. Malyuk, V.I., Radaev, A.E., Silkina, G.Y. Procedure for determining the characteristics for development of industrial enterprises using optimization modeling tools. *St. Petersburg State Polytechnical University Journal. Economics*. 2018. 11 (6). Pp. 195–211. DOI: 10.18721/JE.11617
20. Leventsov, V.A., Radaev, A.E., Nikolaevskiy, N.N. The aspects of the «industry 4.0» concept within production process design. *St. Petersburg State Polytechnical University Journal. Economics*. 2017. 1. Pp. 19–31. DOI: 10.18721/JE.10102
21. Porro, S., Musso, S., Giorcelli, M., Chiodoni, A., Tagliaferro, A. Optimization of a thermal-CVD system for carbon nanotube growth. *Physica E: Low-Dimensional Systems and Nanostructures*. 37(1–2). Pp. 16–20. DOI: 10.1016/j.physe.2006.07.010. (2007)
22. Samant, K.M., Haram, S.K., Kapoor, S. Synthesis of carbon nanotubes by catalytic vapor decomposition (CVD) method: Optimization of various parameters for the maximum yield. *Pramana - Journal of Physics*. 68(1). Pp. 51–60. DOI: 10.1007/s12043-007-0005-9. (2007)
23. Khan, Y., Shukrullah, S., Naz, M.Y., Ghaffar, A., Ahmad, I., Alsuhaibani, S. Ferrocene weight optimization for CVD growth of carbon nanotubes over Si/SiO₂/Al₂O₃. *Digest Journal of Nanomaterials and Biostructures*. 12 (4). Pp. 957–963. (2017)
24. Excel Solver – Define and solve a problem / Frontline Systems.Inc. URL: <https://www.solver.com/excel-solver-define-and-solve-problem>

Contacts:

Artemiy Cherkashin, jizm@mail.ru
Anton Radaev, TW-inc@yandex.ru
Yanis Olekhnovich, oyanis@list.ru
Kirill Sulatskiy, ksulatskiy@mail.ru



ПОЛИТЕХ
Санкт-Петербургский
политехнический университет
Петра Великого

Инженерно-строительный институт
Центр дополнительных профессиональных программ

195251, г. Санкт-Петербург, Политехническая ул., 29,
тел/факс: 552-94-60, www.stroikursi.spbstu.ru,
stroikursi@mail.ru

Приглашает специалистов проектных и строительных организаций,
не имеющих базового профильного высшего образования
на курсы профессиональной переподготовки (от 500 часов)
по направлению «Строительство» по программам:

П-01 «Промышленное и гражданское строительство»

Программа включает учебные разделы:

- Основы строительного дела
- Инженерное оборудование зданий и сооружений
- Технология и контроль качества строительства
- Основы проектирования зданий и сооружений
- Автоматизация проектных работ с использованием AutoCAD
- Автоматизация сметного дела в строительстве
- Управление строительной организацией
- Управление инвестиционно-строительными проектами. Выполнение функций технического заказчика

П-02 «Экономика и управление в строительстве»

Программа включает учебные разделы:

- Основы строительного дела
- Инженерное оборудование зданий и сооружений
- Технология и контроль качества строительства
- Управление инвестиционно-строительными проектами. Выполнение функций технического заказчика и генерального подрядчика
- Управление строительной организацией
- Экономика и ценообразование в строительстве
- Управление строительной организацией
- Организация, управление и планирование в строительстве
- Автоматизация сметного дела в строительстве

П-03 «Инженерные системы зданий и сооружений»

Программа включает учебные разделы:

- Основы механики жидкости и газа
- Инженерное оборудование зданий и сооружений
- Проектирование, монтаж и эксплуатация систем вентиляции и кондиционирования
- Проектирование, монтаж и эксплуатация систем отопления и теплоснабжения
- Проектирование, монтаж и эксплуатация систем водоснабжения и водоотведения
- Автоматизация проектных работ с использованием AutoCAD
- Электроснабжение и электрооборудование объектов

П-04 «Проектирование и конструирование зданий и сооружений»

Программа включает учебные разделы:

- Основы сопротивления материалов и механики стержневых систем
- Проектирование и расчет оснований и фундаментов зданий и сооружений
- Проектирование и расчет железобетонных конструкций
- Проектирование и расчет металлических конструкций
- Проектирование зданий и сооружений с использованием AutoCAD
- Расчет строительных конструкций с использованием SCAD Office

П-05 «Контроль качества строительства»

Программа включает учебные разделы:

- Основы строительного дела
- Инженерное оборудование зданий и сооружений
- Технология и контроль качества строительства
- Проектирование и расчет железобетонных конструкций
- Проектирование и расчет металлических конструкций
- Обследование строительных конструкций зданий и сооружений
- Выполнение функций технического заказчика и генерального подрядчика

По окончании курса слушателю выдается диплом о профессиональной переподготовке
установленного образца, дающий право на ведение профессиональной деятельности

